LONG WAVES IN CHANNELS OF NON-UNIFORM CROSS-SECTION

A Dissertation

Presented to the Faculty of the Graduate School

of Cornell University

in Partial Fulfillment of the Requirements for the Degree of

Doctor of Philosophy

by

Patricio Winckler Grez

January 2015

LONG WAVES IN CHANNELS OF NON-UNIFORM CROSS-SECTION

Patricio Winckler Grez, Ph.D.

Cornell University 2015

A cross-sectionally averaged one-dimensional long wave model is developed. Three dimensional equations of motions for inviscid and incompressible fluid are first integrated over a channel cross section. To express the resulting one-dimensional equations in terms of the longitudinal component of the cross-sectional averaged velocity and span-wise averaged free surface elevation, the characteristic lengths of the channel cross-section in the vertical and transverse directions are assumed to be smaller than the typical wavelength, resulting in the Boussinesq-type equations. The effects of viscous damping are also added in a heuristic manner.

The new model is, therefore, adequate for describing weakly-nonlinear and weakly-dispersive waves along a channel of arbitrary non-uniform cross-section. More specifically, the new model has the following new capabilities: *i*) The arbitrary channel cross-section can be asymmetric with respect to the direction of wave propagation, *ii*) the channel cross-section can change significantly within a wavelength, *iii*) the effects of viscosity inside the bottom boundary layer can be considered, and *iv*) the three dimensional flow features in a cross-section can be recovered from the perturbation solutions.

Analytical and numerical examples for uniform channels, channels where the cross-sectional geometry changes slowly and channels where the depth and width variation is appreciable within the wavelength scale are discussed to illustrate the scope of applicability of the present theory. By considering viscous

boundary layer effects, the theory agrees well with experimental results for converging and diverging channels (Chang *et al.*, 1979) and with experiments in a uniform channel with a sloping beach (Liu *et al.*, 1979). The results for a solitary wave propagating in a channel in which the width variation is important within the wavelength are discussed.

Curvature is introduced by means of orthogonal curvilinear coordinates following the channel. The resulting one-dimensional cross-sectional averaged equations contain new coefficients depending only on the geometry of the channel. To the level of approximation considered, these equations do not capture the free surface tilting due to curvature and show that the wave field is locally affected by the magnitude and sign of the curvature.

The theory provides practical model equations for calculating long waves (e.g. tsunamis, tides or flood) propagation in fjord or river, which could have compelling applications in the field of hydraulics and coastal engineering. As an example, for long distance propagation of landslide tsunami in fjords, travel-times and maximum wave heights can be rapidly estimated from one-dimensional governing equations, making the present theory suitable for warning systems.

BIOGRAPHICAL SKETCH

Patricio Winckler was born in Valparaíso, Chile, on October 15^{th}, 1974. He earned a civil engineering degree from Universidad Técnica Federico Santa María, Chile (2002), a MSc. in Environmental Technology from University of Wolverhampton, England (2002), and a Master in Port and Coastal Engineering at the Centro de Estudios y Experimentación de Obras Públicas, Spain (2004). After years working as coastal engineer in the South African consulting firm PRDW, in 2005 he joined the Ocean Engineering Group at Universidad de Valparaíso to begin his career in academia. In 2010 he joined the PhD. program in civil engineering with specialization in environmental fluid mechanics, under the guidance of Prof. Philip Liu at Cornell University. His research interest is coastal engineering, ranging from environmental conditions to the design of coastal works. As a complement to his professional carrier, he has participated in various art exhibitions in Chile, Finland and the United States.

I dedicate these words to Claudia, Tomás and Martina,

for the magical days in Ithaca.

ACKNOWLEDGEMENTS

It is a pleasure to thank all those who made this story possible. First and foremost, to Professor Philip Liu, whose guidance and patience made this a formidable stay in Ithaca. His profound knowledge of fluid mechanics has significantly impacted my own understanding of these and other subjects; though perhaps the most significant lesson I get from him is the need to question every established fact, critically think and never rest in the pursue of scientific truth.

I am also honored to my thesis committee members. Professor Bill Philpot, an exceptionally kind person, provided guidance on the field of remote sensing I aim to use in the near future. Professor Matthew Pritchard played a significant role in introducing the subjects of seismology and tectonics. Professor Jim Jenkins gave me the chance to enjoy his exquisite lectures on natural particle flows and in many ways he taught me how to learn from and interact with students.

I'd also like to recognize the people at the School. To Professor Peter Diamessis for his music, thoughts and humanity; to Professor Todd Cohen for his electrifying lectures and to Professor Willfred Brutsaert for helping me to decode my genealogical tree, among other interesting findings. I also express my gratitude to Professor Chiang C. Mei, from MIT, for the guidance on an initial research on mixing properties in the surf zone, carried out during the first two years of the program.

These years at Cornell have been delightful with the company of Blair Johnson, Qi Zhou, Jorge Escobar, Allie King, Yong Sung Park, Erika Johnson, Seth Schweitzer, Peter Lo, Che-wei Chang, Gustavo Rivera, Fahad Mohammed and specially Ignacio Sepúlveda. I will definitely miss those never-ending and often controversial chalkboard conversations with Mahmoud Sadek, Nimish Pujara and Jose Gonzalez-Ondina, and the scientific and not so scientific discussions

with Professor Atle Jensen and his family during their stay in Ithaca. Thanks to Jeff Daves for those daily conversations on the mysteries of American culture and to Tania Sharpsteen and Jeannette Little for the many little things that made life comfortable in Hollister Hall.

I acknowledge the financial support of Fulbright, CONICYT (Becas Chile) and Cornell University; and express gratitude to the people of the School of Ocean Engineering at Universidad de Valparaíso, who kindly assumed my duties in these almost five years at Cornell.

To our friends Beto and Sol, Amir and Margo, Isabel and Santiago, Alegna and Armando, Keka and Marcial, Silvano and Elsa, and all their little ones for the best days of our lives in Westview. I'm infinitely grateful to my parents Huguito and Mariana for the unconditional love and support in the early days, and to Alice for being as she is. I'd like to thanks my friend and mentor Javier Vasquez for his contagious passion for coastal engineering in those early days.

Finally, thanks to my beautiful Claudia and our little kids Tomás and Martina, who came as little ones and grew to become adorable individuals in this wonderful land. Claudia's support has been unconditional all these years and this achievement is definitely ours.

TABLE OF CONTENTS

LIST OF TABLES

LIST OF FIGURES

CHAPTER 1

INTRODUCTION

1.1 Scope of the dissertation

The study of surface gravity waves in channels of arbitrary geometry is relevant in many engineering applications, such as tsunami wave propagation in fjord systems, storm surge penetration in estuaries, ocean waves in river mouths and iceberg calving in fjords systems. Understanding long wave dynamics in channels becomes an important task in the design of effective counter-measures against overtopping in coastal facilities or planning tsunami disaster prevention schemes, among other mitigation measures.

Existing theories for long wave propagation in channels reduce the three-dimensional phenomena to fewer dimensions by *i*) depth averaging or *ii*) by averaging on the channel's cross-section. The former approach gives rise to two-dimensional forms, such as the Nonlinear Shallow Water or Boussinesq Equations, whereas the latter results in one-dimensional theories. Among their advantages, these theories do not require solving the moving boundary problem at the sidewall shoreline (making the solution independent of wetting-drying techniques) and provide a quick tool to evaluate bulk wave properties. In contrast, they fail to reproduce complex surface patterns which may arise when curvature or branching is present on the channel.

Existing one-dimensional theories for channels of arbitrary cross-section (Peters, 1966; Peregrine, 1968 and 1969; Shen, 1969; Fenton, 1973; Shuto, 1974; Chou, 1981; Kirby & Vengayil, 1988; Teng, 1990 and 2000; Teng & Wu, 1992,

1994 and 1997) incorporate frequency dispersion and cross-sectional effects in the conservation laws. The most relevant gap however, is that none of them is able to account simultaneously for *i*) non-uniform arbitrary cross-sections and *ii*) appreciable changes of channel geometry within the wavelength scale in the direction of wave propagation, which together are commonly found in real cases such as fjords, estuaries or natural streams.

To fill this gap, a theory for long waves propagating in a straight channel with arbitrary cross-sections is developed and checked with experimental data. The theory is constructed by integrating the three-dimensional equations for irrotational flows over the channel cross-section and applying the boundary conditions on the free surface and channel bottom. To obtain a set of one-dimensional governing equations in terms of the cross-sectionally averaged velocity in the direction of wave propagation, $\langle u \rangle$, and the spanwise averaged free surface elevation, $\widetilde{\eta}$, the Boussinesq approximation is adopted. In addition, the channel's sidewall slopes are assumed to be of order one. The resulting equations are of the Boussinesq-type with coefficients that depend on the configuration of the channel cross-section, which can be precomputed once the bathymetry is prescribed. Velocity components, pressure and surface elevation on a cross-section are recovered from higher order approximations in the perturbation scheme and can be calculated once Boussinesq-type equations are solved.

The present theory can be simplified to Teng & Wu's (1997) theory in the case of symmetric channels with slowly-varying geometry in the longitudinal direction, to Peregrine's (1968) for uniform channels of arbitrary cross-sections and to Shuto's (1974) theory for rectangular channels with slowly-varying width and depth.

The effects of viscous damping through the channel's bottom boundary layer are heuristically included following Liu & Orfila's (2004) approach, assuming the free-stream velocity corresponds to the cross-sectionally averaged velocity $\langle u \rangle$. The boundary layer flow is driven by the cross-sectionally averaged pressure gradient in the direction of wave propagation, and induces a normal mass flux into the core region where the velocity is essentially irrotational. Thus, the continuity equation is modified by adding the mass flux across the channel boundary, which has the form of a convolution integral. The effects of the surface boundary layer, on the other hand, are neglected. This analytical approach is solely appropriate for small-scale laboratory experiments where the boundary layer remains laminar. Other cases requiring the implementation of turbulent models or bottom friction are not covered in this dissertation.

To illustrate the capability of the theory, analytical and numerical examples for uniform channels, channels where the cross-sectional geometry changes slowly and channels where the depth and width variation is appreciable within the wavelength scale are presented. These cases are characterized by $dA_0/dx = 0$, $O(\epsilon)$ and $O(1)$, respectively, A_0 being the cross-sectional area under the quiescent state, ϵ a small parameter representing nonlinearity and x the coordinate along the channel. The theory is used to investigate solitary wave propagation in straight uniform channels with rectangular, triangular and trapezoidal cross-sectional shapes. Numerical computations show marked changes in the surface elevation along the spanwise direction for trapezoidal and triangular cross-sections, earlier observed in experiments (Sandover & Taylor, 1962; Peregrine, 1969; Treske, 1994 and Teng & Wu, 1997). Some complex three-dimensional flow features reported by other authors however (e.g. Sandover & Taylor; 1962; Fenton, 1973 and Treske, 1994), cannot captured by the theory.

The present theory is then validated with experiments for solitary wave evolution in converging and diverging rectangular channels, in which the width changes linearly (Chang *et al.*, 1979). The theory is used in its irrotational form to isolate the contribution of the new terms containing α and β, both parameters depending on the cross-sectional geometry. Viscous effects are then included to compare to Chang *et al.*'s experiments. Teng & Wu's (1997) theory for symmetric cross-sections with slowly-varying changes in the channel's geometry is used for comparison. The contributions of the new terms containing α and β are found to be relatively small as a consequence of the slowly-varying condition in the experiments. Consequently, the present and Teng & Wu's (1997) theories provide comparable results; both overestimating the wave amplitudes throughout the channels. The role of viscous dissipation is shown to be relevant in explaining the differences between theory and experimental data.

Another set of experiments (Liu *et al.*, 2006) is used to show that viscous damping and wave shoaling are well represented by the present theory within both the uniform section of a rectangular channel and the sloping beach.

By means of a hypothetical case where solitary waves propagate through a uniform channel where the length contraction is comparable to the wavelength, the role of the new terms containing α and β is proven to be significant. The relative difference in wave amplitude estimated by the present and Teng & Wu's (1997) theories can be of the order of 10% after a contraction of a length comparable to the wavelength. This deviation is strongly dependent on the nonlinearity and the cross-sectional geometry. Though the present theory is expected to better describe long wave evolution in channels with rapid cross-sectional changes in geometry, no experiments are available for comparison.

The effects of curvature are studied in channels where the radius of curvature is significantly larger than the typical wavelength. The derivation is based on a system of orthogonal curvilinear coordinates following the channel. The resulting one-dimensional cross-sectional averaged equations explicitly contain the curvature and new coefficients which can be computed based on the geometry of the channel. To the order of approximation used, these equations do not capture the free surface tilting due to curvature. However, curvature is implicitly included in the coordinate system tracing the channel. It is concluded that the wave field is locally affected by the magnitude and sign of the curvature, and that cumulative effects of curvature are minor in meandering channels.

1.2 Structure of the Dissertation

The dissertation is structured as follows. Chapter 2 reviews the current state of the knowledge and analyzes some of the existing theories. This chapter is complemented with Appendix A, where a comprehensive analysis of the existing one-dimensional theories for weakly nonlinear weakly dispersive waves is included.

Chapter 3 introduces the basic governing equations of the potential flow theory where the forcing through ambient pressure, the effects of moving bottom and viscous effects are neglected. The cross-sectional averaged equations for waves propagating in the longitudinal direction are obtained after invoking the Boussinesq approximation. Analytical expressions for the velocity components in the spanwise and vertical dimensions, pressure and surface elevation on a cross-sectional plane are also proposed.

The numerical tools developed to solve both *i*) cross-sectional boundary value problems and *ii*) the Boussinesq-type equations for the longitudinal flow are introduced in Chapter 4. Numerical experiments for benchmark cases are carried out to validate the numerical schemes.

In Chapter 5, analytical and numerical examples for uniform channels, channels where the cross-sectional geometry changes slowly and channels where the depth and width variation is appreciable within the wavelength scale are presented. These examples are carried out to compare the present results with Teng & Wu's (1997) theory and to investigate the features of long waves propagating along channels of arbitrary cross-section.

In Chapter 6 the theory is extended to account for the effects of viscous damping occurring along the channel's wetted perimeter. Results are compared to experimental data for converging and diverging channels of constant depth (Chang *et al.*, 1979) and to a sloping channel of a constant width (Liu *et al.*, 2006).

An attempt to incorporate the effects of curvature is included in Chapter 7. The extended theory is valid for channels where the typical wavelength is small compared to the local radius of curvature. Due to lack of experimental data, simple examples are discussed to illustrate the implications of the new terms stemming for the curvature.

The main outcomes of the dissertation are discussed in Chapter 8. A comprehensive set of Appendices is also included. With the exception of Appendices A and G, they consist of detailed derivations and analysis of mathematical expressions used throughout the dissertation. A compatibility condition is derived in Appendix G to solve for the flow field in branching channels.

1.3 Motivation

One-dimensional theories for long waves in channels of arbitrary geometry may be used in a variety of problems. As an example, for long distance propagation of landslide tsunami in fjords, travel-times and the amplitude of the leading wave can be rapidly estimated from one-dimensional governing equations, making the one-dimensional theory suitable for warning systems. The theory would also be applicable to river dynamics, flood and tidal waves in estuaries, and nearshore coastal engineering, among other phenomena. A few examples are discussed in this section.

1.3.1 Landslide tsunamis

Landslide are largely known to generate destructive waves in fjords, reservoirs and rivers. Fjords are usually characterized by very intricate geomorphology with sharp turns and bifurcations. Landslides are common and can generate large waves that propagate long distances through the fjord network. Historical records indicate that wave runups can be of several tens of meters (e.g. Harbitz *et al.*, 2014).

The evolution of a landslide tsunami from its generation to its propagation in the far field is schematized in Figure 1.2. In the near source, the interaction between the landslide and the water body is important and extremely complex due to wave breaking, turbulence and air entrainment. The leading waves can be affected by frequency dispersion and nonlinearity when the landslide speed is large. As waves propagate from the source region, wave amplitude decays as

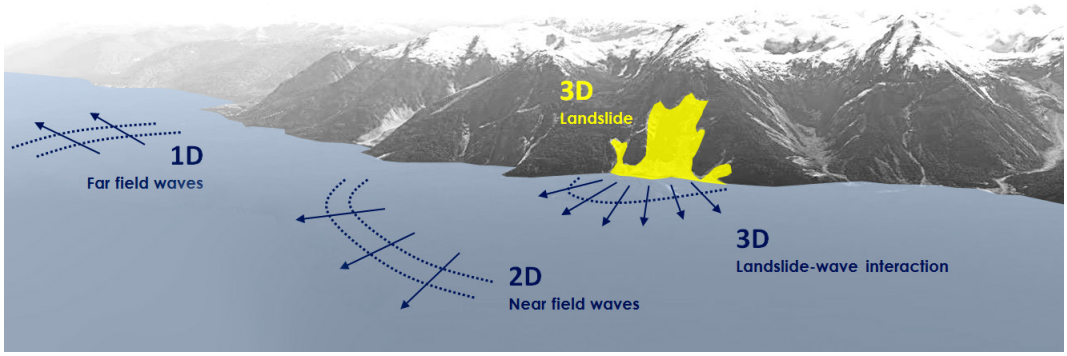

Figure 1.1: Different stages of landslide tsunami generation and propagation.

the consequence of directional spreading and larger water depths throughout the fjord system. Hence, waves evolve to a regime where both dispersion and nonlinearity become weaker, but not negligible. The flows in this regime tend to become almost one-dimensional, with wave fronts that are approximately perpendicular to the main axis of the fjord. Therefore, the main flow features may be captured by a set of cross-sectionally averaged equations for weakly-nonlinear weakly-dispersive waves. This wave regime is the focus of present research.

Numerical modeling of landslide-generated tsunamis in complex fjord systems is a challenging task (Brocchini, 2013). The computation of landslide tsunamis over complex bathymetries can be achieved by coupling landslide models, open-fjord propagation models with appropriate degree of nonlinearity and dispersion and the near-shore inundation models (Harbitz *et al.*, 2014). The scientific challenge of such an approach is on the coupling of different hydrodynamic models in which the boundaries and the cross-sectional distribution of the velocity, among other flow features, are treated differently. The present theory could be used in this context to characterize the far field propagation at a low

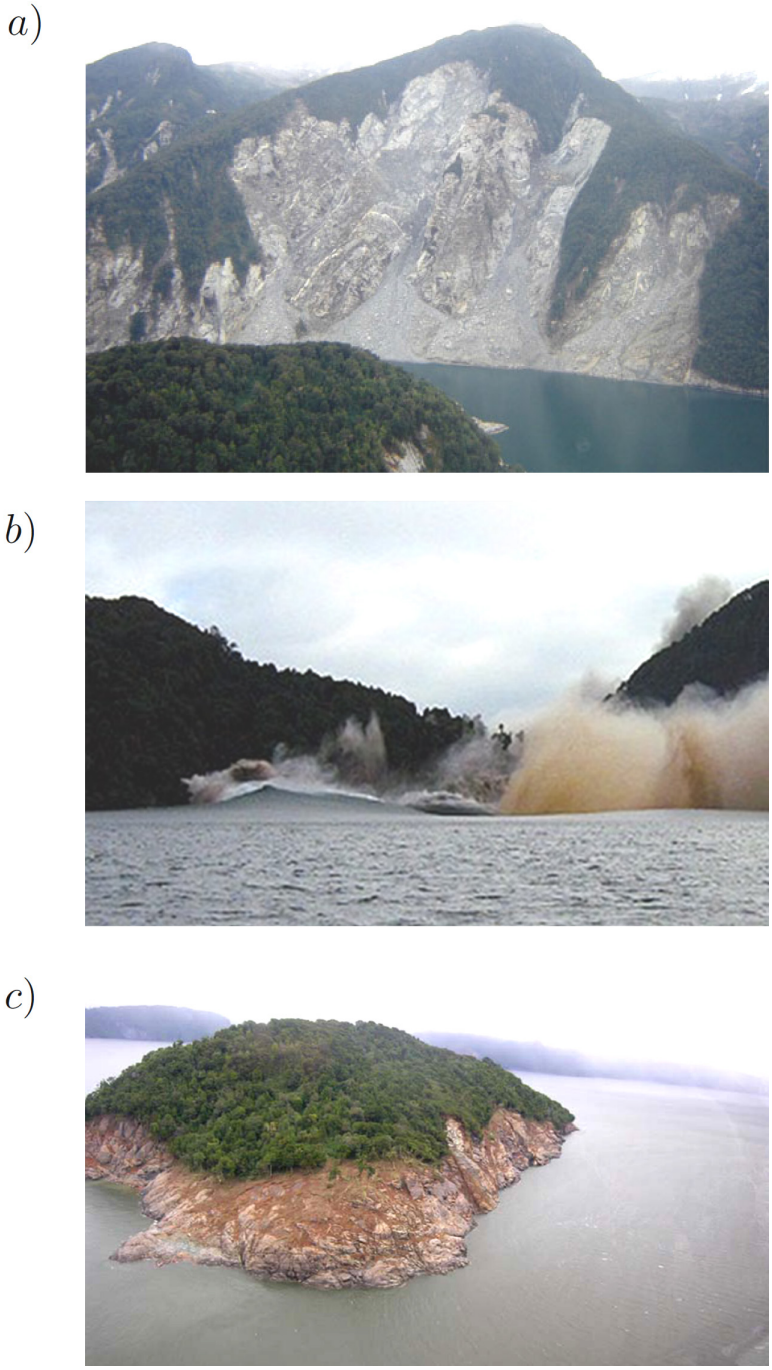

Figure 1.2: Images of the April 2007 tsunami generated by a series of landslides in Aysen fjord, Chile. *a*) Solid rock slide of 71 millions m^3 in front of Mentirosa Island (Naranjo et al., 2009; Sepulveda et al., 2010). *b*) The first wave impacting Isla Mentirosa's eastern coast with elevations of around 15 m (Naranjo et al., 2009). *c*) Runup in Isla Mentirosa (courtesy of Dante Gutierrez).

computational cost, in conjunction with two- or three-dimensional models characterizing the source and runup.

An outstanding example is the 21^{st} April 2007 tsunami generated by a series of landslides in Aysen fjord, Chile. The landslides were triggered by a 6.2 earthquake following 2 months of intense seismic activity. As a consequence of the tsunami 10 people died, salmon cages were destroyed and various houses were washed away. Maximum runups of 50 m were measured in Isla Metirosa, located in the vicinity of one of the landslides (SERNAGEOMIN, 2007), and waves propagated through the fjord for about 14 km to reach Puerto Chacabuco. Figure 1.1 shows photographs of this event.

1.3.2 Tsunamis in rivers

Large tsunamis occurring in the last decade have caused severe damage to hydraulic facilities and riverine towns (Adityawan *et al.*, 2013). Understanding tsunami propagation in rivers is therefore essential for disaster prevention and warning systems. The evolution of tsunamis in rivers is usually initiated by the attack of an earthquake-generated tsunami offshore, which evolves into a bore-shaped wave in the nearshore. An example of the complex hydrodynamics, large velocities and local effects involved is depicted in Figure 1.3, where the leading wave of the 2011 Tohoku tsunami entered Kido river, Japan.

As waves advance along the river, meandering, branching, the presence of embankments and the flow discharge may play a significant role in wave propagation along rivers. Waves on the water body may reach significant distances when compared to overland flow, due to the lower friction of the river bottom.

Figure 1.3: Leading wave of the 2011 Tohoku tsunami entering Kido river (37°15′59″N 141°00′53″E), approximately 16 km south of Fukushima Daiichi Nuclear Power Station, Japan. Images are depicted approximately every 10 s. (Images extracted from a video available at www.youtube.com / watch?v=z0rYqoY5drA).

For the 2011 Tohoku earthquake and tsunami, Adityawan *et al.* (2013) showed that arrival times of the leading tsunami wave are generally smaller along riversides, since celerity on land is significantly smaller. Damage to riverine structures due to large tsunamis propagating upstream has also been recorded in the past. An example of damage produced by the 2010 Chile Tsunami to a reinforced concrete house located 2.5 km upstream from the mouth of Maule River is depicted in Figure 1.4, where a flow depth of about 10 m was measured and high velocities inferred form visual observation during the field survey (Fritz *et al.*, 2011; Contreras & Winckler, 2013).

Another consequence of tsunamis in rivers is the significant impact they have on the morphology, triggered by the high velocities and sediment transport (e.g. Morton *et al.* , 2011; Villagrán *et al.*).

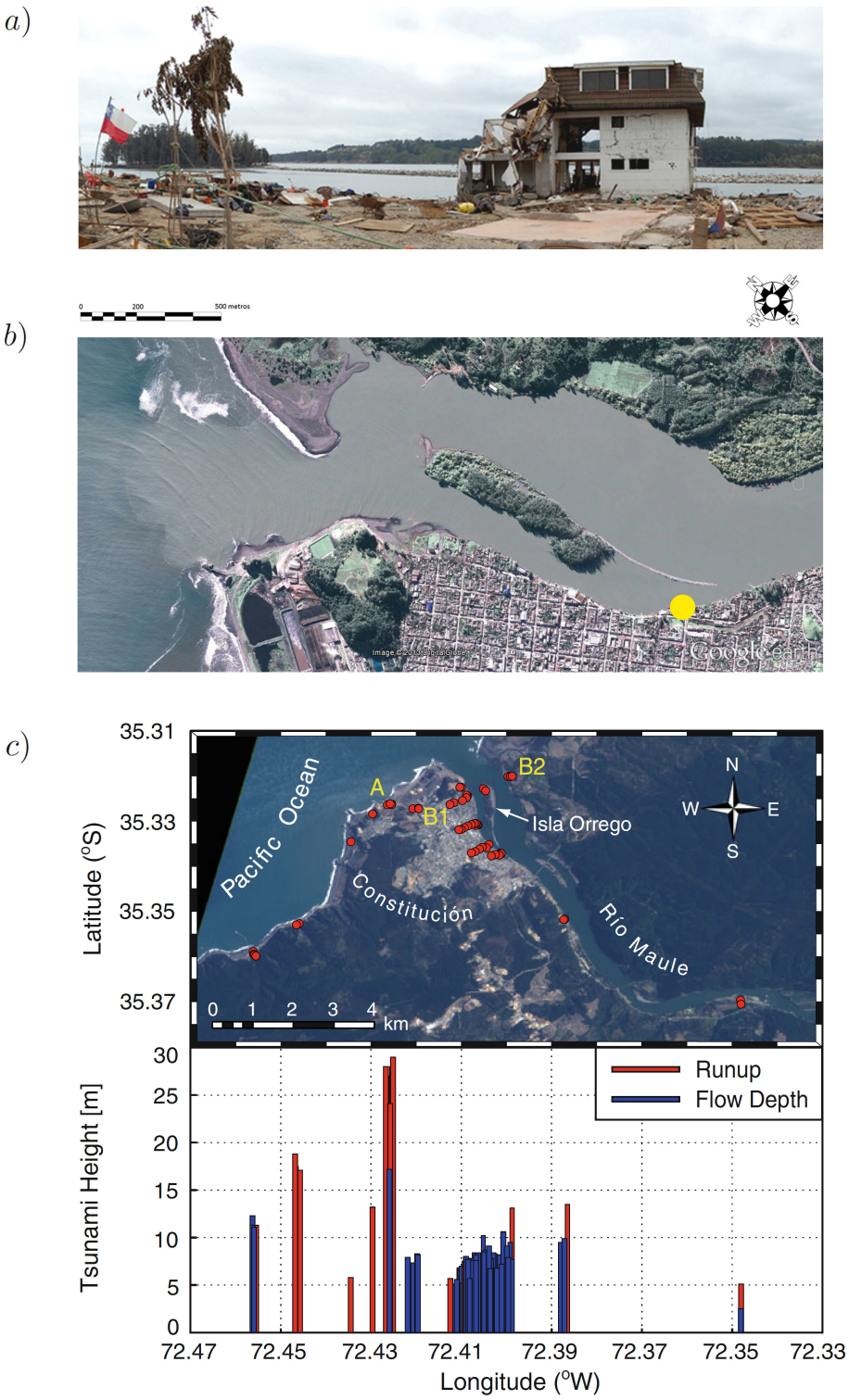

Figure 1.4: *a*) Damage to a reinforced concrete house in Maule River, due to the 2010 Chile Tsunami. The roof is located 12 m above the water level. *b*) The location of the house is shown in a yellow dot (Contreras & Winckler, 2013). *c*) Post-tsunami satellite image combined with measured flow depths and runup heights (Fritz *et al.*, 2011).

CHAPTER 2

LITERATURE REVIEW

An extensive literature review is presented in this Chapter, from which gaps and opportunities for further extensions of existing theories are identified. Section 2.1 reviews the different wave theories, with particular emphasis on the treatment of dimensionality, frequency dispersion and nonlinearity. A specific review of the existing one-dimensional theories is presented in Section 2.2. Seminal papers which enlightened the author's work are mentioned, most of which are analyzed in detail in Appendix A. Section 2.3 reviews some interesting features of long wave propagation observed in the field and under controlled experimental conditions.

2.1 Two-dimensional theories for waves modeling

Free surface flows can be studied by means of one dimensional (1D), two dimensional vertical (2DV), two dimensional horizontal (2DH) and three dimensional models (3D), as shown in Figure 2.1. In engineering practice, 1D non-dispersive models are broadly employed for river hydraulics. 2DH models are used for long waves in water bodies where the depth is small relative to the wavelength, such as estuaries, fjords and the coastal near-shore. The application of 3D models is seldom used due to the complexity involved in the calibration process and computational costs.

As surface waves propagate on a varying bottom, wave characteristics are transformed by both frequency dispersion -a linear phenomena- and nonlinear processes. Frequency dispersion is the spreading of energy in the direction of wave

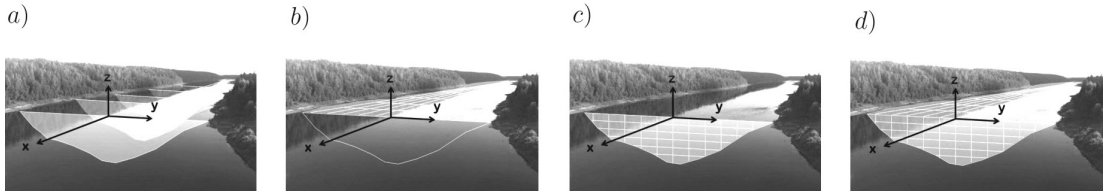

Figure 2.1: Different dimensions used in wave models. *a*) 1D model, *b*) 2DH model *c*) 2DV model and *d*) 3D model.

advance due the to different phase speed for modes of different lengths (Glimsdal, 2013). Nonlinear effects, on the other hand, include *i*) the transfer of energy between different frequency components, *ii*) changes in the shape of individual waves and *iii*) the evolution of wave groups. It is well-known that nonlinearity steepens the waves crests while dispersion counteracts this trend by dispersing into waves of different lengths (Mei *et al*., 2005). Besides frequency dispersion, waves in relatively shallow waters exhibit amplitude dispersion, by which waves of larger amplitude travel faster than smaller waves. The relative importance of frequency dispersion and non-linearity with respect to the inertial and gravity forces determine the wave properties in the far field. For detailed analysis on the effects of nonlinearity and dispersion, the reader is referred to Dingemans (1997) and Nwogu (1993, 1994). Based on the relative importance of frequency dispersion and nonlinearity, long waves can be studied in increasing levels of complexity and computational costs assuming

- linear and nondispersive wave theories (small amplitude theory)
- nonlinear and nondispersive wave theories (shallow water theory)
- weakly-nonlinear weakly-dispersive wave theories (Boussinesq theory)
- Boussinesq theories with improved dispersive properties
- fully-nonlinear weakly-dispersive wave theories

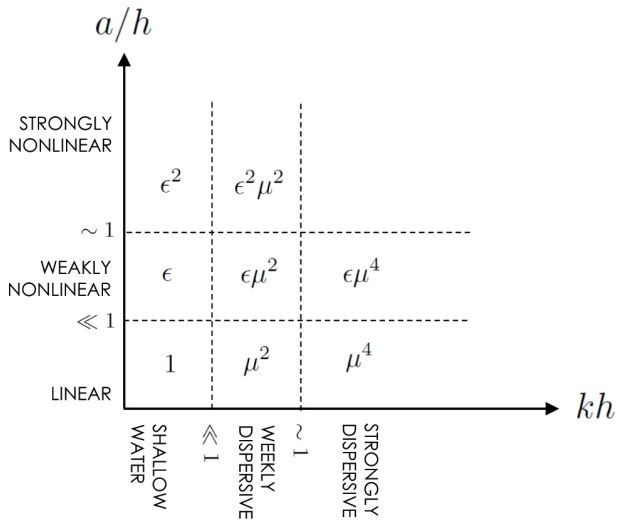

Figure 2.2: Definitions of wave theories according to frequency dispersion, represented by $\mu = h/\lambda$, and the nonlinear parameter defined by $\epsilon = a/h$. a is the wave amplitude, h the depth, λ the wavelength, $k = 2\pi/\lambda$ represents the wavenumber. Adapted from Galán *et al.* (2012).

A standard definition of wave theories according to dispersion and nonlinearity is shown in Figure 2.2. The choice of the proper model depends on the physics of the specific problem and on the efficiency for obtaining solutions (Shi *et al.*, 2005). The small amplitude theory (Rayleigh, 1876; Lamb, 1932) is based on the assumption that amplitude is infinitesimal and makes no restriction on the vertical distribution of velocity. The theory fails to explain nonlinear free surface phenomena -which may become important in long distance propagation- but fully accounts for frequency dispersion.

On the other extreme, the shallow water equations (Lamb, 1932; Stoker, 1968) are based on the assumption that vertical accelerations are negligible, or equivalently, the pressure is hydrostatic and the horizontal velocities are constant in depth (Figure 2.1*b*). While the nonlinear effects can be incorporated exactly, frequency dispersion is neglected. This assumption reduces the dimensionality of the flow problem, thus decreasing the computational costs and simplifying the

definition of the boundary conditions. The loss of important physics, however, is the price payed for such assumption. Saint-Venant equations (Saint-Venant, 1871; Chanson, 2004) are slightly modified shallow water equations extensively used in river hydraulics, where friction is incorporated in a longitudinal axis coinciding with the local slope of the channel.

For cases where nonlinearity and dispersion are both small but finite, the Boussinesq equations (Boussinesq, 1872; Peregrine, 1967) and its simplification to unidirectional KdV equations (Korteweg & deVries, 1895) are appropriate. Brocchini (2013) states that these models are the most favored approximations of Navier-Stokes equations among coastal engineers since they provide a good tool to represent the main physical phenomena with computational ease. Boussinesq equations represent the depth-integrated expressions of conservation of mass and momentum for weakly-nonlinear weakly-dispersive waves, where the vertical profile of velocity potential is parabolic (Figure 2.1*c*). These equations reproduce the nonlinear transformation of irregular, multidirectional long waves due to the effects of shoaling, refraction, diffraction and reflection (Nwogu, 1993). The application of Boussinesq equations is not valid in shallow depths where nonlinearity becomes larger than dispersion, and in deep waters where frequency dispersion is order one (Liu & Losada, 2002). Extended Boussinesq equations with improved dispersive properties (e.g. Nwogu, 1993) or higher order Boussinesq models (e.g. Wei *et al.*, 1995; Galan *et al.*, 2012) are used to extend the standard Boussinesq equations to larger depths and amplitudes.

The ocean surface is characterized by different type of waves, among which wind waves, tides and tsunami are relevant form the engineering perspective.

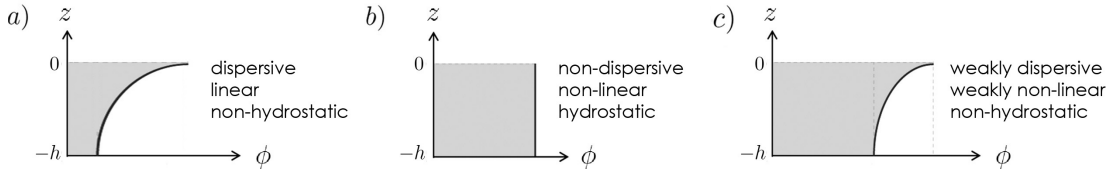

Figure 2.3: Vertical profiles of the velocity potential ϕ for *a*) the small amplitude wave theory (exponential), *b*) the shallow water theory (constant) and *c*) Boussinesq theory (parabolic).

These types of waves are characterized by different time and space scales which define the relative importance for frequency dispersion and nonlinearity. In their evolution from the generation to the runup in the coast, they also undergo different regimes. In wind waves for example, high nonlinearity and dispersion rarely coexist since in deep waters dispersion is relevant and nonlinearity almost negligible. In shallower depths, nonlinearity becomes important due to shoaling and dispersion is negligible as a consequence of the reduction in depth (Galan *et al.*, 2012). Tides and earthquake tsunamis, on the other hand, behave as linear nondispersive waves in the open oceans and can be affected by nonlinear effects near the coasts. In landslide tsunamis, in contrast, initial waves can be significantly nonlinear and dispersive near the source, evolve into a weakly-nonlinear weakly-dispersive regime at larger depths and become highly nonlinear and nondispersive in the nearshore. Consequently, a clear understanding of the relative importance of frequency dispersion and nonlinearity is needed when defining the appropriate theory to model wave evolution.

2.2 One-dimensional theories for long waves in channels

Existing one-dimensional theories (Peregrine, 1968 and 1969; Shen, 1969; Fenton, 1973; Shuto, 1974; Chou, 1981; Kirby & Vengayil, 1988; Teng, 1990 and

Geometric Features	P68	S69	F73	S74	C81	KV88	TW97	Present
Cross-Section Shape	Arbitrary	Arbitrary	Arbitrary	Rectangle	Rectangle Trinangle	Rectangle	Symmetric	Arbitrary
Geometry	Uniform	Uniform	Uniform	Weakly Varying	Weakly Varying	Weakly Varying	Weakly Varying	Rapidly Varying
Sidewall Slope	O(1)	O(1)	O(1)	Vertical	O(1)	Vertical	O(1)	O(1)
Sidewall Effects	Yes	No	No	No	No	No	Yes	Yes
Pressure Forcing	No	No	No	No	No	No	Weak	No
Bottom Forcing	No	No	No	No	No	No	Weak	No

Table 2.1: Cross-sectional features in some of the existing theories. Here P68 stands for Peregrine (1968, 1969), S69 for Shen (1969), F73 for Fenton (1973), S74 for Shuto (1974), C81 for Chou (1981) and KV88 for Kirby & Vengayil (1988). For simplicity, the set of papers by Teng (1990 and 2000) and Teng & Wu (1992, 1994 and 1997) are referred as TW97. The present theory is included in the last column.

2000; and Teng & Wu, 1992, 1994 and 1997) are based on conservation principles and perturbation techniques, only diverging on some geometric constrains, as shown in Table 2.1 and Figure A.1 As common assumptions, these theories assume constant density, no surface tension, inviscid fluid and irrotational flow in absence of breaking waves. The three-dimensional Euler equations are reduced to one-dimension after imposing the boundary conditions. The integration on the wetted area yields Boussinesq or KdV type of equations for section-mean quantities describing the dominant wave motions along the channel. Excepting Shuto (1974) , theories include constant coefficients on the dispersive terms which are obtained from a boundary value problem on the undisturbed channel cross-section. Three-dimensional features are recovered from higher order approximations arising from the perturbation scheme, once the longitudinal Boussinesq (or KdV) equations are solved.

Essentially, these theories assume that wave motion along the channel dominates the flow structure and cross-flow motions are less important. The long

wave assumption implies that the characteristic wavelength is larger than the typical dimensions of the cross-section, so that longitudinal variables are scaled by the wavelength and vertical and lateral variables are scaled by the unperturbed mean water depth. This assumption limits theories to channels which are not notably broad, where wave motions are characterized by slow longitudinal changes. Accordingly, transverse velocities are small compared with the longitudinal velocity.

Theories are expressed in terms of Boussinesq-type equations for section averaged surface elevation and longitudinal velocity (e.g. Peregrine, 1968; Shen, 1969 and Teng & Wu, 1997) or KdV-type equations for one of these or equivalent variables (e.g. Peregrine, 1968; Shen, 1969; Fenton, 1973; Shuto, 1974; Kirby & Vengayil, 1988 and Teng & Wu, 1997). Since KdV-type equations are derived for unidirectional wave motion, they neglect reflection along channels of variable cross-section and consequently, mass and energy conservation is violated (Teng, 1990; Miles, 1979). Teng & Wu (1994) showed that, in spite of the weakness, their KdV model is found to predict transmitted waves in good agreement with both the Boussinesq model and experimental data. This conclusion provides an opportunity of efficient application in the context of tsunami early warning systems, where the estimated time of arrival and amplitudes of the leading wave have to be computed fast. Conversely, the Boussinesq-type of equations conserve mass exactly, retain more physics and demand more computational costs.

The above mentioned theories are limited to channels which are not notably broad. In most rivers, estuaries and fjords, however, the aspect ratio is large, thus one-dimensional theories may seem inappropriate. For channels with arbitrary uniform cross-section bounded by sloping sidewalls, Mathew & Akylas

(1990) derived a Kadomtsev-Petviashvili equation for long, weakly nonlinear waves, by matching asymptotic expansions for outer and inner regions. This equation is nevertheless two-dimensional. In the author's view, wide channels cannot be adequately modeled with a one-dimensional theory as lateral flow features may eventually become significant.

Another restriction of existing theories is that they are valid only for straight channels, thus strictly appropriate for a few man-made canals and laboratory flumes. In natural streams, however, the flow meanders, branching occurs, the banks may not be straight and the cross-section is highly non-uniform. Some of these cases are depicted in Figure 2.4. Due to the importance of curvature and branching in wave evolution, a separate analysis is included in section 7.

The theoretical achievements explained before has been complemented by experimental, analytic and field studies of long waves of moderate amplitude in channels of arbitrary cross-section. Table 2.2 illustrates the different cross-sections used in the literature to *i*) derive governing equations, *ii*) find analytical and/or numerical solutions, *iii*) carry out experiments or *iv*) study mathematical or physical properties of the governing equations. This table is by no means definitive and is intended to provide a broad view of the historical development on the subject. Analytical solutions have been found for simple cross-sections resembling man-made canals or wave flumes. These solutions provide insights to the dominant features of generation, propagation and arrival of long waves, and may be used to test conservation properties of the equations and numerical schemes. Experimental studies are useful to calibrate wave theories in consideration of viscous effects. A few field surveys described in the literature may be used to validate wave theories on a natural scale.

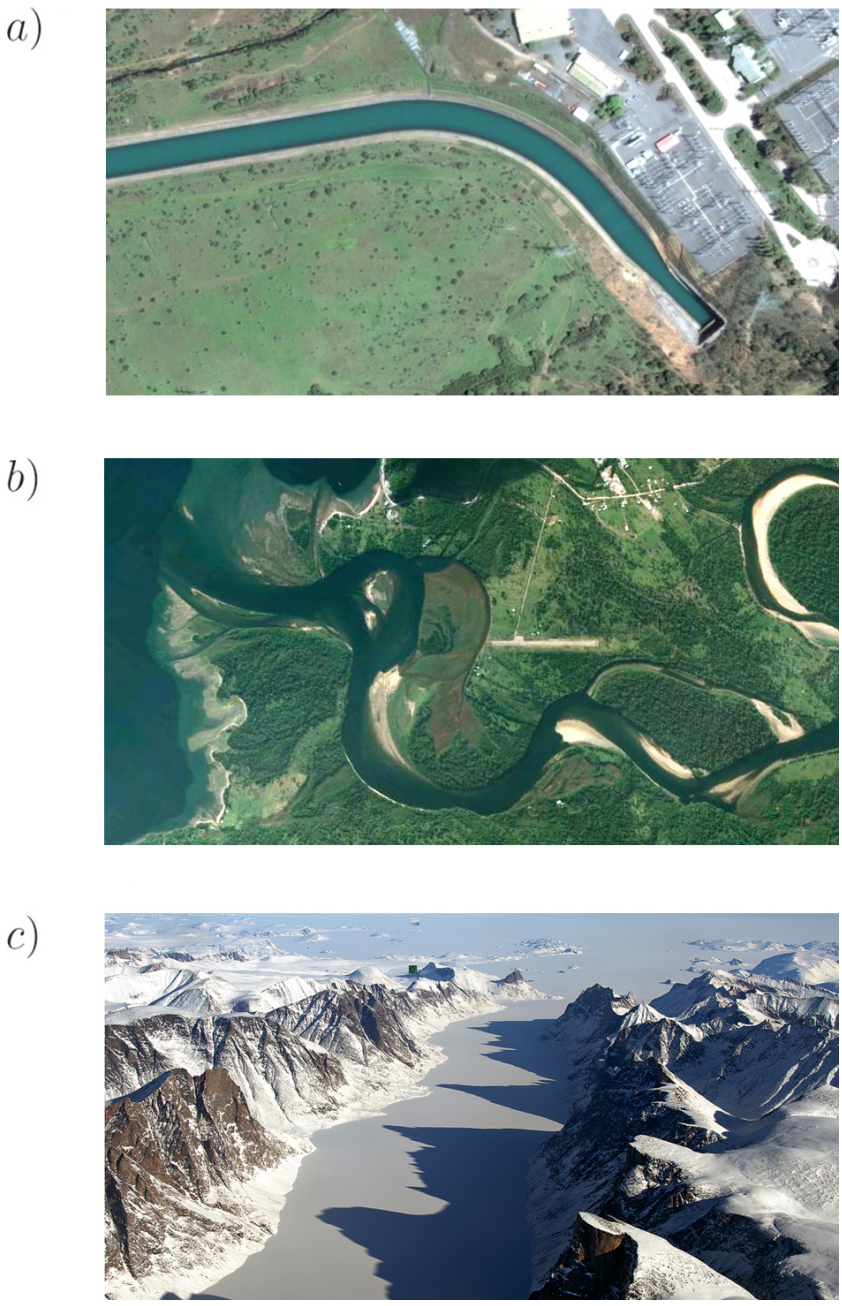

Figure 2.4: Examples on man-made and natural streams where the present theory for straight channels may (*c*) or may not be used (*a* and *b*). *a*) man-made channel in the evacuation of Colbun dam, Chile. *b*) A significantly curved river, Rio Cisnes, Chile with branching channels. *c*) Davis Strait in Canada's Baffin Island where non-uniform cross-sections (sources: *a* and *b* were obtained from Google Earth and *c* from Nasa's image gallery).

	Cross-sectional shape					
Title	**REC**	**TRI**	**PAR**	**CIR**	**TRA**	**ARB**
Russell, 1844		E				F
Sandover & Taylor, 1962					T,E	
Tricker, 1964						F
Peters, 1966	S			S		T
Preissmann & Cunge, 1967					E,S	
Peregrine, 1968	S	S				T
Peregrine, 1969					S	
Shen, 1969						T
Benet & Cunge, 1971					T,E	
Fenton, 1973						T,A
Shuto, 1974	T,A					
Chang *et al.*, 1979	A					
Miles, 1979a	A					
Miles, 1979b	A					
Chou, 1981	T	T				T
Shen & Zhong, 1981						T
Kirby & Vengayil, 1988	N					T
Teng, 1990	S	S		S		T
Teng & Wu, 1992	S	S	S	S		T
Teng & Wu, 1994		A	A			
Treske, 1994					E	
Teng & Wu, 1997	A,E				S,E	T
Shi *et al.*, 1998	A					
Teng, 2000	A	A				T
Didenkulova & Pelinovsky, 2009			A			
Didenkulova & Pelinovsky, 2011			A			
Eidsvig *et al.*, 2011						A
Bonneton *et al.*, 2012						F
Chanson, 2012						A,F
Nachbim & da Silva, 2012						A
Harbitz *et al.*, 2014						E,F
Linstrom *et al.*, 2014						E

Table 2.2: Relevant papers in chronological order and typical cross-sections analyzed in the literature. Rectangular (REC), triangular (TRI), parabolic (PAR), semicircular (CIR), trapezoidal (TRA) and arbitrary (ARB) cross-sections are shown. The types of studies are classified in (T) derivation of a theory, (S) analytic solution of theory for a simple cross-section, (E) experiments, (A) theoretical or numerical analysis of specific issues of an existing theory and (F) field survey or observation.

From the detailed analysis of the existing one-dimensional theories included in Appendix A, it is concluded that Shen's (1969) approach of successively finding solutions at different orders may be cumbersome from the perspective of numerical implementation. Fenton's (1973), Shuto's (1974) and Chou's (1981) theories on the other hand, cannot account for bidirectional waves, making them inadequate for cases where reflection significant. Kirby & Vengayil's (1988) theory provides an interesting approach which unfortunately cannot cope with channel where cross-sections vary significantly within a wavelength. In view of the author, Peregrine (1968) and Teng & Wu (1997) rescue interesting features of the phenomena and provide the most complete one-dimensional models currently available.

Differences among Peregrine's and Teng & Wu's theories arise in *i*) the dependent variables used in the governing equations, *ii*) the structure of the dispersive terms in the Boussinesq equations, *iii*) in whether they include or neglect forcing terms and *iii*) in the restrictions of channel geometry. Peregrine's theory is valid for an arbitrary uniform cross-sections whereas Teng & Wu's theory considers slowly varying and symmetric cross-sections, where no rapid changes in the geometry are allowed. None of them consequently, cover the more general case of channels with significant changes of the cross-sections within a wavelength, where no restriction on the sidewall slopes, cross-sectional aspect ratio, branching and curvature are required.

The present theory is therefore intended to relax some of the limitations of the existing theories, namely, the assumptions of slowly-varying geometry along the channel and the symmetry of the cross-sectional geometry.

2.3 Field observations and experiments

Experimental studies in channels of arbitrary cross-section have been carried out by Sandover & Taylor (1962), Peregrine (1969), Preissmann and Cunge (1967), Benet & Cunge (1971), Chang *et al*. (1979), Teng (1990), Treske (1994) and Teng & Wu (1997). Experiments have generally shown a marked lateral change of surface elevation with steeper and higher waves close to the sidewalls, a tendency for waves to break at the sidewall slopes and other three-dimensional effects, such as curvature of the wave crest in plan. Unsteady waves and a marked fish-tail pattern obscuring the main wave system for wide shallow channels have also been observed (Sandover & Taylor, 1962; Fenton, 1973). Depending on the wave amplitude, waves can degenerate into bores.

Figure 2.5 depicts experimental results by Treske (1994) for different Froude numbers -defined as the ratio of the wave propagation speed of hydraulic jumps to the phase speed of infinitesimal waves- in which some of these features are observed. Panel *a* shows a quasi one-dimensional wave pattern with the main variations occurring along the channel, in which the present theory could be applicable. Panels *b* and *c* show the fish-tail pattern arising from the combined effect of refraction and reflection at the sidewalls whereas panel *d* shows a leading bore with a complex flow structure in the trailing waves. The detailed physics of *b*, *c* and *d* cannot be fully recovered with a one-dimensional theory for irrotational flows, requiring more dimensions and wave breaking, friction or turbulence models. Indeed, only by means of a two-dimensional wave model, Mathew & Akylas (1990) found a qualitatively resemblance between numerical results and the fish-tail pattern from the experiments of Sandover & Taylor (1962) and Treske (1994).

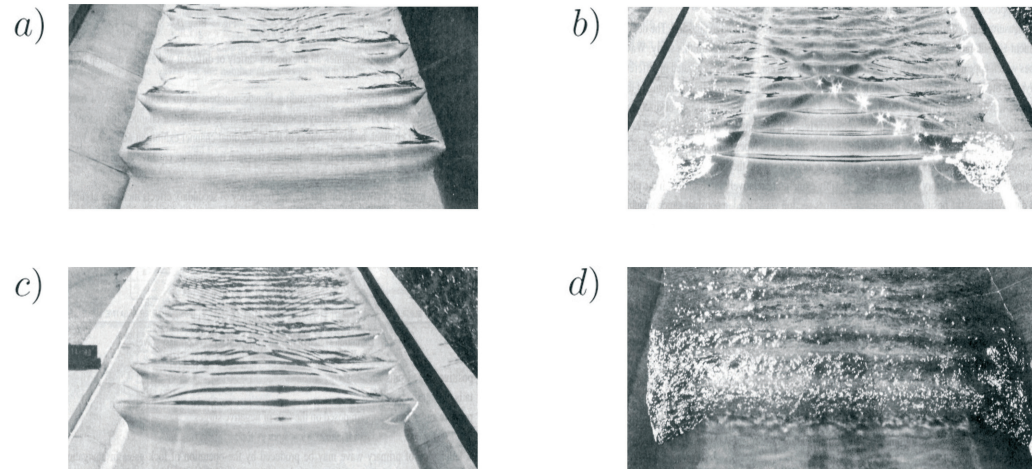

Figure 2.5: Positive surges in a trapezoidal channel. Undular bore with a Froude number of *a*) Fr = 1.10, *b*) Fr = 1.20 and *c*) Fr = 1.12. Image *d*) depicts a bore with Fr = 1.35. The 'fish tail' pattern is enhanced in images *b*) and *c*). The Froude number is defined as the ratio between the propagation speed of hydraulic jumps and the phase speed of infinitesinal waves (Treske's equation 1). Source: Adapted from Treske (1994).

Despite their simplicity, the existing one-dimensional theories are able to account for some of the reported three-dimensional wave features. The lateral amplifications of the amplitude of the surface, for example, can be reproduced using the theories by Peters (1966), Peregrine (1968), Shen (1969) and Teng & Wu (1997), through second order approximations.

Field observations of bores in natural streams are found in Tricker (1964), Chanson (2012) and Bonneton *et al*. (2012), among others (Figure 2.6). Field surveys provide qualitative descriptions of lateral changes of wave properties but few useful measurements to validate wave theories. The primary reason for this lieas in the inherent complexity of measuring a rapid phenomena, such as bores or landslide tsunamis, with a low probability of occurrence. Bores, for example, are observed at a particular site from a few seconds to a few minutes as they occur only under spring tidal ranges and low freshwater flow conditions (Chanson, 2012).

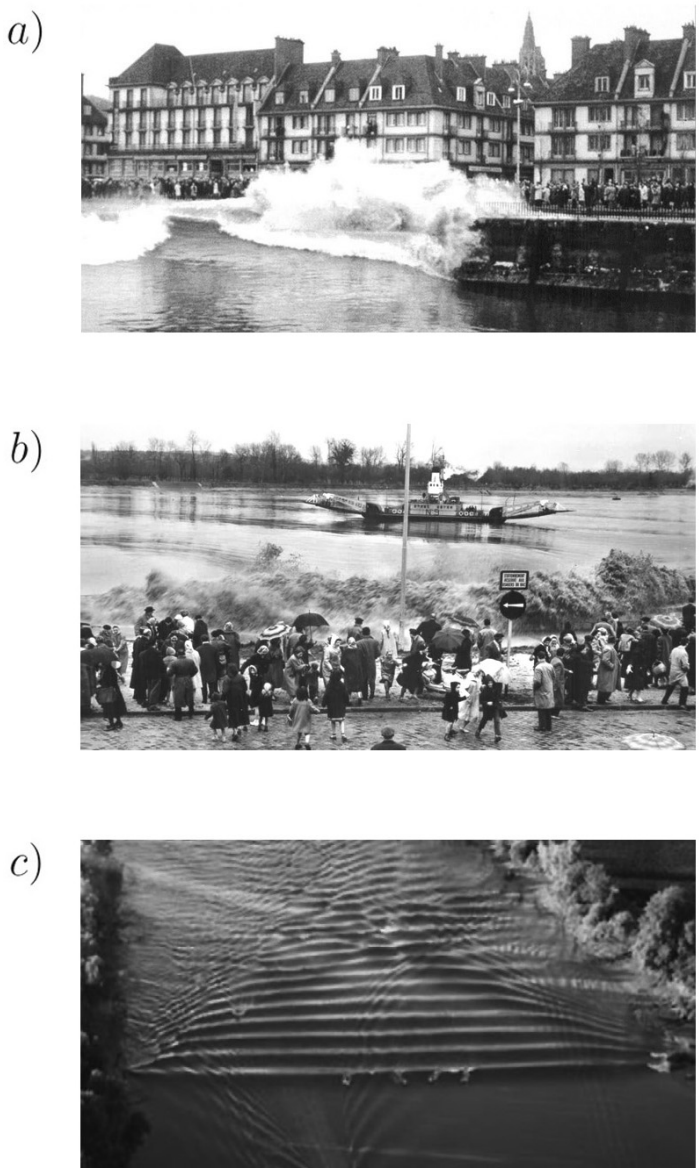

Figure 2.6: *a*) Mascaret on the Seine river at Caudebec-en Caux around 1960, view from the ferry looking at the right bank. *b*) Bac de Caudebec-en Caux facing the mascaret in 1958, view from the right bank. Sidewall overtopping is caused by the increment in the wave amplitude towards the river boundaries. *c*) Undular tidal bore propagating in Garonne River, 500 m downstream Podensac, where the fish-tail pattern is observed. Sources: http://staff.civil.uq.edu.au/h.chanson/photo.html and Bonneton *et al.*(2012).

CHAPTER 3

GOVERNING EQUATIONS

The derivation of a theory for weakly non-linear weakly-dispersive waves in non-uniform channels of arbitrary cross-section is presented in this chapter. The theory is grounded on the Euler equations with kinematic and boundary conditions on both the free surface and the wetted area. These set of equations constitute a three-dimensional non-linear system of partial differential equations whose solutions are difficult to determine. By introducing a perturbation expansion and performing an integration on the wetted area, one-dimensional Boussinesq equations describing the dominant wave motions in the longitudinal axis are derived. The Boussinesq approximation implies that non-linearity and dispersion are relatively small, but are of the same order of magnitude. These equations include constant coefficients obtained from boundary value problems on the undisturbed channel cross-section. Three dimensional features are recovered once the longitudinal problem is solved from higher order approximations in the perturbation scheme.

The fundamental forces including inertia, fluid pressure and gravity are considered in this chapter. Forcing through spatial gradients of the ambient pressure are neglected but could be included following Teng & Wu's (1992) approach. In the present derivation boundary-layer dynamics and its effect of the irrotational bulk of water are neglected. Viscous effects from the boundary-layer are heuristically included in Chapter 6. The theory is limited to straight channels with no plan curvature and branching, and to cross-sections where the depth and width are comparable. No attempt to develop a KdV type of equation is carried out due to its inherent limitation in conserving mass.

3.1 Definitions

In this section, variables with hats are dimensional, e.g. $\hat{x}$, and variables without hats are dimensionless, e.g. x. A typical channel with a non-uniform arbitrary cross-section is depicted in Figure 3.1. The bottom is considered fixed and impermeable, therefore the channel cross-section is described by $\hat{z} = -\hat{h}(\hat{x}, \hat{y})$, where $\hat{z}$ is the vertical coordinate pointing upwards and $\hat{z} = 0$ denotes the still water level (SWL). The $\hat{x}-$ axis is the longitudinal direction, while the $\hat{y}-$ axis represents the spanwise direction. The channel cross-section geometry can alternatively be defined by $\hat{y} = \hat{y}^l(\hat{x}, \hat{z})$ and $\hat{y} = -\hat{y}^r(\hat{x}, \hat{z})$ for the left and right channel bottom boundaries, measured from the channel axis ($\hat{y} = 0$). The intersections between the SWL and the channel boundary, describing the still water shorelines, are defined by

$$\hat{y} = \hat{y}^l(\hat{x}, 0) \equiv \hat{b}_l(\hat{x}) \qquad \text{and} \qquad \hat{y} = -\hat{y}^r(\hat{x}, 0) \equiv -\hat{b}_r(\hat{x}), \tag{3.1}$$

respectively. Therefore, the channel width on the SWL is given by

$$\hat{B}(\hat{x}, \hat{z}) = \hat{y}^l(\hat{x}, \hat{z}) + \hat{y}^r(\hat{x}, \hat{z}), \qquad \text{on} \quad -\hat{h} \leq \hat{z} \leq 0, \tag{3.2}$$

and, furthermore

$$\hat{B}_0(\hat{x}) \equiv \hat{B}(\hat{x}, 0) = \hat{b}_l(\hat{x}) + \hat{b}_r(\hat{x}), \qquad \text{on} \quad \hat{z} = 0 \tag{3.3}$$

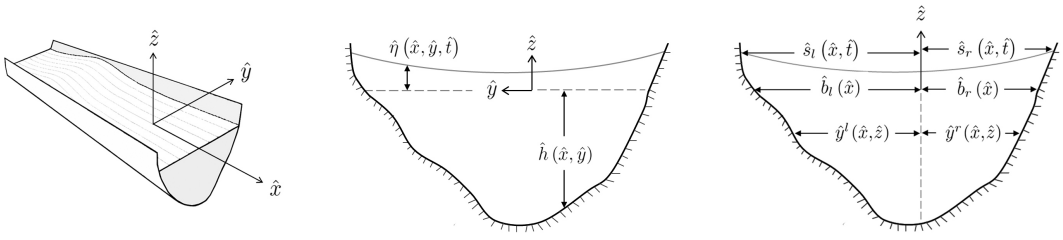

Figure 3.1: Definition of coordinate system and boundaries.

represents the surface width at the quiescent state. The instantaneous free surface elevation is expressed as $\hat{z} = \hat{\eta}(\hat{x}, \hat{y}, \hat{t})$, and the moving shorelines are defined by

$$\hat{y} = \hat{y}^l(\hat{x}, \hat{\eta}(t)) \equiv \hat{s}^l(\hat{x}, \hat{t}) \qquad \text{and} \qquad \hat{y} = -\hat{y}^r(\hat{x}, \hat{\eta}(t)) \equiv -\hat{s}^r(\hat{x}, \hat{t}), \tag{3.4}$$

for the left and right boundaries, respectively.

3.2 Fundamental equations in dimensional form

The governing equations and boundary conditions for an inviscid and incompressible fluid of density ρ are presented herein in dimensional form. The conservation of mass is

$$\hat{\nabla} \cdot \hat{\mathbf{V}} = \frac{\partial \hat{u}}{\partial \hat{x}} + \frac{\partial \hat{v}}{\partial \hat{y}} + \frac{\partial \hat{w}}{\partial \hat{z}} = 0, \tag{3.5}$$

where $\hat{\mathbf{V}} = (\hat{u}, \hat{v}, \hat{w})$ defines the velocities in the longitudinal, lateral and vertical axis $\hat{x}$, $\hat{y}$ and $\hat{z}$ respectively. The fluid is inviscid and the flow is assumed initially irrotational so it remains irrotational throughout the domain, i.e. $\hat{\nabla} \times \hat{\mathbf{V}} = 0$. Thus, the flow field can also be expressed in terms of a velocity potential $\hat{\nabla}\hat{\phi} = \hat{\mathbf{V}}$.

The conservation of momentum including inertial, gravity and pressure forces, is completely defined by the Euler equations

$$\frac{\partial \vec{\hat{V}}}{\partial \hat{t}} + \hat{\nabla} \cdot \left(\vec{\hat{V}} \otimes \vec{\hat{V}} \right) = -\frac{1}{\hat{\rho}} \hat{\nabla} \hat{p} + \hat{\mathbf{g}}, \tag{3.6}$$

where $\hat{t}$ represents time, $\hat{\rho}$ is the density of the fluid, $\hat{p}(\hat{x}, \hat{y}, \hat{z}, \hat{t})$ is the fluid pressure and $\hat{\mathbf{g}} = (0, 0, -\hat{g})$ is acceleration due to gravity acting vertically downwards. No acceleration due to curvature between consecutive sections along the channel is considered, so that the theory is restricted to straight channels.

The conservation of energy is expressed by means of the Bernoulli equation

$$\frac{\partial \hat{\phi}}{\partial \hat{t}} + \frac{1}{2}\left[\hat{u}^2 + \hat{v}^2 + \hat{w}^2\right] + \frac{\hat{p}}{\hat{\rho}} + \hat{g}\hat{z} = 0, \tag{3.7}$$

where the Bernoulli constant has been absorbed into the velocity potential (Dean & Dalrymple, 1991).

The free surface kinematic boundary condition is

$$\hat{w} = \frac{\partial \hat{\eta}}{\partial \hat{t}} + \hat{u}\frac{\partial \hat{\eta}}{\partial \hat{x}} + \hat{v}\frac{\partial \hat{\eta}}{\partial \hat{y}} \qquad \text{on} \quad \hat{z} = \hat{\eta}\,(\hat{x}, \hat{y}, \hat{t}), \tag{3.8}$$

implying that fluid particles at the boundary cannot be detached from it. Note also that the position of the surface is not known a priori. In contrast, the bottom kinematic boundary condition

$$\hat{w} = -\hat{u}\frac{\partial \hat{h}}{\partial \hat{x}} - \hat{v}\frac{\partial \hat{h}}{\partial \hat{y}} \qquad \text{on} \quad \hat{z} = -\hat{h}\,(\hat{x}, \hat{y}), \tag{3.9}$$

is defined for a prescribed position of the bottom. The kinematic boundary conditions at the left and right moving shorelines are

$$\hat{v} = \frac{\partial \hat{s}_l}{\partial \hat{t}} + \hat{u}\frac{\partial \hat{s}_l}{\partial \hat{x}} \qquad \text{on} \quad \hat{y} = \hat{s}_l\,(\hat{x}, \hat{t}) \tag{3.10}$$

and

$$\hat{v} = -\frac{\partial \hat{s}_r}{\partial \hat{t}} - \hat{u}\frac{\partial \hat{s}_r}{\partial \hat{x}} \qquad \text{on} \quad y = -\hat{s}_r\,(\hat{x}, \hat{t}), \tag{3.11}$$

respectively. Finally, the atmospheric pressure is ignored by means of the dynamic boundary condition at the surface

$$\hat{p}_a = 0 \qquad \text{on} \quad \hat{z} = \hat{\eta}\,(\hat{x}, \hat{y}, \hat{t}). \tag{3.12}$$

An extensive review of the mathematical structure of the boundary conditions is included in Dean & Dalrymple (1991). Equations (3.5) to (3.12) constitute the governing equations and boundary conditions for a general three-dimensional nonlinear water wave problem. Additional initial conditions for free surface elevation and velocity, and up-stream and down-stream boundary conditions are needed for a specific problem of interest.

3.3 Fundamental equations in non-dimensional form

The derivation of approximate equations by means of asymptotic methods is based on the use of dimensionless quantities and typical scales. This approach is beneficial since the order of magnitude of the dimensionless terms, expressed in terms of small parameters, is explicit in the equations. Different kinds of problems are therefore defined when choosing the typical scales for the specific problem (Dingemans, 1997).

To describe the problem in terms of dimensionless variables, the characteristic wavelength $\hat{\lambda}$ is employed as the length scale in the longitudinal direction and the characteristic unperturbed water depth $\hat{h}_0$ as the length scale for the vertical and spanwise directions. The time scale is chosen as $\hat{\lambda}/\hat{c}_0$, where $\hat{c}_0 = \sqrt{\hat{g}\hat{h}_0}$ is the linear phase speed in shallow water and $\hat{g}$ denotes the gravitational acceleration. Thus, the following dimensionless variables are introduced:

$$x = \frac{\hat{x}}{\hat{\lambda}}\,, \qquad\qquad t = \frac{\sqrt{\hat{g}\hat{h}_0}}{\hat{\lambda}}\hat{t}\,, \tag{3.13}$$

$$(y, z, h, b_l, b_r, s_l, s_r, B) = \frac{1}{\hat{h}_0}\left(\hat{y}, \hat{z}, \hat{h}, \hat{b}_l, \hat{b}_r, \hat{s}_l, \hat{s}_r, \hat{B}\right). \tag{3.14}$$

Scaling of $\hat{y}$ and $\hat{z}$ with respect to the same length scale $\hat{h}_0$ implies that attention is restricted to channels where the depth and width are comparable. The corresponding derivatives, using the chain rule, become

$$\frac{\partial}{\partial\hat{x}} = \frac{1}{\hat{\lambda}}\frac{\partial}{\partial x}, \qquad \left(\frac{\partial}{\partial\hat{y}}, \frac{\partial}{\partial\hat{z}}\right) = \frac{1}{\hat{h}_0}\left(\frac{\partial}{\partial y}, \frac{\partial}{\partial z}\right), \qquad \frac{\partial}{\partial\hat{t}} = \frac{\sqrt{\hat{g}\hat{h}_0}}{\hat{\lambda}}\frac{\partial}{\partial t}. \tag{3.15}$$

The velocity components are scaled as

$$u = \frac{1}{\epsilon\sqrt{\hat{g}\hat{h}_0}}\hat{u}, \qquad (v, w) = \frac{\mu}{\epsilon\sqrt{\hat{g}\hat{h}_0}}\left(\hat{v}, \hat{w}\right), \tag{3.16}$$

where two parameters

$$\mu = \frac{\hat{h}_0}{\hat{\lambda}} \qquad \text{and} \qquad \epsilon = \frac{\hat{a}_0}{\hat{h}_0}, \tag{3.17}$$

represent the nonlinearity and frequency dispersion, in which $\hat{a}_0$ is the characteristic wave amplitude[1]. The dimensionless surface elevation and pressure are

$$\eta = \frac{\hat{\eta}}{\hat{a}_0}, \qquad \text{and} \qquad p = \frac{\hat{p}}{\hat{\rho}\hat{g}\hat{a}_0}. \tag{3.18}$$

This normalization is similar to the one used by Nwogu (1993)), differing only on the scaling of the spanwise variables. The governing equations in the dimensionless form become

$$\frac{\partial u}{\partial x} + \frac{1}{\mu^2}\left(\frac{\partial v}{\partial y} + \frac{\partial w}{\partial z}\right) = 0, \tag{3.19}$$

for the mass conservation, and

$$\frac{\partial u}{\partial t} + \epsilon\left[\frac{\partial}{\partial x}\left(u^2\right) + \frac{1}{\mu^2}\left\{\frac{\partial}{\partial y}\left(uv\right) + \frac{\partial}{\partial z}\left(uw\right)\right\}\right] = -\frac{\partial p}{\partial x}, \tag{3.20}$$

$$\frac{\partial v}{\partial t} + \epsilon\left[\frac{\partial}{\partial x}\left(uv\right) + \frac{1}{\mu^2}\left\{\frac{\partial}{\partial y}\left(v^2\right) + \frac{\partial}{\partial z}\left(vw\right)\right\}\right] = -\frac{\partial p}{\partial y}, \tag{3.21}$$

$$\frac{\partial w}{\partial t} + \epsilon\left[\frac{\partial}{\partial x}\left(uw\right) + \frac{1}{\mu^2}\left\{\frac{\partial}{\partial y}\left(vw\right) + \frac{\partial}{\partial z}\left(w^2\right)\right\}\right] = -\frac{\partial p}{\partial z} - \frac{1}{\epsilon}, \tag{3.22}$$

for the conservation of momentum. Note that only the x-momentum equation is used in the present formulation. The conservation of energy reads

$$\frac{\partial \phi}{\partial t} + \frac{1}{2}\epsilon\left[u^2 + \frac{1}{\mu^2}\left(v^2 + w^2\right)\right] + p + \frac{z}{\epsilon} = 0. \tag{3.23}$$

[1]The scaling of velocities is based on the linear wave theory. The expression of the velocity potential for a regular wave train with angular frequency $\hat{\omega}$ and wave-number $\hat{k}$ (Svendsen, 2006) is scaled using the shallow water approximation, i.e. $\hat{k}\hat{h} \to 0$

$$\hat{\phi} = \hat{a}_0 \frac{\hat{g}}{\hat{\omega}} \frac{\cosh(\hat{k}\left[\hat{z} + \hat{h}_0\right])}{\cosh(\hat{k}\hat{h}_0)} \sin\left(\hat{k}\hat{x} - \hat{\omega}\hat{t}\right) \approx \hat{a}_0 \frac{\hat{g}}{\hat{\omega}}\phi = \epsilon\hat{\lambda}\sqrt{\hat{g}\hat{h}_0}\phi,$$

where $\phi = \sin(\hat{k}\hat{x} - \hat{\omega}\hat{t})$. Since $\hat{\nabla}\hat{\phi} = \hat{\mathbf{V}}$, it is easily shown that $(\hat{u}, \hat{v}, \hat{w}) = \epsilon\hat{\lambda}\sqrt{\hat{g}\hat{h}_0}\left(u/\hat{\lambda}, v/\hat{h}_0, w/\hat{h}_0\right)$.

The kinematic boundary condition on the free surface is expressed as

$$w = \mu^2 \left(\frac{\partial \eta}{\partial t} + \epsilon u \frac{\partial \eta}{\partial x} \right) + \epsilon v \frac{\partial \eta}{\partial y}, \qquad \text{on} \quad z = \epsilon \eta (x, y, t). \tag{3.24}$$

The no-flux boundary condition along the bottom requires

$$w = -\mu^2 u \frac{\partial h}{\partial x} - v \frac{\partial h}{\partial y}, \qquad \text{on} \quad z = -h (x, y). \tag{3.25}$$

Along the moving shorelines, the kinematic boundary conditions are

$$\epsilon v = \mu^2 \left(\frac{\partial s_l}{\partial t} + \epsilon u \frac{\partial s_l}{\partial x} \right), \qquad \text{on} \quad y = s_l (x, t) \tag{3.26}$$

and

$$\epsilon v = -\mu^2 \left(\frac{\partial s_r}{\partial t} + \epsilon u \frac{\partial s_r}{\partial x} \right), \qquad \text{on} \quad y = -s_r (x, t). \tag{3.27}$$

Finally, the atmospheric pressure on the free surface is ignored, thus

$$p = 0, \qquad \text{on } z = \epsilon \eta (x, y, t). \tag{3.28}$$

Equations (3.19) to (3.28) constitute the non-dimensional governing equations and boundary conditions for a general three-dimensional nonlinear water wave problem, without considering the viscous effects.

3.4 Cross-sectional averaged Boussinesq equations

The flow problem stated in the previous section can be reduced to a set of one-dimensional governing equations by averaging over a channel cross-section and applying the boundary conditions on the free surface and solid boundaries. Expressions for the cross-section area and three different types of averages extensively used in this theory are introduced in Section 3.4.1. The exact governing equations are derived in section 3.4.2.

3.4.1 Definitions on a cross-sectional plane

The cross-sectional area at the quiescent state $A_0(x)$ is defined by

$$A_0(x) = \int_{-b_r}^{b_l} h(x,y)dy = \int_{-\max(h)}^{0} B(x,z)dz. \tag{3.29}$$

The instantaneous cross-sectional area $A(x,t)$

$$A(x,t) = \int_{-s_r}^{s_l}\int_{-h}^{\epsilon\eta} dzdy \tag{3.30}$$

can be expressed as the sum of the cross-sectional area at the quiescent state and the contribution due to waves

$$A(x,t) = A_0 + \int_{-s_r}^{-b_r} (\epsilon\eta - h)\, dy + \epsilon \int_{-b_r}^{b_l} \eta dy + \int_{b_l}^{s_l} (\epsilon\eta - h)\, dy, \tag{3.31}$$

where the limits of integration are defined in Figure 3.1 and the second integral on the RHS is, by definition,

$$\int_{-b_r}^{b_l} \eta dy = B_0\widetilde{\eta} \tag{3.32}$$

In the regions $-s_r < y < -b_r$ and $b_l < y < s_l$, the surface is approximated to $\eta = \widetilde{\eta}$ and the slope is assumed to be linear above the SWL (Figure 3.2). The contribution of the left and right triangles are

$$\int_{-s_r}^{-b_r} (\epsilon\eta - h)\, dy + \int_{b_l}^{s_l} (\epsilon\eta - h)\, dy = \frac{\epsilon^2}{2}\left\{\left.\frac{dy^r}{dz}\right|_{z=0} + \left.\frac{dy^l}{dz}\right|_{z=0}\right\}\widetilde{\eta}^2, \tag{3.33}$$

where the terms in brackets represent the sidewall slopes at the still water level at both sides of the channel and are assumed to be $O(1)$ or smaller. For convenience these terms are grouped and referred to as B_0'. Contributions from the regions $-s_r < y < -b_r$ and $b_l < y < s_l$ are of order $O(\epsilon^2\mu^2, \epsilon^3)$ or smaller given the assumptions of $\partial\eta/\partial x = O(\mu^2)$ from the perturbation scheme (3.77) and that the difference between the sidewall slopes above the SWL and at $z = 0$ is small, i.e.

$$\left.\frac{dy^r}{dz}\right|_{z>0} - \left.\frac{dy^r}{dz}\right|_{z=0} = O(\epsilon). \tag{3.34}$$

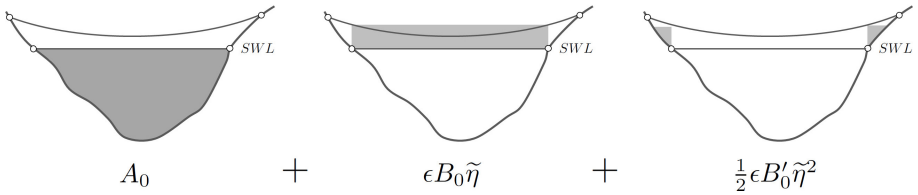

Figure 3.2: Definition of components of the cross-section area.

The area is therefore

$$A = A_0 + \epsilon B_0\widetilde{\eta} + \epsilon^2\frac{B_0'}{2}\widetilde{\eta}^2 + O(\epsilon^2\mu^2, \epsilon^3). \tag{3.35}$$

in which

$$B_0'(x) \equiv \frac{\partial B}{\partial z}(x, 0). \tag{3.36}$$

Three different averages on the channel's cross-section are introduced. The cross-sectional average of a function $f(x, y, z, t)$ in the instantaneous cross-section is defined as

$$\langle f\rangle(x, t) = \frac{1}{A(x, t)}\int_{-s_r}^{s_l}\int_{-h}^{\epsilon\eta} f(x, y, z, t)\, dzdy. \tag{3.37}$$

The averaged value over the channel cross-section area at the quiescent state is

$$\overline{f}(x, t) = \frac{1}{A_0(x)}\int_{-b_r}^{b_l}\int_{-h}^{0} f(x, y, z, t)\, dzdy. \tag{3.38}$$

The instantaneous cross-section average $\langle f\rangle$ and the cross-sectional average at the quiescent state $\overline{f}$ can be related for channels where the sidewall slope at the still water level is $B_0' = O(1)$. Indeed, equation (3.37) is divided into segments

$$\begin{aligned}\langle f\rangle \;=\; & \frac{1}{A}\int_{-b_r}^{b_l}\int_{-h}^{0} f\,dzdy + \frac{1}{A}\int_{-b_r}^{b_l}\int_{0}^{\epsilon\eta} f\,dzdy \\ & + \frac{1}{A}\int_{-s_r}^{-b_r}\int_{-h}^{\epsilon\eta} f\,dzdy + \frac{1}{A}\int_{b_l}^{s_l}\int_{-h}^{\epsilon\eta} f\,dzdy,\end{aligned} \tag{3.39}$$

where the last three integrals are $O(\epsilon)$ as ϵ in explicit in the upper limit of integration. Using the Taylor expansion for the area

$$\frac{1}{A} = \frac{1}{A_0 + O(\epsilon)} = \frac{1}{A_0} + O(\epsilon) \tag{3.40}$$

yields

$$\langle f \rangle = \frac{1}{A_0} \int_{-b_r}^{b_l} \int_{-h}^{0} f dz dy + O(\epsilon) = \overline{f} + O(\epsilon). \tag{3.41}$$

Note that the instantaneous cross-section average $\langle f \rangle$ depends on the flow, whereas the cross-sectional average at the quiescent state $\overline{f}$ is only dependent on the local geometry, thus can be precomputed once the bathymetry is prescribed.

The averaged value over the channel surface width at the quiescent state is

$$\widetilde{f|_{z=0}}(x,t) = \frac{1}{B_0} \int_{-b_r}^{b_l} f(x,y,0,t)\, dy, \tag{3.42}$$

and a depth averaged quantity is defined as

$$\breve{f}(x,y,t) = \frac{1}{\epsilon\eta + h} \int_{-h}^{\epsilon\eta} f(x,y,z,t)\, dz. \tag{3.43}$$

Finally, the Leibniz rule

$$\frac{\partial}{\partial t} \int_{m(t)}^{n(t)} f(x,t) dx = \int_{m(t)}^{n(t)} \frac{\partial f}{\partial t}(x,t) dx + f(x=n,t) \frac{\partial n}{\partial t} - f(x=m,t) \frac{\partial m}{\partial t}. \tag{3.44}$$

for domains which limits on integration $x = m(t)$ and $n(t)$ that may vary in time is used in the derivation.

3.4.2 Exact governing equations

Although the procedure of deriving the exact cross-sectional averaged conservation of mass (3.58) and momentum equations (3.75) is straightforward, the

existing literature (Peregrine, 1968; Teng, 1990) have adopted approximations that appear to be unnecessary. For completeness, the procedure of derivation is detailed in this section.

Conservation of mass

The exact equation of mass conservation is derived by integrating (3.19) in the vertical direction from the bottom $z = -h\,(x, y)$ to the surface $z = \epsilon\eta\,(x, y, t)$.

$$\int_{-h}^{\epsilon\eta} \frac{\partial u}{\partial x} dz + \frac{1}{\mu^2}\left(\int_{-h}^{\epsilon\eta} \frac{\partial v}{\partial y} dz + \int_{-h}^{\epsilon\eta} \frac{\partial w}{\partial z} dz\right) = 0. \tag{3.45}$$

The first two integrals are expressed using the Leibniz rule

$$\int_{-h}^{\epsilon\eta} \frac{\partial u}{\partial x} dz = \frac{\partial}{\partial x}\int_{-h}^{\epsilon\eta} u dz - \epsilon u(\epsilon\eta)\frac{\partial \eta}{\partial x} - u(-h)\frac{\partial h}{\partial x}, \tag{3.46}$$

$$\int_{-h}^{\epsilon\eta} \frac{\partial v}{\partial y} dz = \frac{\partial}{\partial y}\int_{-h}^{\epsilon\eta} v dz - \epsilon v(\epsilon\eta)\frac{\partial \eta}{\partial y} - v(-h)\frac{\partial h}{\partial y}, \tag{3.47}$$

and the third integral is obtained from the fundamental theorem of calculus

$$\int_{-h}^{\epsilon\eta} \frac{\partial w}{\partial z} dz = w(\epsilon\eta) - w(-h). \tag{3.48}$$

The kinematic boundary conditions (3.24) and (3.25) can be recast as

$$\frac{\partial \eta}{\partial t} = -\epsilon u(\epsilon\eta)\frac{\partial \eta}{\partial x} - \frac{\epsilon}{\mu^2} v(\epsilon\eta)\frac{\partial \eta}{\partial y} + \frac{1}{\mu^2} w(\epsilon\eta), \tag{3.49}$$

$$0 = -u(-h)\frac{\partial h}{\partial x} - \frac{1}{\mu^2} v(-h)\frac{\partial h}{\partial y} - \frac{1}{\mu^2} w(-h) \tag{3.50}$$

so equation (3.45) becomes

$$\frac{\partial}{\partial x}\int_{-h}^{\epsilon\eta} u dz + \frac{1}{\mu^2}\frac{\partial}{\partial y}\int_{-h}^{\epsilon\eta} v dz + \frac{\partial \eta}{\partial t} = 0. \tag{3.51}$$

Using (3.43) to introduce the depth averaged velocities

$$\breve{u} = \frac{1}{\epsilon\eta + h}\int_{-h}^{\epsilon\eta} u dz, \qquad \text{and} \qquad \breve{v} = \frac{1}{\epsilon\eta + h}\int_{-h}^{\epsilon\eta} v dz, \tag{3.52}$$

and defining the total water depth as $H = \epsilon\eta + h$, implies that (3.51) becomes

$$\frac{1}{\epsilon}\frac{\partial H}{\partial t} + \frac{\partial}{\partial x}\left(H\breve{u}\right) + \frac{1}{\mu^2}\frac{\partial}{\partial y}\left(H\breve{v}\right) = 0. \tag{3.53}$$

Integrating (3.53) from the right boundary $y = -s_r(x,t)$ to the left boundary $y = s_l(x,t)$ and using the Leibniz rule yield

$$\begin{aligned}\frac{1}{\epsilon}\frac{\partial}{\partial t}\int_{-s_r}^{s_l} H dy + \frac{\partial}{\partial x}\int_{-s_r}^{s_l} H\breve{u} dy + H(s_l)\left[-\frac{1}{\epsilon}\frac{\partial s_l}{\partial t} - \breve{u}(s_l)\frac{\partial s_l}{\partial x} + \frac{1}{\mu^2}\breve{v}(s_l)\right] \\ + H(-s_r)\left[-\frac{1}{\epsilon}\frac{\partial s_r}{\partial t} - \breve{u}(-s_r)\frac{\partial s_r}{\partial x} - \frac{1}{\mu^2}\breve{v}(-s_r)\right] = 0,\end{aligned} \tag{3.54}$$

in which the parenthesis, $(-s_r)$ and (s_l), denote the physical quantities being evaluated at $y = -s_r$ and $y = s_l$, respectively. By definition, the total water depth at the shoreline vanishes for cross-sections where sidewalls are not vertical, i.e., $H(-s_r)$ and $H(s_l) = 0$. Thus, the last two terms in the equation above vanish. On the other hand, when the channel banks are vertical, the kinematic boundary conditions at the sidewalls can be depth integrated to show that the last two terms in (3.54) also vanish. For example, equation (3.26) is recast and integrated

$$-\frac{1}{\epsilon}\frac{\partial s_l}{\partial t}\int_{-h}^{\epsilon\eta} dz - \frac{\partial s_l}{\partial x}\int_{-h}^{\epsilon\eta} u(s_l) dz + \frac{1}{\mu^2}\int_{-h}^{\epsilon\eta} v(s_l) dz = 0. \tag{3.55}$$

to yield, after depth averaging (3.43)

$$H(s_l)\left[-\frac{1}{\epsilon}\frac{\partial s_l}{\partial t} - \breve{u}(s_l)\frac{\partial s_l}{\partial x} + \frac{1}{\mu^2}\breve{v}(s_l)\right] = 0. \tag{3.56}$$

Equation of conservation of mass (3.54) therefore becomes

$$\frac{1}{\epsilon}\frac{\partial}{\partial t}\int_{-s_r}^{s_l} H dy + \frac{\partial}{\partial x}\int_{-s_r}^{s_l} H\breve{u} dy = 0, \tag{3.57}$$

The first integral in the equation is simply the cross section area as defined by equation (3.30) whereas the second integral represents the total flux per cross sectional area, as defined by equation (3.37). The final expression is therefore

$$\frac{1}{\epsilon}\frac{\partial A}{\partial t} + \frac{\partial \left(\langle u \rangle A\right)}{\partial x} = 0. \tag{3.58}$$

It is noted here that if the effects of viscous boundary layer flows are considered, additional mass fluxes along the outer edge of the boundary layer must be added. Viscous effects in the boundary layer are analyzed in Chapter 6.

Conservation of momentum

Following a similar averaging procedure, the cross-sectional averaged momentum equation is obtained. Namely, the x-component of the Euler equations, (3.20), is first integrated in the vertical direction

$$\int_{-h}^{\epsilon\eta} \frac{\partial u}{\partial t} dz + \epsilon \int_{-h}^{\epsilon\eta} \frac{\partial}{\partial x}\left(u^2\right) dz + \frac{\epsilon}{\mu^2} \int_{-h}^{\epsilon\eta} \frac{\partial}{\partial y}\left(uv\right) dz + \frac{\epsilon}{\mu^2} \int_{-h}^{\epsilon\eta} \frac{\partial}{\partial z}\left(uw\right) dz = -\int_{-h}^{\epsilon\eta} \frac{\partial p}{\partial x} dz, \tag{3.59}$$

where the derivatives are expressed using the Leibniz rule

$$\int_{-h}^{\epsilon\eta} \frac{\partial u}{\partial t} dz = \frac{\partial}{\partial t} \int_{-h}^{\epsilon\eta} u dz - \epsilon u(\epsilon\eta) \frac{\partial \eta}{\partial t} - u(-h) \frac{\partial h}{\partial t}, \tag{3.60}$$

$$\int_{-h}^{\epsilon\eta} \frac{\partial}{\partial x}\left(u^2\right) dz = \frac{\partial}{\partial x} \int_{-h}^{\epsilon\eta} u^2 dz - \epsilon u^2(\epsilon\eta) \frac{\partial \eta}{\partial x} - u^2(-h) \frac{\partial h}{\partial x}, \tag{3.61}$$

$$\int_{-h}^{\epsilon\eta} \frac{\partial}{\partial y}\left(uv\right) dz = \frac{\partial}{\partial y} \int_{-b}^{\epsilon\eta} uv dz - \epsilon u(\epsilon\eta) v(\epsilon\eta) \frac{\partial \eta}{\partial y} - u(-h) v(-h) \frac{\partial h}{\partial y}, \tag{3.62}$$

and the fundamental theorem of calculus

$$\int_{-h}^{\epsilon\eta} \frac{\partial}{\partial z}\left(uw\right) dz = u(\epsilon\eta) w(\epsilon\eta) - u(-h) w(-h). \tag{3.63}$$

Combining the boundary conditions (3.24) and (3.25) with (3.59) yields

$$\frac{\partial}{\partial t}\int_{-h}^{\epsilon\eta} u dz + \epsilon\frac{\partial}{\partial x}\int_{-h}^{\epsilon\eta} u^2 dz + \frac{\epsilon}{\mu^2}\frac{\partial}{\partial y}\int_{-h}^{\epsilon\eta} uv dz = -\int_{-h}^{\epsilon\eta}\frac{\partial p}{\partial x}dz. \tag{3.64}$$

Introducing the depth average quantities (3.43)

$$\frac{\partial}{\partial t}(H\breve{u}) + \epsilon\frac{\partial}{\partial x}(H\breve{u}\breve{u}) + \frac{\epsilon}{\mu^2}\frac{\partial}{\partial y}(H\breve{u}\breve{v}) = -\int_{-h}^{\epsilon\eta}\frac{\partial p}{\partial x}dz \tag{3.65}$$

and integrating between $y = -s_r(x,t)$ to $y = -s_l(x,t)$ yields

$$\int_{-s_r}^{s_l}\frac{\partial}{\partial t}(H\breve{u})\,dy + \epsilon\int_{-s_r}^{s_l}\frac{\partial}{\partial x}(H\breve{u}\breve{u})\,dy + \frac{\epsilon}{\mu^2}\int_{-s_r}^{s_l}\frac{\partial}{\partial y}(H\breve{u}\breve{v})\,dy = -\int_{-s_r}^{s_l}\int_{-h}^{\epsilon\eta}\frac{\partial p}{\partial x}dzdy, \tag{3.66}$$

where the derivatives are expressed using the Leibniz rule and the fundamental theorem of calculus

$$\int_{-s_r}^{s_l}\frac{\partial}{\partial t}(H\breve{u})\,dy = \frac{\partial}{\partial t}\int_{-s_r}^{s_l} H\breve{u}dy - H(s_l)\breve{u}(s_l)\frac{\partial s_l}{\partial t} - H(-s_r)\breve{u}(-s_r)\frac{\partial s_r}{\partial t}, \tag{3.67}$$

$$\int_{-s_r}^{s_l}\frac{\partial}{\partial x}(H\breve{u}\breve{u})\,dy = \frac{\partial}{\partial x}\int_{-s_r}^{s_l} H\breve{u}\breve{u}dy - H(s_l)\breve{u}\breve{u}(s_l)\frac{\partial s_l}{\partial x} - H(-s_r)\breve{u}\breve{u}(-s_r)\frac{\partial s_r}{\partial x}, \tag{3.68}$$

$$\int_{-s_r}^{s_l}\frac{\partial}{\partial y}(H\breve{u}\breve{v})\,dy = H(s_l)\breve{u}\breve{v}(s_l) - H(-s_r)\breve{u}\breve{v}(-s_r). \tag{3.69}$$

Equation (3.65) therefore becomes

$$\begin{aligned}\frac{\partial}{\partial t}\int_{-s_r}^{s_l} H\breve{u}dy + \epsilon\frac{\partial}{\partial x}\int_{-s_r}^{s_l} H\breve{u}\breve{u}dy + H(s_l)\left[-\breve{u}(s_l)\frac{\partial s_l}{\partial t} - \epsilon\breve{u}\breve{u}(s_l)\frac{\partial s_l}{\partial x} + \frac{\epsilon}{\mu^2}\breve{u}\breve{v}(s_l)\right]\\ +H(-s_r)\left[-\breve{u}(-s_r)\frac{\partial s_r}{\partial t} - \epsilon\breve{u}\breve{u}(-s_r)\frac{\partial s_r}{\partial x} - \frac{\epsilon}{\mu^2}\breve{u}\breve{v}(-s_r)\right] = -\int_{-s_r}^{s_l}\int_{-h}^{\epsilon\eta}\frac{\partial p}{\partial x}dzdy.\end{aligned} \tag{3.70}$$

As stated before, $H(-s_r), H(s_l) = 0$ for sloping sidewalls so

$$\frac{\partial}{\partial t}\int_{-s_r}^{s_l} H\breve{u}dy + \epsilon\frac{\partial}{\partial x}\int_{-s_r}^{s_l} H\breve{u}\breve{u}dy = -\int_{-s_r}^{s_l}\int_{-h}^{\epsilon\eta}\frac{\partial p}{\partial x}dzdy. \tag{3.71}$$

For vertical sidewalls where $H(-s_r), H(s_l) \neq 0$ and the kinematic boundary conditions must be invoked. For example, the left boundary (3.26) is multiplied by $u(s_l)$ and integrated over the depth

$$\frac{1}{\epsilon}\frac{\partial s_l}{\partial t}\int_{-h}^{\epsilon\eta} u(s_l)dz - \frac{\partial s_l}{\partial x}\int_{-h}^{\epsilon\eta} uu(s_l)dz + \frac{1}{\mu^2}\int_{-h}^{\epsilon\eta} uv(s_l)dz = 0 \tag{3.72}$$

to yield, upon depth averaging (3.43)

$$H(s_l)\left[-\breve{u}(s_l)\frac{\partial s_l}{\partial t} - \epsilon\breve{u}u(s_l)\frac{\partial s_l}{\partial x} + \frac{\epsilon}{\mu^2}\breve{u}v(s_l)\right] = 0. \tag{3.73}$$

Equation (3.71) is recovered after applying the same argument for the right boundary. Returning to original quantities

$$\frac{\partial}{\partial t}\int_{-s_r}^{s_l}\int_{-h}^{\epsilon\eta} udzdy + \epsilon\frac{\partial}{\partial x}\int_{-s_r}^{s_l}\int_{-h}^{\epsilon\eta} uudzdy = -\int_{-s_r}^{s_l}\int_{-h}^{\epsilon\eta}\frac{\partial p}{\partial x}dzdy, \tag{3.74}$$

which can be rewritten in terms of the cross-sectional averaged quantities as

$$\frac{\partial}{\partial t}\left(A\left\langle u\right\rangle\right) + \epsilon\frac{\partial}{\partial x}\left(A\left\langle uu\right\rangle\right) = -A\left\langle\frac{\partial p}{\partial x}\right\rangle. \tag{3.75}$$

Equations (3.58) and (3.75) are exact for a channel of arbitrary cross-section. No restriction has yet been imposed on the parameters, ϵ and μ. A similar set of equations was derived by Teng & Wu (1992, Eqs. 12 and 13 in their paper) in dimensional form. In their derivation, the channel cross-section was required to be symmetric with respect to the centerline of the channel. It is shown herein that this requirement is unnecessary.

3.4.3 Perturbation expansion

In (3.58) and (3.75), $\langle uu\rangle$ and $\langle\partial p/\partial x\rangle$ need to be further related to the cross-sectional averaged velocity $\langle u\rangle$ and surface-width averaged free surface elevation $\widetilde{\eta}$. To accomplish this, additional approximations are needed. First of all the

Boussinesq approximation is invoked, i.e., $O(\epsilon) = O(\mu^2) \ll O(1)$, therefore, the resulting theory is applicable only for weakly-nonlinear and weakly-dispersive waves. A second step is to expand the dimensionless physical variables as power series of μ^2

$$\phi = \phi_1(x,t) + \mu^2\phi_2(x,y,z,t) + O\left(\mu^4\right), \tag{3.76}$$

$$\eta = \eta_1(x,t) + \mu^2\eta_2(x,y,t) + O\left(\mu^4\right), \tag{3.77}$$

$$u = u_1(x,t) + \mu^2 u_2(x,y,z,t) + O\left(\mu^4\right), \tag{3.78}$$

$$v = \mu^2 v_2(x,y,z,t) + O\left(\mu^4\right), \tag{3.79}$$

$$w = \mu^2 w_2(x,y,z,t) + O\left(\mu^4\right). \tag{3.80}$$

The scaling of the velocities implies the vertical and transverse velocity components are comparable and are smaller than the longitudinal velocity, i.e., $O(v) = O(w) \ll O(u)$.

Equation (3.78) is used to express $\langle uu \rangle$ in terms of the cross-sectional averaged velocity $\langle u \rangle$. The following expressions are derived from (3.78):

$$\langle u \rangle = u_1 + \mu^2 \langle u_2 \rangle + O\left(\mu^4\right), \tag{3.81}$$

$$\langle u \rangle \langle u \rangle = u_1^2 + 2\mu^2 u_1 \langle u_2 \rangle + O\left(\mu^4\right), \tag{3.82}$$

$$uu = u_1^2 + 2\mu^2 u_1 u_2 + O\left(\mu^4\right), \tag{3.83}$$

$$\langle uu \rangle = u_1^2 + 2\mu^2 u_1 \langle u_2 \rangle + O\left(\mu^4\right). \tag{3.84}$$

Equations (3.82) and (3.84) imply

$$\langle uu \rangle = \langle u \rangle \langle u \rangle + O\left(\mu^4\right). \tag{3.85}$$

To find an expression for $\langle \partial p/\partial x \rangle$, the perturbation expansions are substituted into the Bernoulli equation (3.23) to obtain

$$\frac{\partial \phi_1}{\partial t} + \mu^2 \frac{\partial \phi_2}{\partial t} + \frac{1}{2}\epsilon u_1^2 + p + \frac{z}{\epsilon} = O\left(\epsilon\mu^2, \mu^4\right). \tag{3.86}$$

Note that the leading order error in the above expression is equivalent to $O\left(\epsilon^2, \epsilon\mu^2, \mu^4\right)$ by virtue of the Boussinesq approximation. For convention, the latter expression of the leading order error will be used hereafter, unless otherwise noted. First, taking the derivative of (3.86) with respect to x and then averaging the resulting equation over the cross-section of the channel yields

$$\frac{\partial^2 \phi_1}{\partial x \partial t} + \mu^2 \left\langle \frac{\partial^2 \phi_2}{\partial x \partial t} \right\rangle + \frac{1}{2}\epsilon \frac{\partial}{\partial x}\left(u_1^2\right) + \left\langle \frac{\partial p}{\partial x} \right\rangle = O\left(\epsilon^2, \epsilon\mu^2, \mu^4\right). \tag{3.87}$$

Evaluating the Bernoulli equation (3.86) at the surface $z = \epsilon\eta$ yields

$$\frac{\partial \phi_1}{\partial t} + \mu^2 \left.\frac{\partial \phi_2}{\partial t}\right|_{z=\epsilon\eta} + \frac{1}{2}\epsilon u_1^2 + \eta = O\left(\epsilon^2, \epsilon\mu^2, \mu^4\right). \tag{3.88}$$

Note that ϕ_1 and u_1 are constants at the cross-section and the atmospheric pressure on the free surface has been assumed to be zero. The second term in the equation above is evaluated on the free surface $z = \epsilon\eta$ and can be approximated by the corresponding term evaluated on the still water level $z = 0$, i.e.,

$$\left.\frac{\partial \phi_2}{\partial t}\right|_{z=\epsilon\eta} = \left.\frac{\partial \phi_2}{\partial t}\right|_{z=0} + O(\epsilon). \tag{3.89}$$

Therefore, (3.88) becomes

$$\frac{\partial \phi_1}{\partial t} + \mu^2 \left.\frac{\partial \phi_2}{\partial t}\right|_{z=0} + \frac{1}{2}\epsilon u_1^2 + \eta = O\left(\epsilon^2, \epsilon\mu^2, \mu^4\right), \tag{3.90}$$

Taking the spanwise average across the still water surface (3.42) of the above equation, and then differentiating with respect to x yields

$$\frac{\partial^2 \phi_1}{\partial x \partial t} + \mu^2 \frac{\partial}{\partial x}\left(\widetilde{\left.\frac{\partial \phi_2}{\partial t}\right|_{z=0}}\right) + \frac{1}{2}\epsilon \frac{\partial}{\partial x}\left(u_1^2\right) + \frac{\partial \widetilde{\eta}}{\partial x} = O\left(\epsilon^2, \epsilon\mu^2, \mu^4\right). \tag{3.91}$$

Subtracting (3.91) from (3.87) yields

$$\left\langle \frac{\partial p}{\partial x} \right\rangle = \frac{\partial \widetilde{\eta}}{\partial x} + \mu^2 \left[\frac{\partial}{\partial x}\left(\widetilde{\left.\frac{\partial \phi_2}{\partial t}\right|_{z=0}}\right) - \left\langle \frac{\partial^2 \phi_2}{\partial x \partial t} \right\rangle \right] + O\left(\epsilon^2, \epsilon\mu^2, \mu^4\right), \tag{3.92}$$

where the last term is approximated using the relation (3.41), thus

$$\left\langle \frac{\partial p}{\partial x} \right\rangle = \frac{\partial \widetilde{\eta}}{\partial x} + \mu^2 \left[\frac{\partial}{\partial x}\left(\widetilde{\left.\frac{\partial \phi_2}{\partial t}\right|_{z=0}}\right) - \overline{\frac{\partial^2 \phi_2}{\partial x \partial t}} \right] + O\left(\epsilon^2, \epsilon\mu^2, \mu^4\right). \tag{3.93}$$

This last approximation -valid for channels with the sidewall slope being $O(1)$- facilitates the computation of the last term in the above, which is integrated on the cross-sectional area at the quiescent state. Expressions (3.35), (3.85) and (3.93) are used to derive approximate expressions for the equations of conservation of mass and momentum, in closed form.

Conservation of mass

Substituting the (3.35) into the continuity equation (3.58) yields

$$\frac{\partial \widetilde{\eta}}{\partial t} + \epsilon \frac{B_0'}{2B_0} \frac{\partial \widetilde{\eta}^2}{\partial t} + \frac{1}{B_0} \frac{\partial}{\partial x} \left[\langle u \rangle \left(A_0 + \epsilon B_0 \widetilde{\eta} \right) \right] = O\left(\epsilon^2, \epsilon\mu^2, \mu^4 \right). \tag{3.94}$$

The second term in the equation above can be manipulated by replacing the time derivative of $\widetilde{\eta}$ with a spatial derivative obtained from the leading order terms of the same equation. Thus, conservation of mass becomes

$$\frac{\partial \widetilde{\eta}}{\partial t} + \frac{1}{B_0} \frac{\partial}{\partial x} \left[\langle u \rangle A_0 \right] - \epsilon \frac{B_0'}{B_0^2} \widetilde{\eta} \frac{\partial}{\partial x} \left[\langle u \rangle A_0 \right] + \frac{\epsilon}{B_0} \frac{\partial}{\partial x} \left[\langle u \rangle B_0 \widetilde{\eta} \right] = O\left(\epsilon^2, \epsilon\mu^2, \mu^4 \right). \tag{3.95}$$

Conservation of momentum

Substituting expressions (3.35), (3.85) and (3.93) into the momentum equation (3.75) yields, after simple manipulations,

$$\frac{\partial \langle u \rangle}{\partial t} + \frac{\partial \widetilde{\eta}}{\partial x} + \epsilon \left[\frac{B_0}{A_0} \frac{\partial}{\partial t} \left(\widetilde{\eta} \langle u \rangle \right) + \frac{1}{A_0} \frac{\partial}{\partial x} \left(A_0 \langle u \rangle \langle u \rangle \right) + \frac{B_0}{A_0} \widetilde{\eta} \frac{\partial \widetilde{\eta}}{\partial x} \right] + \mu^2 \mathfrak{D} = O\left(\epsilon^2, \epsilon\mu^2, \mu^4 \right), \tag{3.96}$$

where

$$\mathfrak{D}(x,t) = \frac{\partial}{\partial x} \left(\widetilde{\left. \frac{\partial \phi_2}{\partial t} \right|_{z=0}} \right) - \overline{\frac{\partial^2 \phi_2}{\partial x \partial t}}. \tag{3.97}$$

is a function characterizing frequency dispersion. The term

$$I \equiv \frac{B_0}{A_0} \frac{\partial}{\partial t} \left(\widetilde{\eta} \langle u \rangle \right) + \frac{B_0}{A_0} \widetilde{\eta} \frac{\partial \widetilde{\eta}}{\partial x} = \frac{B_0}{A_0} \left[\widetilde{\eta} \left\{ \frac{\partial \langle u \rangle}{\partial t} + \frac{\partial \widetilde{\eta}}{\partial x} \right\} + \langle u \rangle \frac{\partial \widetilde{\eta}}{\partial t} \right] \tag{3.98}$$

is manipulated using the leading order expressions for the conservation of momentum (3.96) and mass (3.95)

$$\frac{\partial \langle u \rangle}{\partial t} + \frac{\partial \widetilde{\eta}}{\partial x} = O\left(\epsilon, \mu^2 \right), \qquad \frac{\partial \widetilde{\eta}}{\partial t} + \frac{1}{B_0} \frac{\partial}{\partial x} \left[\langle u \rangle A_0 \right] = O\left(\epsilon, \mu^2 \right), \tag{3.99}$$

to yield

$$I = -\frac{1}{A_0}\langle u\rangle \frac{\partial}{\partial x}\left[A_0\langle u\rangle\right] + O\left(\epsilon, \mu^2\right). \tag{3.100}$$

The bracketed expression in (3.96) can be manipulated to yield

$$I + \frac{1}{A_0}\frac{\partial}{\partial x}\left(A_0\langle u\rangle\langle u\rangle\right) = \langle u\rangle \frac{\partial\langle u\rangle}{\partial x}, \tag{3.101}$$

so the conservation of momentum (3.96) becomes

$$\frac{\partial\langle u\rangle}{\partial t} + \frac{\partial\widetilde{\eta}}{\partial x} + \epsilon\langle u\rangle\frac{\partial\langle u\rangle}{\partial x} + \mu^2\mathfrak{D} = O\left(\epsilon^2, \epsilon\mu^2, \mu^4\right), \tag{3.102}$$

Equations (3.95) and (3.102) are the governing equations for $\langle u\rangle$, the cross-sectional averaged longitudinal velocity component, and $\widetilde{\eta}$, the spanwise averaged free surface elevation. However, $\mathfrak{D}$ or ϕ_2 still needs to be described.

3.4.4 Boundary value problems on a cross-sectional plane

On a channel cross-section, the governing equation for ϕ_2 can be derived by substituting the perturbation expansions (3.76) to (3.80) into the conservation of mass (3.19) and considering, by virtue of (3.78), the relation $\langle u\rangle = u_1 + O\left(\mu^2\right)$. This yields

$$\frac{\partial^2\phi_2}{\partial y^2} + \frac{\partial^2\phi_2}{\partial z^2} = -\frac{\partial\langle u\rangle}{\partial x} + O\left(\epsilon, \mu^2\right), \qquad \text{on} \quad -h(x,y) < z < 0. \tag{3.103}$$

Using the leading order terms of (3.95) in the linearized version of the free surface boundary condition (3.24) yields

$$\frac{\partial\phi_2}{\partial z} = -\frac{A_0}{B_0}\frac{\partial\langle u\rangle}{\partial x} - \frac{1}{B_0}\frac{dA_0}{dx}\langle u\rangle + O\left(\epsilon, \mu^2\right), \qquad \text{on} \quad z = 0. \tag{3.104}$$

The bottom boundary condition (3.25) can be recast as

$$(v, w)\cdot\left(\frac{\partial h}{\partial y}, 1\right) = -\mu^2 u\frac{\partial h}{\partial x}, \qquad z = -h(x,y). \tag{3.105}$$

For convenience, the cross-sectional gradient $\nabla_t F = \left(\frac{\partial F}{\partial y}, \frac{\partial F}{\partial z}\right)$ and a unit normal vector $\mathbf{n}$ at a fixed x which is parallel to the cross-section (in the $y-z$ plane), are introduced (Figure 3.3). For a fixed cross-section, the bottom boundary is defined by $F = z + h(y,t)$, so $\mathbf{n}$ becomes

$$\mathbf{n} = \frac{\nabla_t F}{\|\nabla_t F\|} = \frac{\left(\frac{\partial h}{\partial y}, 1\right)}{\sqrt{\left(\frac{\partial h}{\partial y}\right)^2 + 1}}, \qquad \Rightarrow \qquad \left(\frac{\partial h}{\partial y}, 1\right) = \mathbf{n}\sqrt{\left(\frac{\partial h}{\partial y}\right)^2 + 1}. \tag{3.106}$$

As shown in Appendix B, the definition of $\mathbf{n}$ fulfills the solvability condition for the boundary value problem. On the other hand, by definition

$$(v, w) = \left(\frac{\partial \phi}{\partial y}, \frac{\partial \phi}{\partial z}\right) = \nabla\phi \qquad \text{and} \qquad \frac{\partial \phi}{\partial n} = \nabla\phi \cdot \mathbf{n}. \tag{3.107}$$

Plugging (3.106) and (3.107) into (3.105) yields

$$\frac{\partial \phi}{\partial n} = -\frac{\mu^2 u \frac{\partial h}{\partial x}}{\sqrt{\left(\frac{\partial h}{\partial y}\right)^2 + 1}}, \qquad z = -h. \tag{3.108}$$

Expanding the velocity potential and using the relation $u_1 = \langle u \rangle + O(\mu^2)$ yields

$$\frac{\partial \phi_2}{\partial n} = -\frac{\langle u \rangle \frac{\partial h}{\partial x}}{\sqrt{\left(\frac{\partial h}{\partial y}\right)^2 + 1}} + O\left(\epsilon, \mu^2\right), \qquad \text{on} \quad z = -h(x,y). \tag{3.109}$$

If the channel is bounded by vertical walls, say at $y = b_l(x)$, and $y = -b_r(x)$, two additional boundary conditions are required

$$\frac{\partial \phi_2}{\partial n} = \langle u \rangle \left(-\frac{db_l}{dx}, \frac{db_r}{dx}\right) + O\left(\mu^2\right), \qquad \text{on} \quad y = b_l(x), \text{ and } -b_r(x). \tag{3.110}$$

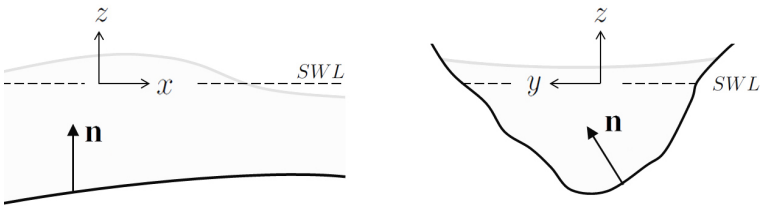

Figure 3.3: Definition of the unit normal in the $y-z$ plane, $\mathbf{n}$.

The leading order error of the boundary value problem for ϕ_2 given by equations (3.103), (3.104), (3.109) and (3.110) is consistent with that of the momentum equation (3.102), where $\mathfrak{D}$ is being multiplied by μ^2.

Since the boundary value problem for ϕ_2 is linear and is only forced by $\langle u \rangle$ and $\partial \langle u \rangle / \partial x$, the following solution form is sought:

$$\phi_2(x,y,z,t) = \chi_1(x,y,z)\langle u \rangle + \chi_2(x,y,z)\frac{\partial \langle u \rangle}{\partial x} + F(x,t), \tag{3.111}$$

in which $F(x,t)$ is an arbitrary function and does not contribute to the velocity field. Indeed, its contribution is canceled out in the dispersive function (3.97). Substituting (3.111) into (3.103), (3.104) and (3.109), the boundary value problems for χ_1 and χ_2 are expressed as

$$\frac{\partial^2 \chi_1}{\partial y^2} + \frac{\partial^2 \chi_1}{\partial z^2} = 0 \qquad \text{on} \quad -h(x,y) < z < 0, \tag{3.112}$$

$$\frac{\partial \chi_1}{\partial z} = -\frac{1}{B_0}\frac{dA_0}{dx} \qquad \text{on} \quad z = 0, \tag{3.113}$$

$$\frac{\partial \chi_1}{\partial n} = -\frac{\frac{\partial h}{\partial x}}{\sqrt{\left(\frac{\partial h}{\partial y}\right)^2 + 1}} \qquad \text{on} \quad z = -h(x,y), \tag{3.114}$$

and

$$\frac{\partial^2 \chi_2}{\partial y^2} + \frac{\partial^2 \chi_2}{\partial z^2} = -1 \qquad \text{on} \quad -h(x,y) < z < 0, \tag{3.115}$$

$$\frac{\partial \chi_2}{\partial z} = -\frac{A_0}{B_0} \qquad \text{on} \quad z = 0, \tag{3.116}$$

$$\frac{\partial \chi_2}{\partial n} = 0 \qquad \text{on} \quad z = -h(x,y). \tag{3.117}$$

As pointed out before, if the sidewalls are vertical, two additional no-flux boundary conditions for χ_1 and χ_2 derived from (3.110) must be invoked:

$$\frac{\partial \chi_1}{\partial y} = \left(-\frac{db_l}{dx}, \frac{db_r}{dx}\right) \quad \text{and} \quad \frac{\partial \chi_2}{\partial y} = 0, \qquad \text{on} \quad y = b_l(x), -b_r(x). \tag{3.118}$$

The function χ_1 is a new contribution of the present theory, representing the effects of a fast varying cross-section in the direction of wave propagation, which

were not considered in Peregrine (1968) and Teng & Wu (1992). Functions χ_1 and χ_2 depend only on the geometry of the channel and can be calculated once the channel configuration is prescribed. Moreover, if the channel cross-section is uniform in the x-direction, i.e., $d(A_0, h, b_l, b_r)/dx = 0$, the boundary value problem for χ_1 becomes homogeneous and thus, $\chi_1 = 0$.

Analytical solutions for χ_1 and χ_2 can be obtained for simple geometries, as shown in section in Section 3.5 and Appendix C. Numerical integration, however, is required for irregular geometries. Several numerical methods, i.e., finite difference, finite element and boundary element, can be used to solve the boundary value problems. Examples of numerical solutions for χ_1 and χ_2 are included in Section 5.1.1.

3.4.5 Cross-sectional averaged Boussinesq equations

Once χ_1 and χ_2 are calculated for a given channel geometry, (3.111) can be substituted into (3.97) to get

$$\mathfrak{D}(x,t) = \alpha \frac{\partial \langle u \rangle}{\partial t} + \beta \frac{\partial^2 \langle u \rangle}{\partial t \partial x} + \gamma \frac{\partial^3 \langle u \rangle}{\partial t \partial x^2}, \tag{3.119}$$

where

$$\alpha(x) = \frac{\partial}{\partial x}\left[\widetilde{\chi_1|_{z=0}}\right] - \overline{\frac{\partial \chi_1}{\partial x}}, \tag{3.120}$$

$$\beta(x) = \widetilde{\chi_1|_{z=0}} - \overline{\chi_1} + \frac{\partial}{\partial x}\left[\widetilde{\chi_2|_{z=0}}\right] - \overline{\frac{\partial \chi_2}{\partial x}}, \tag{3.121}$$

$$\gamma(x) = \widetilde{\chi_2|_{z=0}} - \overline{\chi_2}, \tag{3.122}$$

can be readily calculated for a given channel configuration. In the above, the averages of the gradients, i.e. $\overline{\partial \chi_i/\partial x}$ $(i = 1, 2)$, are expressed using the Leibniz

rule as

$$\overline{\frac{\partial \chi_i}{\partial x}} = \frac{1}{A_0}\frac{\partial}{\partial x}\left(\overline{\chi}_i A_0\right) - \frac{1}{A_0}\int_{-b_r}^{b_l} \chi_i\left(x, y, -h\right)\frac{\partial h}{\partial x} dy - \frac{1}{A_0}\frac{\partial b_l}{\partial x}\int_{-h}^{0} \chi_i\left(x, b_l, z\right) dz - \frac{1}{A_0}\frac{\partial b_r}{\partial x}\int_{-h}^{0} \chi_i\left(x, -b_r, z\right) dz, \quad (3.123)$$

where the last two integrals are zero for vertical sidewalls. Section 3.5 includes analytical expressions for constant coefficients α, β and γ for rectangular and triangular symmetric cross-sections. Numerical computations of these coefficient in irregular geometries are found in Section 5.1.1. Recall that these coefficients have the leading order error of $O\left(\epsilon, \mu^2\right)$, consistent with the accuracy of the cross-averaged momentum equation, since they are factored by μ^2.

Finally the momentum equation (3.102) can be rewritten in the following form:

$$\left(1 + \mu^2\alpha\right)\frac{\partial \langle u\rangle}{\partial t} + \frac{\partial \widetilde{\eta}}{\partial x} + \epsilon\langle u\rangle\frac{\partial \langle u\rangle}{\partial x} + \mu^2\beta\frac{\partial^2 \langle u\rangle}{\partial t \partial x} + \mu^2\gamma\frac{\partial^3 \langle u\rangle}{\partial t \partial x^2} = O\left(\epsilon^2, \epsilon\mu^2, \mu^4\right). \quad (3.124)$$

Equations (3.95) and (3.124) are the governing equations for the cross-sectional averaged longitudinal velocity, $\langle u\rangle$, and the span-wise averaged free surface elevation, $\widetilde{\eta}$. Properly described initial conditions, upstream and downstream boundary conditions in the channel are needed to solve the initial boundary value problem. Since $O(\epsilon) \sim O(\mu^2)$ has been employed, the governing equations are of Boussinesq-type suitable for modeling weakly-nonlinear and weakly-dispersive waves.

The coefficients α, β, and γ in these equations depend only on the cross-sectional geometry and are allowed to vary significantly within a wavelength. Specifically, the term associated with α represents a correction to the local acceleration due to changes in the cross-section, and the term associated with β denotes the wave decay or amplification caused such changes. Both terms can be neglected

when the channel variations in the longitudinal direction become very small, e.g. $\alpha, \beta, \gamma = O(\epsilon, \mu^2)$. The term associated with γ represents the frequency dispersive effects, which remains important even when the channel variations in the longitudinal direction become very small.

3.4.6 Simplification to other long wave models

Equations (3.95) and (3.124) constitute a weakly-nonlinear weakly-dispersive system from which other models may be regarded as subclasses. Simpler models can be derived following Ursell's classification of long wave regimes, expressed in terms of the nondimensional parameter $U = \epsilon/\mu^2$. (Ursell, 1953). The simplest model consist of the linear nondispersive long wave equations, which are essentially the leading order solution of equations (3.95) and (3.124)

$$\frac{\partial \widetilde{\eta}}{\partial t} + \frac{1}{B_0}\frac{\partial}{\partial x}\left[\langle u \rangle A_0\right] = 0, \tag{3.125}$$

$$\frac{\partial \langle u \rangle}{\partial t} + \frac{\partial \widetilde{\eta}}{\partial x} = 0. \tag{3.126}$$

This model fails to explain nonlinear free surface phenomena and neglects frequency dispersion, which may become important in long distance propagation.

A channel-type form of nonlinear shallow water equations, on the other hand, is obtained by neglecting the $O\left(\mu^2\right)$ terms. The corresponding expressions

$$\frac{\partial \widetilde{\eta}}{\partial t} + \frac{1}{B_0}\frac{\partial}{\partial x}\left[\langle u \rangle A_0\right] - \epsilon\frac{B_0'}{B_0^2}\widetilde{\eta}\frac{\partial}{\partial x}\left[\langle u \rangle A_0\right] + \frac{\epsilon}{B_0}\frac{\partial}{\partial x}\left[\langle u \rangle B_0\widetilde{\eta}\right] = 0), \tag{3.127}$$

$$\frac{\partial \langle u \rangle}{\partial t} + \frac{\partial \widetilde{\eta}}{\partial x} + \epsilon \langle u \rangle \frac{\partial \langle u \rangle}{\partial x} = 0, \tag{3.128}$$

are valid for $U \gg O(1)$. These expressions are adequate if, for example, nonlinear wave interaction is of concern. Similar expressions were derived by Airy

(1845) and predict that due to nonlinearity in the momentum equation, the wave front will steepen during propagation until a shock is formed (Dingemans, 1997:487-488). The sidewall slope at the water level, B_0', however, incorporates a complementary nonlinear behavior in wave evolution.

Finally, a linear weakly-dispersive model is obtained by enforcing $U \ll O(1)$ to yield the following expressions

$$\frac{\partial \widetilde{\eta}}{\partial t} + \frac{1}{B_0}\frac{\partial}{\partial x}\left[\langle u \rangle A_0\right] = 0, \tag{3.129}$$

$$\frac{\partial \langle u \rangle}{\partial t} + \frac{\partial \widetilde{\eta}}{\partial x} + \mu^2 \left[\alpha \frac{\partial \langle u \rangle}{\partial t} + \beta \frac{\partial^2 \langle u \rangle}{\partial t \partial x} + \gamma \frac{\partial^3 \langle u \rangle}{\partial t \partial x^2}\right] = 0. \tag{3.130}$$

Non-linear terms may be neglected in the momentum equation for low Reynolds numbers where inertia is small and/or viscous forces are relatively important.

Equations Boussinesq-type equations (3.95) and (3.124) are applicable when the wave regime is unknown or in cases where, due to spatial changes in the water depth, wave characteristics significantly vary on the modeling domain. Further simplifications to other regimes are therefore restricted to conditions where the physical phenomena is clearly linear/nonlinear or dispersive/non-dispersive.

3.5 Analytical expressions of coefficients α, β and γ

Analytical solutions of χ_1 and χ_2 and the derived coefficients α, β, and γ for rectangular and triangular symmetric channels are presented in this section. These expressions are derived in Appendix C.

3.5.1 Analytical expressions for a rectangular channel

Figure 3.4 *a* depicts a rectangular channel with a width, B_0, depth h and boundaries located at $y = B_0/2$, and $-B_0/2$. For this configuration, functions $\chi_1(x, y, z)$ and $\chi_2(x, y, z)$ have the following expressions

$$\chi_1 = \frac{1}{2B_0}\frac{dB_0}{dx}\left[-2hz - z^2 + y^2\right] - \frac{dh}{dx}z, \tag{3.131}$$

$$\chi_2 = -hz - \frac{z^2}{2}. \tag{3.132}$$

The corresponding coefficients in equation (3.124) can be readily obtained as

$$\alpha = -\frac{h^2}{3B_0}\frac{d^2B_0}{dx^2} + \left(\frac{1}{12} + \frac{h^2}{3B_0^2}\right)\left(\frac{dB_0}{dx}\right)^2 - \frac{h}{2B_0}\frac{dh}{dx}\frac{dB_0}{dx} - \frac{h}{2}\frac{\partial^2 h}{\partial x^2}, \tag{3.133}$$

$$\beta = -h\left(\frac{h}{3B_0}\frac{dB_0}{dx} + \frac{dh}{dx}\right), \tag{3.134}$$

$$\gamma = -\frac{h^2}{3}. \tag{3.135}$$

Clearly, the coefficients $\alpha(x)$ and $\beta(x)$ depend on the rate of change in channel width and depth along the direction of wave propagation, whereas $\gamma(x)$ depends only on the local depth. For the case where the channel has a constant width, i.e. B_0 = constant, the above coefficients reduce to

$$\alpha = -\frac{h}{2}\frac{d^2h}{dx^2}, \qquad \beta = -h\frac{dh}{dx}, \qquad \gamma = -\frac{h^2}{3}. \tag{3.136}$$

Using the above coefficients in equation (3.124), the one-dimensional version of the original Boussinesq equations derived by Peregrine (1967; eqs. 13 and 14)

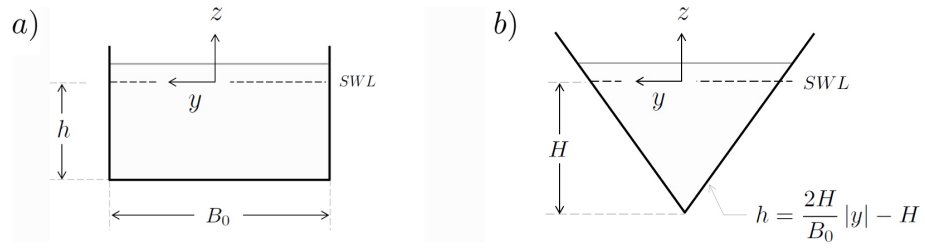

Figure 3.4: Definitions for rectangular and triangular cross-sections.

are recovered. In Peregrine's equations, the percentage change of water depth within a wavelength is allowed to be of order one, thus no restriction on slowly-varying bottom geometry is required. This characteristic of the present theory is an advantage compared to existing theories (e.g. Peregrine, 1968 and Teng & Wu, 1997) which do not reduce to Peregrine's equations.

For the case where the water depth remains constant while the channel width varies, the coefficients become

$$\alpha = \left(\frac{1}{12} + \frac{h^2}{3B_0^2}\right)\left(\frac{dB_0}{dx}\right)^2, \qquad \beta = -\frac{h^2}{3B_0}\frac{dB_0}{dx}, \qquad \gamma = -\frac{h^2}{3}. \tag{3.137}$$

Finally, for uniform channels, the coefficients in the governing equations become

$$\alpha = \beta = 0, \qquad \gamma = -\frac{h^2}{3}. \tag{3.138}$$

Note that for rectangular channel, γ is always negative.

Section 5 includes numerical and experimental results for solitary waves propagating over uniform channels, a uniform slope (Liu *et al.*, 2004) and convergent and divergent channels (Chang *et al.*, 1979). Expressions, (3.136), (3.137) and (3.138) are used in the computations.

3.5.2 Analytical expressions for a triangular channel

For a channel with a symmetric triangular cross-section, the channel boundary is expressed as

$$z = -h(x, y) = \frac{2H}{B_0}|y| - H, \tag{3.139}$$

where B_0 is the surface width and H denotes the maximum depth along the centerline (Figure 3.4 *b*). The bottom boundary conditions for χ_1 (3.114) and χ_2

(3.117) therefore become

$$\frac{2H}{B_0}\frac{|y|}{y}\frac{\partial \chi_1}{\partial y} - \frac{\partial \chi_1}{\partial z} = \frac{\partial H}{\partial x} - \frac{\partial}{\partial x}\left(\frac{2H}{B_0}\right)|y|, \qquad z = \frac{2H}{B_0}|y| - H, \tag{3.140}$$

$$\frac{2H}{B_0}\frac{|y|}{y}\frac{\partial \chi_2}{\partial y} - \frac{\partial \chi_2}{\partial z} = 0, \qquad z = \frac{2H}{B_0}|y| - H. \tag{3.141}$$

The analytical solutions for χ_1 and χ_2 can be obtained as

$$\chi_1 = -\frac{1}{2}\left(\frac{H}{B_0}\frac{dB_0}{dx} + \frac{dH}{dx}\right)z + \left(\frac{1}{4H}\frac{dH}{dx} - \frac{1}{4B_0}\frac{dB_0}{dx}\right)\left(z^2 - y^2\right), \tag{3.142}$$

$$\chi_2 = -\frac{1}{4}(2Hz + z^2 + y^2), \tag{3.143}$$

and the coefficients in the Boussinesq-type equations read

$$\begin{aligned}\alpha = {} & \left(\frac{H^2}{3B_0} - \frac{B_0}{48}\right)\frac{d^2B_0}{dx^2} + \left(\frac{1}{16} - \frac{H^2}{3B_0^2}\right)\left(\frac{dB_0}{dx}\right)^2 \\ & -\left(\frac{B_0}{24H} + \frac{2H}{3B_0}\right)\frac{dB_0}{dx}\frac{dH}{dx} + \left(\frac{1}{3} - \frac{B_0^2}{48H^2}\right)\left(\frac{dH}{dx}\right)^2 + \left(\frac{B_0^2}{48H} - H\right)\frac{d^2H}{dx^2},\end{aligned} \tag{3.144}$$

$$\beta = \left(\frac{B_0^2}{48H} - \frac{5H}{3}\right)\frac{dH}{dx} + \left(\frac{B_0}{16} - \frac{H^2}{3B_0}\right)\frac{dB_0}{dx}, \tag{3.145}$$

$$\gamma = \frac{B_0^2}{48} - \frac{H^2}{3}. \tag{3.146}$$

The analysis of these coefficients is difficult as complex relations between H and B_0 determine their values. For example, $\gamma(x)$ could be either positive ($B_0 > 4H$), zero ($B_0 = 4H$) or negative ($B_0 < 4H$), resulting in significant differences in the dispersive properties of the governing equations.

3.6 Flow features on a cross-sectional plane

The velocity field, the surface elevation and the pressure on a cross-sectional plane can be recovered once χ_1 and χ_2 are computed from the boundary value problems (3.112) to (4.46) and the averaged quantities $\langle u \rangle$ and $\widetilde{\eta}$ are solved from the Boussinesq-type equations (3.95) and (3.124). The derivation of the relevant expressions is presented as follows.

Expressions for the velocity field

Upon cross-sectional averaging, equation (3.78) becomes

$$\langle u \rangle = u_1 + \mu^2 \langle u_2 \rangle + O\left(\mu^4\right). \tag{3.147}$$

Subtracting the above from (3.78) and using the relation between the velocity and the potential yields

$$u = \langle u \rangle + \mu^2 \left(u_2 - \langle u_2 \rangle\right) + O\left(\mu^4\right) = \langle u \rangle + \mu^2 \left(\frac{\partial \phi_2}{\partial x} - \overline{\frac{\partial \phi_2}{\partial x}} \right) + O\left(\mu^4\right), \tag{3.148}$$

where (3.41) has been used to switch the last term to an average over the channel cross-section at the quiescent state. Invoking (3.111) and the Boussinesq approximation implies

$$u\left(x, y, z, t\right) = \langle u \rangle + \mu^2 \left(\chi_1 - \overline{\chi_1}\right) \frac{\partial \langle u \rangle}{\partial x} + \mu^2 \left(\chi_2 - \overline{\chi_2}\right) \frac{\partial^2 \langle u \rangle}{\partial x^2} + O\left(\epsilon^2, \epsilon\mu^2, \mu^4\right). \tag{3.149}$$

For the transverse velocities, equations (3.79) and (3.80) become

$$v\left(x, y, z, t\right) = \mu^2 \left(\frac{\partial \chi_1}{\partial y} \langle u \rangle + \frac{\partial \chi_2}{\partial y} \frac{\partial \langle u \rangle}{\partial x} \right) + O\left(\epsilon^2, \epsilon\mu^2, \mu^4\right), \tag{3.150}$$

$$w\left(x, y, z, t\right) = \mu^2 \left(\frac{\partial \chi_1}{\partial z} \langle u \rangle + \frac{\partial \chi_2}{\partial z} \frac{\partial \langle u \rangle}{\partial x} \right) + O\left(\epsilon^2, \epsilon\mu^2, \mu^4\right). \tag{3.151}$$

It is noted that $(v, w)/u = O\left(\mu^2\right)$ has been assumed, which in combination with (3.16) implies

$$(\hat{v}, \hat{w}) = \frac{\hat{h}_0}{\hat{\lambda}} \hat{u} \tag{3.152}$$

thus the transverse velocities are smaller than the longitudinal velocity. To the author's level of knowledge, no experimental studies measuring the cross-sectional variations of the velocity field have been carried to contrast these results.

Expression for the surface elevation

The surface elevation is obtained by combining the Bernoulli equation (3.90) invoking the relation $\langle u \rangle = u_1 + O\left(\mu^2\right)$ obtained from (3.78):

$$\eta = -\frac{\partial \phi_1}{\partial t} - \mu^2 \left.\frac{\partial \phi_2}{\partial t}\right|_{z=0} - \frac{\epsilon}{2} \langle u \rangle^2 + O\left(\epsilon^2, \epsilon\mu^2, \mu^4\right). \tag{3.153}$$

Taking the surface mean yields the expression

$$\frac{\partial \phi_1}{\partial t} = -\widetilde{\eta} - \mu^2 \left.\widetilde{\frac{\partial \phi_2}{\partial t}}\right|_{z=0} - \frac{\epsilon}{2} \langle u \rangle^2 + O\left(\epsilon^2, \epsilon\mu^2, \mu^4\right), \tag{3.154}$$

which plugged into (3.153) yields

$$\eta = \widetilde{\eta} + \mu^2 \left\{ \left.\widetilde{\frac{\partial \phi_2}{\partial t}}\right|_{z=0} - \left.\frac{\partial \phi_2}{\partial t}\right|_{z=0} \right\} + O\left(\epsilon^2, \epsilon\mu^2, \mu^4\right). \tag{3.155}$$

The expression for surface elevation is, after invoking (3.111),

$$\eta(x, y, t) = \widetilde{\eta} + \mu^2 \left(\widetilde{\chi_1|_{z=0}} - \chi_1|_{z=0}\right) \frac{\partial \langle u \rangle}{\partial t} + \mu^2 \left(\widetilde{\chi_2|_{z=0}} - \chi_2|_{z=0}\right) \frac{\partial^2 \langle u \rangle}{\partial t \partial x} + O\left(\epsilon^2, \epsilon\mu^2, \mu^4\right). \tag{3.156}$$

Spanwise changes in the surface elevation for trapezoidal and triangular cross-sections have been earlier observed in experiments (Sandover & Taylor, 1962; Peregrine, 1968; Treske, 1994 and Teng & Wu, 1997) and numerical computations (Peregrine, 1968 and Teng & Wu, 1992). The presence of χ_1 and χ_2 in equation (3.156) justifies such changes from an analytic standpoint.

Expression for the pressure

The pressure is recovered from the Bernoulli equation (3.86)

$$p = -\frac{\partial \phi_1}{\partial t} - \mu^2 \frac{\partial \phi_2}{\partial t} - \frac{\epsilon}{2} u^2 - \frac{z}{\epsilon} + O\left(\epsilon^2, \epsilon\mu^2, \mu^4\right), \tag{3.157}$$

where $u_1^2 = u^2 + O\left(\mu^2\right)$ by virtue of (3.78) has bee used. Invoking (3.154) and (3.111) yields

$$p\left(x,y,z,t\right) = \widetilde{\eta} + \mu^2\left(\widetilde{\chi_1|_{z=0}} - \chi_1\right)\frac{\partial\left\langle u\right\rangle}{\partial t} + \mu^2\left(\widetilde{\chi_2|_{z=0}} - \chi_2\right)\frac{\partial^2\left\langle u\right\rangle}{\partial t\partial x} - \frac{z}{\epsilon} + O\left(\epsilon^2, \epsilon\mu^2, \mu^4\right). \tag{3.158}$$

It should be noted that there are three-dimensional flow features which cannot not be captured on a cross-sectional plane. Some of the features the theory fails to reproduce are *i*) the tendency for waves to break at the sidewall slopes or degenerate into bores, *ii*) the plan curvature of the wave crest, *iii*) the generation of unsteady waves and *iv*) a fish-tail pattern obscuring the main wave system for wide shallow channels. Some of these features have been observed by Sandover & Taylor (1962), Fenton (1973), Treske (1994) and Mathew & Akylas (1990) on both experimental and analytical grounds.

3.7 Comparison with other models

A comparison with the one-dimensional models proposed by Peregrine (1968) and Teng & Wu (1997) and the standard Boussinesq equations (Peregrine, 1967) is done in this section. The reader is referred to Appendices A.1 and A.7 for further details.

One dimensional models

Teng & Wu's (1997) Boussinesq-type equations (A.17) and (A.18) have a similar structure to equations (3.95) and (3.124) in the present theory[2]. Teng & Wu's (1997) theory, however, is restricted to slow changes in the cross-section occurring over various wavelengths, i.e. $\partial A_0/\partial x = O(\epsilon)$, and includes forcing through a slowly moving bathymetry and a free-surface pressure distribution moving along the channel. Surface effects may be relevant, for example, in large domains where atmospheric pressure gradients become a significant driving force, or when the surface is perturbed by a floating body. The bottom forcing is important, for example, in submarine landslide generation. The inclusion of both sources of forcing could therefore be incorporated in equations (3.95) and (3.124) following Teng & Wu's (1992) approach. The theory is restricted to symmetric cross-sections and do not include the terms containing α and β as a consequence of the slow-varying assumption.

Peregrine's (1968) equations (A.1) and (A.2), on the other hand, consider a fixed bottom and no ambient pressure gradients acting on the surface. The independent variables representing the surface elevation $\zeta = \eta + O\left(\varepsilon^2\right)$ and the longitudinal velocity $u = u' + O\left(\varepsilon^2\right)$ are a combination of the leading and second order approximations, making their interpretation somewhat difficult. The model is valid for uniform channels, i.e $\partial A_0/\partial x = 0$, so its application is very limited. The dispersive term is included in the continuity equation, a fact which has implications in the linear dispersive properties, as discussed in Appendix D.

Perhaps the most relevant difference among these and the present theory deals

[2]The conversion from Teng & Wu's (1997) notation to the present theory is carried out with the following equivalences: $2b_0 = B_0$, $2S = B_0'$, $2b_0\widetilde{h}_0 = A_0$, $\zeta = \eta$ and $\beta = -\frac{1}{3}\kappa^2\widetilde{h}_0^2$.

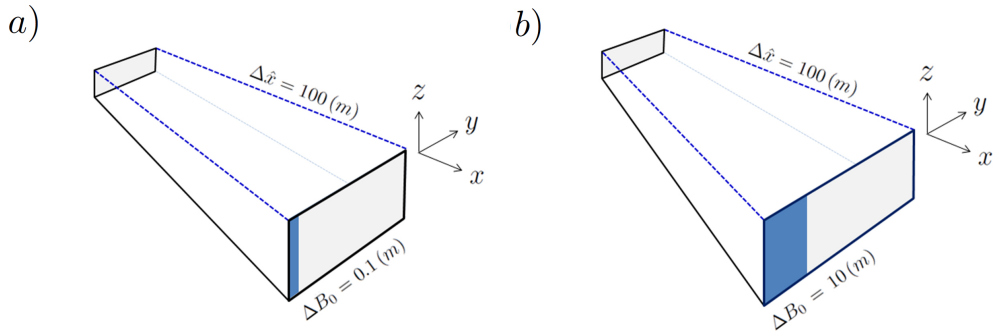

Figure 3.5: Changes in the cross-section for *a*) a slowly varying channel and *b*) a channel with significant changes of the cross-section within a wavelength. Computation is for a wave of amplitude $\hat{a}_0 = 1$ m and a wavelength of $\hat{\lambda} = 1000$ m, propagating on a depth of $\hat{h}_0 = 100$ m. Values should be interpreted as orders of magnitude.

with how the changes of the cross-section along the channel are considered. The assumption of slow cross-sectional changes in the area used in Teng & Wu's model, i.e. $\partial A_0/\partial x = O(\epsilon)$, implies that changes in wave properties occur at distances much longer than a wavelength. Peregrine's model is even more restrictive, as uniform channels with $\partial A_0/\partial x = 0$ are considered.

To illustrate the consequences in engineering applications, the case of a rectangular channel of constant depth is analyzed herein. The slow varying assumption considered by Teng & Wu (1987) is simplified to $\partial B_0/\partial x = O(\epsilon)$, which in dimensional form reads

$$\frac{\partial \hat{B}_0/\hat{B}_0}{\partial \hat{x}/\hat{\lambda}} \sim \frac{\hat{a}_0}{\hat{h}_0}. \tag{3.159}$$

The above implies that the ratio of the relative change of width and the relative change in the wavelength is small. In the present theory, the assumption $\partial A_0/\partial x = O(1)$ in dimensional form reads

$$\frac{\partial \hat{B}_0/\hat{B}_0}{\partial \hat{x}/\hat{\lambda}} \sim 1, \tag{3.160}$$

implying that changes in the width may occur within a wavelength. For example, a long wave with amplitude $\hat{a}_0 = 1$ m and typical wavelength of $\hat{\lambda} = 1000$

m, propagating on a depth of $\hat{h}_0 = 100$ m, implies that $\partial\hat{B}_0/\partial\hat{x} = 0.1$ m/m and $\partial\hat{B}_0/\partial\hat{x} = 0.001$ m/m for the rapid and slow varying assumptions, respectively. Note that the nonlinear parameter is $\epsilon = \hat{a}_0/\hat{h}_0 = 0.01$ and the dispersion is characterized by $\mu^2 = \hat{h}_0^2/\hat{\lambda}^2 = 0.01$, so the Boussinesq approximation $O(\epsilon) = O\left(\mu^2\right) \ll O(1)$ is achieved. For a reach of $\Delta\hat{x} = 100$ m, changes in the width are $\Delta\hat{B}_0 = 10$ m for and of $\Delta\hat{B}_0 = 0.1$ m for the rapid and slowly varying channels, as shown in Figure 3.5. Few natural streams exhibit the small changes in the cross-section given by the slow-varying assumption by Teng & Wu (1997), so its range of applicability is narrow. Peregrine's (1968) theory is indeed more restrictive as consequence on the uniform channel assumption. In the present theory, on the other hand, changes in the cross-section are allowed to vary within a wavelength. Thus, the computation of steps, contractions or expansions is possible as long as $\partial A_0/\partial x = O(1)$. Indeed, the equation of conservation of mass (3.95) can be written as

$$\frac{\partial\widetilde{\eta}}{\partial t} + \frac{A_0}{B_0}\frac{\partial\langle u\rangle}{\partial x} + \frac{1}{B_0}\frac{\partial A_0}{\partial x}\langle u\rangle = O\left(\epsilon,\mu^2\right), \tag{3.161}$$

implying $\partial A_0/\partial x$ cannot be $O(1/\epsilon)$ or larger. In the above example, this implies $\partial\hat{B}_0/\partial\hat{x} \leq 0.1$ m/m.

Standard Boussinesq equations

Peregrine (1967, equations 13 and14) derived a set of non-dimensional momentum and continuity equations in terms of the depth averaged velocity $\mathbf{U} = (u, v)$

$$\frac{\partial\eta}{\partial t} + \nabla\cdot[(h+\eta)\,\mathbf{U}] = 0, \tag{3.162}$$

$$\frac{\partial\mathbf{U}}{\partial t} + \nabla\eta + (\mathbf{U}\cdot\nabla)\,\mathbf{U} - \frac{h}{2}\nabla\left[\nabla\cdot\left(h\frac{\partial\mathbf{U}}{\partial t}\right)\right] + \frac{h^2}{6}\nabla\left[\nabla\cdot\frac{\partial\mathbf{U}}{\partial t}\right] = 0, \tag{3.163}$$

where $\nabla = (\partial/\partial x, \partial/\partial y)$. These expressions are sometimes referred as the standard Boussinesq equations in the literature (Nwogu, 1993). For a one-dimensional case, these expressions are reduced to

$$\frac{\partial \eta}{\partial t} + \frac{\partial}{\partial x}\left[(h+\eta)\,\overline{u}\right] = 0, \tag{3.164}$$

$$\frac{\partial \overline{u}}{\partial t} + \frac{\partial \eta}{\partial x} + \overline{u}\frac{\partial \overline{u}}{\partial x} - \frac{h}{2}\frac{\partial^2 h}{\partial x^2}\frac{\partial \overline{u}}{\partial t} - h\frac{\partial h}{\partial x}\frac{\partial^2 \overline{u}}{\partial x \partial t} - \frac{h^2}{3}\frac{\partial^3 \overline{u}}{\partial x^2 \partial t} = 0, \tag{3.165}$$

which can be interpreted as the governing equations for a rectangular channel of constant width. To compare these expressions with the present model, $B_0' = 0$ due to vertical walls and $A_0 = hB_0$, where B_0 is a constant in x. Equations (3.95) and (3.124) may then be reduced to

$$\frac{\partial \widetilde{\eta}}{\partial t} + \frac{\partial}{\partial x}\left[(h+\epsilon\widetilde{\eta})\,\overline{u}\right] = 0, \tag{3.166}$$

$$\frac{\partial \overline{u}}{\partial t} + \frac{\partial \widetilde{\eta}}{\partial x} + \epsilon\overline{u}\frac{\partial \overline{u}}{\partial x} + \mu^2\alpha\frac{\partial \overline{u}}{\partial t} + \mu^2\beta\frac{\partial^2 \overline{u}}{\partial t \partial x} + \mu^2\gamma\frac{\partial^3 \overline{u}}{\partial t \partial x^2} = 0. \tag{3.167}$$

By inspection, the values of the coefficients in the momentum equations are

$$\alpha = -\frac{h}{2}\frac{\partial^2 h}{\partial x^2}, \qquad \beta = -h\frac{\partial h}{\partial x}, \qquad \gamma = -\frac{h^2}{3}, \tag{3.168}$$

which correspond exactly in structure with the coefficients in equation (3.136). This implies the equations (3.95) and (3.124) are consistent with the standard Boussinesq equations derived by Peregrine (1967).

CHAPTER 4

NUMERICAL SCHEMES

This chapter reviews the numerical schemes used to solve the flow field in a channel. Section 4.1 introduces the Adams-Bashforth-Moulton scheme used for the one-dimensional Boussinesq-type equations (3.95) and (3.124), with the averaged quantities $\langle u \rangle$ and $\widetilde{\eta}$ as unknowns. A simple two-dimensional finite difference scheme, used to compute the coefficients α, β and γ from boundary value problems given by (3.112) to (3.117), is introduced in section 4.2.

Throughout this chapter, a general function $f(x, y, z, t)$ in discretized as

$$f(x, y, z, t) \qquad \rightarrow \qquad \left\{ f^{\tau}_{(i,j,k)} \right\}^{n}, \tag{4.1}$$

where i, j and k correspond to the counters in the x, y and z spatial coordinates, τ corresponds to the discretization of time and n stands for the iteration step, when required. Figure 4.1 depicts the discretization scheme used. For the Boussinesq-type equations, the longitudinal axis is discretized by N_x grid points ($x_i = i\Delta x,\ i = 1, ..., N_x$) where the physical boundaries are located at x_1 and x_{N_x} respectively. Time is discretized as $t = \tau \Delta t$, where level t refers to information at the present, known time level. Both Δx and Δt are assumed constant and defined based on Courant-type stability conditions.

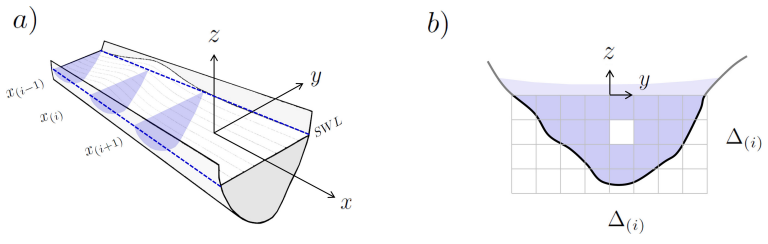

Figure 4.1: *a*) Definition of cross-sections and *b*) grid in each cross-section.

To solve the boundary value problems, each cross-section is discretized in a rectangular domain in the (y, z) plane using a uniformly spaced grid (i.e. $\Delta y = \Delta z$). N_y grid points are considered in the spanwise y-direction ($y_j = j\Delta y,\ j = 1, ..., N_y$) and N_z points are used in the vertical z-direction ($z_k = k\Delta z,\ k = 1, ..., N_z$). The numerical scheme is implemented herein in dimensional form and hats for dimensional quantities are omitted for convenience.

4.1 Numerical scheme for the longitudinal flow problem

This section describes the numerical technique used to solve the Boussinesq-type equations (3.95) and (3.124). Existing approaches include finite difference and finite volume methods, among others. Finite difference schemes are extensively used because of the wealth of specific literature available and ease of implementation. Finite element methods, on the other hand, provide excellent performance when dealing with complex geometries but are relatively difficult to implement (Brocchini, 2013).

A finite difference scheme based on a third-order Adams-Bashforth predictor step and a fourth-order Adams-Moulton corrector step to advance in time is used herein. The scheme was initially described by Wei & Kirby (1995), extended to include fully nonlinear effects (Wei *et al.*, 1995; Gobbi *et al.*, 2000) and used in Funwave (Fully Nonlinear Boussinesq Model) after including bottom friction, wave breaking and wave absorption by damping at the boundaries (Kirby *et al.*, 1998). The scheme is extended herein to include the effect of the sidewalls in the conservation of mass (3.95) and the new terms associated with changes in the cross-sectional geometry in the conservation of

momentum(3.124)[1].

4.1.1 Governing equations

The dimensional form of equations (3.95) and (3.124) is recast as

$$\frac{\partial \widetilde{\eta}}{\partial t} = E\left(\widetilde{\eta}, \langle u \rangle\right), \tag{4.2}$$

$$\frac{\partial U}{\partial t} = F\left(\widetilde{\eta}, \langle u \rangle\right), \tag{4.3}$$

where

$$E\left(\widetilde{\eta}, \langle u \rangle\right) = -\frac{1}{B_0}\frac{\partial}{\partial x}\left(\langle u \rangle A_0\right) + \frac{B_0'}{B_0^2}\widetilde{\eta}\frac{\partial}{\partial x}\left(\langle u \rangle A_0\right) - \frac{1}{B_0}\frac{\partial}{\partial x}\left(\langle u \rangle B_0\widetilde{\eta}\right), \tag{4.4}$$

$$F\left(\widetilde{\eta}, \langle u \rangle\right) = -g\frac{\partial \widetilde{\eta}}{\partial x} - \langle u \rangle \frac{\partial \langle u \rangle}{\partial x}, \tag{4.5}$$

$$U\left(\langle u \rangle\right) = (1+\alpha)\langle u \rangle + \beta\frac{\partial \langle u \rangle}{\partial x} + \gamma\frac{\partial^2 \langle u \rangle}{\partial x^2}. \tag{4.6}$$

The last equation defines a tridiagonal system relating $\langle u \rangle$ with U. The linear model can be recovered if

$$E\left(\widetilde{\eta}, \langle u \rangle\right) = -\frac{1}{B_0}\frac{\partial}{\partial x}\left(\langle u \rangle A_0\right), \qquad \text{and} \qquad F\left(\widetilde{\eta}, \langle u \rangle\right) = -g\frac{\partial \widetilde{\eta}}{\partial x}. \tag{4.7}$$

For a non-dispersive model with slow changes in the cross-section, $\alpha, \beta, \gamma = 0$, so equation (4.6) is reduced to $U = \langle u \rangle$, and there is no need to solve a tridiagonal system. In this case, the Boussinesq equations are reduced to the non-linear shallow water equations, with an extra term accounting for the sidewall slope.

[1] The scheme used herein is a simplified version of Kirby *et al.*' (1998) equations 23 and 24 with some simplifications: The system is weakly non-linear ($\gamma = 0$); no source function in the conservation of mass is considered ($f = 0$); Bottom friction, wave breaking, turbulence and absorption at boundaries are neglected ($F_b, F_{br}, F_{bs}, F_{sp} = 0$); an impermeable seabed is considered ($\kappa = 1$ and $\Lambda = h + \eta$) and no third-order spatial derivatives exist in the momentum equation ($a_1, a_2 = 0$).

4.1.2 Numerical scheme

The numerical scheme consists of predictor and corrector steps for each time step, where the governing equations are differenced on an unstaggered grid in x and t. First-order spatial derivatives are differenced to fourth-order accuracy using a five-point stencil whereas second-order spatial derivatives in the dispersive term are differenced to second-order accuracy. The error is eliminated as $\Delta x, \Delta t \to 0$. The predictor and corrector steps are schematized in Figure 4.2. The computational five-point stencil for both the predictor and corrector steps is depicted in Figure 4.3. Boundary and initial conditions together with a note of a optional filter used in the algorithm are also explained in this section.

Predictor step

The predictor step is achieved using the third-order explicit Adams-Bashforth scheme, where variables in the future time step $\tau+1$ are functions of the already known steps τ, $\tau-1$ and $\tau-2$. Equations (4.2) and (4.3) are expressed as

$$\widetilde{\eta}_{(i)}^{\tau+1} = \widetilde{\eta}_{(i)}^{\tau} + \frac{\Delta t}{12}\left[23E_{(i)}^{\tau} - 16E_{(i)}^{\tau-1} + 5E_{(i)}^{\tau-2}\right], \tag{4.8}$$

$$U_{(i)}^{\tau+1} = U_{(i)}^{\tau} + \frac{\Delta t}{12}\left[23F_{(i)}^{\tau} - 16F_{(i)}^{\tau-1} + 5F_{(i)}^{\tau-2}\right]. \tag{4.9}$$

which are explicit for $\widetilde{\eta}_{(i)}^{\tau+1}$ and $U_{(i)}^{\tau+1}$ since all terms on the right hand side are known from previous calculations. Functions E and F are discretized as

$$E_{(i)}^{\tau} = -\frac{1}{B_{0(i)}}\frac{\partial}{\partial x}\left(A_0\left\langle u\right\rangle\right)_{(i)}^{\tau} + \frac{B'_{0(i)}}{B_{0(i)}^2}\widetilde{\eta}_{(i)}^{\tau}\frac{\partial}{\partial x}\left(\left\langle u\right\rangle A_0\right)_{(i)}^{\tau} - \frac{1}{B_{0(i)}}\frac{\partial}{\partial x}\left(B_0\left\langle u\right\rangle\widetilde{\eta}\right)_{(i)}^{t}, \tag{4.10}$$

$$F_{(i)}^{\tau} = -g\frac{\partial\widetilde{\eta}^{\tau}}{\partial x}_{(i)} - \left\langle u\right\rangle_{(i)}^{\tau}\frac{\partial\left\langle u\right\rangle^{\tau}}{\partial x}_{(i)}. \tag{4.11}$$

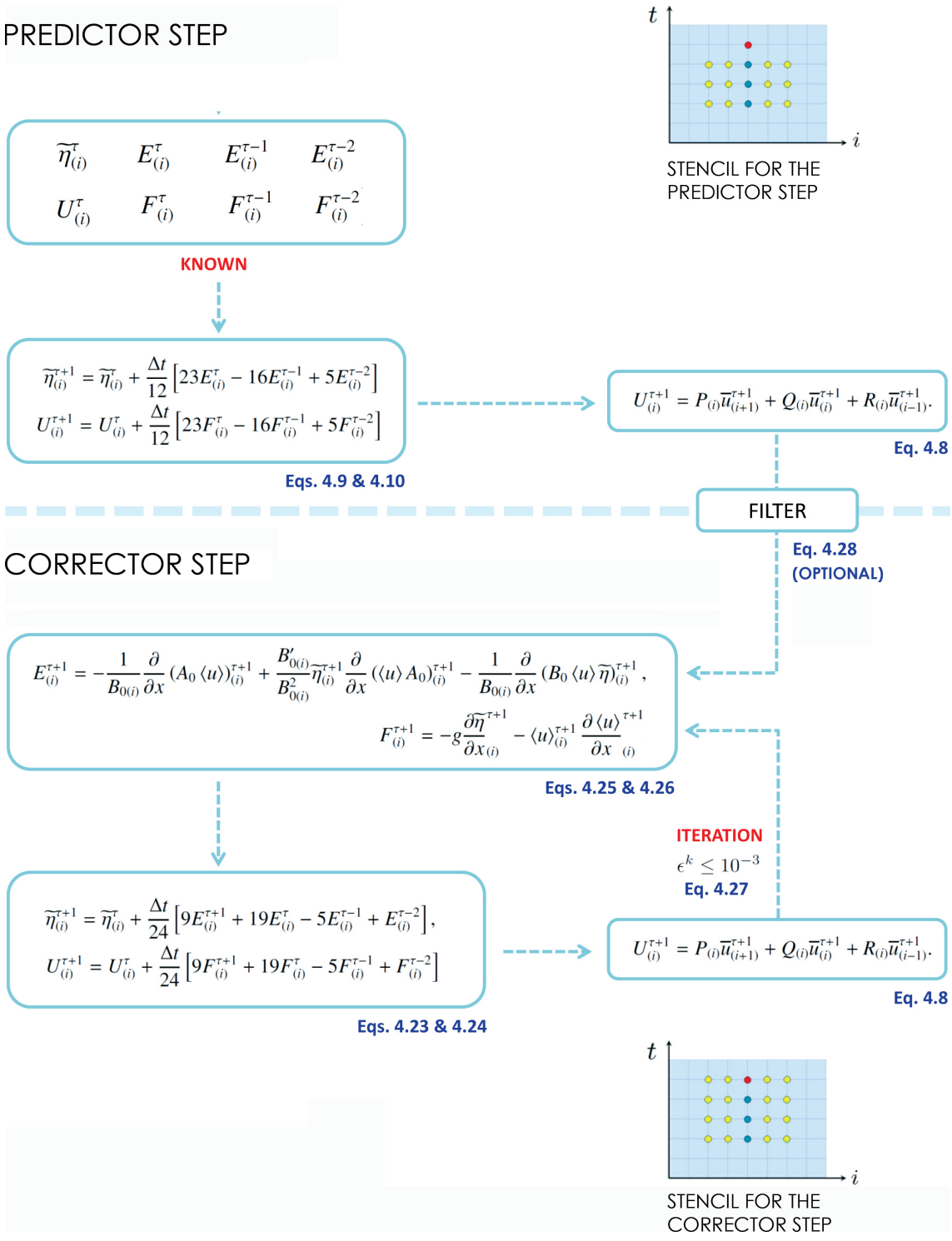

Figure 4.2: Schematic representation of key steps between equations used in the computation of the Boussinesq-type equations using the Adams-Bashforth-Moulton predictor-corrector scheme.

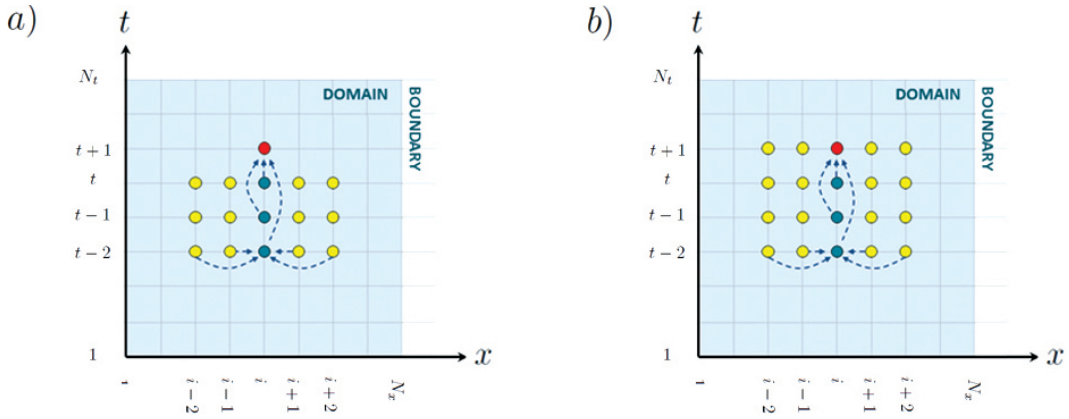

Figure 4.3: Computational stencil for *a*) the predictor step and *b*) the corrector step. To compute the unknown quantities $\widetilde{\eta}$ and $\langle u \rangle$ in the red dots, the quantities E and F are computed in blue circles from known values of $\widetilde{\eta}$ and $\langle u \rangle$ in yellow circles.

The expression for first-order spatial derivatives using a five-point stencil in interior points $i = 3, ..., N_x - 2$ at any time τ is

$$\frac{\partial f}{\partial x}_{(i)} = \frac{f_{(i-2)} - 8f_{(i-1)} + 8f_{(i+1)} - f_{(i+2)}}{12\Delta x} + O\left(\Delta x^4\right). \tag{4.12}$$

At the boundaries

$$\frac{\partial f}{\partial x}_{(1)} = \frac{-25f_{(1)} + 48f_{(2)} - 36f_{(3)} + 16f_{(4)} - 3f_{(5)}}{12\Delta x} + O\left(\Delta x^4\right), \tag{4.13}$$

$$\frac{\partial f}{\partial x}_{(2)} = \frac{-3f_{(1)} - 10f_{(2)} + 18f_{(3)} - 6f_{(4)} + f_{(5)}}{12\Delta x} + O\left(\Delta x^4\right), \tag{4.14}$$

$$\frac{\partial f}{\partial x}_{(N_x-1)} = \frac{3f_{(N_x)} + 10f_{(N_x-1)} - 18f_{(N_x-2)} + 6f_{(N_x-3)} - f_{(N_x-4)}}{12\Delta x} + O\left(\Delta x^4\right), \tag{4.15}$$

$$\frac{\partial f}{\partial x}_{(N_x)} = \frac{25f_{(N_x)} - 48f_{(N_x-1)} + 36f_{(N_x-2)} - 16f_{(N_x-3)} + 3f_{(N_x-4)}}{12\Delta x} + O\left(\Delta x^4\right) \tag{4.16}$$

The evaluation of the horizontal velocities at the new time level is achieved through the solution of a tridiagonal matrix system relating $U_{(i)}$ and $\langle u \rangle_{(i)}$. The discretization of U is done with second-order accuracy as follows

$$U_{(i)}^{\tau+1} = \left[1 + \alpha_{(i)}\right] \langle u \rangle_{(i)}^{\tau+1} + \frac{\beta_{(i)}}{2\Delta x} \left[\langle u \rangle_{(i+1)}^{\tau+1} - \langle u \rangle_{(i-1)}^{\tau+1}\right] + \frac{\gamma_{(i)}}{\Delta x^2} \left[\langle u \rangle_{(i+1)}^{\tau+1} - 2\langle u \rangle_{(i)}^{\tau+1} + \langle u \rangle_{(i-1)}^{\tau+1}\right] + O\left(\Delta x^2\right). \tag{4.17}$$

$$
\begin{bmatrix}
Q_1 & 2P_1 & & & & & & & & & \\
R_2 & Q_2 & P_2 & & & & & & & & \\
 & \ddots & \ddots & \ddots & & & & & & & \\
 & & \ddots & \ddots & \ddots & & & & & & \\
 & & & R_{i-1} & Q_{i-1} & P_{i-1} & & & & & \\
 & & & & R_i & Q_i & P_i & & & & \\
 & & & & & R_{i+1} & Q_{i+1} & P_{i+1} & & & \\
 & & & & & & \ddots & \ddots & \ddots & & \\
 & & & & & & & \ddots & \ddots & \ddots & \\
 & & & & & & & & R_{N_x-1} & Q_{N_x-1} & P_{N_x-1} \\
 & & & & & & & & & 2R_{N_x} & Q_{N_x}
\end{bmatrix}
\begin{Bmatrix}
\langle u \rangle_1 \\ \langle u \rangle_2 \\ \vdots \\ \vdots \\ \langle u \rangle_{i-1} \\ \langle u \rangle_i \\ \langle u \rangle_{i+1} \\ \vdots \\ \vdots \\ \langle u \rangle_{N_x-1} \\ \langle u \rangle_{N_x}
\end{Bmatrix}^{\tau+1}
=
\begin{Bmatrix}
U_1 \\ U_2 \\ \vdots \\ \vdots \\ U_{i-1} \\ U_i \\ U_{i+1} \\ \vdots \\ \vdots \\ U_{N_x-1} \\ U_{N_x}
\end{Bmatrix}^{\tau+1}
$$

Figure 4.4: Matrix form of expression (4.19).

Introducing

$$
P_{(i)} = \frac{\beta_{(i)}}{2\Delta x} + \frac{\gamma_{(i)}}{\Delta x^2}, \qquad Q_{(i)} = 1 + \alpha_{(i)} - \frac{2\gamma_{(i)}}{\Delta x^2}, \qquad R_{(i)} = -\frac{\beta_{(i)}}{2\Delta x} + \frac{\gamma_{(i)}}{\Delta x^2}, \quad (4.18)
$$

leads to

$$
U_{(i)}^{\tau+1} = P_{(i)}\overline{u}_{(i+1)}^{\tau+1} + Q_{(i)}\overline{u}_{(i)}^{\tau+1} + R_{(i)}\overline{u}_{(i-1)}^{\tau+1}. \quad (4.19)
$$

Figure 4.4 depicts the expression (4.19) in matrix form, where the first and last rows represent, for the sake of example, Neumann boundary conditions. In matrix form, equation (4.19) is reduced to

$$
\mathbf{M}\left\{\langle u \rangle\right\}^{\tau+1} = \{U\}^{\tau+1}, \quad (4.20)
$$

where the coefficients of the tridiagonal matrix $\mathbf{M}$ are constant.

The algorithms developed for this research were all implemented in Matlab R2010a. In particular, the solution of the linear system was done by defining $\mathbf{M}$ as sparse and performing its LU decomposition. Matlab handles sparse matrices very efficiently, both with respect to memory and operations (Nachbim & Da Silva, 2012), but have limitations with the number of elements that can be stored. The use of a sparse option was tested and results (not included

herein) showed significant savings in computational time for high resolutions. For the computational resources used herein (i.e. a 2.20GHz 3rd generation Intel Core i7-3632QM processor), matrices sizes were limited to a maximum of $18,000 \times 18,000$ elements.

Corrector step

The corrector step is implemented using an implicit fourth-order Adams-Moulton scheme.The governing equations at this step

$$\widetilde{\eta}_{(i)}^{\tau+1} = \widetilde{\eta}_{(i)}^{\tau} + \frac{\Delta t}{24}\left[9E_{(i)}^{\tau+1} + 19E_{(i)}^{\tau} - 5E_{(i)}^{\tau-1} + E_{(i)}^{\tau-2}\right], \tag{4.21}$$

$$U_{(i)}^{\tau+1} = U_{(i)}^{\tau} + \frac{\Delta t}{24}\left[9F_{(i)}^{\tau+1} + 19F_{(i)}^{\tau} - 5F_{(i)}^{\tau-1} + F_{(i)}^{\tau-2}\right] \tag{4.22}$$

are iterated with an initial value for $E_{(i)}^{\tau+1}$ and $F_{(i)}^{\tau+1}$ obtained from the predictor step, i.e.(4.10) and (4.11). Here

$$\begin{aligned} E_{(i)}^{\tau+1} = & -\frac{1}{B_{0(i)}}\frac{\partial}{\partial x}\left(A_0\left\langle u\right\rangle\right)_{(i)}^{\tau+1} + \frac{B'_{0(i)}}{B_{0(i)}^2}\widetilde{\eta}_{(i)}^{\tau+1}\frac{\partial}{\partial x}\left(\left\langle u\right\rangle A_0\right)_{(i)}^{\tau+1} \\ & -\frac{1}{B_{0(i)}}\frac{\partial}{\partial x}\left(B_0\left\langle u\right\rangle\widetilde{\eta}\right)_{(i)}^{\tau+1}, \end{aligned} \tag{4.23}$$

$$F_{(i)}^{\tau+1} = -g\frac{\partial\widetilde{\eta}}{\partial x}_{(i)}^{\tau+1} - \left\langle u\right\rangle_{(i)}^{\tau+1}\frac{\partial\left\langle u\right\rangle}{\partial x}_{(i)}^{\tau+1}. \tag{4.24}$$

The spatial derivatives are computed following the same scheme as in the predictor step. The scheme is applied iteratively until the error between two successive results is lower that a specified tolerance. The error for iteration n is computed for $f_{(i)} = \left\{\widetilde{\eta}_{(i)}\ ,\ \left\langle u\right\rangle_{(i)}\right\}$ as

$$\{\epsilon\}^n = \frac{\sum_{i=1}^{N_x}\left|\left\{f_{(i)}^{\tau+1}\right\}^n - \left\{f_{(i)}^{\tau+1}\right\}^{n-1}\right|}{\sum_{i=1}^{N_x}\left\{f_{(i)}^{\tau+1}\right\}^n}. \tag{4.25}$$

The iteration loops while $\epsilon^n \leq 10^{-3}$ for both variables. Kirby *et al.* (1998) indicate that for the weakly nonlinear case, the scheme typically requires no iteration

unless problems arise from boundaries, or inappropriate values of $\triangle x$ and $\triangle t$ are used. For the cases analyzed herein, only one iteration was required for a few initial steps and no iteration was needed thereafter.

Initial conditions

As a rule of thumb, wave profiles are prescribed for $\widetilde{\eta}$ and $\langle u \rangle$ sufficiently far from the boundaries so that spurious reflections are minimized. In the the present computations, solitary wave profiles derived in Appendix F are used as initial conditions. Gaussian profiles are also applied in the case of uniform channels.

Boundary conditions

Typical boundary conditions for wave problems can be classified as *i*) reflective boundaries, *ii*) wavemaker boundaries, *iii*) absorbing boundaries, *iv*) radiating boundaries, *v*) periodic boundaries, *vi*) moving boundaries or a combination of some of them. Spurious reflections are often expected when boundary conditions are not properly defined, and in general their elimination is not possible (Liu, 2010). In this study, reflective and absorbing boundaries were implemented following Wei & Kirby (1995).

Numerical filtering

Kirby *et al*. (1998) implemented a fourth-order numerical filter in Funwave as a measure to damp out higher harmonics that may arise due to nonlinear interac-

tions in the governing equations. Note that Boussinesq-type equations are not valid for these higher harmonics because of the large depth to wavelength ratio. The filtered values defined for $f_{(i)}^{fil} = \left\{\widetilde{\eta}_{(i)}^{fil}\ ,\ \langle u\rangle_{(i)}^{fil}\right\}$ are derived using 9 adjacent points through the following expression

$$\begin{aligned} f_{(i)}^{fil} &= \frac{1}{256}\left[-f_{(i-4)} + 8f_{(i-3)} - 28f_{(i-2)} + 56f_{(i-1)} + 186f_{(i)}\right. \\ &\quad \left. +56f_{(i+1)} - 28f_{(i+2)} + 8f_{(i+3)} - f_{(i+4)}\right] \end{aligned} \tag{4.26}$$

Kirby *et al.*'s (1998) Figure 4 depicts the ratio of smoothed to unsmoothed amplitudes R as function of the ratio of the wavelength to grid size. Waves with wavelengths twice the grid size are filtered our completely since the corresponding response function R is zero. For wavelengths larger than 6 grid sizes, the effect of the filter is negligible.

For the cases analyzed herein, instabilities were only observed in extreme cases where large values of non-linearity and no dispersion were considered (i.e. $\epsilon = 0.4$ and $\mu = 0$). These unstable cases are, however, beyond the range of validity of the Boussinesq theory. The filter proved to be efficient in the predictor scheme and to have a small effect in the corrector step. For all the cases analyzed in this dissertation, the filter was proven to be unnecessary.

4.1.3 Benchmark case

A benchmark is a standardized problem that serves as a basis for evaluation or comparison. Typical tests used in the literature for one-dimensional problems are *i*) regular or random waves over flat bottom (e.g. Nwogu, 1993; Wei & Kirby, 1995); *ii*) solitary waves over a flat bottom (e.g. Wei & Kirby, 1995; Shiach & Mingham, 2009), *iii*) solitary waves on a uniform parabolic channel (e.g. Teng &

Wu, 1994); *iv*) solitary waves over slopes (e.g. Wei *et al.*, 1995) and *v*) evolution of bores (e.g. Wei *et al.*, 1995), among others.

The propagation of a solitary wave on a flat bottom over a long distance is conventionally used to test the stability and conservative properties of numerical schemes. Solitary waves on uniform channels preserve a permanent form, thus providing *i*) initial conditions for wave modeling and *ii*) a benchmark case for long distance propagation. Numerical experiments for solitary waves on a rectangular uniform channel by Wei & Kirby (1995), referred to as WK95 throughout this section, are replicated herein to validate the numerical scheme. The following expressions for the spanwise averaged free surface elevation and the cross-sectionally averaged velocity, in dimensional form, are derived in Appendix F.

$$\widetilde{\eta} = a_0 sech^2\left(K\left[x - ct\right]\right) \tag{4.27}$$

$$\langle u \rangle = a_0 \sqrt{\frac{g}{\overline{h}}} sech^2\left(K\left[x - ct\right]\right) \tag{4.28}$$

where the wave number, phase speed and mean depth are

$$K = \frac{1}{2}\sqrt{\frac{a_0}{\overline{h}\gamma}\left(\frac{\overline{h}B_0'}{3B_0} - 1\right)}, \qquad c^2 = g\overline{h} + ga_0\left(1 - \frac{\overline{h}B_0'}{3B_0}\right), \qquad \overline{h} = \frac{A_0}{B_0}. \tag{4.29}$$

For a rectangular cross section, $B_0' = 0$ and the dispersive strength is $\gamma \leq 0$.

Definition of grid size and time step

For the numerical computation, the grid size Δx is defined in terms of a typical wavelength λ. Though the length of a solitary wave is theoretically infinite, the wavenumber in equation (4.29) is used to define an effective wavelength

$$\lambda = \frac{2\pi}{K} = 4\pi\sqrt{-\frac{\gamma\overline{h}}{a_0}}. \tag{4.30}$$

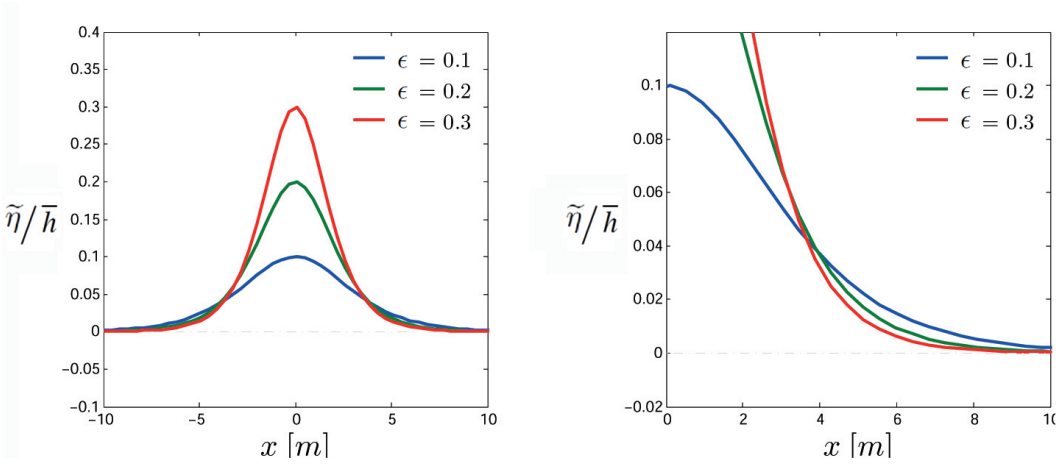

Figure 4.5: Solitary wave profiles for different nonlinearities on a uniform rectangular channel of depth $h = 1$ m.

The grid size Δx is defined so that the wavelength is divided into a suitable number of elements N, i.e.

$$\Delta x = \frac{\lambda}{N} = \frac{4\pi}{N}\sqrt{-\frac{\gamma\overline{h}}{a_0}}. \tag{4.31}$$

To define the time step Δt, a stability condition implying that the numerical speed is faster than the phase speed is guaranteed. This condition is stated as

$$\frac{\Delta x}{\Delta t} = C\sqrt{g\left(\overline{h} + a_0\right)}, \tag{4.32}$$

where $\Delta x/\Delta t$ is the numerical speed and $C > 1$ guarantees stability. The time step is therefore given by

$$\Delta t = \frac{\Delta x}{C\sqrt{g\left(\overline{h} + a_0\right)}}. \tag{4.33}$$

For a solitary wave, the definition of Δx and Δt depends on the amplitude a_0 and depth $\overline{h}$ (thus the nonlinearity ϵ), the number of elements per wavelength N and the coefficient C.

As an example, Figure 4.5 depicts solitary wave profiles over a flat bottom of depth $\overline{h} = 1$ m corresponding to nonlinearities of $\epsilon = 0.1$, 0.2 and 0.3. As ex-

pected, longer wavelengths are observed for smaller nonlinearities. For solitary waves, the definition of the grid size defines the time step (or vice-versa), as the effective wavelength and amplitude are mutually dependent. For other type of waves, this limitations in not required.

Following WK95, the propagation of a solitary wave on a flat bottom of constant depth $\overline{h} = 0.45$ m over a horizontal distance of 450 m was studied. Amplitudes of $a_0 = 0.045$ m and 0.135 m, corresponding to nonlinearities of $\epsilon = 0.1$ and 0.3, were tested. In the present computations, solitary waves were generated inside the domain, whereas WK95 forced the domain from the boundary. An arbitrary value of $C = 2$ was chosen for the benchmark cases, so that the numerical speed doubled the physical wave celerity.

A sensitivity analysis was carried out to define an optimal value of the grid size and time step. Results are shown in Figure 4.6. Panel *a* depicts the phase speed and wavelength of the solitary wave as a function of nonlinearity. As expected, the wavelength is inversely proportional to the nonlinearity whereas the phase speed increases in a slower fashion with increasing amplitudes. Panel *b* shows the grid size and time step for $N = 50$ and 100, computed from equations (4.31) and (4.33). According to panel *c*, the computational time growths exponentially with the number of elements, suggesting a trade-off between numerical stability, computational time and accuracy in the definition of the amount of grid elements per wavelength N. Instabilities were identified below $N = 20$ and an acceptable accuracy was found beyond $N = 50$. As shown in panel *d*, the ratios a/a_0 and $\overline{u}/\overline{u}_0$ for $N > 50$ were slightly larger than unity, coinciding with WK95's Figure 3. For the definitive calculations $N = 51$ nodes were used.

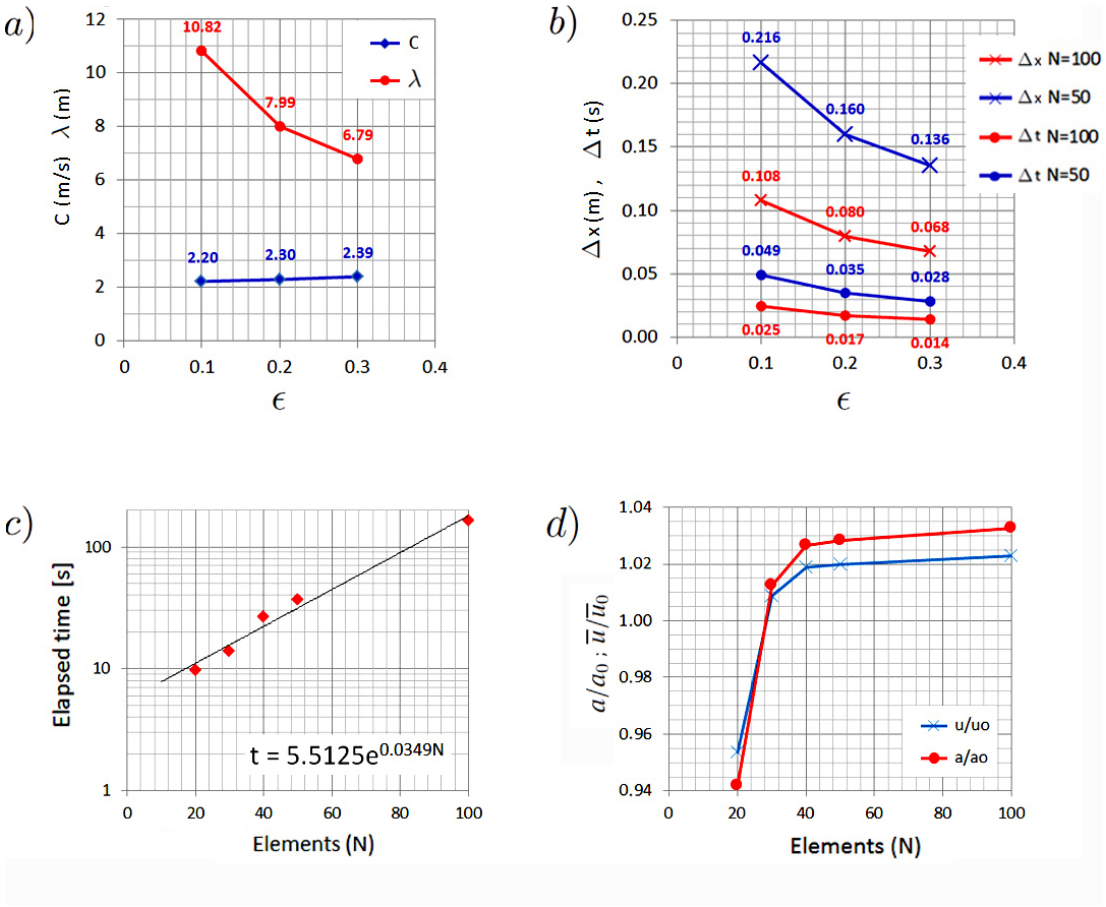

Figure 4.6: *a*) Phase speed and wavelength of the solitary wave as a function of the nonlinearity. *b*) Grid size and time step for $N = 50$ and 100. *c*) Computational times for $N = 20$, 30, 40, 50 and 100 grid elements, a model duration of 20 s and nonlinearity $\epsilon = 0.3$. *d*) Ratios of the numerical elevation and velocity of a solitary wave with respect to initial values a/a_0 and u/u_0 for $\epsilon = 0.3$ and a model duration of 20 s.

Numerical results

Figure 4.7 depicts the numerical and analytic solutions of surface elevation of a solitary wave propagating on a uniform rectangular channel of $\overline{h} = 0.45$ m for nonlinearities of $\epsilon = 0.1$, 0.2 and 0.3. Snapshots at $t = 120$ s for an initial solitary wave centered at $x = 84$ m are shown. Three relevant features identified by WK95 were reproduced in the present computations: First, numerical

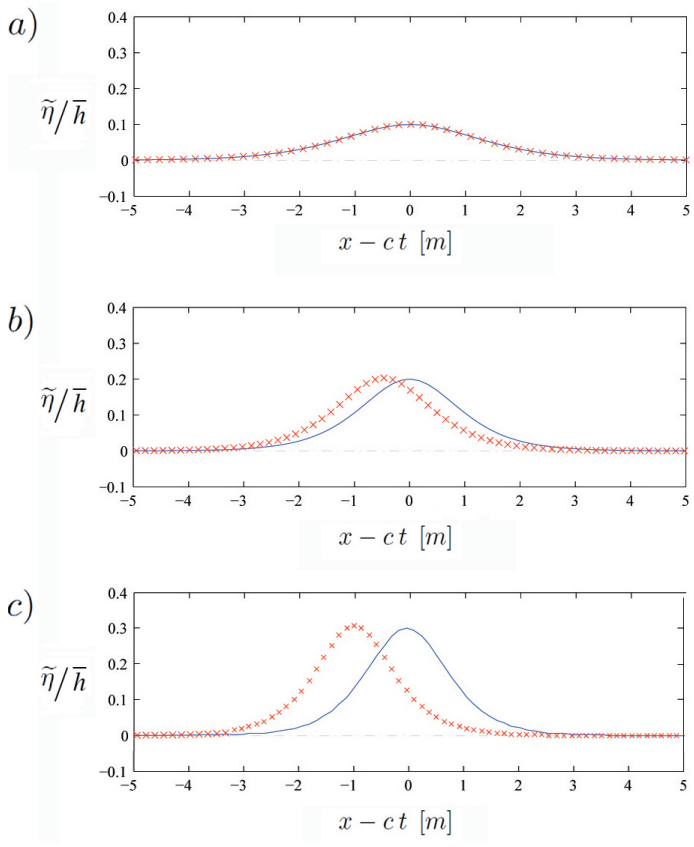

Figure 4.7: Comparison of the analytical (lines) and numerical profiles (crosses) of a solitary wave propagating on a uniform rectangular channel of $\overline{h} = 0.45$ m at computational time of $t = 120$ s, for nonlinearities of *a*) $\epsilon = 0.1$, *b*) $\epsilon = 0.2$ and *c*) $\epsilon = 0.3$. The x–axis is translated to keep the peak of the analytic solution at the center of the plot. This figure is slightly different to WK95's Figure 4, where numerical solutions at $t = 40$ s and 160 s are compared.

solutions have a slightly larger amplitude than analytic solutions (4.27). Second, numerical solutions have slower numerical phase speed when compared to the analytic solution (4.29). Finally, a dispersive wave train of relatively small amplitudes and slower speed than the solitary wave is generated.

Table 4.1 shows that the numerical values of amplitude a_n and velocity u_n at different times are slightly larger than the theoretical values a_0 and $u_0 \equiv a_0\sqrt{g/\overline{h}}$

	a_n/a_0			u_n/u_0		
t	40 s	80 s	120 s	40 s	80 s	120 s
$\epsilon = 0.1$	1.0067	1.0052	1.0064	1.0062	1.0046	1.0057
$\epsilon = 0.3$	1.0312	1.0291	1.0146	1.0219	1.0201	1.0146

Table 4.1: Ratios of elevation and velocity of a solitary wave with respect to initial values at different times.

defined in (4.27) and (4.28). The magnitude of the deviation, however, is relatively small, implying that unwanted dissipative effects due to numerical error are negligible. An inspection of the ratios a_n/a_0 and u_n/u_0 indicates that the magnitude of the deviation from theory increase with nonlinearity and generally, but not always, decays with time. WK95 argues this can be explained by the fact that the fourth-order equation from which the analytical solution is derived is only asymptotically equivalent to the numerical model, so that the initial surface elevation does not correspond exactly to a solitary waveform.

Dispersive trains for amplitudes given by $\epsilon = 0.1$ and $\epsilon = 0.3$ are depicted in Figure 4.8. The size of the dispersive tail is small compared to the solitary wave, so zooms are included to illustrate the wave patterns. It is shown that the dispersive train contains low-frequencies near the solitary wave and high frequencies towards its back. Table 4.2 illustrates the magnitude of the leading wave of the dispersive train (η_{dw}) and its spatial lag with respect to the solitary wave (*lag*) at various times steps. The magnitude of the spatial lag increases with nonlin-

	lag m			η_{dw} m		
t	40 s	80 s	120 s	40 s	80 s	120 s
$\epsilon = 0.1$	–	8	15	–	1.6×10^{-4}	1.4×10^{-4}
$\epsilon = 0.3$	15	25	40	1.2×10^{-3}	1.0×10^{-3}	0.9×10^{-3}

Table 4.2: Lag and magnitude of the leading dispersive wave with respect to the solitary wave at different times. The sign – implies the dispersive tail is embedded in the main solitary wave.

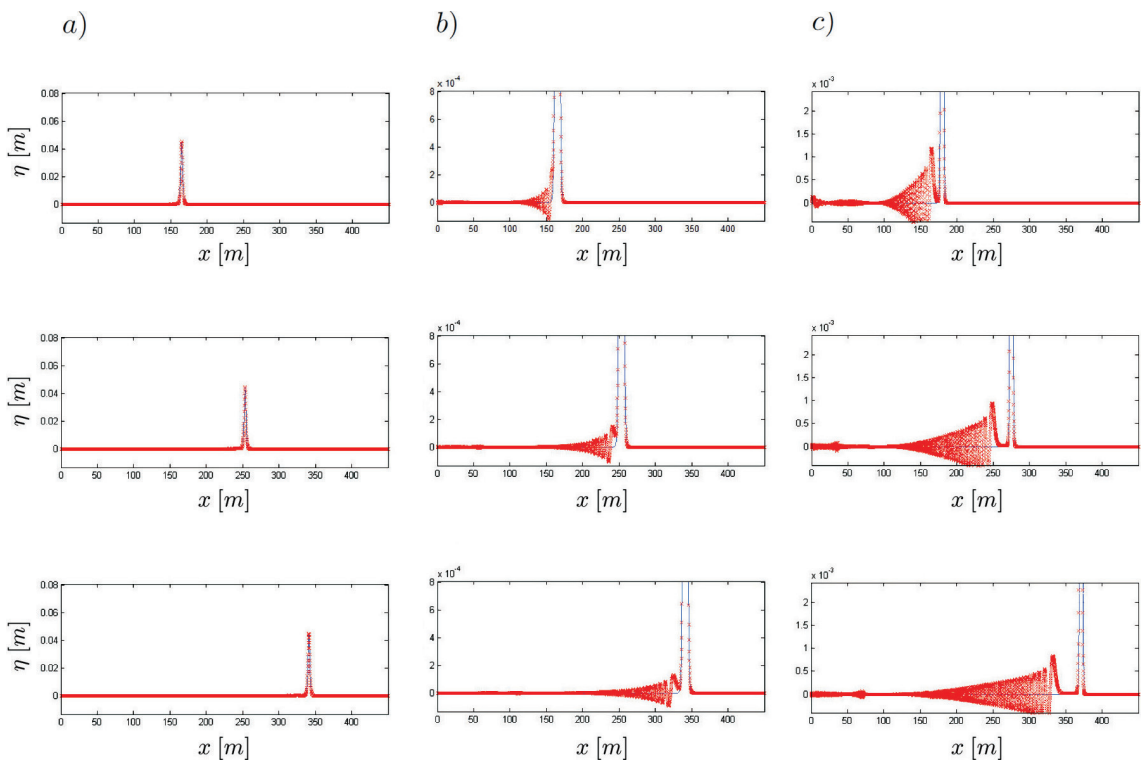

Figure 4.8: Surface elevation for $\epsilon = 0.1$ and $\overline{h} = 0.45$ m at 40 s, 80 s and 120 s for an initial solitary wave centered at $x = 84$ m. Numerical solution in red crosses and the analytic solution in black lines. *b*) Zoom in the surface elevation to highlight the dispersive train for $\epsilon = 0.1$ and *c*) for $\epsilon = 0.3$.

earity and time. Initially, the dispersive train is embedded in the solitary wave and, as time evolves, is dissociated from the latter eventually becoming independent. The amplitude of the leading wave of the dispersive train is orders of magnitude smaller that of the solitary wave and slowly decays with time. The amplitude is observed to be proportional to nonlinearity.

Conservation of mass

The conservation of mass was checked for this benchmark and all cases presented hereafter, excluding those considering viscous effects, where additional

fluxes are induced in the core region where the Boussinesq equations are solved, as a consequence of the momentum deficit the boundary layer (see Chapter 6). The total excess of mass in the system due to waves at time t is given by integrating the surface elevation on the domain

$$m_{exact}(t) = \int_{-\infty}^{\infty} \int_{-s_r}^{s_l} \eta(x, y, t)\, dydx. \tag{4.34}$$

To the level of approximation of the present theory, the total mass is

$$m(t) = \int_{-\infty}^{\infty} \int_{-b_r}^{b_l} \eta(x, y, t)\, dydx = m_{exact} + O(\epsilon), \tag{4.35}$$

where $s_l = b_l + O(\epsilon)$ and $s_r = b_r + O(\epsilon)$. The conservation of mass is defined as

$$\frac{dm}{dt} = \frac{m(t) - m(0)}{t} = 0, \tag{4.36}$$

where $m(0)$ is the initial excess mass in the domain. The expression

$$R(t) = 1 - \frac{m(t)}{m(0)} \tag{4.37}$$

is used to quantify the mass conservation in the present study. Since the spanwise averaged free surface elevation is defined as

$$\widetilde{\eta}(x, t) = \frac{1}{B_0} \int_{-b_r}^{b_l} \eta(x, y, t)\, dy, \tag{4.38}$$

the total mass (4.35) is assessed using the following expression

$$m(t) = \int_{-\infty}^{\infty} B_0(x)\, \widetilde{\eta}(x, t)\, dx. \tag{4.39}$$

For the benchmark case analyzed herein, conservation of mass was preserved throughout the simulations. As an example, for a nonlinearity of $\epsilon = 0.1$, the ratio between the mass at $t = 160$ s and the initial mass resulted in $R(160) = 3.2 \times 10^{-4}$. This instant corresponds to roughly 400 water depths of traveling distance.

From the analysis of the benchmark case, it is concluded that the present numerical scheme is able to propagate waves over long distances without undergoing significant damping in the amplitude, changes in the shape or loss of mass.

4.2 Numerical scheme for the cross-flow problem

Cross-flow boundary value problems (BVP's) are required to solve the propagation of weakly-nonlinear weakly-dispersive waves in channels by means of one-dimensional sectional averaged equations. BVP's have been analytically solved for rectangular, triangular, semi-circular and parabolic cross-sections (e.g. Peregrine, 1968; Teng & Wu, 1992), but for complex cross-sections, they need to be solved numerically.

A finite difference scheme with second-order accuracy in space has been employed to solve the BVPs given by equations (3.112) to (3.117). The accuracy of the scheme is tested by comparing numerical results to analytic solutions for a rectangular uniform channel (Peregrine, 1968) and to the numerical solutions for a trapezoidal uniform channel (Teng & Wu, 1994); the agreements are excellent. The finite difference scheme and benchmark cases are explained in this section.

4.2.1 Governing equations

The BVPs for the unknowns $\chi_1(x, y, z)$ and $\chi_2(x, y, z)$ are well-posed problems, for which the solutions exists and are unique within an arbitrary constant. The function χ_1 satisfies the BVP given by (3.112) to (3.114):

$$\frac{\partial^2 \chi_1}{\partial y^2} + \frac{\partial^2 \chi_1}{\partial z^2} = 0 \qquad \text{on} \quad -h(x, y) < z < 0, \tag{4.40}$$

$$\frac{\partial \chi_1}{\partial z} = -\frac{1}{B_0}\frac{dA_0}{dx} \qquad \text{on} \quad z = 0, \tag{4.41}$$

$$\frac{\partial \chi_1}{\partial n} = -\frac{\frac{\partial h}{\partial x}}{\sqrt{\left(\frac{\partial h}{\partial y}\right)^2 + 1}} \qquad \text{on} \quad z = -h(x, y). \tag{4.42}$$

For a fixed bottom, the function χ_2 satisfies the BVP given by (3.115) to (3.117):

$$\frac{\partial^2 \chi_2}{\partial y^2} + \frac{\partial^2 \chi_2}{\partial z^2} = -1 \qquad \text{on} \quad -h(x,y) < z < 0, \tag{4.43}$$

$$\frac{\partial \chi_2}{\partial z} = -\frac{A_0}{B_0} \qquad \text{on} \quad z = 0, \tag{4.44}$$

$$\frac{\partial \chi_2}{\partial n} = 0 \qquad \text{on} \quad z = -h(x,y). \tag{4.45}$$

If the sidewalls are vertical, two additional no-flux boundary conditions must be invoked:

$$\frac{\partial \chi_1}{\partial y} = \left(-\frac{db_l}{dx}, \frac{db_r}{dx}\right) \quad \text{and} \quad \frac{\partial \chi_2}{\partial y} = 0, \qquad \text{on} \quad y = b_l(x), -b_r(x). \tag{4.46}$$

Once χ_1 and χ_2 are solved for a given cross-section, the coefficients in the momentum equation α, β and γ in the Boussinesq-type equations can be obtained.

The elliptic nature of the Laplace and Poisson equations in the governing equations for χ_1 and χ_2 indicates its solutions are inter-related at all points in the domain. This means that a perturbation propagates at infinite speed within the domain. In this case, the perturbation is induced through the free surface kinematic boundary condition at the free surface by a wave traveling on the x-axis.

4.2.2 Numerical scheme

For irregular geometries where no analytical solutions are available, elliptic partial differential equations can be solved by various techniques, among which a finite difference method are adopted herein (Moin, 2010). The discretization and implementation of the BVPs for χ_1 and χ_2 are explained in this section. For simplicity, a square grid where $\Delta y_{(i,j)} = \Delta z_{(i,k)} = \Delta_{(i)}$ is used. The discretization has a leading order error of $O\left(\Delta_{(i)}^2\right)$, thus in the Boussinesq equations the error is $O\left(\mu^2 \Delta_{(i)}^2\right)$.

Boundary value problem for χ_1

The Laplace equation (4.40) is approximated by the second-order finite difference operator

$$\chi_{1(i,j+1,k)} + \chi_{1(i,j-1,k)} - 4\chi_{1(i,j,k)} + \chi_{1(i,j,k+1)} + \chi_{1(i,j,k-1)} = 0, \tag{4.47}$$

for all interior points located in the area covered by water which are not affected by boundary conditions. For exterior points, this expression is reduced to $\chi_{1(i,j,k)} = 0$. Those points adjacent to the boundaries require special treatment to account for the boundary conditions. As example, for points in the free surface, the kinematic boundary condition (4.41) is discretized as

$$\frac{\chi_{1(i,j,k_s+1)} - \chi_{1(i,j,k_s-1)}}{2\Delta z_{(i,k_s)}} = -\frac{1}{B_{0(i)}} \frac{A_{0(i+1)} - A_{0(i-1)}}{2\Delta x_{(i)}} \tag{4.48}$$

where the location $k_s + 1$ corresponds to an exterior point. Combining with the governing equation (4.47) yields

$$\chi_{1(i,j+1,k_s)} + \chi_{1(i,j-1,k_s)} - 4\chi_{1(i,j,k_s)} + 2\chi_{1(i,j,k_s-1)} = \frac{\Delta_{(i)}}{B_{0(i)}} \left(\frac{A_{0(i+1)} - A_{0(i-1)}}{\Delta x_{(i)}} \right). \tag{4.49}$$

This expression requires that the location $k_s - 1$ is an interior point. It also excludes points in the left and right extremes of the channel. For the surface point at the left extreme, a supplementary no flux boundary condition is assumed

$$\frac{\chi_{1(i,j_l-1,k_s)} - \chi_{1(i,j_l+1,k_s)}}{2\Delta_{(i)}} = 0 \tag{4.50}$$

so that $\chi_{1(i,j_l-1,k_s,t)} = \chi_{1(i,j_l+1,k_s,t)}$. The governing equation (4.47) becomes

$$2\chi_{1(i,j_l+1,k_s)} - 4\chi_{1(i,j_l,k_s)} + 2\chi_{1(i,j_l,k_s-1)} = \frac{\Delta_{(i)}}{B_{0(i)}} \left(\frac{A_{0(i+1)} - A_{0(i-1)}}{\Delta x_{(i)}} \right). \tag{4.51}$$

By analogy, at the right extreme

$$2\chi_{1(i,j_l-1,k_s)} - 4\chi_{1(i,j_l,k_s)} + 2\chi_{1(i,j_l,k_s-1)} = \frac{\Delta_{(i)}}{B_{0(i)}} \left(\frac{A_{0(i+1)} - A_{0(i-1)}}{\Delta x_{(i)}} \right), \tag{4.52}$$

The bottom boundary condition (4.42) simply requires the local computation of $\partial h/\partial x$ and $\partial h/\partial y$, stemming form the geometry.

Boundary value problem for χ_2

The Poisson equation (4.43) reads

$$\chi_{2(i,j+1,k)} + \chi_{2(i,j-1,k)} - 4\chi_{2(i,j,k)} + \chi_{2(i,j,k+1)} + \chi_{2(i,j,k-1)} = -\Delta_{(i)}^2. \tag{4.53}$$

for all interior points. For exterior points this expression is reduced to $\chi_{2(i,j,k)} = 0$. For surface points, the kinematic condition (4.44) is discretized as

$$\frac{\chi_{2(i,j,k_s+1)} - \chi_{2(i,j,k_s-1)}}{2\Delta z_{(i,k_s)}} = -\frac{A_{0(i)}}{B_{0(i)}} \tag{4.54}$$

where the location $k_s + 1$ corresponds to an exterior point. Combining with the governing equation (4.53) yields

$$\chi_{2(i,j+1,k_s)} + \chi_{2(i,j-1,k_s)} - 4\chi_{2(i,j,k_s)} + 2\chi_{2(i,j,k_s-1)} = -\Delta_{(i)}^2 + 2\Delta_{(i)}\frac{A_{0(i)}}{B_{0(i)}}. \tag{4.55}$$

This expression requires that the location $k_s - 1$ immediately below is an interior point. It also excludes those points in the left and right extremes of the channel. For corner points at the surface, a no flux boundary condition is assumed

$$\frac{\chi_{2(i,j_l-1,k_s)} - \chi_{2(i,j_l+1,k_s)}}{2\Delta_{(i)}} = 0, \tag{4.56}$$

so that $\chi_{2(i,j_l-1,k_s,t)} = \chi_{2(i,j_l+1,k_s,t)}$. The governing equation (4.53) therefore becomes

$$2\chi_{2(i,j_l+1,k_s)} - 4\chi_{2(i,j_l,k_s)} + 2\chi_{2(i,j_l,k_s-1)} = -\Delta_{(i)}^2 + 2\Delta_{(i)}\frac{A_{0(i)}}{B_{0(i)}}, \tag{4.57}$$

and

$$2\chi_{2(i,j_r-1,k_s)} - 4\chi_{2(i,j_r,k_s)} + 2\chi_{2(i,j_r,k_s-1)} = -\Delta_{(i)}^2 + 2\Delta_{(i)}\frac{A_{0(i)}}{B_{0(i)}}, \tag{4.58}$$

for the right and left extremes. The bottom boundary condition (4.45) is treated differently depending on whether neighboring points are interior or exterior points. Stencils for interior points, surface points and bottom boundary points are shown in Figure 4.9. Figure 4.10 depicts the application of the boundary conditions on a channel with a trapezoidal irregular cross-section.

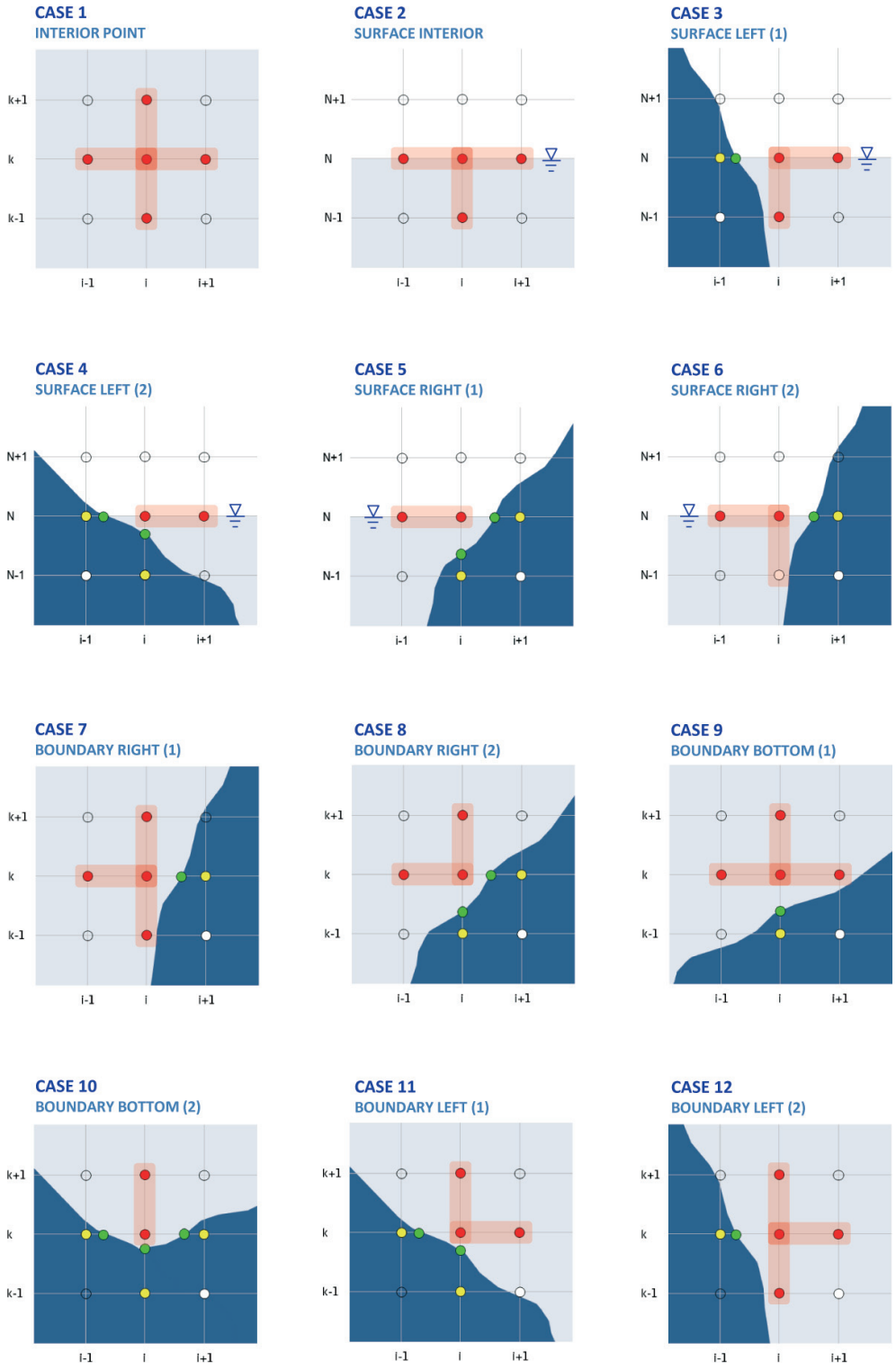

Figure 4.9: Stencils used in interior points, surface points and bottom boundary points. Yellow nodes denote exterior points, green dots the boundaries and red dots the stencil.

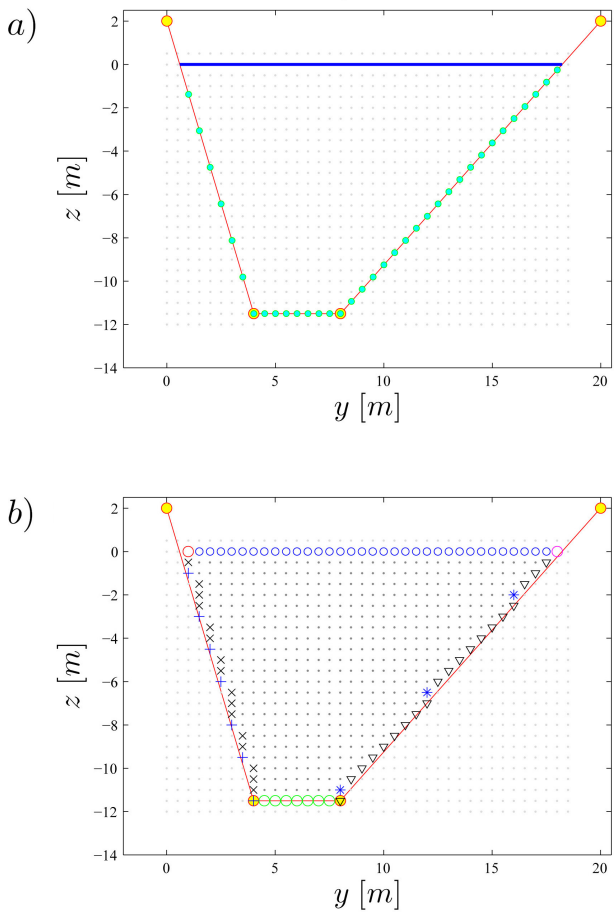

Figure 4.10: Example of definition of the type of exterior, interior and boundary points in a trapezoidal channel. *a*) Raw bathymetric data (yellow dots), interpolated boundary (red line with light green dots) and sea water level (blue) on a discretized domain. *b*) Different symbols defining the types of boundary conditions shown in Figure 4.9 are depicted.

The discretized version of the BVPs for χ_1 and χ_2 can be written as a system of linear algebraic equations of the form

$$\mathbf{A}f = b, \tag{4.59}$$

where $\mathbf{A}$ is a block-tridiagonal matrix and the vector b contains the boundary conditions and forcing. The unknowns $f_{(j,k)}$ are ordered as

$$\left[f_{(1,1)}, f_{(1,2)}, ..., f_{(1,N_z)}, f_{(2,1)}, f_{(2,2)}..., f_{(N_y,N_z)}\right]^T. \tag{4.60}$$

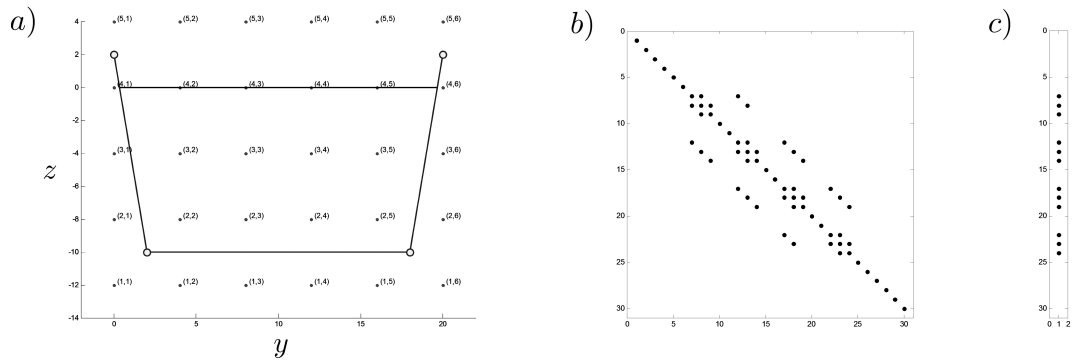

Figure 4.11: Graphical representation of the linear system (4.59) for a trapezoidal cross-section. *a*) Vertices of the trapezoid are located at $(0; 2)$, $(2; -10)$, $(18; -10)$ and $(20, 2)$. The grid is formed by 30 nodes with $N_y = 6$ and $N_z = 5$. *b*) The corresponding matrix A and *c*) vector b on the system of linear equations.

Matrix **A** is conformed by $N_y \times N_y$ blocks of size $N_z \times N_z$ each, following the well-known structure of a Laplace/Poisson equation in two-dimensions and uniform mesh. The diagonal blocks are tridiagonal and the sub- and super-diagonal blocks are diagonal with constant elements throughout.

A typical example of the structure of matrix **A** and vector b for a trapezoidal cross section is presented in Figure 4.11. The system (4.59) is solved using Matlab's built in function $f = A\backslash b$, which performs a general triangular factorization using LU factorization with partial pivoting (Strang, 2007; p.26).

Implementation

The scheme was designed to solve the BVPs for arbitrary cross-sections which are concave upward. The scheme allows simply connected, concave cross-sections where the bottom is unequivocally defined by a function. Figure 4.12 *a* depicts a cross-section within the limitations of the theory. Cases such as non connected domains (Figure 4.12 *b*) and sections defined by bi-valued functions

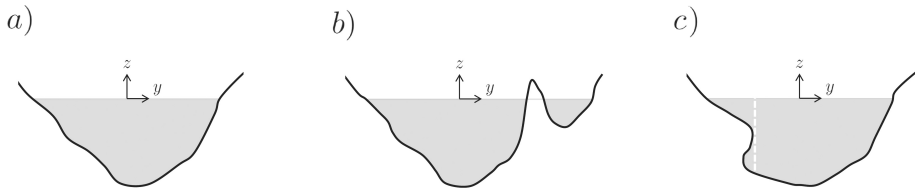

Figure 4.12: *a*) A cross-section within the limitations of the present algorithm. Sections that cannot be analyzed are *b*) a non connected domain and *c*) a section that cannot be defined by one-valued function.

(Figure 4.12 *c*) cannot be solved with the algorithm developed herein.

For a given cross-section, the input data consists of ordered pairs in a two-dimensional Cartesian coordinate system containing the topo-bathymetry. The location of a point in such a coordinate system is given in the format (y, h), where y is the spanwise coordinate and h the elevation with respect to the still water level; being negative for bathymetry and positive for topography. Neighboring points have to be listed with increasing values of the y-coordinate in a counterclockwise sequence. Two or more points cannot have the same y-coordinate. The still water level is automatically generated in the algorithm.

The grid size is arbitrary but should be small enough to properly represent the cross-sectional features. Convergence tests for rectangular and trapezoidal cross-sections were carried out to test the algorithm. The value of the dispersive strength γ given by (3.122) was computed for grid sizes of $\Delta = 0.1$ to 0.5 m. Note that for a rectangular channel, the analytic solution given by equation (3.135) is $\gamma = -h^2/3$. Figure 4.13 shows that, for both rectangular and trapezoidal cross-sections, the value of the dispersive strength tends to converge as the grid size diminishes. There are a few exceptions for which the computation slightly deviates from the trend. This can be explained by the fact that the grid does not match the boundaries exactly. Accurate results were found with $\Delta_{(i)} \leq B_0/30$,

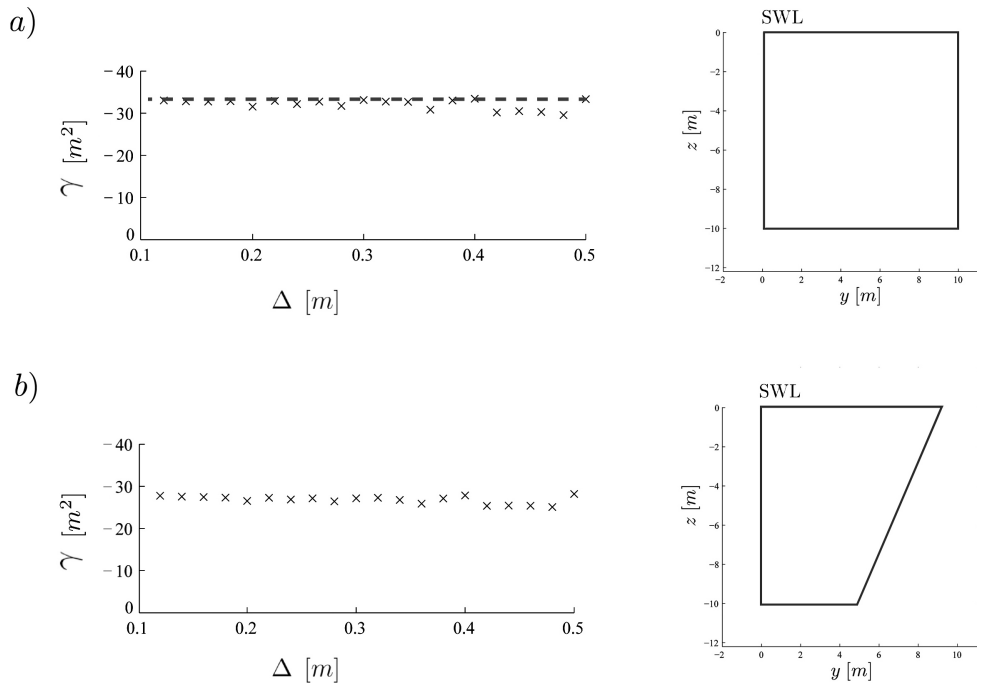

Figure 4.13: *a*) Computation of the dispersive strength γ as function of the grid size Δ for a rectangular cross-section of depth $h = 10$ m and surface width $B_0 = 10$ m. The numerical solution is depicted in crosses and the analytic solution given by $\gamma = -h^2/3$ is shown in dashed line. *b*) Similar plots of the dispersive strength for a trapezoidal cross-section of $h = 10$ m, $B_0 = 10$ m and basal width 5 m.

where B_0 is the surface width under the quiescent state and $\Delta_{(i)}$ the grid size.

In the present algorithm, the values of the cross sectional area A_0 and B_0 are independent from the grid size since they are computed exactly from a polygon built from raw data. A_0 is the area of the polygon formed by the bathymetric soundings and the still surface level. B_0 is the distance between the intersection of the still water level and the interpolated bathymetry.

4.2.3 Benchmark cases

In the literature there are no analytical or numerical computations of the coefficients α and β. Closed-form solutions (analytical) for the dispersive coefficient γ are provided for rectangular, triangular, semi-circular and parabolic cross-sections (e.g. Peregrine, 1968; Teng & Wu, 1992). Numerical solutions for specific trapezoidal shapes are provided by Peregrine (1969) and Teng & Wu (1994). Comparison between the present numerical results and some of the solutions available in the literature is presented in this section.

Peregrine's (1968) analytical solution for a rectangular cross section

For a rectangular channel of constant depth, Peregrine (1968) found

$$\psi(z) = \frac{z^2}{2} + hz, \tag{4.61}$$

where $\psi \equiv \chi_2$ in the present notation. This expression indicates that there is no spanwise change of the flow properties in the cross-section. In Peregrine's formulation, the dispersive term appearing in the conservation of mass (A.1) has the form $\psi_B - \psi_A$, where these functions are given by equations (A.3). Note that the equivalence with the present theory is given by $\gamma = \psi_A - \psi_B$, where $\psi_A = -h^2/3$ and ψ_B is arbitrarily chosen to be zero. Numerical computations for a channel of $h = 10$ m were carried out for different grid sizes (see Figure 4.13 *a*). The analytical solution of $\gamma = -33$ m^2 was approached by the numerical solution for small grid sizes. The patterns of the function χ_2 were also replicated.

Peregrine (1969) carried out numerical computations of γ using the extrapolated Liebmann method for seven trapezoidal channels. He reported a range of

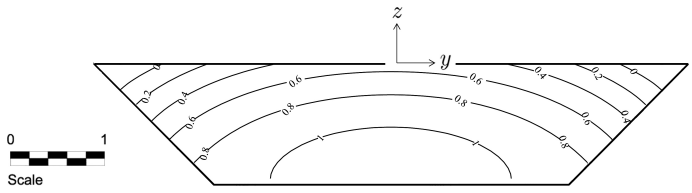

Figure 4.14: Numerical solution for χ_2 in a trapezoidal channel used in Teng & Wu (1994).

values between $\gamma = 0.358$ to 0.25 but gave no details on the value of specific sections. With the present algorithm, values ranging from $\gamma = 0.34$ for the widest channel to $\gamma = 0.18$ for the triangular case were found. These results, however, are not strictly comparable due to lack of information in the original paper.

Teng & Wu's (1994) numerical solution for a trapezoidal cross section

Teng & Wu (1994) numerically computed a value of the shape factor κ for a symmetric trapezoidal channel (Figure 4.14). The shape factor is related to the dispersive strength by

$$\gamma = -\kappa^2 \frac{\breve{h}^2}{3}. \tag{4.62}$$

The geometry is given by a surface width of $2b_s = 6.25$, a bottom width $2b_b = 3.75$, sidewall vertex angle of 45°, a maximum depth of $h_m = 1.25$ and a mean water depth of $\breve{h} = 1$. By means of a Gauss-Seidel iteration method, they computed a value of $\kappa = 0.268$. Using our numerical scheme and a space increment of $\Delta y = \Delta z = 0.025$, a value of $\kappa = 0.285$ was computed with the present algorithm. The agreement with Teng & Wu's computation is excellent.

From the benchmark cases analyzed herein, it is concluded that the accuracy of the numerical scheme is appropriate for the computation of the γ, provided that the number of grid points in the cross-section is larger than 30.

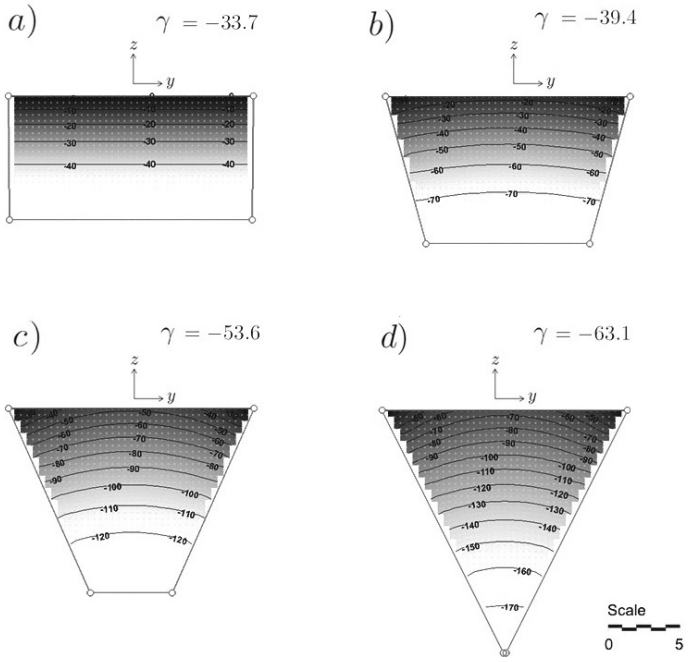

Figure 4.15: Computation of $\chi_2(y,z)$ for *a*) rectangular channel, *b*) and *c*) trapezoidal channels and *d*) triangular channels with same surface width $B_0 = 20$ and mean depth $\breve{h} = 10$. The value of the dispersive coefficients are $\gamma = -33.7$, -39.4, -53.6 and -63.1, respectively. Grey dots depict the grid nodes used in the computation.

4.2.4 Numerical computation of coefficient γ

A few examples are included in this section to gain some physical insight on the role of the cross-sectional geometry. For simplicity, the analysis is focused on the dispersive properties associated with $\chi_2(x,y,z)$ and $\gamma(x)$ which were earlier explored by other authors (e.g. Teng, 1990; Teng & Wu, 1992). Figure 4.15 depicts the numerical computation of χ_2 for rectangular, trapezoidal and triangular cross-sections, defined with the same surface width $B_0 = 20$ and mean depth $\breve{h} = 10$, where

$$\breve{h}(x) = \frac{1}{B_0} \int_{-B_0/2}^{B_0/2} h(x,y)\, dy.$$

In a rectangular channel, χ_2 is uniform across the channel and so do other flow

properties such as the pressure, velocities and surface elevation. For trapezoidal and triangular cross-sections, there is a noticeable variation in χ_2 on the span-wise direction. Due to symmetry, χ_2 is found to increase monotonically from its lowest value at the center-line to its maximum at the sidewalls. The no flux condition at the channel boundaries implies that the iso-contours are perpendicular to them. It can be observed that the greater the departure of the cross-section from the rectangular, the greater the value of γ, therefore the strength of the dispersive term in the Boussinesq equations. In fact, the dispersive coefficient in a triangular cross-section almost doubles that from the rectangular. This influence of the cross-sectional geometry was first observed by Teng & Wu (1992).

It should be noted that γ for rectangular and triangular-symmetric channels can be obtained analytically with expressions derived in section 3.5 whereas for a trapezoidal channel it can only be computed numerically. The effects of cross-sectional geometry in uniform channels is further explored in section 5.1.

Figures 4.16 is intended to explore the role of the small bathymetric features in the dispersive properties of the cross-section. The triangular and irregular geometries in Figures 4.16 *a* and 4.16 *b* have the same surface width $B_0 = 20$ and mean cross-averaged depth $\breve{h} = 5$. The irregular shape has been generated by adding a small random deviation in the vertical position of the bottom, with respect to the triangular shape.

It can be observed in Figures 4.16 *a* and 4.16 *b* that the iso-contours of χ_2 are significantly affected by the large-scale triangular-shaped bathymetric features of the cross-section, whereas the smaller scales associated with sharp changes in the bathymetry in the irregular geometry (Figure 4.16 *b*) only affect flow properties locally. The value of the dispersive coefficients are $\gamma = -21.84$ and -21.76

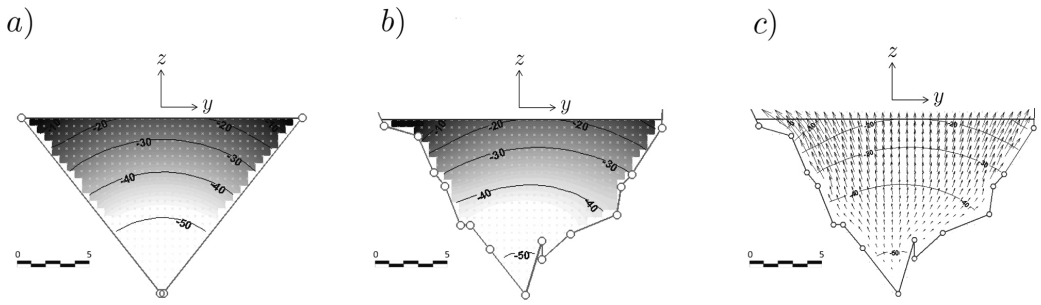

Figure 4.16: Computation of $\chi_2(y,z)$ for a) triangular channel and b) an triangular-shaped irregular channel with same surface width B_0 and mean depth $\breve{h}$. The value of the dispersive coefficients are $\gamma = -21.84$ and -21.76, respectively. c) depicts the velocity structure (not in scale) in the arbitrary cross-section.

for the triangular and irregular cross-sections, respectively, implying that the small bathymetric features play a minor role on the dispersive properties of the channel. This is an interesting result which may lead to recommendations on the accuracy of topo-bathymetric surveys for real applications. In other words, the density of depth soundings has to be accurate enough to capture the main geometrical features of the cross-section.

Figure 4.16 c depicts the velocity pattern in the cross-section. The maximum velocities are found in the surface at the sidewalls, diminishing towards the center and deepest part of the channel. This result may be related to earlier observations (Russell 1837 , Sandover & Taylor, 1962; Peregrine, 1988 and 1969; Treske, 1994 and Teng & Wu, 1997) showing spanwise changes in the flow properties. The analysis of cross-sectional flow properties in the cross-sections are further explored in section 5.1.

CHAPTER 5

APPLICATIONS FOR POTENTIAL FLOWS

To illustrate the capability of the present model, analytical and numerical examples for uniform channels, channels where the geometry changes slowly and channels where changes in cross-section are appreciable within a wavelength are presented in this section. These cases are characterized by $dA_0/dx = 0$, $O(\epsilon)$ and $O(1)$, respectively. Section 5.1 focuses on the effect of the cross-section geometry on the evolution of solitary and initially gaussian waves in a uniform channel. In section 5.2, numerical results of the present model are compared with laboratory experiments on the evolution of a solitary wave in a rectangular channel with slowly-varying width (Chang *et al.*, 1979). These numerical experiments are revisited in Section 6 with the inclusion of viscous boundary layer effects. In section 5.3, solitary wave propagation in channels with rapid contractions and expansions are studied.

5.1 Uniform channel

The standard case of waves propagating on uniform channels is presented to start the discussion. Teng & Wu (1992) stated that the uniformity of the medium implies the existence of permanent solitary waves, even under changes in the water depth across the channel. This result is confirmed in Section 5.1.1 by means of numerical computations of solitary waves in rectangular and non-symmetric trapezoidal and triangular channels. The evolution of an initial gaussian hump in uniform channels with different cross-sections is also studied in Section 5.1.2 using the present theory. In this case, the waveform is not permanent and other propagation features (e.g. dipsersive train) can be studied.

5.1.1 Solitary waves in a uniform channel

Solitary waves are conventionally used in fundamental research on long waves. The reasons behind this are that solitary waveforms reveal the fundamental long wave behavior, avoiding the complex wave-wave interactions existing in regular or irregular long wave trains, which may obscure the main features of interest (Shi *et al.*, 2005). Due to their permanent form in a uniform medium, they are also used to test the stability and conservative properties of numerical schemes (4.1.3).

Analytical solutions for a solitary wave in a uniform channel with inclined sidewalls can be found in Peregrine (1968), Teng & Wu (1997), and Teng (2000). A detailed derivation of the solitary wave solution in channels of arbitrary cross-section is included in Appendix F. Here, the solitary wave solutions are briefly discussed for completeness, since they will be used in the following sections as initial conditions to study waves propagating in non-uniform channels. For uniform channels of arbitrary cross-sectional geometry, the governing equations for the spanwise averaged free surface elevation and the cross-sectional averaged longitudinal velocity are reduced from (3.95) and (3.124) to

$$\frac{\partial \widetilde{\eta}}{\partial t} + \frac{A_0}{B_0}\frac{\partial \langle u \rangle}{\partial x} + \epsilon \frac{A_0 B_0'}{B_0^2}\widetilde{\eta}\frac{\partial \langle u \rangle}{\partial x} + \epsilon \frac{\partial}{\partial x}\left[\langle u \rangle \widetilde{\eta}\right] = O\left(\epsilon^2, \epsilon\mu^2, \mu^4\right), \tag{5.1}$$

$$\frac{\partial \langle u \rangle}{\partial \hat{t}} + \frac{\partial \widetilde{\eta}}{\partial \hat{x}} + \epsilon \langle u \rangle \frac{\partial \langle u \rangle}{\partial \hat{x}} + \mu^2 \gamma \frac{\partial^3 \langle u \rangle}{\partial t \partial x^2} = O\left(\epsilon^2, \epsilon\mu^2, \mu^4\right), \tag{5.2}$$

The leading order solitary wave solutions to these equations are given by

$$\widetilde{\eta} = \operatorname{sech}^2\left[K\left(x - ct\right)\right] + O\left(\epsilon, \mu^2\right), \tag{5.3}$$

$$\langle u \rangle = \frac{1}{\sqrt{\check{h}}} \operatorname{sech}^2\left[K\left(x - ct\right)\right] + O\left(\epsilon, \mu^2\right), \tag{5.4}$$

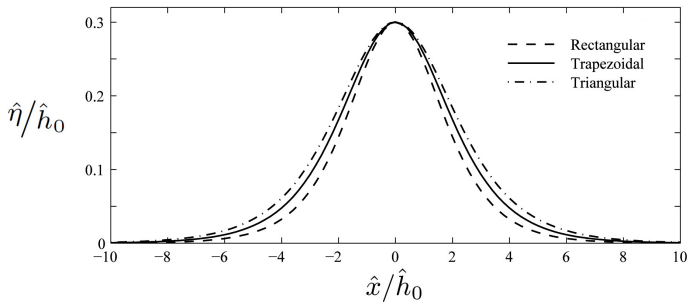

Figure 5.1: Solitary wave profiles for rectangular, trapezoidal and triangular cross-sections with aspect ratio of $B_0/\breve{h} = 2$, where the mean depth is $\breve{h} = A_0/B_0$.

with

$$K = \frac{1}{2}\sqrt{\frac{1}{\breve{h}\gamma}\left(\frac{\breve{h}B_0'}{3B_0} - 1\right)}, \qquad c^2 = \breve{h} + \epsilon\left(1 - \frac{\breve{h}B_0'}{3B_0}\right)\mathrm{Sgn}(\gamma), \qquad \breve{h} = \frac{A_0}{B_0}. \tag{5.5}$$

where $\mathrm{Sgn}(\gamma)$ denotes the sign of γ, K is the effective wave number, c represents the phase speed, and $\breve{h}$ is the mean depth. Examples of solitary wave profiles with $\epsilon = 0.3$ for rectangular, trapezoidal and triangular cross-sections with an aspect ratio of $B_0/\breve{h} = 2$ are depicted in Figure 5.1. The actual geometry is depicted in Figure 5.2. As predicted, the wavelength is the longest in the triangular channel and shortest for the rectangular cross-section. Since the nonlinearity and B_0 are the same for all cases, solitary waves travel at different phase speeds solely due to the effect of the sidewall slope, B_0'.

The solitary wave solution given above is valid only if $(\breve{h}B_0'/3B_0 - 1)/\gamma > 0$. Since the sign of γ depends on cross-sectional geometry and can not be generalized, the following discussions are restricted to three simple geometries, namely, rectangular, triangular and trapezoidal, for which $\gamma < 0$. In these cases the parameters of the cross-sectional geometry (embedded in γ, B_0, $\breve{h}$ and B_0') affect the equivalent wavelength and phase speed. However, the phase speed is independent of the magnitude of γ. Thus, solitary waves traveling in a channel with

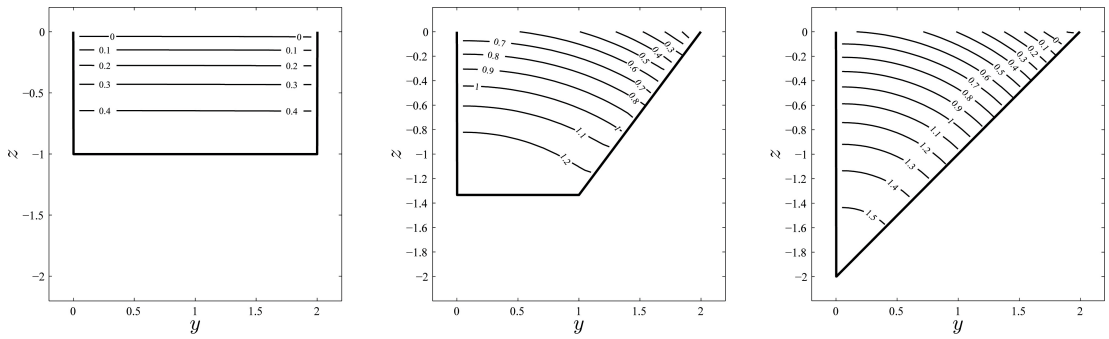

Figure 5.2: Numerical solution for $\chi_2(y, z)$ in rectangular, trapezoidal and triangular cross-sections with aspect ratio of $B_0/\breve{h} = 2$, where the mean depth is $\breve{h} = A_0/B_0$.

outwardly fanning sidewalls at $z = 0$, i.e. $0 < B_0' < 3B_0/\breve{h}$, propagate with longer wavelengths and slower speeds, compared to those in a rectangular channel with $B_0' = 0$. Conversely, in the channel with downwardly fanning sidewalls with $B_0' < 0$ solitary waves have shorter wavelengths and faster wave speeds. The reader is referred to Teng (2000) for a detailed discussion on the effects of cross-sectional geometry in solitary waves of permanent form.

Numerical solutions for χ_2, which are later used to compute γ and other derived quantities for rectangular, trapezoidal and triangular cross-sections characterized by a ratio of $B_0/\breve{h} = 2$, are shown in Figure 5.2. The trapezoidal and triangular cross-sections are non-symmetric with respect to the x-axis. Contour lines of χ_2 are perpendicular to the sidewalls whereas on the still water level ($z = 0$), χ_2 decreases from a maximum value on the vertical walls to a minimum on the sloping walls. The magnitude of the gradient of χ_2 increases in z, implying higher velocities at the free surface. The dispersive coefficients obtained from equation (3.122) are $\gamma = -0.336$ for the rectangular, $\gamma = -0.496$ for the trapezoidal and $\gamma = -0.632$ for triangular cross-sections, implying that frequency dispersion is stronger as the cross-section departs from rectangular.

The expressions for the velocity components on a cross-sectional plane in a uniform channel can be deduced from equations (3.150) and (3.151)

$$v = \mu^2 \frac{\partial \chi_2}{\partial y} \frac{\partial \langle u \rangle}{\partial x}, \qquad w = \mu^2 \frac{\partial \chi_2}{\partial z} \frac{\partial \langle u \rangle}{\partial x}. \tag{5.6}$$

The surface elevation is obtained from (3.156)

$$\eta = \widetilde{\eta} + \mu^2 \eta_2, \qquad \text{with} \qquad \eta_2 = \left(\widetilde{\chi_2|_{z=0}} - \chi_2|_{z=0} \right) \frac{\partial^2 \langle u \rangle}{\partial t \partial x}. \tag{5.7}$$

Figure depicts the 5.3 the second order solution for the surface elevation $\mu^2 \eta_2$ and the velocity on the cross-section $\mathbf{u}_n = (v, w)$ for rectangular, trapezoidal and triangular cross-sections. For the rectangular channel, the free surface elevation η is independent of y (panel a). The spanwise velocity is zero and the vertical velocity varies from a maximum value on the free surface to zero at the bottom.

More interesting flow features are found for non-symmetric trapezoidal and triangular cross-sections (panels b and c), where χ_2 changes in the spanwise direction and so do the surface elevation, velocity and pressure. In fact, at the phase of maximum acceleration, the second-order surface elevation is concave and varies from the minimum value at the vertical sidewall to the maximum value on the inclined sidewalls. At the maximum deceleration phase (not shown), the second-order surface elevation becomes convex. The velocity on the cross-section has a maximum value on the inclined sidewalls and diminishes towards the vertical walls on the opposite side of the channel cross-section. It is noted that the velocity on the cross-sectional plane is one order of magnitude smaller than the cross-sectional averaged longitudinal velocity $\langle u \rangle$ in both cases, being consistent with the assumption that $\langle u \rangle \gg O(v, w)$.

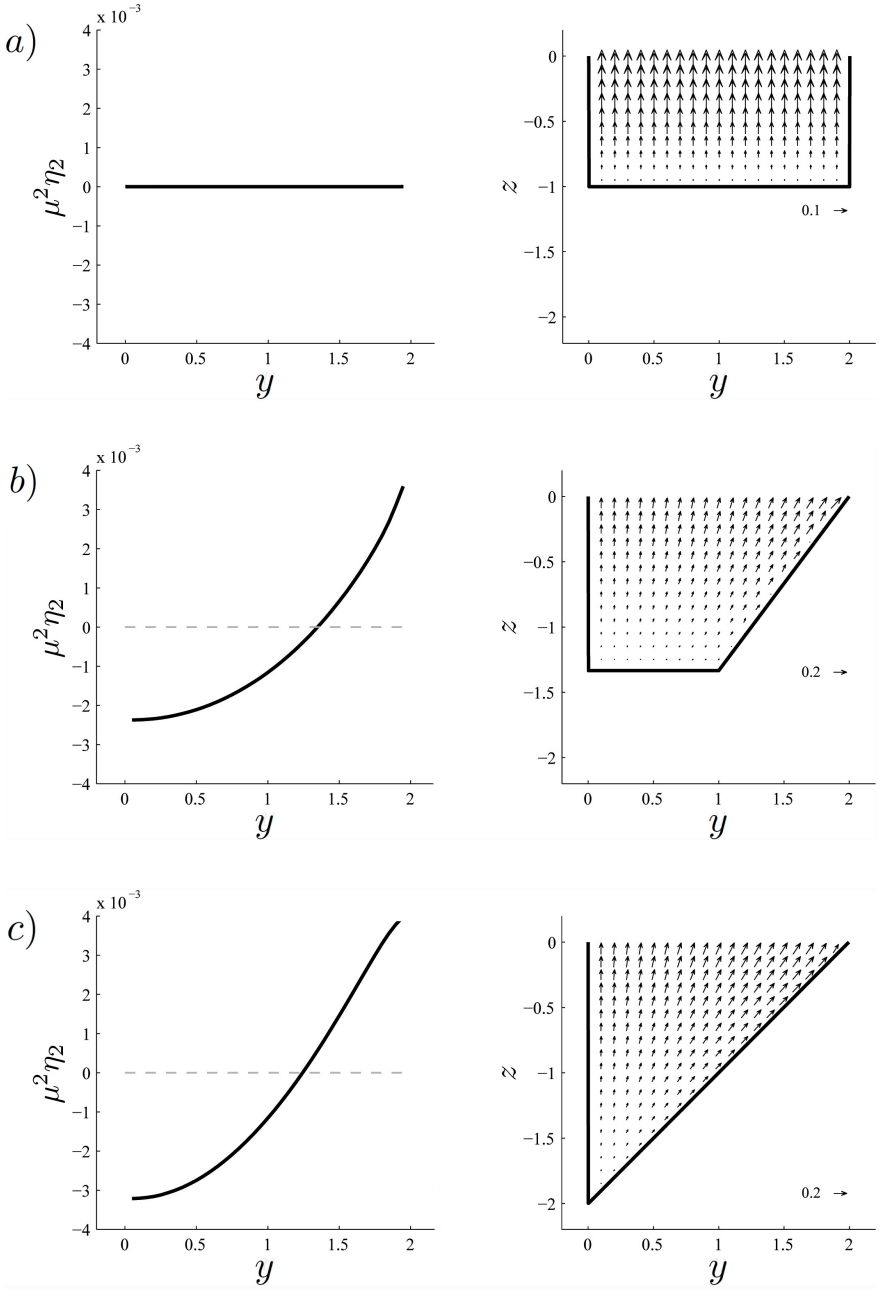

Figure 5.3: Cross-sectional wave features during the instant of maximum acceleration for a solitary wave in uniform channels with aspect ratio of $B_0/\breve{h} = 2$. Left panels show the second order solution for the surface elevation $\mu^2\eta_2$ in *a*) a rectangular channel, *b*) a trapezoidal channel and *c*) a triangular channel. Dash gray horizontal lines denote the still level. Right panels depict the transverse velocities $\mathbf{u}_n = (v, w)$. The magnitude of the velocity is depicted in small arrows on the bottom right corners.

5.1.2 Gaussian waves in a uniform channel

The evolution of an initial Gaussian wave on channels with rectangular, triangular, circular and cross-sections is explored herein. These geometries, depicted in Figure 5.4, are defined with the same surface width B_0 and mean depth $\breve{h}$. The difference in the dispersive properties is triggered by both the value of the dispersive coefficient γ and the sidewall slope at the still water level B_0'. Since all these shapes have analytical forms, both the dispersive coefficient γ and B_0' are obtained without numerically solving the boundary value problem for χ_2. The values of γ for these geometries are computed based on the shape factors k proposed by Teng & Wu (1992, Table 1), where

$$\gamma = -k^2 \frac{\breve{h}^2}{3}. \tag{5.8}$$

and $\breve{h}$ is the mean depth. The values are $k = 1$ for a rectangular channel, $k = 1.06$ for a semicircular channel $k = 1.16$ for a parabolic channel and $k = 1.27$ for a triangular channel. Note that for the rectangular and triangular geometries, these coefficients are represented by the analytic expressions (3.146) and (3.138). In this section, results are presented in dimensional form.

The initial wave is described by a gaussian hump cenetered at the origin with an amplitude of $\widetilde{\eta} = 0.05$ m and a standard deviation of $\sigma_{\widetilde{\eta}} = 2$ m. The channels are defined by $\breve{h} = 0.5$ m, $A_0 = 1$ m^2 and $B_0 = 1$ m. Figure 5.5 depicts snap-

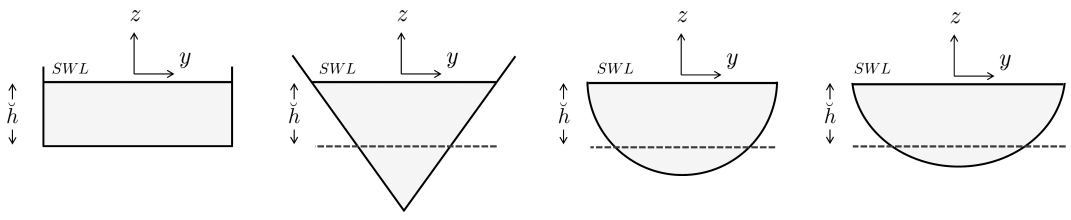

Figure 5.4: Cross-sections analyzed for Gaussian waves.

shots of the wave profiles at $t = 88$ s, corresponding to a traveling distance of approximately 400 water depths. It is clearly observed how the cross-sectional geometry affects the wave features: the more the section departs from rectangular, the slower it becomes while the amplitude of the main hump is reduced. In addition, a dispersive tail becomes evident for the circular, parabolic and triangular triangular cross-sections, being almost negligible in the rectangular case. This behavior may become significant, for example, when assessing the estimated times of arrival of tsunamis on coastal areas distant from the source.

Figure 5.6 depicts typical flow features on a cross-sectional plane for a channel of a symmetric triangular shape. There characteristic instants are shown. For this geometry, the expressions for the flow variables can be obtained analytically, once $\widetilde{\eta}$ and $\langle u \rangle$ are known. Indeed, the second order surface elevation and the velocity field are obtained from the dimensional versions of equations (5.7) and (5.6), respectively. The dynamic pressure (p_{dyn}), on the other hand, is obtained from expression (3.158) after neglecting the hydrostatic contribution

$$p_{dyn} = \rho g \widetilde{\eta} + \rho \left(\widetilde{\chi_2|_{z=0}} - \chi_2 \right) \frac{\partial^2 \langle u \rangle}{\partial t \partial x}. \tag{5.9}$$

Panel *a* corresponds to $t = 87.6$ s, when the surface elevation is positive and experiences a positive acceleration. The second order surface elevation is concave,

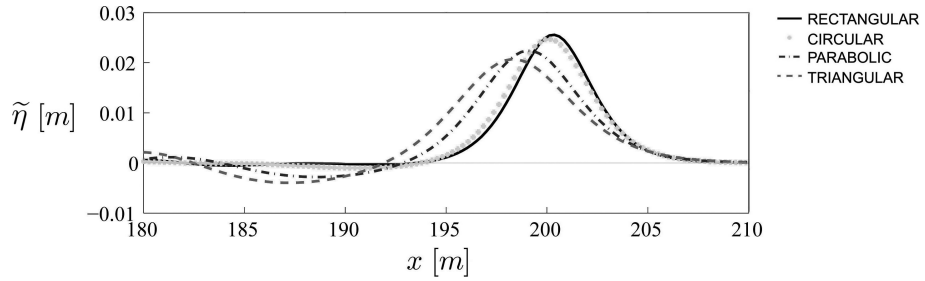

Figure 5.5: Surface elevations at $t = 88$ s generated with an initial Gaussian profile for four different cross-sections.

with maximum values at the sidewalls of $O\left(10^{-5}\right)$ which are significantly lower that the leading order solution $\widetilde{\eta}$, of $O\left(10^{-2}\right)$. Maximum dynamic pressures and velocities are found on the surface at the sidewalls, diminishing towards the deepest part of the channel. Panel *b* is obtained slightly later, at $t = 88.6$ s, when the surface elevation is decelerating. The second order surface elevation becomes concave with minimum values at the sidewalls. The pressure field is inverted, being larger toward the bottom of the channel while the velocities remain upward. Panel *c* is taken at $t = 90.7$ during an instant when the surface is descending rapidly. Here, the second order surface elevation is concave again, the dynamic pressure field increases upward and the velocity field is reversed downwards.

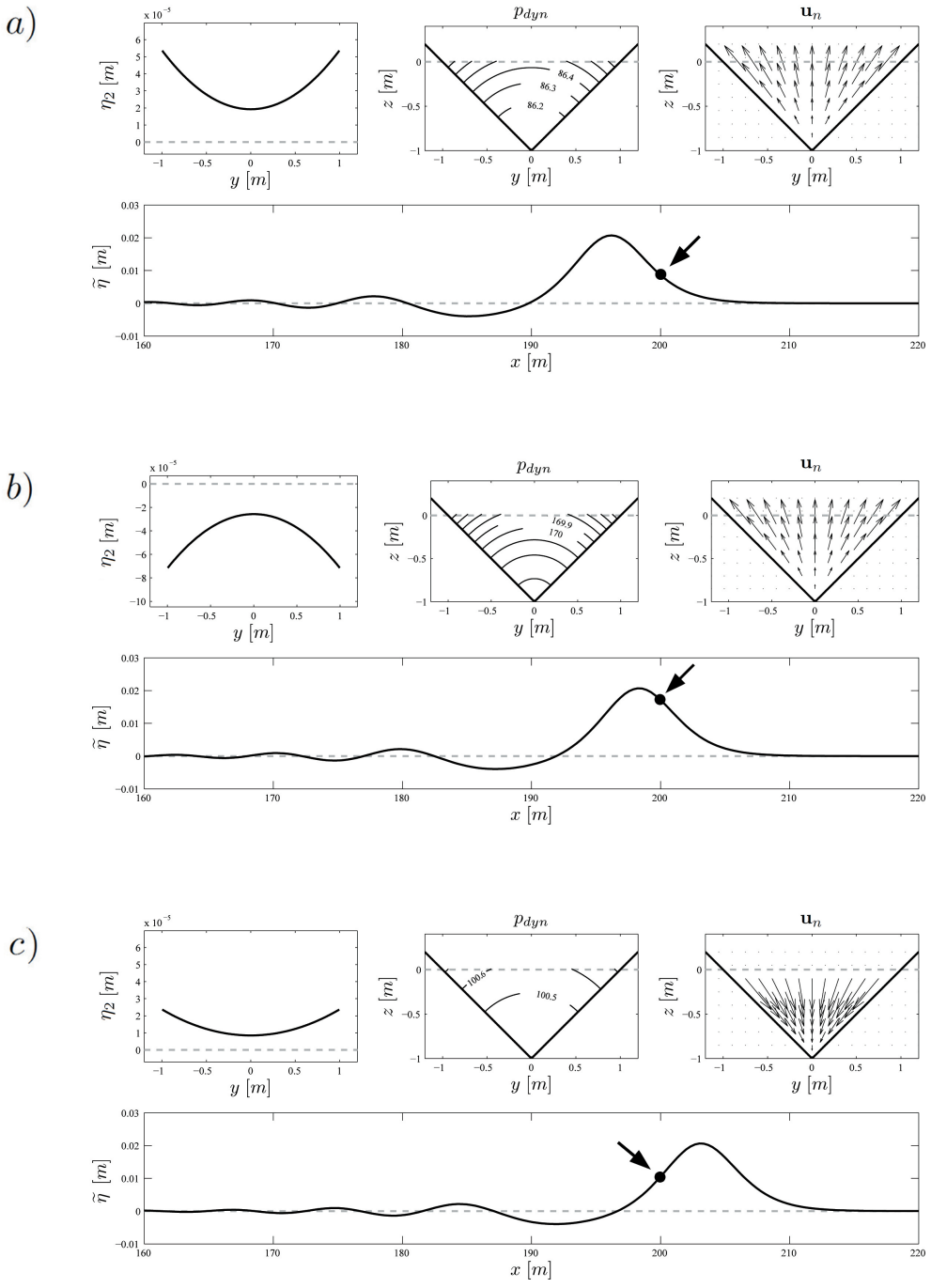

Figure 5.6: Initially Gaussian hump propagating on a triangular cross-section. Second order surface elevation η_2, dynamic pressure p_{dyn}, cross-sectional velocity field $\mathbf{u_n} = (v, w)$ and the surface-mean elevation $\widetilde{\eta}$, are depicted at *a*) $t = 87.6$ s, *b*) $t = 88.6$ s and *c*) $t = 90.7$ s. The channel is defined by $\breve{h} = 0.5$ m, $A_0 = 1$ m^2 and $B_0 = 1$ m. The initial Gaussian hump is defined by $\widetilde{\eta} = 0.05$ m and a standard deviation of $\sigma_{\widetilde{\eta}} = 2$ m.

5.2 Channel of slowly-varying width

Chang *et al.* (1979) (referred as C79 hereafter) presented laboratory data and numerical simulations for the evolution of solitary waves in a rectangular channel of constant depth and gradually varying width. Thirty-six experiments were conducted in converging and diverging channels with different initial nonlinearities. The experimental facility used by C79 is reproduced in Figure 5.7. Details of the experimental setup are found in Chang (1978).

In this section, experimental cases with depths of $\hat{h} = 0.2$ m for divergent channels and $\hat{h} = 0.3$ m for convergent channels are used to check the present theory. Results obtained from Teng & Wu's 1997 theory for slow-varying cross-sections (referred as TW97 hereafter), in which $\alpha, \beta = 0$ and $dA_0/dx = O(\epsilon)$, are also included for comparison. In the present theory, changes in the cross-sectional area are allowed to be significant within a wavelength, i.e. $dA_0/dx = O(1)$. Note that the effect of energy dissipation due to the wall boundary layer flows is ignored herein; it shall be investigated specifically for C79's experiments in section 6.4. For convenience, dimensional quantities denoted with hat are used in this section. For the convergent channel the width is defined as

$$\hat{B}_0(\hat{x}) = \begin{cases} 0.45, & -10 \le \hat{x} < 2.63 \\ 0.45 - 0.01875(\hat{x} - 2.63), & 2.63 \le \hat{x} < 23.96 \\ 0.05, & 23.96 \le \hat{x} < 48 \end{cases}$$

where $\hat{B}_0$ and $\hat{x}$ are expressed in meters. The computational domain is depicted in Figure 5.8. It is noted that in the laboratory measurements, dissipative materials were installed near the end of the converging channel to damp out waves (C79, Figure1). In the present numerical simulations, an additional channel section with uniform width is inserted in the region $\hat{x} \geqslant 23.96$ m to allow waves

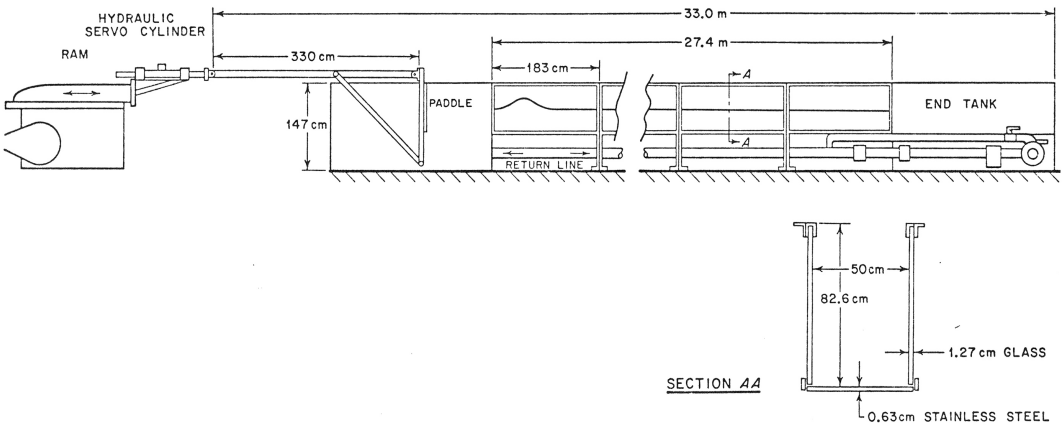

Figure 5.7: Experimental facility used by C79 (Chang, 1978).

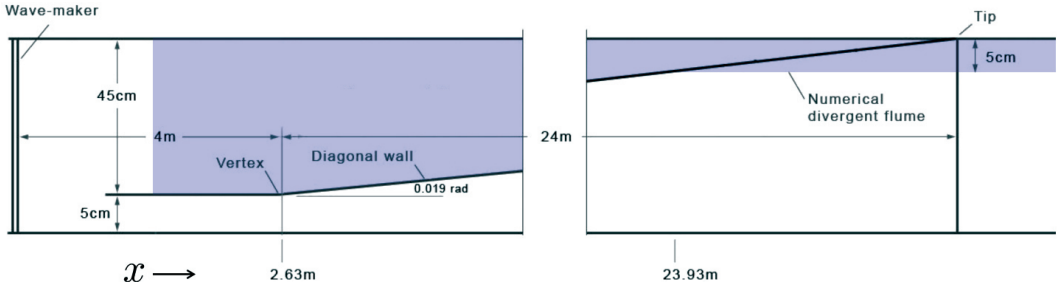

Figure 5.8: Definition of the geometrical domain used in the present calculations for C79's experiments on a convergent channel. The blue shaded area represents the computational domain.

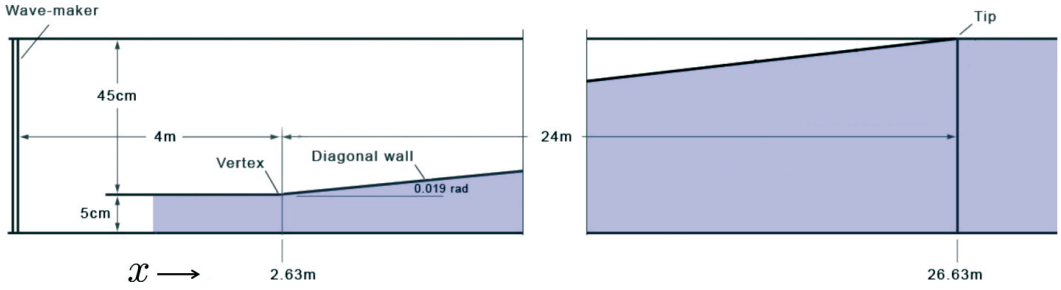

Figure 5.9: Definition of the geometrical domain used in the present calculations for C79's experiments on a divergent channel. The blue shaded area represents the computational domain.

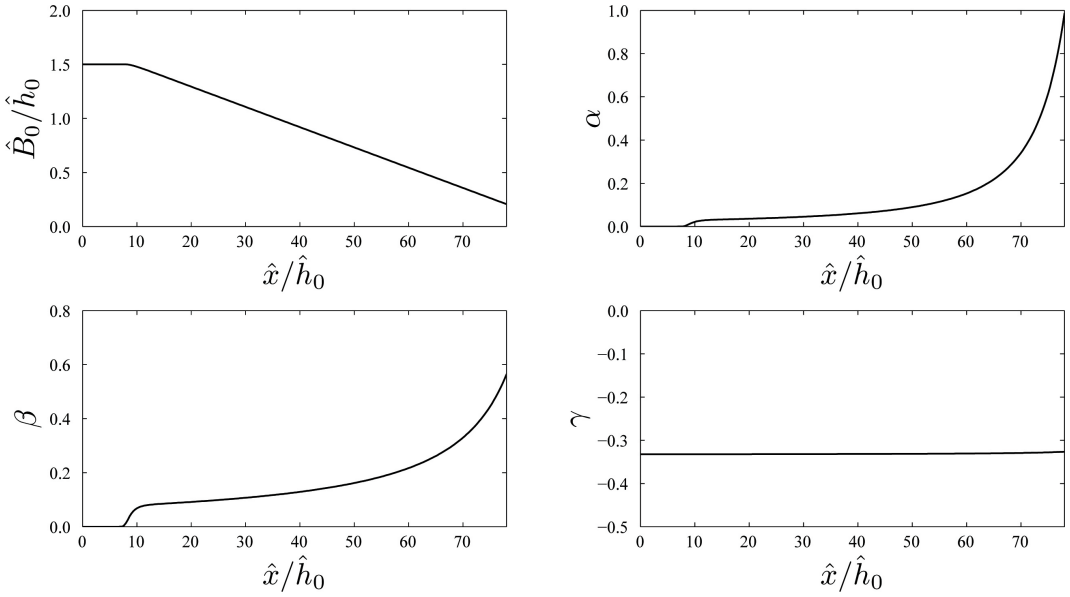

Figure 5.10: Width and coefficients in the momentum equation (3.124) along the linear converging channel used by C79 for an initial solitary wave of $\epsilon = 0.172$.

propagate out of the computational domain. In the divergent channel (Figure 5.9), the width is defined as

$$\hat{B}_0(\hat{x}) = \begin{cases} 0.05, & -10 \le \hat{x} < 2.63 \\ 0.05 + 0.01875(\hat{x} - 2.63), & 2.63 \le \hat{x} < 26.63 \\ 0.5, & 26.63 \le \hat{x} < 48 \end{cases}$$

The coefficients in the momentum equation (3.124) can be readily obtained from equation (3.137) once the geometry is prescribed. Figures 5.10 and 5.11 depict the results for the converging and diverging cases, respectively. The coefficient α is zero in the uniform section and rapidly increases (decreases) in the contraction (expansion) due to the dependence on B_0^{-2}. The coefficient β scales with B_0^{-1}, being it's sign determined by the rate of change of width in x. The dispersive coefficient γ remains constant as it depends solely on the depth.

The governing equations (3.95) and (3.124) are solved numerically using the

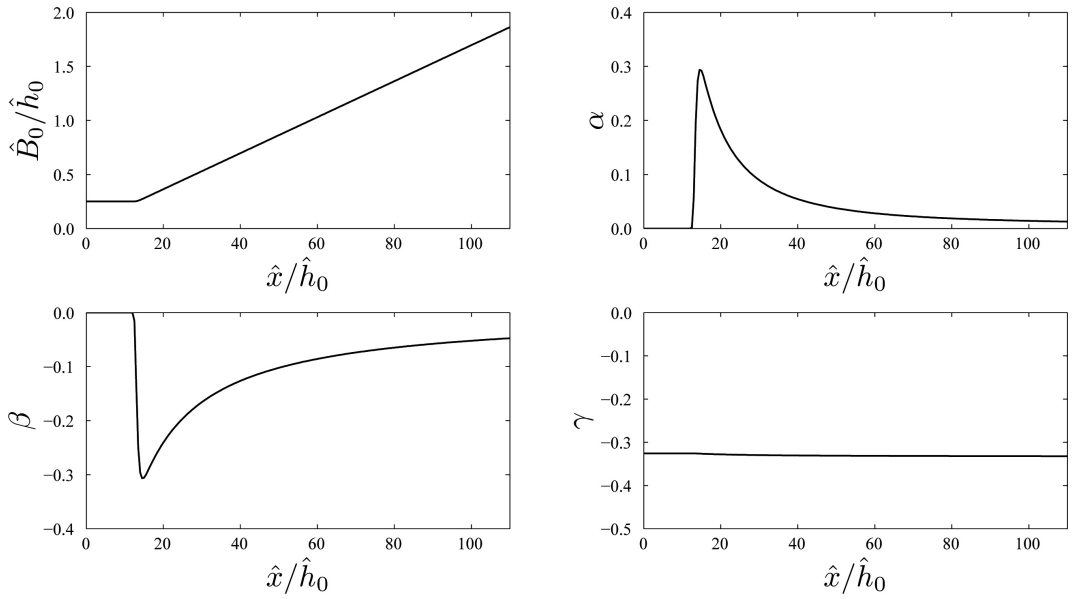

Figure 5.11: Width and coefficients in the momentum equation (3.124) along the linear diverging channel used by C79 for an initial solitary wave of $\epsilon = 0.259$.

fourth-order Adams-Bashforth-Moulton method developed by Wei & Kirby (1995), with minor modifications to account for the new terms of the present theory (Section 4.1). The scheme is found to conserve mass with high accuracy. As an example, for the linear converging channel and nonlinear parameter of $\epsilon = 0.052$, expression (4.37) at $\hat{t} = 12$ s, is $R(12) = 2.0\times10^{-7}$. For the linear diverging channel and nonlinear parameter of $\epsilon = 0.088$, $R(12) = 4.0 \times 10^{-17}$. Figure 5.12 depicts wave profiles every 1 s along the linear converging channel channel for an initial solitary wave of $\epsilon = 0.052$, along with the ratio R. Figure 5.13 depicts wave profiles every 1 s along the linear diverging channel channel for an initial solitary wave of $\epsilon = 0.052$, along with the ratio of the mass at time $\hat{t}$ and the initial mass, $\hat{m}/\hat{m}_0 = 1 - R$.

In C79, solitary waves were generated by a vertical bulkhead moving with the same velocity as that of fluid particles in the water column under a solitary

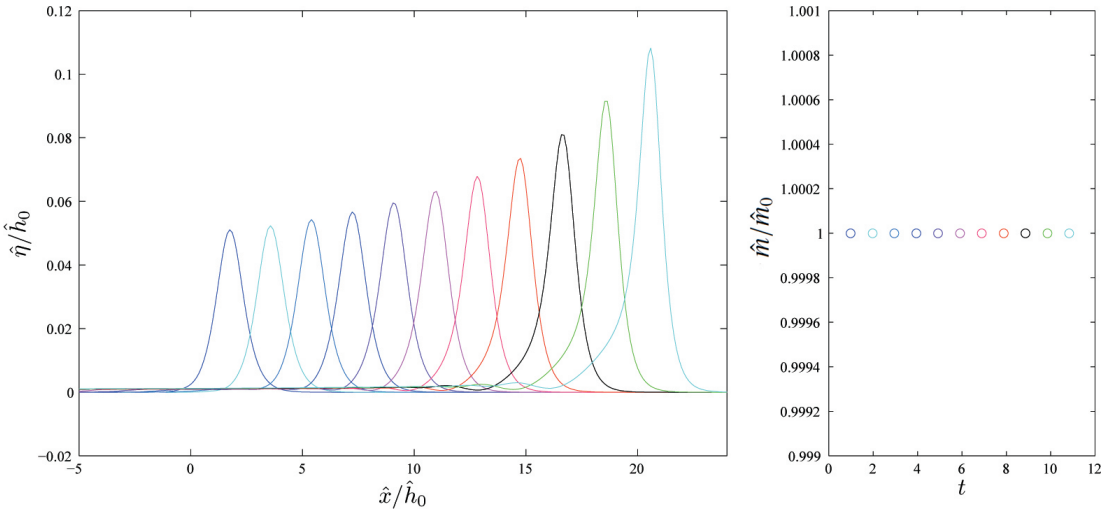

Figure 5.12: Left panel: Profiles every 1 s along the linear converging channel used by C79 for an initial solitary wave of $\epsilon = 0.052$. Right panel: ratio of the mass at time $\hat{t}$ and the initial mass.

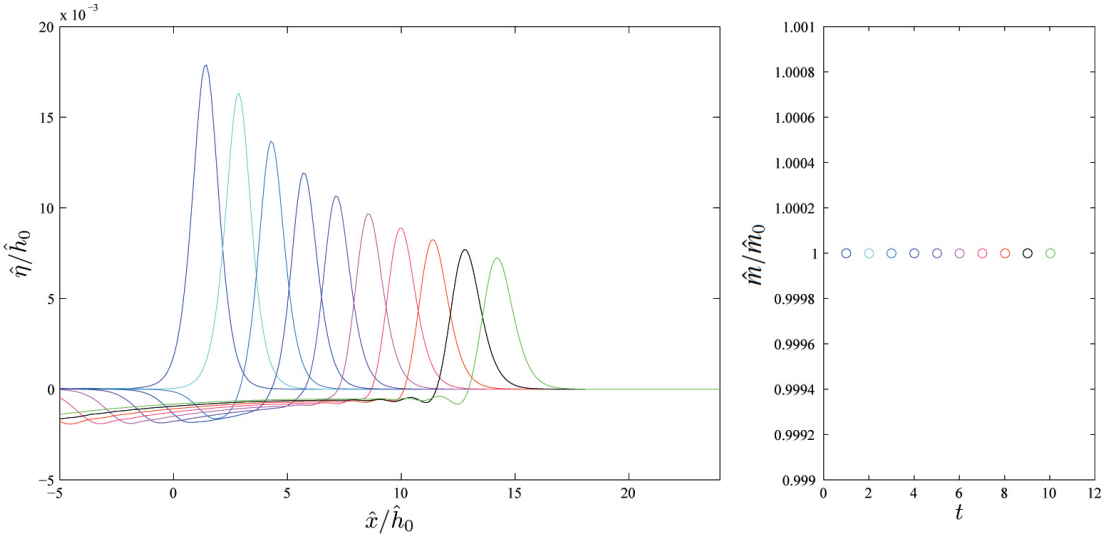

Figure 5.13: Left panel: Profiles every 1 s along the linear diverging channel used by C79 for an initial solitary wave of $\epsilon = 0.088$. Right panel: ratio of the mass at time $\hat{t}$ and the initial mass.

wave. In the present numerical experiments, the solitary wave solutions given in (5.3) and (5.4), are used as the initial conditions for different cases. For the converging channel, initial solitary waves with nonlinearity of ϵ = 0.052, 0.092, 0.142 and 0.174 are used. The wave crest is always located at $\hat{x}$ = 0. On the other hand, in the diverging channel, ϵ = 0.088, 0.185, and 0.259 are examined. The initial wave forms are also centered at $\hat{x}$ = 0. No-flux boundary conditions are applied at upstream and downstream boundaries, located sufficiently far from the converging section so they do not affect the solutions in the region of interest. It should be pointed out that sources of errors coming from digitizing the experimental data in C79's original paper remain unquantified.

5.2.1 Solitary wave in a converging channel

The left panel in Figure 5.14 depicts the evolution of the solitary wave with initial amplitude ϵ = 0.174. The wave profile gradually evolves from a solitary wave to an asymmetric profile of larger amplitude with a longer tail that increases with traveling distance, which was also observed in the laboratory experiments (C79, Figure 7). The long tail actually represents a portion of the reflected waves. Since the channel width changes slowly in the wavelength scale, incident wave is continuously and slowly reflected from the sidewalls. Therefore, the reflected wave does not have a sharp and identifiable wave crest. This can be better observed in Figure 5.12 for a smaller wave of ϵ = 0.052.

Although the amplitude of the reflected wave is almost negligible, the total amount of mass contained in it could be significant if the incident wave has traveled a long distance, i.e., many wavelengths. This was pointed out by Kirby

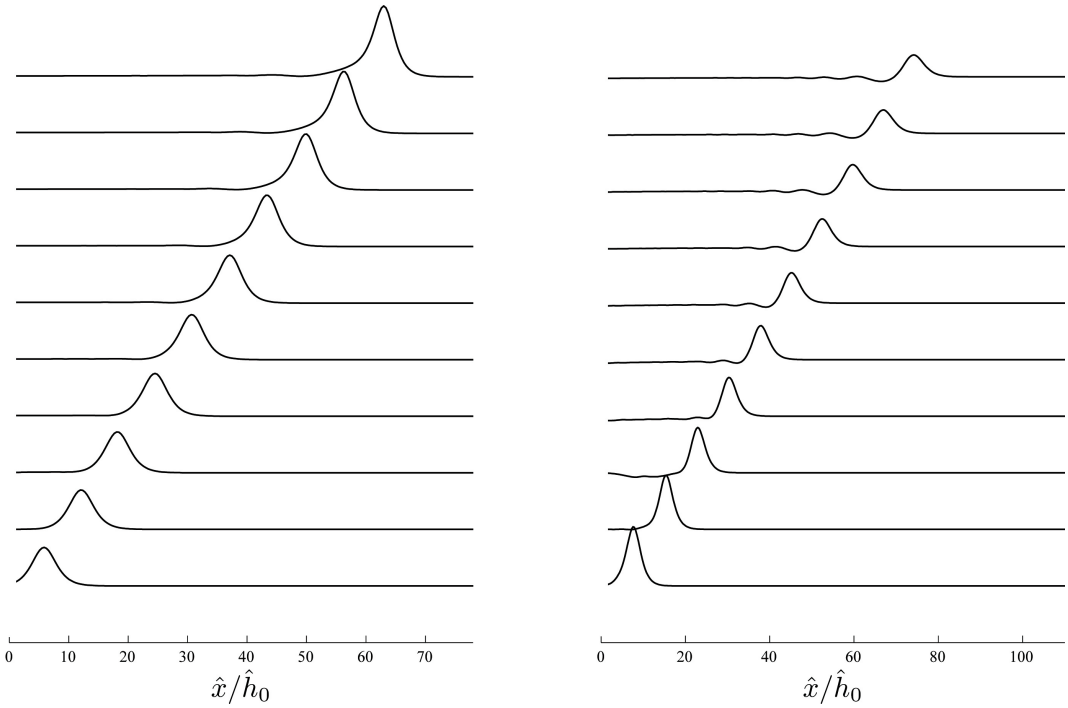

Figure 5.14: Instantaneous surface elevation for an initial solitary wave of $\epsilon = 0.174$ in a converging channel of $\hat{h} = 0.3$ m (left) and $\epsilon = 0.259$ in a diverging channel of $\hat{h} = 0.2$ m (right). Profiles are depicted every 1 s, from $\hat{t} = 1$ to 10 s.

& Vengayil (1988), who used a coupled system of KdV equations to study C79's experiments. However, since the Boussinesq-type equations used herein are solved numerically, the surface profiles shown in Figure 5.14 correspond to the total wave field and cannot be decomposed into the forward and backward wave components, as in Kirby & Vengayil (1988).

The left panel in Figure 5.15 shows the local amplitudes of the evolving waves, normalized by the local water depth, along the channel. Experimental and numerical results obtained with the present and TW97's theories are included. An increase in wave amplitudes along the channel is clearly observed as the consequence of the reduction in the width, which in the present theory is represented by the leading order term in the conservation of mass equation, i.e. $(h/B_0)(\overline{u}B_0)_x$,

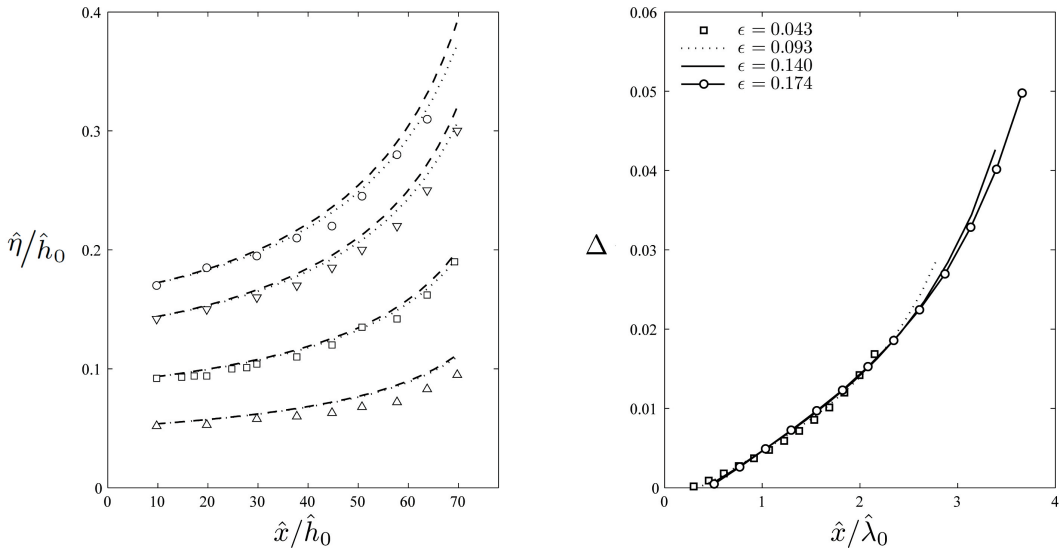

Figure 5.15: Numerical results for the linear converging channel with a mean water depth of $\hat{h}_0$ = 0.3 m used by C79 are shown. Left panel: Numerical solutions for the maximum surface elevations for initial solitary waves of ϵ = 0.043, 0.093, 0.140 and 0.174, obtained from the present model are depicted by dotted lines. Numerical results obtained from TW97's model are shown in dashed lines. Experimental data is denoted by triangles for ϵ=0.043, by squares for ϵ=0.093, by inverse triangles for ϵ=0.140, and by circles for ϵ=0.174. Right panel: Relative difference between two models are depicted along the channel.

and the second order terms associated with α and β in the momentum equation. The coefficients α and β grow significantly as the cross-section becomes narrower since they are proportional to B_0^{-2} and B_0^{-1}, respectively (equation 3.137). Both models consistently overestimate the maximum surface elevation along the channel, though the present model is slightly closer to the experimental data due to the effect of the terms associated with α and β. It is shown in section 6.4 that the introduction of viscous effects provide a much better agreement between the experiments and the present models.

The relative difference between the present and TW97 theories is presented in

the right panel of Figure 5.15. Note that the horizontal axis of this plot is normalized by the effective wavelength of the initial solitary wave. The relative difference is defined as

$$\Delta = \frac{(\eta)_{TW} - \eta}{\eta}, \tag{5.10}$$

where $(\eta)_{TW}$ represents the dimensionless free surface elevation obtained with TW97's theory. First of all, the differences are all positive throughout the entire process, implying that the higher order effects of a narrowing channel cross-section reduce the wave amplitude. In other words, the second order effects due to changes in the cross-section counterbalance the leading order shoaling effect. The relative differences tend to accumulate as the waves propagate along the channel, following similar curves that are weakly dependent on ϵ. Since the wavelength of a solitary wave decreases as the wave height increases, for a lager solitary wave the channel appears to be longer, resulting in a larger Δ value. For example, for the solitary wave of $\epsilon = 0.043$, $\Delta = 0.016$ at the end of the channel, where $\hat{x}/\hat{\lambda}_0 = 2.15$ and $\hat{\lambda} = 2\pi/\hat{K}$. On the other hand, for the largest solitary wave of $\epsilon = 0.174$, $\Delta = 0.050$ at $\hat{x}/\hat{\lambda}_0 = 3.66$.

5.2.2 Solitary wave in a diverging channel

Typical numerical results for an incident solitary wave of $\epsilon = 0.259$ in a diverging channel are shown in the right panel of Figure 5.14. It is clear that the amplitude of the main wave decreases as the channel cross-section widens; thus the dispersive effects become more important and accordingly a dispersive tail arises. These features were also reported by Chang *et al.* (C79, Figure 6).

The experimental measurements for the wave amplitudes along the diverging

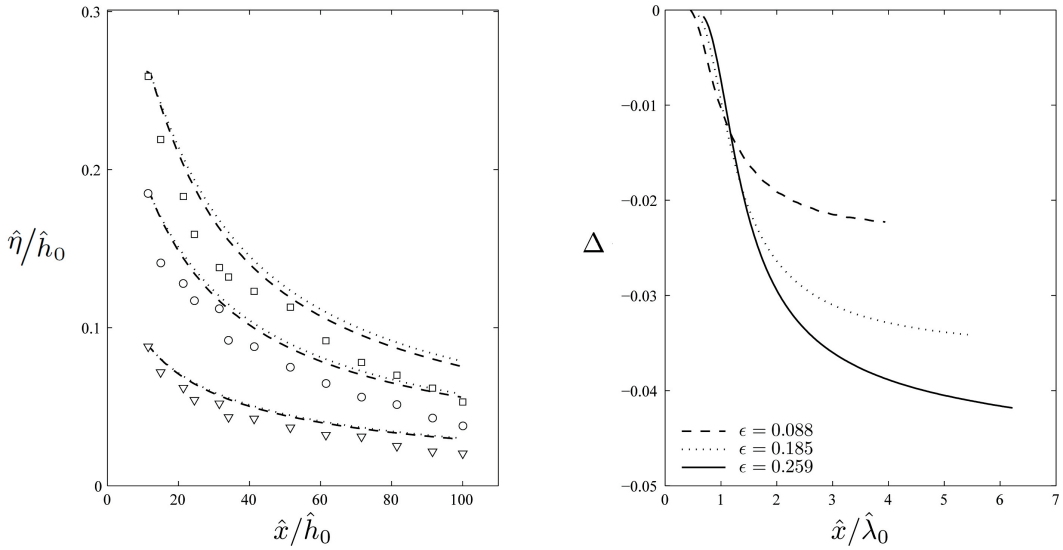

Figure 5.16: Numerical results for the linear diverging channel with a mean water depth of $\hat{h}_0$ = 0.2 m used by C79 are shown. Left panel: Maximum surface elevations for initial solitary waves of ϵ = 0.088, 0.185, and 0.259 obtained from the present model are denoted by dotted lines. Numerical results obtained from TW97's model are shown in dashed lines. Experimental data is shown in triangles for ϵ = 0.088, circles for ϵ = 0.185 and squares for ϵ = 0.259. Right panel: The relative differences between two models along the channel are shown; the distance is normalized by the effective wavelength of the incident solitary wave.

channel are plotted on the left panel of Figure 5.16 (left), together with the numerical results obtained from the present and TW97 theories. Though both theories overestimate the surface elevation along the channel, TW97's theory appears to match experimental data better. The comparison of theories shows that the contributions from the terms associated with α and β cause increases in the amplitudes, and they tend to be stronger with higher nonlinearity. The difference between theories and experimental data is indeed larger than those for the converging case. Viscous effects indeed play a significant role in this case, as is later shown in Section 6.4.

The right panel of Figure 5.16 shows that the relative differences between theories increase with longer traveling distance and stronger nonlinearity. Negative values of Δ imply the present theory provide larger values than TW97 due to the new terms. For example, for the smallest solitary wave of $\epsilon = 0.088$ $\Delta = 0.022$ at the end of the channel where the wave has travelled roughly 3.94 wavelengths in distance. In the case of the largest wave of $\epsilon = 0.259$ a larger difference between theories is observed, i.e., $\Delta = 0.041$ at $\hat{x}/\hat{\lambda}_0 = 6.19$, since the wave has travelled a longer distance with respect to the incident wave wavelength.

In C79's experiments, only slowly-varying cross-sections are considered. Consequently, the contributions of the new terms containing α and β are small, thus both the present and TW97's theories provide similar results. The following section shows results for a channel where the cross-section varies significantly within a wavelength.

5.3 Straight channel with a rapid contraction

Numerical experiments are performed in a channel with a rapid contraction, where the new terms containing α and β in the present theory become significant. Since no laboratory experiments for such conditions can be found in the literature, the analysis is focused in the comparison between the present and TW97's theories. In the numerical simulations, rectangular and triangular cross-sections are compared to evaluate the effects of the new coefficients and the sidewall slope in the wave properties. To compare results, the mean depth $\breve{h} = A_0/B_0$ and the surface width B_0 are the same for both geometries at any x throughout the domain.

For a linear contraction, the surface width is defined by

$$B_0 = \begin{cases} 3.\overline{3} & -33.\overline{3} \le x < 33.\overline{3} \\ 9.6 - 0.188x & 33.\overline{3} \le x < 50 \\ 0.2 & 50 \le x < 100 \end{cases}$$

where the width B_0 and depth x are normalized by the depth. The maximum and minimum depth-to-width ratios are chosen as $B_0 = 3.\overline{3}$ at the entrance and $B_0 = 0.2$ at the end of the contraction, satisfying the assumption of comparable depth and widths. With these values, the change of channel width is appreciable within a wavelength, i.e. $dA_0/dx = O(1)$. As an example, the width and coefficients in the momentum equation for a rectangular channel given by (3.137) are depicted in Figure 5.17. Coefficients α and β are zero in the uniform portion of the channel and increase in the contraction as the section becomes narrower. Compared to the slowly-varying case, the magnitudes of these coefficients are one to two orders of magnitude larger, thus their contributions are expected to be more relevant. The coefficient γ is a constant throughout the channel.

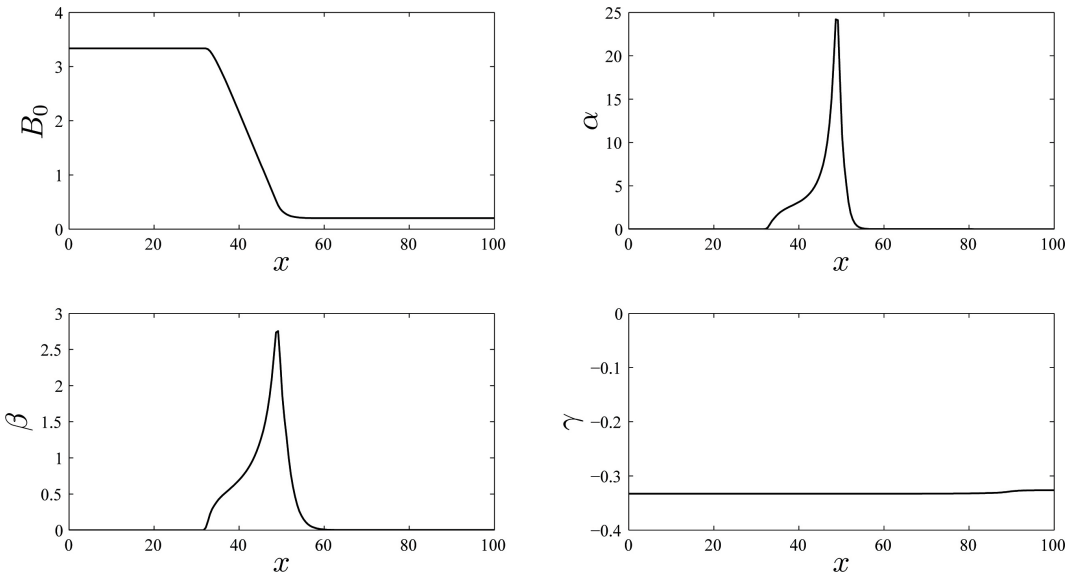

Figure 5.17: Channel width and coefficients in the momentum equation along a uniform rectangular channel with a rapid contraction.

For the rectangular cross-sections, solitary waves with amplitudes of $\epsilon = 0.05$ and 0.1, centered at $x = 0$, are used as initial conditions for the numerical experiments. Figure 5.18 (left) shows the comparison of the maximum surface elevation along the channel, obtained by the present and TW97's theories. As expected, the reduction of the cross-section induces a significant increase in the surface elevation during and after the transition, asymptotically approaching a constant value far downstream from the contraction ($x > 100$). The contributions of the new terms associated with α and β counteract the leading order amplification caused by the contraction of the channel. The results predicted by the new theory tend to be lower than those of TW97.

The differences between models shown in the right panel of Figure 5.18 (right) increase as the wave propagate along the channel. They also increase with larger waves. For instance, for $\epsilon = 0.05$, $\Delta = 0.04$ and for $\epsilon = 0.01$, $\Delta = 0.07$ at the end of the channel, respectively. Note that in these cases the channel transition length

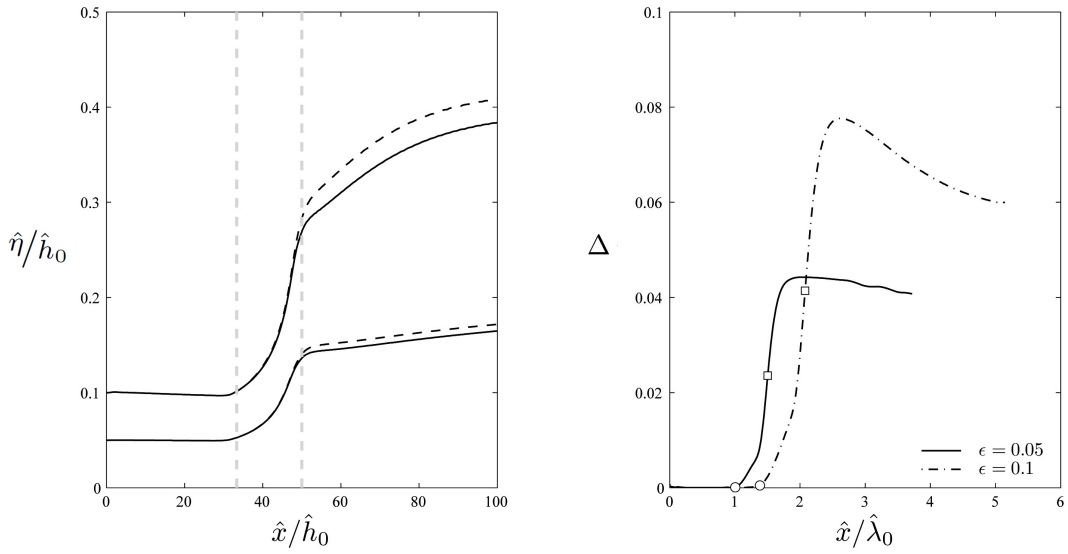

Figure 5.18: Numerical results for a rectangular channel with a rapid contraction. (left) Maximum surface elevation for initial solitary waves of ϵ=0.05 and 0.10. The present theory is depicted in solid lines and TW94's theory in dashed lines. Vertical dashed gray lines denote the initiation and end of the contraction. (right) Relative difference between theories are depicted in terms of relative wavelengths. Circles denote the initiation and squares the end of the contraction.

is roughly one-half of a wavelength. Although the values of Δ are comparable to those shown in the slowly-varying channels, the length of the channel contraction section in terms of the wavelength is much shorter.

For the triangular channel, the effect of sidewall slope also plays a role in determining wave evolution. Indeed, the term associated with B_0' appears in the continuity equation, whereas the coefficients given by equations (3.144) to (3.146) are reduced to

$$\alpha = \left(\frac{1}{16} - \frac{H^2}{3B_0^2}\right)\left(\frac{dB_0}{dx}\right)^2, \qquad \beta = \left(\frac{B_0}{16} - \frac{H^2}{3B_0}\right)\frac{dB_0}{dx}, \qquad \gamma = \frac{B_0^2}{48} - \frac{H^2}{3}. \tag{5.11}$$

As seen in Figure 5.19 (left), the wave shoaling in the triangular channel is milder than that in the rectangular one. The relative differences depicted in Fig-

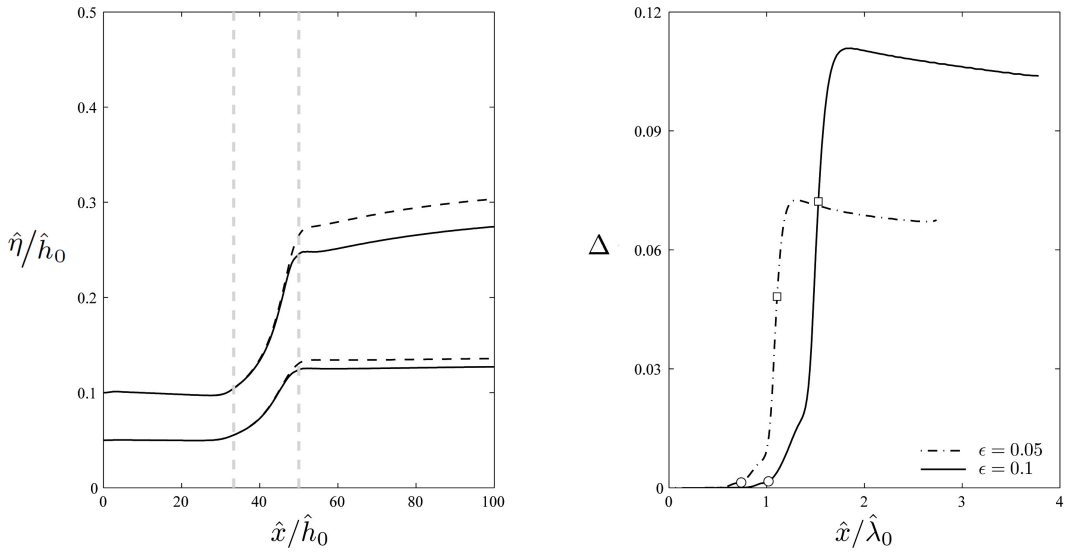

Figure 5.19: Numerical results for a triangular channel with a rapid contraction. (left) Maximum surface elevation for initial solitary waves of ϵ=0.05 and 0.10. The present theory is depicted in solid lines and TW94's theory in dashed lines. Vertical dashed gray lines denote the initiation and end of the contraction. (right) Relative difference between theories are depicted in terms of relative wavelengths. Circles denote the initiation and squares the end of the contraction.

ure 5.19 (right) range between $\Delta = 0.07$ and $\Delta = 0.11$ at the end of the channel for $\epsilon = 0.05$ and 0.01, respectively. These values are larger than the corresponding cases in the rectangular channel.

Figure 5.20 depicts the instantaneous surface elevation for an initial solitary wave in rectangular and triangular cross-sections. The initial profiles are slightly different as the effective wave number K is a function of the cross-sectional geometry. As waves move through the channel contraction, they experience an increase in the surface elevation, evolving from a solitary to an asymmetric profile, followed by a dispersive tail. At the same time small waves are reflected back from the channel contraction, reaching $\hat{x}/\hat{h}_0 = 0$ at $\hat{t} = 15 - 17$ s. The reflected waves are more detectable since the channel width changes

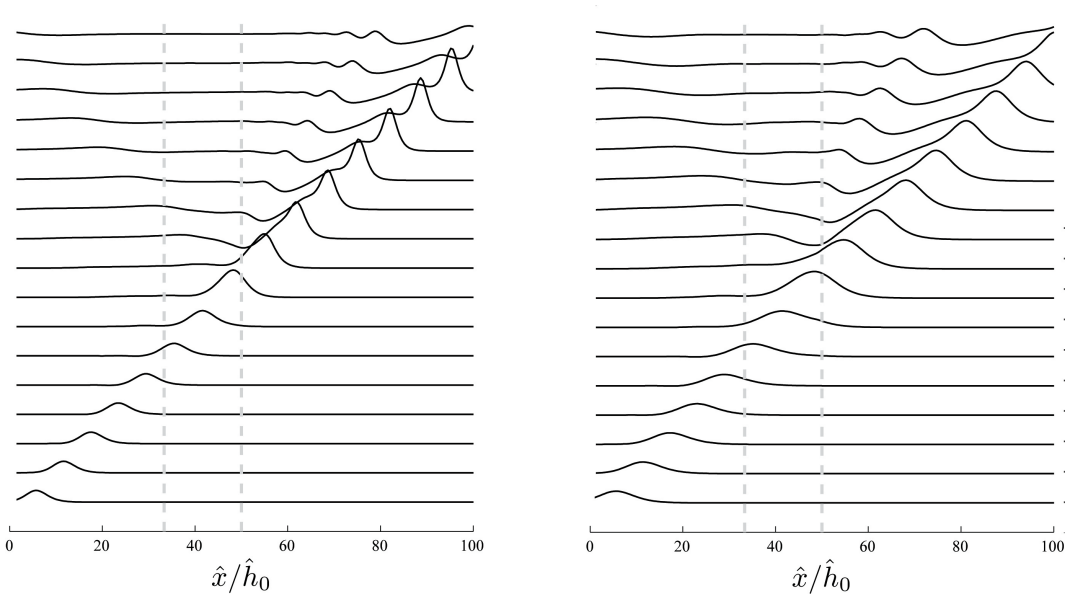

Figure 5.20: Instantaneous surface elevation for an initial solitary wave of $\epsilon = 0.05$ in a rectangular (right) and a triangular (right) cross-section of equivalent depth $\hat{h} = 0.3$ m. Profiles are depicted every 1 s, from $\hat{t} = 1$ to 17 s. Vertical dashed grey lines denote the initiation and end of the contraction.

appreciably within the wavelength scale. The main wave grows stronger in the rectangular cross-section channel, whereas the trailing wave train has larger amplitudes in the triangular channel.

These results suggest that the choice of theory becomes relevant in the estimation of wave parameters when changes in the cross-section of $dA_0/dx = O(1)$ occur within a wavelength. The differences between both theories is strongly dependent on the nonlinearity, the cross-sectional geometry and the ratio between the typical length of the contraction and the wavelength.

CHAPTER 6

VISCOUS EFFECTS

The theory derived in Chapter 3 is suitable for potential flows where gravity acts as the main driving force in the flow. In real situations however, many other forces exist among which bottom friction, surface wind stress, Coriolis stress, tidal rising force, turbulent stresses and atmospheric pressure gradients may be relevant in long-wave modeling. A comprehensive review of these forces are analyzed in Tan (1992) and Liu (2010).

The effects of laminar boundary layer flows adjacent to the channel boundary are added herein in the cross-sectional averaged continuity equation. This approach was developed by Liu & Orfila (2004) for the bottom boundary layer and was extended in Liu *et al.* (2006) to consider the viscous damping of a solitary wave propagating in a rectangular channel, in which both bottom and sidewall boundary layers are considered. This approach is appropriate for small-scale experiments where the boundary layer is either laminar or turbulent and the eddy viscosity is constant. For large-scale phenomena where breaking or turbulent process become relevant, other approaches have to be pursued.

Following the approach suggested by Liu & Orfila (2004), the effects of viscous boundary layer flows on wave damping are introduced in Section 6.1. The computation of the additional term in the equation of conservation of mass due to the viscous effects is explained in Section 6.2. Section 6.3 compares the numerical solutions with laboratory experiments for solitary wave shoaling on a sloping beach (Liu *et al.*, 2006). Chang *et al.*'s (1979) experiments are revisited using the model with viscous effects in Section 6.4.

6.1 Heuristic approach to include viscous effects

It is known from the literature that the viscous effects may become important in small-scale laboratory experiments (e.g., Liu *et al.* 2006). Indeed, Figures 5.15 and 5.16 show the large discrepancies between the theoretical predictions and experimental measurements. Both Chang *et al.* (1979) and Kirby & Vengayil (1988) suggested that these discrepancies are caused by the lack of considering viscous dissipation. Liu & Orfila (2004) showed that the viscous effects generate a flow deficit in the wave propagation direction at the bottom boundary layer, which induces mass fluxes into the core region where Boussinesq-type equations are solved. Consequently, in deriving the cross-sectional averaged equation for conservation of mass, additional mass fluxes along the outer edge of the boundary layer must be added.

Using an heuristic argument based on Liu & Orfila's idea, the inclusion of the viscous effects is presented in Appendix E, from which the main results are summarized herein. The cross-sectional averaged equation for mass conservation for the core region where the flow is assumed irrotational, (3.58), can be modified as

$$\frac{1}{\epsilon}\frac{\partial A}{\partial t} + \frac{\partial}{\partial x}\left(\langle u\rangle A\right) = \frac{\delta}{\mu}U_{\varsigma}, \tag{6.1}$$

where

$$\delta^2 = \frac{\hat{\nu}}{\hat{\lambda}\sqrt{\hat{g}\hat{h}_0}}, \tag{6.2}$$

is the constant eddy viscosity, which can be viewed as the inverse of the Reynolds number. The coordinate ς represents the normal to the bottom boundary, as shown in Figure 6.1. It is assumed that $\delta = O\left(\epsilon^2, \mu^4\right)$ is added to the Boussinesq approximation $\varepsilon = O\left(\mu^2\right) \ll O(1)$, so that the viscous effects are

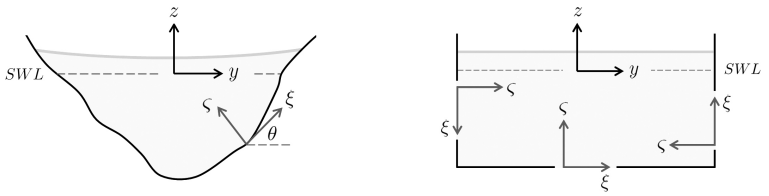

Figure 6.1: Definition of local coordinates for *a*) an arbitrary and *b*) rectangular cross-sections.

slightly weaker than the frequency dispersion and non-linear effects, but not too small to be neglected. The total flux being transferred from the boundary layer to the core region becomes

$$U_\varsigma(x,t) = -\frac{1}{\sqrt{\pi}}\int_0^R \mathcal{H}(\theta)\,ds \times \int_0^t \frac{\langle u\rangle_x(x,\tau)}{\sqrt{t-\tau}}d\tau, \tag{6.3}$$

where

$$\mathcal{H}(\theta) = \frac{\sqrt{\left(\frac{\partial\varsigma}{\partial y}\right)^2 + \left(\frac{\partial\varsigma}{\partial z}\right)^2}}{\frac{\partial\varsigma}{\partial y}\sin\theta - \frac{\partial\varsigma}{\partial z}\cos\theta}, \tag{6.4}$$

is a function that depends on the geometry of the cross-section and $\langle u\rangle_x$ is the spatial gradient of the cross-sectional averaged longitudinal velocity. Using the expression for the area (3.35) in (6.1) yields

$$\begin{aligned}\frac{\partial\widetilde{\eta}}{\partial t} + \frac{1}{B_0}\frac{\partial}{\partial x}\left(\langle u\rangle A_0\right) + \epsilon\frac{B_0'}{2B_0}\frac{\partial\widetilde{\eta}^2}{\partial t} + \frac{\epsilon}{B_0}\frac{\partial}{\partial x}\left(\langle u\rangle B_0\widetilde{\eta}\right)\\ + \frac{\delta}{\mu B_0}\frac{1}{\sqrt{\pi}}\int_0^R \mathcal{H}(\theta)\,ds \times \int_0^t \frac{\langle u\rangle_x(x,\tau)}{\sqrt{t-\tau}}d\tau &= O\left(\epsilon^2, \epsilon\mu^2, \mu^4\right).\end{aligned} \tag{6.5}$$

In dimensional form, the above becomes

$$\begin{aligned}\frac{\partial\hat{\widetilde{\eta}}}{\partial\hat{t}} + \frac{1}{\hat{B}_0}\frac{\partial}{\partial\hat{x}}\left(\langle\hat{u}\rangle\hat{A}_0\right) + \frac{\hat{B}_0'}{2\hat{B}_0}\frac{\partial\hat{\widetilde{\eta}}^2}{\partial\hat{t}} + \frac{1}{\hat{B}_0}\frac{\partial}{\partial\hat{x}}\left(\langle\hat{u}\rangle\hat{B}_0\hat{\widetilde{\eta}}\right)\\ + \sqrt{\frac{\nu}{\pi}}\frac{1}{\hat{B}_0}\int_0^{\hat{R}}\mathcal{H}(\theta)\,ds\int_0^{\hat{t}}\frac{\langle\hat{u}\rangle_{\hat{x}}}{\sqrt{\hat{t}-\tau}}d\tau &= 0.\end{aligned} \tag{6.6}$$

The cross-sectional averaged momentum equation (3.124) remains unchanged. For example, for a rectangular channel as shown in Figure 6.1, the total flux

being transferred from the boundary layer to the core region becomes

$$U_{\varsigma}(x,t) = \frac{B_0 + 2h}{\sqrt{\pi}} \int_0^t \frac{\langle u \rangle_x (x,\tau)}{\sqrt{t-\tau}} d\tau, \tag{6.7}$$

thus

$$\begin{aligned} \frac{\partial \widetilde{\eta}}{\partial t} + \frac{1}{B_0}\frac{\partial}{\partial x}\left(\langle u \rangle A_0\right) + \frac{\epsilon}{B_0}\frac{\partial}{\partial x}\left(\langle u \rangle B_0 \widetilde{\eta}\right) & \\ -\frac{\delta}{\mu}\frac{1}{\sqrt{\pi}}\left(1 + \frac{2h}{\hat{B}_0}\right)\int_0^t \frac{\langle u \rangle_x (x,\tau)}{\sqrt{t-\tau}} d\tau &= O\left(\epsilon^2, \epsilon\mu^2, \mu^4\right). \end{aligned} \tag{6.8}$$

In dimensional form, the above becomes

$$\frac{\partial \hat{\widetilde{\eta}}}{\partial \hat{t}} + \frac{1}{\hat{B}_0}\frac{\partial}{\partial \hat{x}}\left(\langle \hat{u} \rangle \hat{A}_0\right) + \frac{1}{\hat{B}_0}\frac{\partial}{\partial \hat{x}}\left(\langle \hat{u} \rangle \hat{B}_0 \hat{\widetilde{\eta}}\right) - \sqrt{\frac{\nu}{\pi}}\left(1 + \frac{2\hat{h}}{\hat{B}_0}\right)\int_0^{\hat{t}} \frac{\langle \hat{u} \rangle_{\hat{x}}}{\sqrt{\hat{t}-\tau}} d\tau = 0. \tag{6.9}$$

6.2 Numerical integration of the convolution integral

The fourth-order Adams-Bashforth-Moulton method introduced in Section 4 is extended to solve the governing equations (6.5) and (3.124), with a slight modification to account for the convolution integral in the viscous term. This integral is finite given that $\langle u \rangle_x$ is a smooth function, but the integrand has a singularity at $\tau = t$. To handle this singularity, the integral is approximated by

$$\begin{aligned} \int_0^t \frac{\langle u \rangle_x (x,\tau)}{\sqrt{t-\tau}} d\tau &= \int_0^{t_1} \frac{\langle u \rangle_x (x,\tau)}{\sqrt{t-\tau}} d\tau + \int_{t_1}^t \frac{\langle u \rangle_x (x,\tau)}{\sqrt{t-\tau}} d\tau \\ &\approx \int_0^{t_1} \frac{\langle u \rangle_x (x,\tau)}{\sqrt{t-\tau}} d\tau + \langle u \rangle_x (x,t_1) \int_{t_1}^t \frac{d\tau}{\sqrt{t-\tau}} \\ &\approx \int_0^{t_1} \frac{\langle u \rangle_x (x,\tau)}{\sqrt{t-\tau}} d\tau + 2\langle u \rangle_x (x,t_1)\sqrt{t-t_1}. \end{aligned} \tag{6.10}$$

The first integral requires the entire series of values of $\langle u \rangle_x$ to be recorded at each mesh point in all times. This introduces a limitation in the grid size for memory reasons. The discretization of (6.10) yields

$$\int_0^t \frac{\langle u \rangle_x (x,\tau)}{\sqrt{t-\tau}} d\tau \approx \sum_{n=0}^{N_n} \frac{\langle u \rangle_x (i,n)}{\sqrt{t-\tau_n}} \triangle\tau + 2\langle u \rangle_x (i,n_{t1})\sqrt{t-t_1}, \tag{6.11}$$

where the first integral is computed using the Gauss-Quadrature method. The algorithm (*convolution.m*) was tested for a simple case where $\langle u \rangle_x = 1$ with 5 quadrature points, as shown in Figure 6.2. For actual computation of solitary wave in channels, 30 quadrature points were used and the upper limit of the integral t_1 was set so $t - \tau = 0.9\Delta t$, after a convergence test.

6.3 Solitary waves in the shoaling zone

The theory is compared to experimental data by Liu *et al.* (2006) in a rectangular channel with a sloping beach. Experiments were performed in the 32 m long, 0.6 m wide and 0.9 m deep wave tank in the DeFrees Hydraulics Laboratory at Cornell University. The channel consists of an initial uniform rectangular cross-section of water depth $\hat{h} = 0.15$ m and a 1:20 sloping glass beach. Surface elevations were recorded at 6 locations with a constant spacing of 2.5 m in the constant depth region and of approximately 0.5 m in the shoaling zone. Figure 6.3 depicts the experimental setup by Liu *et al.* (2006). Several solitary waves with different wave amplitudes were generated. At $\hat{x} = 6.5$ m from the wave-maker solitary waves with $\epsilon = 0.091$, 0.174, 0.270, 0.352, and 0.409 were measured. In the numerical simulations, the water depth is defined by

$$\hat{h} = \begin{cases} 0.15 & -10 \le \hat{x} < 19.88 \\ 1.144 - 0.05\hat{x} & 19.88 \le \hat{x} < 22 \\ 0.044 & 22 \le \hat{x} \le 32 \end{cases}$$

where $\hat{h}$ and $\hat{x}$ are expressed in meters. A section of constant depth for $\hat{x} \ge 22$ *m*, nonexistent in the physical experiments, is considered to avoid unfeasible wave heights at shallow depths.

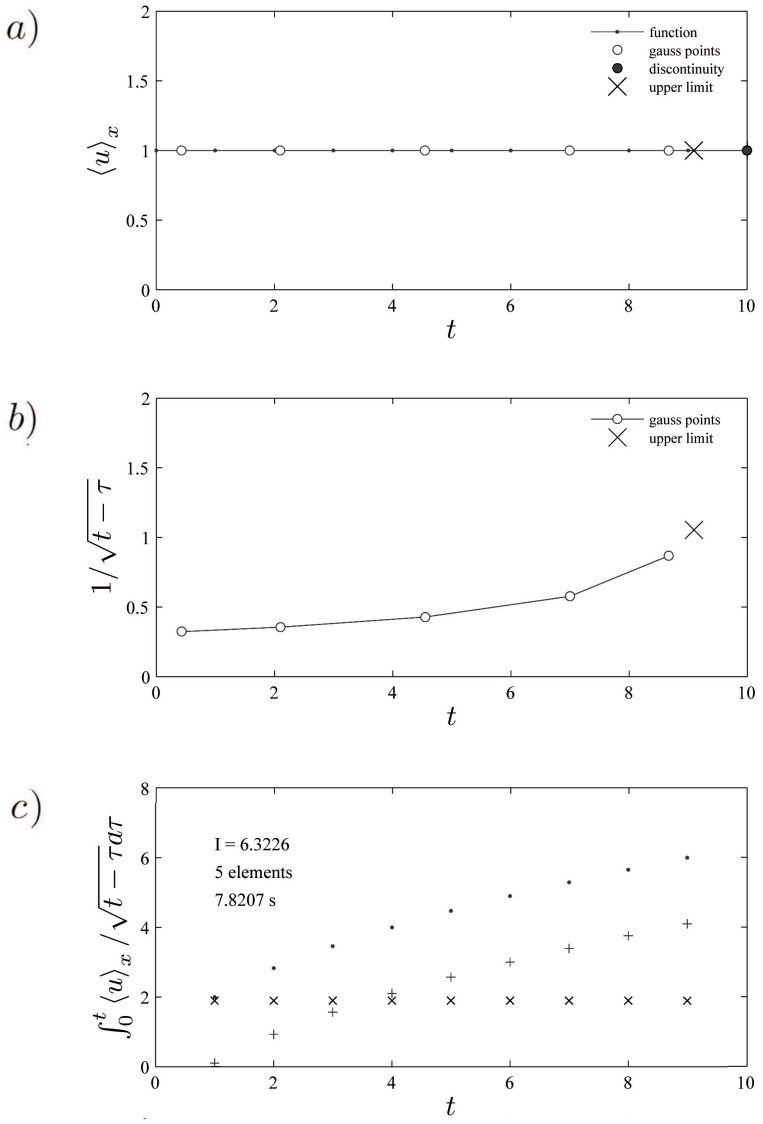

Figure 6.2: Example of computation of the convolution integral. *a*) The function to be integrated, $\langle u \rangle_x = 1$. Points used for the Gaussian quadrature, the upper limit t_1 and the discontinuity were $t = \tau$ are shown. *b*) Sampling function. *c*) The computation of the integral (6.11) is shown in dots. The first term of (6.11) is shown in + and the second term in *x*.

According to Sumer *et al.*'s (2010) classification, the experiments for solitary waves remained far from turbulent regimes where three-dimensional phenomena may occur. This is consistent with the assumption of constant eddy viscosity made by Liu & Orfila's (2004).

Since the channel cross-section remains a constant, the cross-sectional averaged equation of mass conservation (6.8), can be simplified to be

$$\frac{\partial \widetilde{\eta}}{\partial t} + \frac{\partial}{\partial x}\left(\langle u\rangle\left[h + \epsilon\widetilde{\eta}\right]\right) - \frac{\delta}{\mu}\frac{1 + 2h/B_0}{\sqrt{\pi}}\int_0^t \frac{\langle u\rangle_x(x,\tau)}{\sqrt{t-\tau}}d\tau = 0. \tag{6.12}$$

The coefficients in the momentum equation, (3.124), are defined by (3.136). Note that $\alpha = 0$ throughout the domain, whereas $\beta = 0$ in the constant depth region and decreases over the slope ($\beta \sim h$). Thus, without considering the viscous effects, TW97's and the present theory are the same in the uniform section and differ by the term associated with β in the shoaling zone. The dispersive term scales as $\gamma \sim h^2$, becoming smaller in shallower waters.

Solitary waves were generated in the experiments with a piston-type hydraulically driven wave-maker. Therefore, initial conditions given by (5.3) and (5.4) are used in the present numerical computations. The comparisons between the experiments and numerical results are presented in Figure 6.4. Both the present

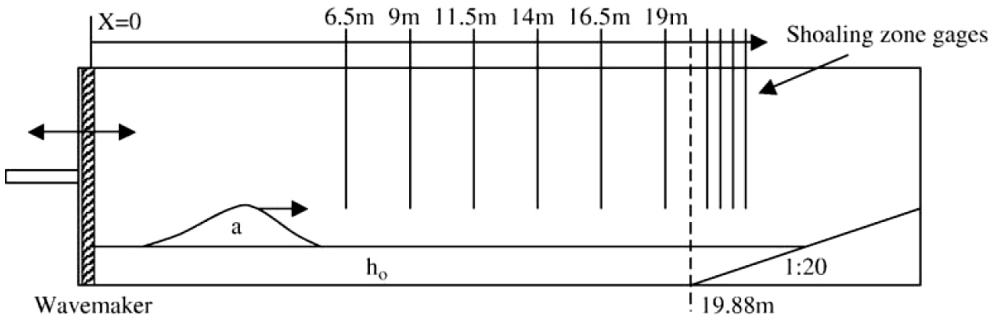

Figure 6.3: Experimental setup by Liu *et al.* (2006), showing the location of wave gages in the constant depth region.

theory and TW97's theory with viscous effects are computed. Results are shown as the difference between the local wave height and the corresponding value at the first measuring station located at $\hat{x} = 6.5$ m. For convenience, this difference is defined as

$$\nabla = \eta - (\eta)_{6.5} \,. \tag{6.13}$$

Numerical results from both theories are identical and compare reasonably well with the experimental data in the constant depth section; experimental amplitudes are slightly above the predicted curves. The amplitude decays almost linearly along the uniform section of the flume. In the shoaling zone, the results of the present theory are in much better agreement with the experimental data because it considers the effects of beach slope accurately. There are exceptions for smaller waves ($\epsilon = 0.091$ and 0.174) where TW97's modified theory better resolves the shoaling process. As the nonlinearity increases the wavelength of the solitary wave becomes shorter. Consequently, the beach slope effects also become more important. The second order contributions of the terms containing α and β tend to counteract the leading order effect of shoaling by means of a reduction in the surface elevation.

Relative differences between the present and TW97's modified theories also become more significant for larger waves, as shown in Figure 6.5. A relative difference between theories of $\Delta = 0.03 \sim 0.1$ appear over the sloping beach for different wave amplitudes. In conclusion, the present theory with consideration of viscous effects in the bottom boundary layer properly predicts the wave amplitude along the uniform section of the flume and provides a good estimation in the shoaling zone for relatively high values of the nonlinearity.

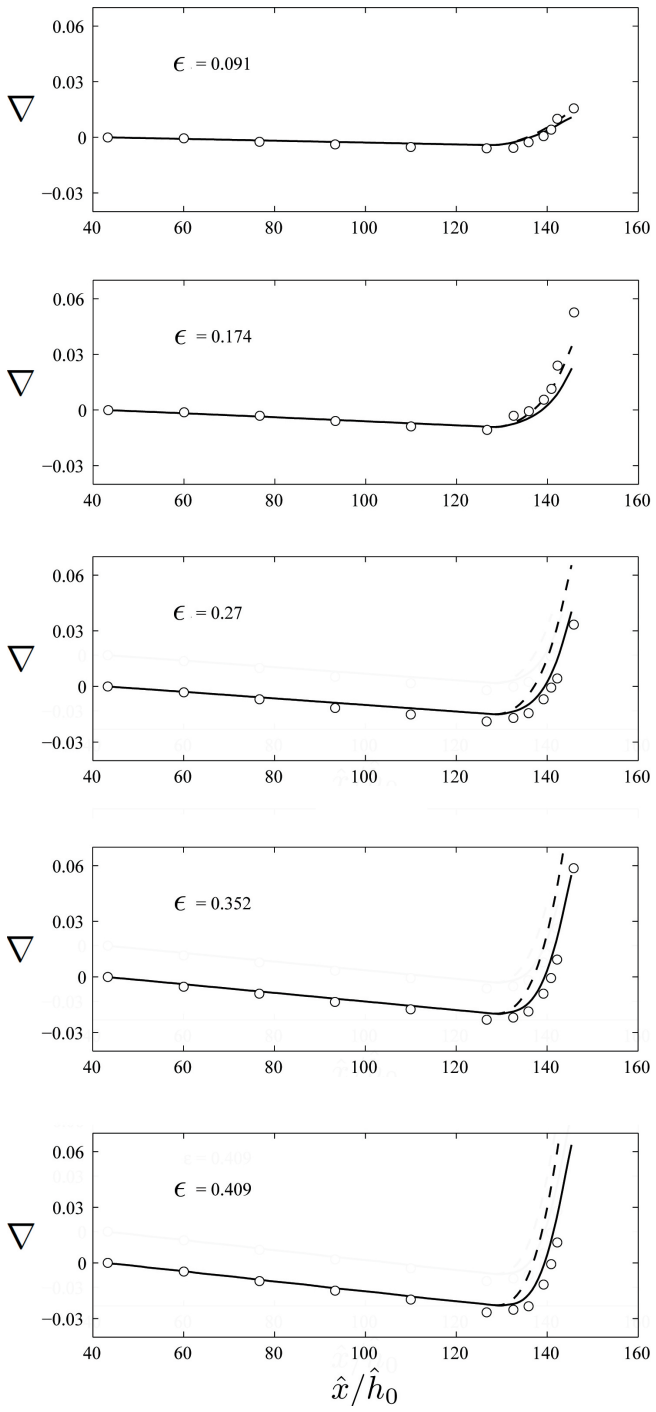

Figure 6.4: Numerical results for the experiments by Liu *et al.* (2006). Maximum surface elevations for solitary waves of $\epsilon = 0.091$, 0.174, 0.270, 0.352 and 0.409 at $\hat{x} = 6.5$ m are shown along the wave flume. The results obtained from the present theory are depicted in solid lines. Results from TW97's modified theory are depicted in dashed lines. Both theories include viscous effects. Experimental data by Liu *et al.* (2006) is shown in circles.

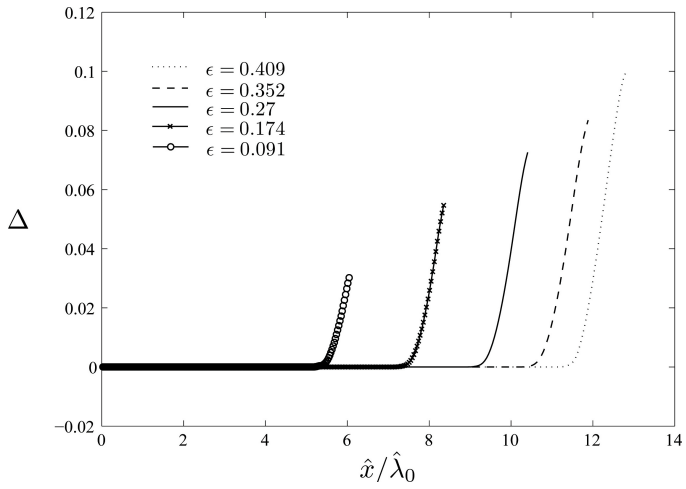

Figure 6.5: Numerical results for the experiments by Liu *et al.* (2006). Relative differences between the present and TW97 theories in the wave flume are shown. Note that the distance is normalized by the effective wavelength of the incident solitary wave.

6.4 Solitary waves in a converging/diverging channel

In Sections 5.2.1 and 5.2.2 numerical solutions, based on the inviscid flow assumption were obtained for solitary waves propagating in converging and diverging channels with a rectangular cross-section. An observation inferred from Figures 5.15 and 5.16 is that the prediction overestimates experimental data since viscous forces are not considered in the governing equations. Results considering viscous boundary effects are shown in this section.

For the converging channel cases, the wave amplitude evolution for different nonlinearities is shown on the left panel in Figure 6.6. The introduction of viscous dissipation is reflected in a cumulative decay on the wave amplitude along the channel. The new results consistently match with experimental data for initial values of ϵ = 0.093, 0.140 and 0.174. The agreement is less impressive for the case of ϵ = 0.043, where the initial wave height is very small.

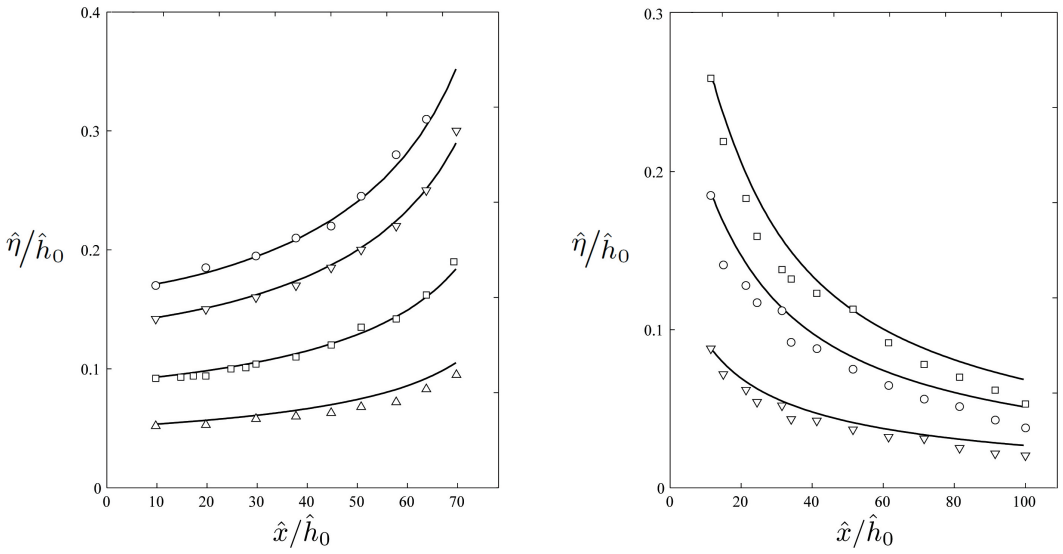

Figure 6.6: Numerical results considering viscous boundary layer effects for the linear converging and diverging channels used by C79. Left panel: Maximum surface elevations on the converging channel for initial solitary waves of ϵ = 0.043, 0.093, 0.140 and 0.174. Experimental data is denoted by triangles for ϵ = 0.043, squares for ϵ = 0.093, inverse triangles for ϵ = 0.140 and circles for ϵ = 0.174. Right panel: Maximum surface elevations on the diverging channel for initial solitary waves of ϵ = 0.088, 0.185 and 0.259. Experimental data is denoted by inverse triangles for ϵ = 0.088, circles for ϵ = 0.185 and squares for ϵ = 0.259. Solid lines are numerical results.

For the diverging channel, the new numerical results are shown on the right panel of Figure 6.6. Although the agreement between the viscous boundary layer theory and the experimental data is improved over that without considering the viscous effects (see 5.16), the refinement is not as significant as the converging channel case. The causes for this discrepancy are still unknown.

CHAPTER 7

THEORY FOR CURVED CHANNELS

Existing one-dimensional theories for weakly-nonlinear weakly-dispersive waves are valid only for straight channels, thus appropriate for example, for man-made canals or laboratory flumes. In natural streams, however, riverbanks are not straight, channels can often have bends and the cross-section may be highly non-uniform. Examples of such are found in flood waves traveling in a river, ocean tides in estuaries or storm surge entering harbors (Shi *et al.*, 2005).

An attempt to explicitly incorporate the effects of curvature in a one-dimensional Boussinesq theory for narrow channels where the depth and width are significantly smaller than the typical wavelength is presented herein. Section 7.1 reviews the literature for channels with curvature in the horizontal plane. Section 7.2 presents the derivation of channel-mean equations in curvilinear coordinates, which is an extension of the methodology introduced in Chapter 3 for straight channels. The analysis of the new equations for curved channels is presented in Section 7.3. As a complement to the problem of curvature, Appendix G.1 provides an analytical approach in the form of compatibility conditions to solve junctions in narrow channels.

7.1 Literature review

There are a few studies reviewing the hydraulic effects of curvature in long wave propagation on channels (e.g. Fenton and Nadler, 1995; Shi & Teng, 1996, 1998; Shi *et al.*, 1998, 2005 and Nachbim & da Silva, 2012). Most of the literature is based on the application of two dimensional numerical models at bends

or junctions, whilst only a few theoretical studies accounting for curvature in one-dimensional models have been published. Fenton & Nadler (1995), for example, proposed a set of long wave equations for curved waterways without a rigorous justification. Indeed, the control volume approach used in their derivation excludes the explicit treatment of the kinematic and dynamic conditions at the free surface. The effects of frequency dispersion are also neglected. From their relatively simple system of equations, they argue that in real rivers floods travel faster due to the effects of curvature than they would in the same channel straightened out fictitiously for computational purposes.

From a more practical perspective, Adityawan *et al.* (2012) provides a comprehensive list of studies addressing long wave propagation on rivers. From their observations of the 2011 Japan tsunami, they concluded that waves propagate faster and with less energy dissipation on rivers than on land. The also noted that tsunami heights may locally be amplified along curved rivers.

From the numerical perspective, the series of papers by Shi and collaborators (Shi & Teng, 1996, 1998; Shi *et al.*, 1998, 2005) are perhaps the most comprehensive ones dealing with curved channels. Shi & Teng (1996) used a two-dimensional Boussinesq wave model on a curvilinear coordinate system to study the evolution of solitary waves in narrow channels of equal and constant depths and widths. Focusing on narrow channels with two 180° smooth and 90° sharp bends, they found that solitary wave profiles are almost fully transmitted with little reflection or scattering.

Using the same wave model, Shi *et al.* (1998) showed that solitary waves traveling through narrow channel with a 90° sharp bend, are almost completely transmitted, with little reflection and scattering (Figure 7.1.*a*). Within the bend,

they observed that wave crests tilt higher against the outer wall as a consequence of the centrifugal force. The transmitted wave, however, was found to be uniform across the channel. For wide channels, the complex features of the reflected waves resulted from the change in traveling direction and diffraction around the 90° sharp bend. For smooth bends (Figure 7.1.*b*), waves were transmitted almost completely, with no significant wave reflection. The amplitude of the leading reflected (or transmitted) wave increased (decreased) as the ratio of channel width to the effective wavelength of the initial solitary wave, b/λ_e, grew. Indeed, this parameter played a key role in the amount of transmission and reflection. For small values of b/λ_e, the wave was almost completely transmitted and reflection was small but not negligible, regardless of the nonlinearity. Yuhi *et al.* (2002) replicated Shi *et al.*'s (1998) results for a 90° sharp bend by numerically solving a two dimensional Boussinesq model for solitary waves. The main focus of their work was, however, in branching channels.

Shi & Teng (1998) replicated Shi *et al.'s* (1998) numerical experiments for long waves propagating through 90° sharp bends and found that the Boussinesq model predicts more detailed and realistic wave features than the linear nondispersive approximation. Though slightly smaller wave amplitudes and slower phase speeds were found with the latter, they concluded that both models are fundamentally consistent in predicting wave transmission and reflection of solitary waves through bends.

Shi & Teng (2005) experimentally showed the influence of the relative width on wave amplitudes on a 90° sharp bend. Their results, shown in Figure 7.3, confirm the pattern found by Shi *et al.* (1998). They also showed that the averaged phase speed for a solitary wave traveling through smoothly curved channels is

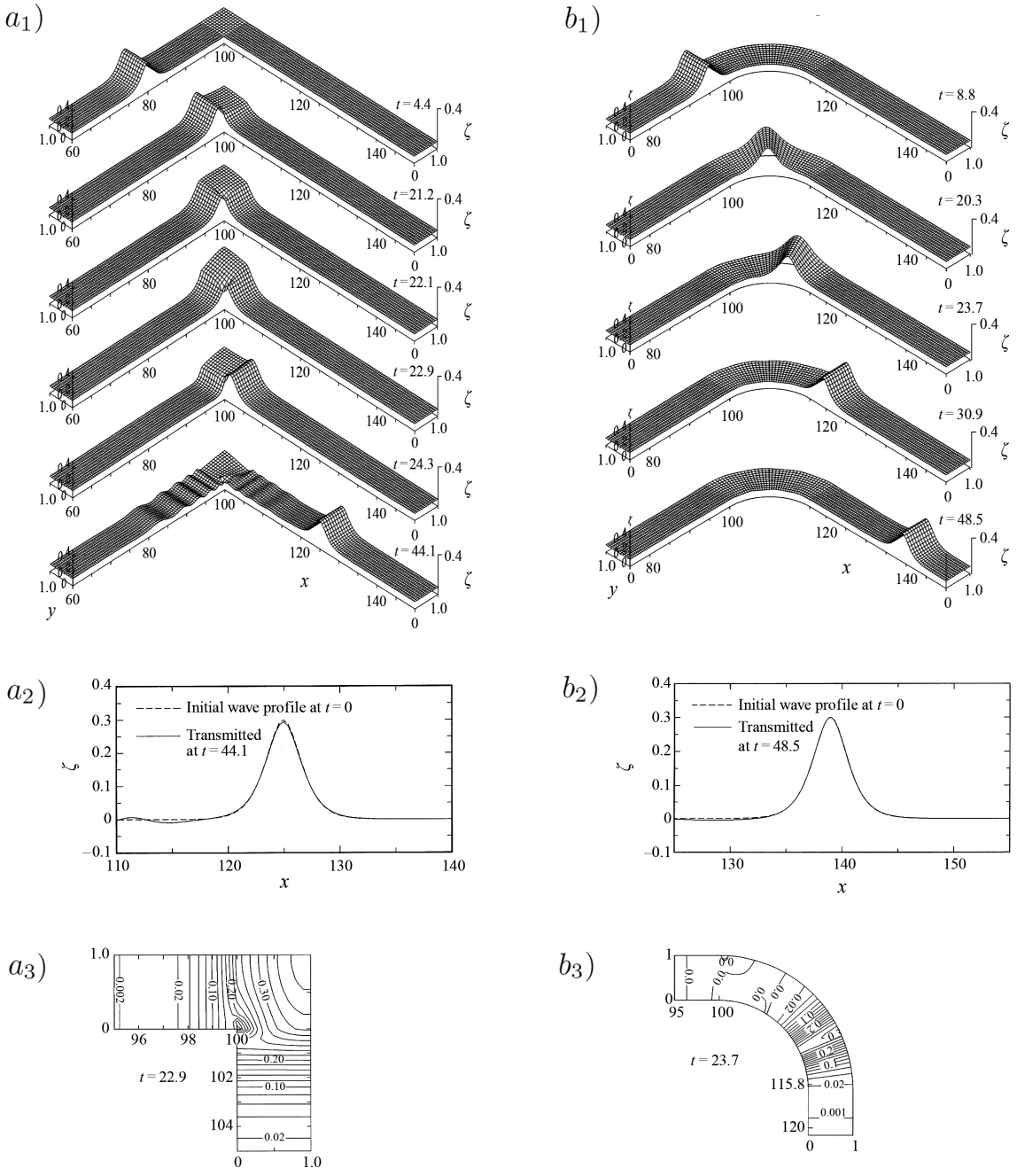

Figure 7.1: Numerical results for solitary waves propagating through a *a*) narrow 90° sharp bend and *b*) a narrow smoothed bend. Panels a_1 and b_1 depict the elevations at different times from bird's eye view. Panels a_2 and b_2 show the comparison between the original and transmitted wave profiles along the channel centerline. Panels a_2 and b_2 depict an example of the instantaneous surface elevation. Adapted from Shi *et al.* (1998).

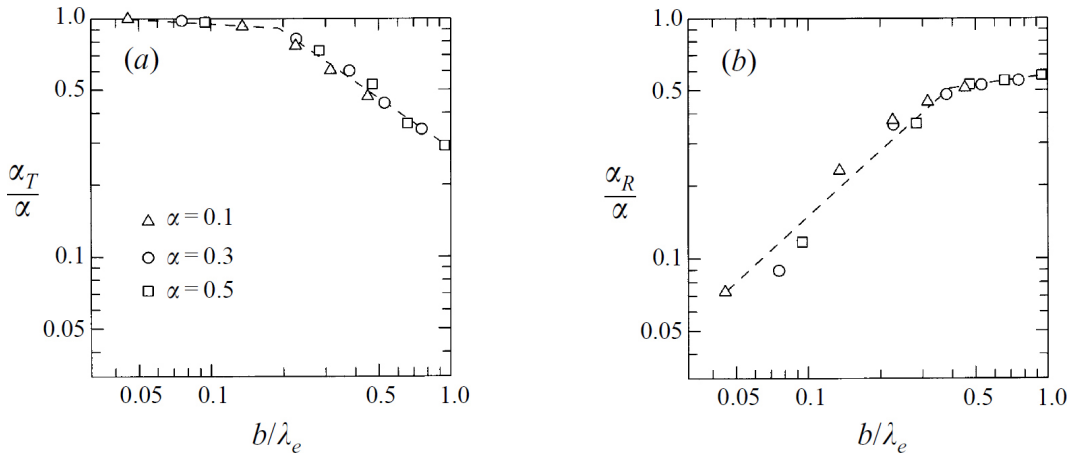

Figure 7.2: Ratios of *a*) transmitted and *b*) reflected wave amplitude α_T and α_R to the initial amplitude α as function of the ratio of channel width b to wavelength λ_e. Results correspond to numerical computations of a solitary wave propagating along 90^o sharp bends. Adapted from Shi *et al.* (1998).

almost the same as that in a straight channel. Overall, the work by Shi and collaborators is based on a two-dimensional Boussinesq wave model in curvilinear orthogonal coordinate system. The purpose of the present study, however, is to reduce the two-dimensional flow problem to one dimension.

A few other studies aimed to compute the effects of curvature in channels have been published. Kirby *et al.* (1994), for example, found by means of the parabolic approximation of the linear wave equations, that wave reflection and diffraction generate complex wave patterns in channel bends. They however, did not analyze narrow channels as in the present study. Nachbim & da Silva (2012), on the other hand, modified the curvilinear Boussinesq model proposed by Shi & Teng (1996) by means of conformal mapping, to study the evolution of solitary waves through a 90° sharp bend in a narrow channel. They confirmed Shi *et al.*'s (1998) results showing that long waves retain its traveling features after the bend. Their work, however, is confined to specific geometries.

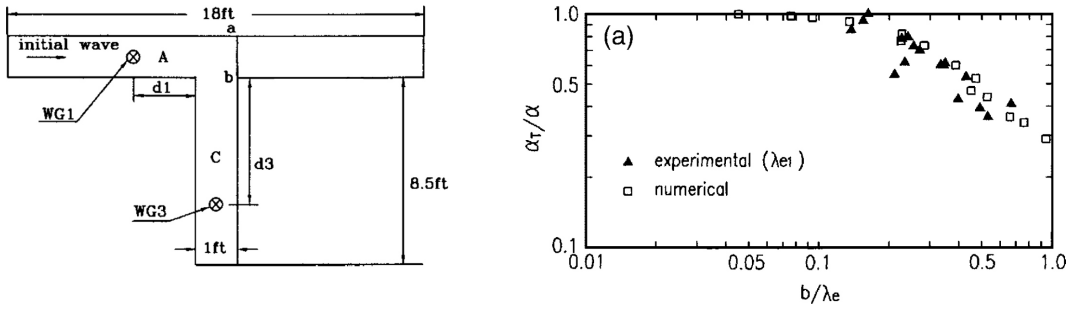

Figure 7.3: Ratio of transmitted wave amplitude α_T to the initial amplitude α as function of the ratio of channel width b to wavelength λ_e for a 90° sharp bend. Experimental data of a solitary wave by Shi & Teng (2005) and numerical computations by Shi *et al.* (1998), Figure 7.2, are shown. Numerical values of different nonlinearities have been grouped into one data set. Adapted from Shi & Teng (2005).

Studies carried in other fields are presented, as is the author's impression that they provide good analogies to understand wave propagation on hydraulic channels. Rostaffinski (1972), for example, studied the propagation of acoustic waves in smoothly curved rectangular ducts whose width was at least two orders of magnitude smaller than the wavelength. He analytically found that in a narrow curved duct, waves propagate as if the line was straight. For relatively wider channels, however, wave patterns were found to be significantly influenced by the sharpness of the bend. Cai *et al.* (2013), on the other hand, found that the shape of a solitary pulse is well preserved without being disintegrated even under 90° and 180° bends along a granular chain. Based on experiments and numerical simulations, they argued that despite the loss of energy, such bent chains can serve as an efficient information line for engineering applications. Finally, Maurel *et al.* (2014) introduced a multi-modal method to describe the acoustic propagation in waveguides with varying curvature and cross section. Their methodology was based on a flexible geometrical transformation to a virtual space in which the waveguide is straight and has unitary cross section.

From the literature review, it is concluded that the main features of waves going through a bend are very different in narrow and wide channels. For relatively narrow channels as those considered herein, the curvature has an almost negligible effect on the shape of the transmitted waves. Reflected waves on the other hand, are small but not negligible. It is also noted that wave features away from the singularities are essentially uniform in the spanwise dimension.

To the best of the author's knowledge, there is no existing one-dimensional Boussinesq wave theory which is able to account simultaneously for *i*) arbitrary cross-sections, *ii*) rapid changes in the cross-sectional geometry occurring within a wavelength and *iii*) curvature in the horizontal plane; all features which may be found in natural streams. In the following section, a new set of equations accounting for these processes is derived.

7.2 Channel-mean equations in curvilinear coordinates

A generalization of the cross-sectional averaged one-dimensional long wave model for straight channels derived in Chapter 3 is proposed herein to account for curvature in the horizontal plane. The main geometrical assumptions are that $\hat{R} \gg \hat{\lambda}_0 \gg \hat{h}_0 \gg \hat{a}_0$, where $\hat{R}$ is the characteristic radius of curvature, $\hat{\lambda}_0$ the characteristic wavelength, $\hat{h}_0$ the characteristic water depth and $\hat{a}_0$ the characteristic wave amplitude. The channel width and depth are comparable and the sidewall slope is order $O(1)$. The derivation is based on a specific set of orthogonal curvilinear coordinates, arbitrarily defined from one of the channel's sidewalls. The curvilinear orthogonal coordinate system is adapted from Dressler (1978), who developed a set of two dimensional nonlinear shallow water equa-

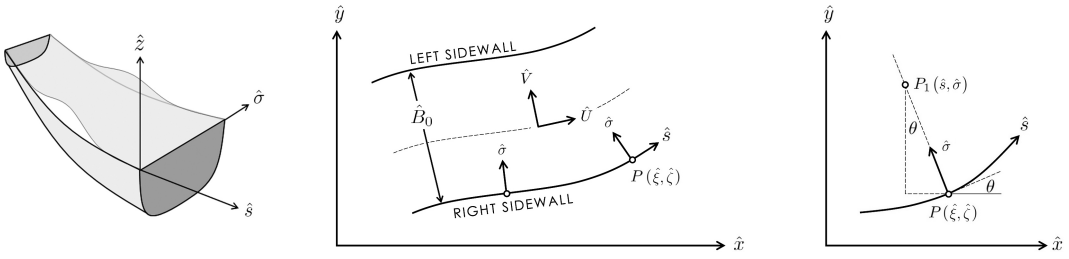

Figure 7.4: Definition of the curvilinear coordinate system.

tions considering bottom curvature, where the reference level is located at the channel's bottom. The derivation proceeds following the methodology shown in Chapter 3, thus details are omitted whenever possible. The new equations are of the Boussinesq form, implying that frequency dispersion is small but not negligible and balanced by nonlinearity. The equations explicitly contain the curvature and reduce to equations (3.95) and (3.124) for a straight channel.

7.2.1 Definition of the coordinate system

Consider a channel of arbitrary cross-section with a specific curvilinear coordinate system $(\hat{s}, \hat{\sigma}, \hat{z})$ as depicted in Figure 7.4. Here $\hat{s}$ is the arclength measured along the right sidewall at still water level, $\hat{\sigma}$ denotes the distance measured orthogonally into the flow domain and $\hat{z}$ is the vertical coordinate pointing upwards; $\hat{z} = 0$ denotes the still water level (SWL). The $\hat{s}-$axis is required to be continuous and smooth and the channel is curved only on the horizontal $\hat{s} - \hat{\sigma}$ plane. The transformation between Cartesian coordinates $(\hat{x}, \hat{y}, \hat{z})$ and curvilinear orthogonal coordinates for an arbitrary point at the still water level within the fluid domain $P_1(\hat{s}, \hat{\sigma}, \hat{z} = 0)$ is

$$\hat{x}(\hat{s}, \hat{\sigma}) = \hat{\xi} - \hat{\sigma} \sin\theta, \qquad \hat{y}(\hat{s}, \hat{\sigma}) = \hat{\zeta} + \hat{\sigma} \cos\theta, \tag{7.1}$$

where P is a point at $\hat{x} = \hat{\xi}(\hat{s})$, $\hat{y} = \hat{\zeta}(\hat{s})$ on the reference curve, $\theta(\hat{s})$ is the angle between $\hat{x}$ and the right sidewall, measured counterclockwise, and $\hat{B}_0$ the surface width of the channel at the quiescent state. The velocity $\hat{\mathbf{U}} = (\hat{u},\hat{v},\hat{w})$ is defined by components in the longitudinal $\hat{s}$, spanwise $\hat{\sigma}$, and vertical direction $\hat{z}$, respectively. The hats denote dimensional quantities. The curvature is defined by

$$\hat{\kappa}(\hat{s}) \equiv \frac{d\theta}{d\hat{s}}, \tag{7.2}$$

where $\hat{\kappa} > 0$ for concave channels and $\hat{\kappa} < 0$ for convex channels. The radius of curvature is defined by $\hat{R} \equiv 1/|d\hat{\kappa}|$. For applications where the geometry of the channel is obtained in geographic Cartesian coordinates from in topographic maps, the geometry of the reference curve can be defined by $\hat{y} = \hat{y}(\hat{x})$. The local curvature is defined as

$$\hat{\kappa}(\hat{x}) = \frac{\hat{y}_{\hat{x}\hat{x}}}{\left(1+\hat{y}_{\hat{x}}^2\right)^{3/2}}, \qquad \text{or} \qquad \hat{\kappa}(\hat{y}) = \frac{\hat{x}_{\hat{y}\hat{y}}}{\left(1+\hat{x}_{\hat{y}}^2\right)^{3/2}}, \tag{7.3}$$

for curves where the tangent to the curve is parallel to the $\hat{y}-$axis. The derivatives in both coordinate systems are related through the Jacobian matrix

$$\left\{\begin{array}{c} \partial/\partial\hat{s} \\ \partial/\partial\hat{\sigma} \\ \partial/\partial\hat{z} \end{array}\right\} = \hat{\mathbf{J}}\left(\frac{\hat{x},\hat{y},\hat{z}}{\hat{s},\hat{\sigma},\hat{z}}\right)\left\{\begin{array}{c} \partial/\partial\hat{x} \\ \partial/\partial\hat{y} \\ \partial/\partial\hat{z} \end{array}\right\}, \tag{7.4}$$

which, using the geometric relations $\partial\hat{\xi}/\partial\hat{s} = \cos\theta$ and $\partial\hat{\zeta}/\partial\hat{s} = \sin\theta$, becomes

$$\hat{\mathbf{J}}\left(\frac{\hat{x},\hat{y},\hat{z}}{\hat{s},\hat{\sigma},\hat{z}}\right) = \left[\begin{array}{ccc} \partial\hat{x}/\partial\hat{s} & \partial\hat{y}/\partial\hat{s} & \partial\hat{z}/\partial\hat{s} \\ \partial\hat{x}/\partial\hat{\sigma} & \partial\hat{y}/\partial\hat{\sigma} & \partial\hat{z}/\partial\hat{\sigma} \\ \partial\hat{x}/\partial\hat{z} & \partial\hat{y}/\partial\hat{z} & \partial\hat{z}/\partial\hat{z} \end{array}\right] = \left[\begin{array}{ccc} (1-\hat{\sigma}\hat{\kappa})\cos\theta & (1-\hat{\sigma}\hat{\kappa})\sin\theta & 0 \\ -\sin\theta & \cos\theta & 0 \\ 0 & 0 & 1 \end{array}\right]. \tag{7.5}$$

The Jacobian determinant is

$$\hat{J} \equiv 1 - \hat{\sigma}\hat{\kappa}. \tag{7.6}$$

The curvilinear coordinate system is required be one to one, implying every element $(\hat{x},\hat{y},\hat{z})$ corresponds to exactly one element of $(\hat{s},\hat{\sigma},\hat{z})$. For a convex channel

with $\hat{\kappa} < 0$, no restriction is required. For a concave channel with $\hat{\kappa} > 0$ however, any point within the fluid domain needs the additional requirement of $\hat{\sigma} < \hat{R}$ (indeed, for $\hat{\sigma} = \hat{R}$, $\hat{J} = 0$ and the transformation is singular). In other words, the channel width must be smaller than the radius of curvature, i.e. $\hat{B}_0 < \hat{R}$.

The scale factors of the transformation, or Lami coefficients, are

$$\hat{h}_{\hat{s}} = \sqrt{\left(\frac{\partial \hat{x}}{\partial \hat{s}}\right)^2 + \left(\frac{\partial \hat{y}}{\partial \hat{s}}\right)^2 + \left(\frac{\partial \hat{z}}{\partial \hat{s}}\right)^2} = \hat{J}, \tag{7.7}$$

$$\hat{h}_{\hat{\sigma}} = \sqrt{\left(\frac{\partial \hat{x}}{\partial \hat{\sigma}}\right)^2 + \left(\frac{\partial \hat{y}}{\partial \hat{\sigma}}\right)^2 + \left(\frac{\partial \hat{z}}{\partial \hat{\sigma}}\right)^2} = 1, \tag{7.8}$$

$$\hat{h}_{\hat{z}} = \sqrt{\left(\frac{\partial \hat{x}}{\partial \hat{z}}\right)^2 + \left(\frac{\partial \hat{y}}{\partial \hat{z}}\right)^2 + \left(\frac{\partial \hat{z}}{\partial \hat{z}}\right)^2} = 1. \tag{7.9}$$

Since the flow problem is studied in terms of the curvilinear coordinate system that best match the channel geometry, operators are defined accordingly. For a general transform from Cartesian coordinates (x_1, x_2, x_3) to curvilinear coordinates (u_1, u_2, u_3) with scale factors h_1, h_2, and h_3, the gradient of a scalar $f(u_1, u_2, u_3)$ is

$$\nabla f = \left(\frac{1}{h_1}\frac{\partial f}{\partial u_1}, \frac{1}{h_2}\frac{\partial f}{\partial u_2}, \frac{1}{h_3}\frac{\partial f}{\partial u_2}\right). \tag{7.10}$$

The divergence of a vector $\mathbf{F}(u_1, u_2, u_3) = (F_1, F_2, F_3)$ is

$$\nabla \cdot \mathbf{F} = \frac{1}{h_1 h_2 h_3} \sum_{i=1}^{3} \frac{\partial}{\partial u_i}\left(\frac{h_1 h_2 h_3}{h_i} F_i\right), \tag{7.11}$$

and the j^{st} component of the divergence of a tensor $\mathbf{T}(u_1, u_2, u_3)$

$$(\nabla \cdot \mathbf{T})_j = \frac{h_j}{h_1 h_2 h_3} \sum_{i=1}^{3} \frac{\partial}{\partial u_i}\left(\frac{h_1 h_2 h_3}{h_i h_j} T_{ij}\right) + \sum_{i=1}^{3} \frac{1}{h_j h_i}\left[\left(T_{ji} + T_{ij}\right)\frac{\partial h_j}{\partial u_i} - T_{ii}\frac{\partial h_i}{\partial u_j}\right]. \tag{7.12}$$

These and other operators are found elsewhere (e.g. Clarke, 2011). For the equivalences $(u_1, u_2, u_3) = (s, \sigma, z)$, and $(h_1, h_2, h_3) = (J, 1, 1)$ these expressions become, in dimensional form

$$\hat{\nabla}\hat{f} = \left(\frac{1}{\hat{J}}\frac{\partial \hat{f}}{\partial \hat{s}}, \frac{\partial \hat{f}}{\partial \hat{\sigma}}, \frac{\partial \hat{f}}{\partial \hat{z}}\right), \tag{7.13}$$

$$\hat{\nabla} \cdot \hat{\mathbf{F}} = \frac{1}{\hat{f}} \frac{\partial \hat{F}_1}{\partial \hat{s}} + \frac{\partial \hat{F}_2}{\partial \hat{\sigma}} - \frac{\hat{\kappa}}{\hat{f}} \hat{F}_2 + \frac{\partial \hat{F}_3}{\partial \hat{z}}, \tag{7.14}$$

and

$$\left(\hat{\nabla} \cdot \hat{\mathbf{T}}\right)_1 = \frac{1}{\hat{f}} \frac{\partial}{\partial \hat{s}} \left(\hat{T}_{11}\right) + \frac{\partial}{\partial \hat{\sigma}} \left(\hat{T}_{12}\right) + \frac{\partial}{\partial \hat{z}} \left(\hat{T}_{13}\right) - \frac{2\hat{\kappa}}{\hat{f}} \hat{T}_{12}, \tag{7.15}$$

where only the first component of the tensor $\hat{\mathbf{T}} = \hat{\mathbf{U}} \otimes \hat{\mathbf{U}}$ in the momentum equation is of interest. For the coordinate transform (7.1), the conditions

$$\frac{\partial \hat{x}}{\partial \hat{s}} \frac{\partial \hat{x}}{\partial \hat{\sigma}} + \frac{\partial \hat{y}}{\partial \hat{s}} \frac{\partial \hat{y}}{\partial \hat{\sigma}} + \frac{\partial \hat{z}}{\partial \hat{s}} \frac{\partial \hat{z}}{\partial \hat{\sigma}} = 0 \tag{7.16}$$

$$\frac{\partial \hat{x}}{\partial \hat{s}} \frac{\partial \hat{x}}{\partial \hat{z}} + \frac{\partial \hat{y}}{\partial \hat{s}} \frac{\partial \hat{y}}{\partial \hat{z}} + \frac{\partial \hat{z}}{\partial \hat{s}} \frac{\partial \hat{z}}{\partial \hat{z}} = 0 \tag{7.17}$$

$$\frac{\partial \hat{x}}{\partial \hat{\sigma}} \frac{\partial \hat{x}}{\partial \hat{z}} + \frac{\partial \hat{y}}{\partial \hat{\sigma}} \frac{\partial \hat{y}}{\partial \hat{z}} + \frac{\partial \hat{z}}{\partial \hat{\sigma}} \frac{\partial \hat{z}}{\partial \hat{z}} = 0 \tag{7.18}$$

are fulfilled, implying the coordinate system is orthogonal.

Note that defining the $\hat{s}-$axis on the right sidewall under quiescent condition is simpler than considering the instantaneous water level as the reference. However, this definition may become subtle in rivers, which tend to have a main channel and flooding plains at both sides. It is emphasized that the $\hat{s}-$axis could also be chosen, for example, at the left boundary or along path followed by the deepest part of the channel, as long as the curvilinear orthogonal system follows the right hand rule and new conditions for the validity of the one-to-one correspondence of the coordinate system are imposed. This alternative is further explored in Section 7.3. In any case, its definition should be based on topo-bathymetric surveys or aerial photographs.

On a cross-sectional level, the channel cross-section is described by $\hat{z} = -\hat{h}(\hat{s}, \hat{\sigma})$, as depicted in Figure 7.5. The channel boundaries are rigid and impermeable. The channel cross-section geometry can alternatively be defined by $\hat{\sigma} = \hat{\sigma}^l(\hat{s}, \hat{z})$ and $\hat{\sigma} = \hat{\sigma}^r(\hat{s}, \hat{z})$ for the left and right channel bottom boundaries, measured from the $s-$axis ($\hat{\sigma} = 0$). The intersections between the SWL and the channel

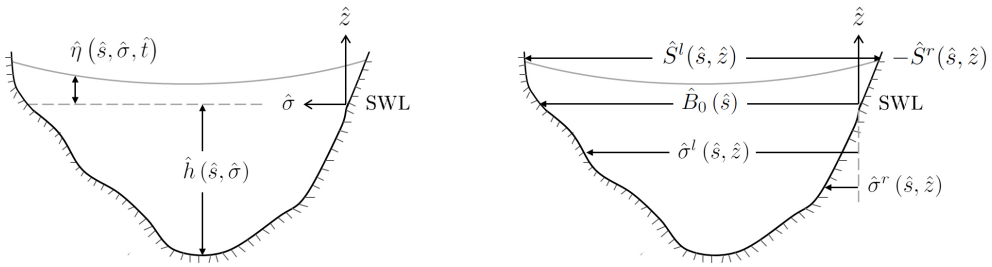

Figure 7.5: Geometric parameters of the cross-section.

boundary, describing the still water shorelines, are defined by

$$\hat{\sigma}^l(\hat{s},0) \equiv \hat{B}_0(\hat{s}) \qquad \text{and} \qquad \hat{\sigma}^r(\hat{s},0) = 0, \tag{7.19}$$

for the left and right sidewalls, respectively. The channel width below the SWL is therefore

$$\hat{B}(\hat{s},\hat{z}) = \hat{\sigma}^l(\hat{s},\hat{z}) - \hat{\sigma}^r(\hat{s},\hat{z}), \qquad \text{on} \qquad -\hat{h} \le \hat{z} < 0, \tag{7.20}$$

The instantaneous free surface elevation is expressed as $\hat{z} = \hat{\eta}(\hat{s},\hat{\sigma},\hat{t})$, where $\hat{t}$ represents time, and the moving shorelines can be defined by

$$\hat{\sigma}^l(\hat{s},\hat{\eta}) \equiv \hat{S}_l(\hat{s},\hat{t}) \qquad \text{and} \qquad \hat{\sigma}^r(\hat{s},\hat{\eta}) \equiv -\hat{S}_r(\hat{s},\hat{t}). \tag{7.21}$$

7.2.2 Equations in dimensional form

The conservation of mass for an incompressible fluid with density $\hat{\rho}$ can be stated, invoking (7.14), as

$$\hat{\nabla}\cdot\hat{\mathbf{U}} = \frac{1}{\hat{f}}\frac{\partial\hat{u}}{\partial\hat{s}} + \frac{\partial\hat{v}}{\partial\hat{\sigma}} + \frac{\partial\hat{w}}{\partial\hat{z}} - \frac{\hat{\kappa}}{\hat{f}}\hat{v} = 0. \tag{7.22}$$

The fluid is considered inviscid and the flow initially irrotational. The conservation of momentum is expressed in terms of the Euler equations

$$\frac{\partial\hat{\mathbf{U}}}{\partial\hat{t}} + \hat{\nabla}\cdot\left(\hat{\mathbf{U}}\otimes\hat{\mathbf{U}}\right) = -\frac{1}{\hat{\rho}}\hat{\nabla}\hat{p} + \hat{\mathbf{g}}, \tag{7.23}$$

where $\hat{p}(\hat{s},\hat{\sigma},\hat{z},\hat{t})$ is the fluid pressure and $\hat{\mathbf{g}} = (0,0,-\hat{g})$ is the acceleration due to gravity acting vertically downwards. Note that only the conservation along the channel's axis is required for the present derivation. Invoking (7.15) for the advective term and (7.13) for the pressure term, the momentum equation in the $s-$axis becomes

$$\frac{\partial \hat{u}}{\partial \hat{t}} + \frac{1}{\hat{J}}\frac{\partial}{\partial \hat{s}}\left(\hat{u}^2\right) + \frac{\partial}{\partial \hat{\sigma}}\left(\hat{u}\hat{v}\right) + \frac{\partial}{\partial \hat{z}}\left(\hat{u}\hat{w}\right) - \frac{2\hat{\kappa}}{\hat{J}}\hat{u}\hat{v} = -\frac{1}{\hat{\rho}\hat{J}}\frac{\partial \hat{p}}{\partial \hat{s}}. \tag{7.24}$$

The flow is assumed irrotational $\hat{\nabla}\times\hat{\mathbf{U}} = 0$, thus a velocity potential $\hat{\nabla}\hat{\phi} = \hat{\mathbf{U}}$ is introduced. The conservation of energy is expressed by means of the Bernoulli equation

$$\frac{\partial \hat{\phi}}{\partial \hat{t}} + \frac{1}{2}\left[\hat{u}^2 + \hat{v}^2 + \hat{w}^2\right] + \frac{\hat{p}}{\hat{\rho}} + \hat{g}\hat{z} = 0, \tag{7.25}$$

where the Bernoulli constant has been absorbed into the velocity potential. The mathematical expression of the kinematic condition at a boundary defined by $\hat{F}(\hat{s},\hat{\sigma},\hat{z},\hat{t})$ is

$$\frac{d\hat{F}}{d\hat{t}} = \frac{\partial \hat{F}}{\partial \hat{t}} + \hat{\mathbf{U}}\cdot\hat{\nabla}\hat{F} = 0, \tag{7.26}$$

implying that if one moves with the surface in a Lagrangian fashion, it does not change. The above is evaluated at the free surface $\hat{F} = \hat{z} - \hat{\eta}(\hat{s},\hat{\sigma},\hat{t})$, bottom $\hat{F} = \hat{z} + \hat{h}(\hat{s},\hat{\sigma})$, right sidewall $\hat{F}(\hat{s},\hat{\sigma},\hat{t}) = \hat{\sigma} + \hat{S}_r(\hat{s},\hat{t})$ and left sidewall $\hat{F}(\hat{s},\hat{\sigma},\hat{t}) = \hat{\sigma} - \hat{S}_l(\hat{s},\hat{t})$ as follows

$$-\frac{\partial \hat{\eta}}{\partial \hat{t}} - \frac{1}{\hat{J}}\frac{\partial \hat{\eta}}{\partial \hat{s}}\hat{u} - \frac{\partial \hat{\eta}}{\partial \hat{\sigma}}\hat{v} + \hat{w} = 0, \qquad \text{on} \quad \hat{z} = \hat{\eta}(\hat{s},\hat{\sigma},\hat{t}), \tag{7.27}$$

$$\frac{1}{\hat{J}}\frac{\partial \hat{h}}{\partial \hat{s}}\hat{u} + \frac{\partial \hat{h}}{\partial \hat{\sigma}}\hat{v} + \hat{w} = 0, \qquad \text{on} \quad \hat{z} = -\hat{h}(\hat{s},\hat{\sigma}), \tag{7.28}$$

$$\frac{\partial \hat{S}_r}{\partial \hat{t}} + \frac{1}{\hat{J}}\frac{\partial \hat{S}_r}{\partial \hat{s}}\hat{u} + \hat{v} = 0, \qquad \text{on} \quad \hat{\sigma} = -\hat{S}_r(\hat{s},\hat{t}), \tag{7.29}$$

$$-\frac{\partial \hat{S}_l}{\partial \hat{t}} - \frac{1}{\hat{J}}\frac{\partial \hat{S}_l}{\partial \hat{s}}\hat{u} + \hat{v} = 0, \qquad \text{on} \quad \hat{\sigma} = \hat{S}_l(\hat{s},\hat{t}). \tag{7.30}$$

Note that at the free surface and lateral boundaries the position of the surface is not known a priori. The ambient pressure is neglected

$$\hat{p} = \hat{p}_a = 0, \qquad \text{on} \quad \hat{z} = \hat{\eta}\left(\hat{s}, \hat{\sigma}, \hat{t}\right). \tag{7.31}$$

Equations (7.22) to (7.31) constitute the governing equations and boundary conditions for a general three-dimensional non-linear water wave problem for a irrotational flow. Additional initial conditions for free surface elevation and velocity, and up-stream and down-stream boundary conditions are needed for a specific problem of interest.

7.2.3 Equations in dimensionless form

To describe the problem in terms of dimensionless variables, the characteristic wavelength $\hat{\lambda}_0$ is employed as the length scale in the longitudinal direction, the characteristic unperturbed water depth $\hat{h}_0$ as the length scale for the vertical and spanwise directions and the typical wave amplitude $\hat{a}_0$ is used to account to effects of the free surface on the motion. The variables scaled by different lengths are considered to be of different orders of magnitude, where $\hat{a}_0 \ll \hat{h}_0 \ll \hat{\lambda}_0$. The non-dimensional parameters

$$\mu = \frac{\hat{h}_0}{\hat{\lambda}_0} \qquad \text{and} \qquad \epsilon = \frac{\hat{a}_0}{\hat{h}_0} \tag{7.32}$$

are introduced as measures of the frequency dispersion and nonlinearity, respectively. The Boussinesq approximation is assumed, thus $O(\epsilon) = O\left(\mu^2\right) \ll 1$. The independent variables are scaled as

$$\hat{s} = \hat{\lambda}_0 s, \qquad \left(\hat{\sigma}, \hat{z}, \hat{S}, \hat{h}, \hat{B}\right) = \hat{h}_0\left(\sigma, z, S, h, B\right), \qquad \hat{t} = \frac{\hat{\lambda}}{\sqrt{\hat{g}\hat{h}_0}} t, \tag{7.33}$$

where $\hat{c}_0^2 = \hat{g}\hat{h}_0$ is the linear phase speed in shallow water. The radius of curvature $\hat{R}$ and the curvature $\hat{\kappa}$ are scaled as

$$\hat{R} = \frac{\hat{\lambda}_0}{\Upsilon} R, \qquad \text{and} \qquad \hat{\kappa} = \frac{\Upsilon}{\hat{\lambda}_0}\kappa, \tag{7.34}$$

where $\Upsilon = \epsilon$ and μ denotes the degree of curvature of the channel with respect to the wavelength. For $\Upsilon = \mu$ the radius of curvature is smaller than that for $\Upsilon = \epsilon$ and in both cases the radius of curvature is smaller than the wavelength, i.e. $\hat{R} \gg \hat{\lambda}_0$. The velocities are scaled as

$$\hat{u} = \epsilon\sqrt{\hat{g}\hat{h}_0}u, \qquad \text{and} \qquad (\hat{v}, \hat{w}) = \frac{\epsilon}{\mu}\sqrt{\hat{g}\hat{h}_0}\,(v, w)\,. \tag{7.35}$$

The surface elevation and pressure are scaled using the typical wave amplitude

$$\hat{\eta} = \hat{a}_0\eta, \qquad \text{and} \qquad \hat{p} = \hat{\rho}\hat{g}\hat{a}_0 p. \tag{7.36}$$

With these scalings, the determinant of the Jacobian matrix (7.6) becomes

$$J = 1 - \Upsilon\mu\sigma\kappa, \tag{7.37}$$

the conservation of mass (7.22) therefore reads

$$\frac{1}{J}\frac{\partial u}{\partial s} + \frac{1}{\mu^2}\frac{\partial v}{\partial \sigma} + \frac{1}{\mu^2}\frac{\partial w}{\partial z} - \frac{\Upsilon}{\mu}\frac{\kappa}{J}v = 0, \tag{7.38}$$

the conservation of momentum (7.24) becomes

$$\frac{\partial u}{\partial t} + \frac{\epsilon}{J}\frac{\partial}{\partial s}\left(u^2\right) + \frac{\partial}{\partial \sigma}(uv) + \frac{\partial}{\partial z}(uw) - 2\Upsilon\mu\frac{\kappa}{J}uv = -\frac{1}{J}\frac{\partial p}{\partial s}, \tag{7.39}$$

and the Bernoulli equation is written as

$$\frac{\partial \phi}{\partial t} + \frac{1}{2}\left[\epsilon u^2 + v^2 + w^2\right] + p + \frac{z}{\epsilon} = 0. \tag{7.40}$$

The boundary conditions become

$$-\frac{\partial \eta}{\partial t} - \frac{\epsilon}{J}\frac{\partial \eta}{\partial s}u - \frac{\partial \eta}{\partial \sigma}v + \frac{1}{\mu^2}w = 0, \qquad z = \epsilon\eta\,(s, \sigma, t)\,, \tag{7.41}$$

$$\frac{\mu}{J}\frac{\partial h}{\partial s}u + \frac{1}{\mu}\frac{\partial h}{\partial \sigma}v + \frac{1}{\mu}w = 0, \qquad z = -h(s,\sigma), \tag{7.42}$$

$$\frac{1}{\epsilon}\frac{\partial S_r}{\partial t} + \frac{1}{J_{(-S_r)}}\frac{\partial S_r}{\partial s}u + \frac{1}{\mu^2}v = 0, \qquad \sigma = -S_r(s,t), \tag{7.43}$$

$$-\frac{1}{\epsilon}\frac{\partial S_l}{\partial t} - \frac{1}{J_{(S_l)}}\frac{\partial S_l}{\partial s}u + \frac{1}{\mu^2}v = 0, \qquad \sigma = S_l(s,t), \tag{7.44}$$

where $J_{(-S_r)} = 1 + \Upsilon\mu S_r\kappa$ and $J_{(S_l)} = 1 - \Upsilon\mu S_l\kappa$.

7.2.4 Depth-averaged equations

The three-dimensional flow problem is reduced to two dimensions by integrating the equations of continuity and conservation of momentum over the depth and applying the free surface and bottom kinematic boundary conditions. For convenience, the depth-average mean

$$\check{f}(s,\sigma,t) = \frac{1}{H}\int_{-h}^{\epsilon\eta} f(s,\sigma,z,t)\,dz, \tag{7.45}$$

and the total water depth

$$H(s,\sigma,t) = \epsilon\eta(s,\sigma,t) + h(s,\sigma), \tag{7.46}$$

are introduced. To eliminate the vertical coordinate, the equation of conservation of mass (7.38) is integrated in the depth. Using the Leibniz rule, the fundamental theorem of calculus and the kinematic boundary conditions (7.41) and (7.42) yields

$$\frac{\partial\eta}{\partial t} + \frac{1}{J}\frac{\partial}{\partial s}\int_{-h}^{\epsilon\eta} u\,dz + \frac{1}{\mu^2}\frac{\partial}{\partial\sigma}\int_{-h}^{\epsilon\eta} v\,dz - \frac{\Upsilon}{\mu}\frac{\kappa}{J}\int_{-h}^{\epsilon\eta} v\,dz \;= 0. \tag{7.47}$$

Invoking (7.45) and (7.46) yields

$$\frac{J}{\epsilon}\frac{\partial H}{\partial t} + \frac{\partial}{\partial s}(H\check{u}) + \frac{J}{\mu^2}\frac{\partial}{\partial\sigma}(H\check{v}) - \frac{\Upsilon}{\mu}\kappa H\check{v} \;= 0, \tag{7.48}$$

where the equation is multiplied by the Jacobian to facilitate the succeeding derivation. This equation has the same structure as Tan's (1992) equation (1.5.50). Following similar procedure, the equation of conservation of momentum (7.39) is also integrated on the depth to yield

$$J\frac{\partial}{\partial t}\left(H\check{u}\right)+\epsilon\frac{\partial}{\partial s}\left(H\check{u}\check{u}\right)+J\frac{\partial}{\partial\sigma}\left(H\check{u}\check{v}\right)-2\Upsilon\mu\kappa\int_{-h}^{\epsilon\eta}uvdz=-\int_{-h}^{\epsilon\eta}\frac{\partial p}{\partial s}dz. \tag{7.49}$$

This equation has the same structure as Tan's (1992) equation (1.5.51).

7.2.5 Perturbation expansion

The flow problem is further reduced to one dimension by averaging over a channel cross-section. A perturbation expansion of the flow variables and supplementary definitions for the cross-averaging process are thus needed. The cross-sectional area at the quiescent state is defined by

$$A_0\left(s\right)=\int_0^{B_0}h\left(s,\sigma\right)d\sigma. \tag{7.50}$$

As shown in the derivation for a straight channel, i.e. (3.35), the instantaneous cross-sectional area is expressed as

$$A\left(s,t\right)=A_0+\epsilon B_0\widetilde{\eta}+\epsilon^2\frac{B_0'}{2}\widetilde{\eta}^2+O\left(\epsilon^2\mu^2,\epsilon^3\right) \tag{7.51}$$

in which

$$B_0'\left(s\right)=\frac{\partial B}{\partial z}\left(s,0\right)=O\left(1\right). \tag{7.52}$$

is assumed. The cross-sectional average of a function $\langle f\rangle$ and the cross-sectional average at the quiescent state $\overline{f}$ are defined as

$$\langle f\rangle\left(s,t\right)=\frac{1}{A}\int_{-S_r}^{S_l}\int_{-h}^{\epsilon\eta}f\left(s,\sigma,z,t\right)dzd\sigma, \tag{7.53}$$

and

$$\overline{f}(s,t) = \frac{1}{A_0}\int_0^{B_0}\int_{-h}^{0} f(s,\sigma,z,t)\,dzd\sigma. \tag{7.54}$$

For channels where (7.52) holds, $\langle f\rangle = \overline{f} + O(\epsilon)$. Finally, the spanwise average over the channel's still water surface width is

$$\widetilde{f}(s,t) = \frac{1}{B_0}\int_0^{B_0} f(s,\sigma,0,t)\,dzd\sigma. \tag{7.55}$$

To close the system, the dimensionless physical variables are expanded as

$$\phi = \phi_1(s,t) + \mu^2\phi_2(s,\sigma,z,t) + O\left(\mu^4\right), \tag{7.56}$$

$$\eta = \eta_1(s,t) + \mu^2\eta_2(s,\sigma,t) + O\left(\mu^4\right), \tag{7.57}$$

$$u = u_1(s,t) + \mu^2 u_2(s,\sigma,z,t) + O\left(\mu^4\right), \tag{7.58}$$

$$v = \mu^2 v_2(s,\sigma,z,t) + O\left(\mu^4\right), \tag{7.59}$$

$$w = \mu^2 w_2(s,\sigma,z,t) + O\left(\mu^4\right), \tag{7.60}$$

implying the transverse velocities are comparable and smaller than the longitudinal velocity , i.e. $O(v) = O(w) \ll u$.

7.2.6 Channel-averaged conservation of mass

Invoking (7.37) and integrating (7.48) across the channel yields

$$\begin{aligned}\frac{1}{\epsilon}\int_{-S_r}^{S_l}\frac{\partial H}{\partial t}d\sigma + \int_{-S_r}^{S_l}\frac{\partial}{\partial s}(H\check{u})\,d\sigma + \frac{1}{\mu^2}\int_{-S_r}^{S_l}\frac{\partial}{\partial\sigma}(H\check{v})\,d\sigma \\ \underbrace{-\frac{\Upsilon}{\mu}\kappa\int_{-S_r}^{S_l}\sigma\frac{\partial H}{\partial t}d\sigma}_{I_1} \underbrace{-\frac{\Upsilon}{\mu}\kappa\int_{-S_r}^{S_l}\sigma\frac{\partial}{\partial\sigma}(H\check{v})\,d\sigma}_{I_2} \underbrace{-\frac{\Upsilon}{\mu}\kappa\int_{-S_r}^{S_l}H\check{v}d\sigma}_{I_3} = 0,\end{aligned} \tag{7.61}$$

where I_1, I_2 and I_3 are analyzed later. Derivatives are manipulated using the Leibniz rule and the fundamental theorem of calculus to yield

$$\begin{aligned}\frac{1}{\epsilon}\frac{\partial}{\partial t}\int_{-S_r}^{S_l} H d\sigma + \frac{\partial}{\partial s}\int_{-S_r}^{S_l} H\check{u} d\sigma - I_1 - I_2 - I_3 \\ + H_{(S_l)}\left[-\frac{1}{\epsilon}\frac{\partial S_l}{\partial t} - \check{u}_{(S_l)}\frac{\partial S_l}{\partial s} + \frac{1}{\mu^2}\check{v}_{(S_l)}\right] \\ + H_{(-S_r)}\left[-\frac{1}{\epsilon}\frac{\partial S_r}{\partial t} - \check{u}_{(-S_r)}\frac{\partial S_r}{\partial s} - \frac{1}{\mu^2}\check{v}_{(-S_r)}\right] = 0. \end{aligned} \tag{7.62}$$

Note that $H_{(S_l)}$, $H_{(-S_r)}$, S_l and S_r are unknowns and need to be expressed in term of geometrical properties, when needed.

Manipulation of the lateral boundary conditions

Boundary conditions (7.43) and (7.44) are treated using the series expansion

$$\frac{1}{J_{(-S_r)}} = \frac{1}{1 + \Upsilon\mu S_r\kappa} = 1 - \Upsilon\mu S_r\kappa + O\left(\Upsilon^2\mu^2\right), \tag{7.63}$$

$$\frac{1}{J_{(S_l)}} = \frac{1}{1 - \Upsilon\mu S_l\kappa} = 1 + \Upsilon\mu S_l\kappa + O\left(\Upsilon^2\mu^2\right), \tag{7.64}$$

to yield

$$\frac{1}{\epsilon}\frac{\partial S_r}{\partial t} + \frac{\partial S_r}{\partial s}u_{(-S_r)} + \frac{1}{\mu^2}v_{(-S_r)} = \Upsilon\mu S_r\kappa\frac{\partial S_r}{\partial s}u_{(-S_r)} + O\left(\Upsilon^2\mu^2\right), \tag{7.65}$$

$$-\frac{1}{\epsilon}\frac{\partial S_l}{\partial t} - \frac{\partial S_l}{\partial s}u_{(-S_r)} + \frac{1}{\mu^2}v_{(-S_r)} = \Upsilon\mu S_l\kappa\frac{\partial S_l}{\partial s}u_{(-S_r)} + O\left(\Upsilon^2\mu^2\right). \tag{7.66}$$

The sidewall assumption (7.52), in addition, implies

$$S_l(s,t) = B_0(s) + O(\epsilon), \qquad S_r(s,t) = O(\epsilon). \tag{7.67}$$

Using the relation $u = \langle u\rangle + O\left(\mu^2\right)$ by virtue of (7.58), and depth averaging (7.65) and (7.66) yields

$$\frac{1}{\epsilon}\frac{\partial S_r}{\partial t} + \frac{\partial S_r}{\partial s}\check{u}_{(-S_r)} + \frac{1}{\mu^2}\check{v}_{(-S_r)} = O(\Upsilon\epsilon\mu), \tag{7.68}$$

$$-\frac{1}{\epsilon}\frac{\partial S_l}{\partial t} - \frac{\partial S_l}{\partial s}\check{u}_{(S_l)} + \frac{1}{\mu^2}\check{v}_{(S_l)} = \Upsilon\mu\kappa B_0\frac{\partial B_0}{\partial s}\langle u\rangle + O(\Upsilon\epsilon\mu). \tag{7.69}$$

Using expressions (7.68) and (7.69) in the conservation of mass (7.62) yields

$$\frac{1}{\epsilon}\frac{\partial}{\partial t}\int_{-\sigma_r}^{\sigma_l} H d\sigma + \frac{\partial}{\partial s}\int_{-\sigma_r}^{\sigma_l} H\check{u} d\sigma - I_1 - I_2 - I_3 + \Upsilon\mu\kappa h_{(B_0)} B_0 \frac{\partial B_0}{\partial s}\langle u\rangle = O(\Upsilon\epsilon\mu). \quad (7.70)$$

where $H_{(S_l)} = h_{(S_l)} + O(\epsilon)$ based on the definition (7.46), and $h_{(S_l)} = h_{(B_0)} + O(\epsilon)$ by virtue or the Taylor expansion has been used.

Analytic expressions for integrals I_1, I_2 and I_3

For I_1, the following expression based on (7.46) and (7.57) is used

$$\frac{\partial H}{\partial t} = \epsilon\frac{\partial \eta}{\partial t}(s,\sigma,z,t) = \epsilon\frac{\partial \widetilde{\eta}}{\partial t}(s,t) + O\left(\epsilon\mu^2\right). \quad (7.71)$$

I_1 becomes

$$I_1 = \frac{\Upsilon}{\mu}\kappa\int_{-S_r}^{S_l}\sigma\frac{\partial H}{\partial t}d\sigma = \Upsilon\mu\kappa\frac{\partial \widetilde{\eta}}{\partial t}\int_{-S_r}^{S_l}\sigma d\sigma + O(\Upsilon\epsilon\mu) = \Upsilon\mu\kappa\frac{B_0^2}{2}\frac{\partial \widetilde{\eta}}{\partial t} + O(\Upsilon\epsilon\mu), \quad (7.72)$$

where (7.67) is invoked. For I_2 and I_3, expression (7.121) later derived for the boundary value problem at the cross-section

$$v(s,\sigma,z,t) = \mu^2\frac{\partial \chi_1}{\partial\sigma}\langle u\rangle + \mu^2\frac{\partial \chi_2}{\partial\sigma}\frac{\partial\langle u\rangle}{\partial s} + O\left(\mu^4\right) \quad (7.73)$$

is used, where $\langle u\rangle(s,t)$, $\chi_1(s,\sigma,z)$ and $\chi_2(s,\sigma,z)$. Thus

$$I_2 = \Upsilon\mu\kappa\int_0^{B_0}\sigma\frac{\partial}{\partial\sigma}\left(h\frac{\partial\check{\chi}_1}{\partial\sigma}\right)d\sigma\langle u\rangle + \Upsilon\mu\kappa\int_0^{B_0}\sigma\frac{\partial}{\partial\sigma}\left(h\frac{\partial\check{\chi}_2}{\partial\sigma}\right)d\sigma\frac{\partial\langle u\rangle}{\partial s} + O\left(\Upsilon\mu^3\right) \quad (7.74)$$

and

$$I_3 = \Upsilon\mu\kappa\int_0^{B_0} h\frac{\partial\check{\chi}_1}{\partial\sigma}d\sigma\langle u\rangle + \Upsilon\mu\kappa\int_0^{B_0} h\frac{\partial\check{\chi}_2}{\partial\sigma}d\sigma\frac{\partial\langle u\rangle}{\partial s} + O\left(\Upsilon\mu^3\right) \quad (7.75)$$

where the definition (7.46) is used to replace the unknown quantity H by h and (7.67) has been used for the limits of integration.

Back to conservation of mass

Using the expressions of the integrals (7.72), (7.74) and (7.75) in the conservation of mass (7.70), and defining the quantities

$$\vartheta = \int_0^{B_0} \sigma \frac{\partial}{\partial \sigma}\left(h \frac{\partial \breve{\chi}_1}{\partial \sigma}\right) d\sigma + \int_0^{B_0} h \frac{\partial \breve{\chi}_1}{\partial \sigma} d\sigma - h_{(B_0)} B_0 \frac{\partial B_0}{\partial s}, \tag{7.76}$$

and

$$\Gamma = \int_0^{B_0} \sigma \frac{\partial}{\partial \sigma}\left(h \frac{\partial \breve{\chi}_2}{\partial \sigma}\right) d\sigma + \int_0^{B_0} h \frac{\partial \breve{\chi}_2}{\partial \sigma} d\sigma \tag{7.77}$$

yields

$$\frac{1}{\epsilon}\frac{\partial A}{\partial t} + \frac{\partial}{\partial s}\left(A \langle u \rangle\right) - \Upsilon \mu \kappa \frac{B_0^2}{2}\frac{\partial \widetilde{\eta}}{\partial t} - \Upsilon \mu \kappa \vartheta \langle u \rangle - \Upsilon \mu \kappa \Gamma \frac{\partial \langle u \rangle}{\partial s} = O\left(\Upsilon \epsilon \mu\right). \tag{7.78}$$

Using the expansion of the area (7.51) yields

$$\begin{aligned} &\left(1 - \Upsilon \mu \kappa \frac{B_0}{2}\right)\frac{\partial \widetilde{\eta}}{\partial t} + \epsilon \frac{B_0'}{2B_0}\frac{\partial \widetilde{\eta}^2}{\partial t} \\ &+ \frac{1}{B_0}\frac{\partial}{\partial s}\left(\left[A_0 + \epsilon B_0 \widetilde{\eta}\right] \langle u \rangle\right) - \Upsilon \mu \frac{\kappa}{B_0}\left(\vartheta \langle u \rangle + \Gamma \frac{\partial \langle u \rangle}{\partial s}\right) = O\left(\Upsilon \epsilon \mu\right). \end{aligned} \tag{7.79}$$

The second term in the equation above can be manipulated by replacing the time derivative of $\widetilde{\eta}$ with a spatial derivative obtained from the leading order terms of the same equation, thus

$$\begin{aligned} &\left(1 - \Upsilon \mu \kappa \frac{B_0}{2}\right)\frac{\partial \widetilde{\eta}}{\partial t} + \epsilon \frac{B_0'}{B_0^2}\widetilde{\eta}\frac{\partial}{\partial s}\left(A_0 \langle u \rangle\right) \\ &+ \frac{1}{B_0}\frac{\partial}{\partial s}\left(\left[A_0 + \epsilon B_0 \widetilde{\eta}\right] \langle u \rangle\right) - \Upsilon \mu \frac{\kappa}{B_0}\left(\vartheta \langle u \rangle + \Gamma \frac{\partial \langle u \rangle}{\partial s}\right) = O\left(\Upsilon \epsilon \mu\right). \end{aligned} \tag{7.80}$$

Note that the leading order error in the above consists of terms of order $O\left(\epsilon^2, \epsilon\mu^2, \mu^4\right)$ already present in a straight channel, and terms of order $O\left(\Upsilon \epsilon \mu\right)$ stemming from the presence of curvature.

7.2.7 Channel-averaged conservation of momentum

Equation (7.49) is integrated in σ, invoking the expression of the Jacobian (7.37)

$$\int_{-S_r}^{S_l} \frac{\partial}{\partial t}\left(H\check{u}\right) d\sigma + \epsilon \int_{-S_r}^{S_l} \frac{\partial}{\partial s}\left(Hu\check{u}\right) d\sigma + \int_{-S_r}^{S_l} \frac{\partial}{\partial \sigma}\left(Hu\check{v}\right) d\sigma$$
$$+ \int_{-S_r}^{S_l}\int_{-h}^{\epsilon\eta} \frac{\partial p}{\partial s} dz d\sigma \underbrace{- \Upsilon\mu\kappa \int_{-S_r}^{S_l} \sigma \frac{\partial}{\partial t}\left(H\check{u}\right) d\sigma}_{I_4} \underbrace{- \Upsilon\mu\kappa \int_{-S_r}^{S_l} \sigma \frac{\partial}{\partial \sigma}\left(Hu\check{v}\right) d\sigma}_{I_5} = 0. \quad (7.81)$$

Note that the last term in the left hand side of (7.49) is order $O\left(\Upsilon\mu^3\right)$ and is thus a higher order term. Also, due to the expansion of v in (7.59), $I_5 = O\left(\Upsilon\epsilon\mu\right)$. Derivatives are manipulated using the Leibniz rule and the fundamental theorem of calculus to yield

$$\frac{\partial}{\partial t}\int_{-S_r}^{S_l} H\check{u} d\sigma + \epsilon\frac{\partial}{\partial s}\int_{-S_r}^{S_l} Hu\check{u} d\sigma + \int_{-S_r}^{S_l}\int_{-h}^{\epsilon\eta} \frac{\partial p}{\partial s} dz d\sigma - I_4$$
$$+ H_{(S_l)}\left[-\check{u}_{(S_l)}\frac{\partial S_l}{\partial t} - \epsilon u\check{u}_{(S_l)}\frac{\partial S_l}{\partial s} + u\check{v}_{(S_l)}\right]$$
$$+ H_{(-S_r)}\left[-\check{u}_{(-S_r)}\frac{\partial S_r}{\partial t} - \epsilon u\check{u}_{(-S_r)}\frac{\partial S_r}{\partial s} - u\check{v}_{(-S_r)}\right] = O\left(\Upsilon\epsilon\mu\right). \quad (7.82)$$

Manipulation of the lateral boundary conditions

Multiplying the kinematic conditions (7.43) and (7.44) by $u_{(-S_r)}$ and $u_{(S_l)}$, respectively , and using expansions of the Jacobian (7.63) and (7.64) yields

$$\frac{1}{\epsilon}\frac{\partial S_r}{\partial t}u_{(-S_r)} + \frac{\partial S_r}{\partial s}u^2_{(-S_r)} + \frac{1}{\mu^2}uv_{(-S_r)} = \Upsilon\mu S_r\kappa\frac{\partial S_r}{\partial s}u^2_{(-S_r)} + O\left(\Upsilon^2\mu^2\right), \quad (7.83)$$
$$-\frac{1}{\epsilon}\frac{\partial S_l}{\partial t}u_{(S_l)} - \frac{\partial S_l}{\partial s}uu_{(S_l)} + \frac{1}{\mu^2}uv_{(S_l)} = \Upsilon\mu S_l\kappa\frac{\partial S_l}{\partial s}uu_{(S_l)} + O\left(\Upsilon^2\mu^2\right). \quad (7.84)$$

Upon multiplication by ϵ and depth integration the above reads

$$-\frac{\partial S_r}{\partial t}\check{u}_{(-S_r)} - \epsilon\frac{\partial S_r}{\partial s}u\check{u}_{(-S_r)} - u\check{v}_{(-S_r)} = -\Upsilon\epsilon\mu S_r\kappa\frac{\partial S_r}{\partial s}u\check{u}_{(-S_r)} + O\left(\Upsilon^2\epsilon\mu^2\right), \quad (7.85)$$
$$-\frac{\partial S_l}{\partial t}\check{u}_{(S_l)} - \epsilon\frac{\partial S_l}{\partial s}u\check{u}_{(S_l)} + u\check{v}_{(S_l)} = \Upsilon\epsilon\mu S_l\kappa\frac{\partial S_l}{\partial s}u\check{u}_{(S_l)} + O\left(\Upsilon^2\epsilon\mu^2\right), \quad (7.86)$$

implying that the terms in brackets in (7.82) are small, i.e. $O(\Upsilon\epsilon\mu)$.

Analytic expressions for integral I_4

The integral I_4 reads

$$\begin{aligned} I_4 &= \Upsilon\mu\kappa \int_{-S_r}^{S_l} \sigma \frac{\partial}{\partial t}(H\check{u})\, d\sigma = \Upsilon\mu\kappa\sigma_c \int_{-S_r}^{S_l} \frac{\partial}{\partial t}(H\check{u})\, d\sigma \\ &= \Upsilon\mu\kappa\sigma_c \left[\frac{\partial}{\partial t} \int_{-S_r}^{S_l} (H\check{u})\, d\sigma \underbrace{-H\check{u}_{(S_l)} \frac{\partial S_l}{\partial t} - H\check{u}_{(-S_r)} \frac{\partial S_r}{\partial t}}_{T} \right], \end{aligned} \tag{7.87}$$

where the centroid is

$$\sigma_c = \frac{\int_{-S_r}^{S_l} \sigma \frac{\partial}{\partial t}(H\check{u})\, d\sigma}{\int_{-S_r}^{S_l} \frac{\partial}{\partial t}(H\check{u})\, d\sigma} = \frac{\int_{-S_r}^{S_l} \sigma h d\sigma}{\int_{-S_r}^{S_l} h d\sigma} + O\left(\epsilon\mu^2\right) = \frac{\int_0^{B_0} \sigma h d\sigma}{\int_0^{B_0} h d\sigma} + O(\epsilon) \tag{7.88}$$

since due to the expansion (7.58) and the total depth (7.46)

$$\frac{\partial}{\partial t}(H\check{u}) = \frac{\partial}{\partial t}\left[(\epsilon\eta + h)\left(\check{u}_1 + \mu^2\check{u}_2\right)\right] + O\left(\mu^4\right) = h\frac{\partial \check{u}_1}{\partial t} + O\left(\epsilon, \mu^2\right). \tag{7.89}$$

Note that σ_c represents the centroid of the cross-section. For inclined sidewalls, $H_{(S_l)}, H_{(-S_r)} = 0$ thus $T = 0$. For vertical sidewalls, (7.67) implies

$$T = -H\check{u}_{(B_0)} \frac{\partial B_0}{\partial t} + O(\epsilon) = O(\epsilon), \tag{7.90}$$

thus (7.87) becomes

$$I_4 = \Upsilon\mu\kappa\sigma_c \frac{\partial}{\partial t} \int_{-S_r}^{S_l} (H\check{u})\, d\sigma + O(\Upsilon\epsilon\mu). \tag{7.91}$$

regardless of the sidewall slope.

Back to conservation of momentum

The conservation of momentum (7.82) becomes, after invoking the averages (7.45), (7.53) and expression (7.91)

$$(1 - \Upsilon\mu\kappa\sigma_c) \frac{\partial}{\partial t}(A\langle u\rangle) + \epsilon \frac{\partial}{\partial s}(A\langle uu\rangle) + A\left\langle \frac{\partial p}{\partial s} \right\rangle = O(\Upsilon\epsilon\mu). \tag{7.92}$$

Expressions (3.85) and (3.93) originally derived for straight channel, are also valid in the $s-\sigma$ coordinate system; i.e.

$$\langle uu\rangle = \langle u\rangle^2 + O\left(\epsilon^2\right), \qquad \left\langle \frac{\partial p}{\partial s}\right\rangle = \frac{\partial \widetilde{\eta}}{\partial s} + \mu^2 \mathcal{D} + O\left(\epsilon^2\right), \tag{7.93}$$

where the function

$$\mathcal{D} = \frac{\partial}{\partial s}\left(\widetilde{\left.\frac{\partial \phi_2}{\partial t}\right|_{z=0}} \right) - \overline{\frac{\partial^2 \phi_2}{\partial s \partial t}} + O(\epsilon), \tag{7.94}$$

represents frequency dispersion. Combining these expressions and the expansion for the area (7.51) with (7.92) yields

$$(1 - \Upsilon \mu \kappa \sigma_c) \frac{\partial \langle u\rangle}{\partial t} + \frac{\partial \widetilde{\eta}}{\partial s} + \epsilon \langle u\rangle \frac{\partial \langle u\rangle}{\partial s} + \mu^2 \mathcal{D} = O(\Upsilon \epsilon). \tag{7.95}$$

Boundary value problem to solve for $\mathcal{D}$

A boundary value problem must be solved to obtain the expression for $\mathcal{D}$. As this function is factored by μ^2 in (7.95), it suffices to find expressions for ϕ_2 to the leading order. Since the flow is assumed irrotational, equation (7.38) can be written in terms of the velocity potential $\nabla\phi = \mathbf{U}$

$$\frac{\partial^2 \phi_2}{\partial \sigma^2} + \frac{\partial^2 \phi_2}{\partial z^2} - \Upsilon \mu \frac{\kappa}{J} \frac{\partial \phi_2}{\partial \sigma} = -\frac{1}{J}\frac{\partial u}{\partial s}, \tag{7.96}$$

where the perturbation of the potential (7.56) has been invoked. Using the relation $u_1 = \langle u\rangle + O(\epsilon)$ obtained from (7.58) and expanding the Jacobian (7.37) yields

$$\frac{\partial^2 \phi_2}{\partial \sigma^2} + \frac{\partial^2 \phi_2}{\partial z^2} = -\frac{\partial \langle u\rangle}{\partial s} + O(\Upsilon \mu). \tag{7.97}$$

The free surface kinematic boundary condition (3.24) can be written as

$$\frac{\partial \phi}{\partial z} = \mu^2 \frac{\partial \eta}{\partial t} + \frac{\epsilon \mu^2}{J} u \frac{\partial \eta}{\partial s} + \mu^2 v \frac{\partial \eta}{\partial \sigma}, \qquad \text{on} \quad z = \epsilon \eta(s, \sigma, t), \tag{7.98}$$

where, due to the Taylor expansion

$$\left.\frac{\partial \phi}{\partial z}\right|_{z=0} + \epsilon \eta \left.\frac{\partial^2 \phi}{\partial z^2}\right|_{z=0} = \mu^2 \frac{\partial \eta}{\partial t} + O\left(\epsilon \mu^2\right). \tag{7.99}$$

Invoking (7.56) and the relation $\widetilde{\eta} = \eta + O\left(\mu^2\right)$ by virtue of (7.57) implies

$$\left.\frac{\partial \phi_2}{\partial z}\right|_{z=0} = \frac{\partial \widetilde{\eta}}{\partial t} + O(\epsilon). \tag{7.100}$$

Using the leading order approximation of (7.80) yields

$$\left.\frac{\partial \phi_2}{\partial z}\right|_{z=0} = -\frac{A_0}{B_0}\frac{\partial \langle u \rangle}{\partial s} - \frac{1}{B_0}\frac{\partial A_0}{\partial s}\langle u \rangle + O(\epsilon), \qquad \text{on} \quad z = 0. \tag{7.101}$$

The bottom boundary condition (3.25) can be recast as

$$(v, w)\left(\frac{\partial h}{\partial \sigma}, 1\right) = -\frac{\mu^2}{J} u \frac{\partial h}{\partial s}, \qquad \text{on} \quad z = -h(s, \sigma) \tag{7.102}$$

which by the definition of the Jacobian (7.37), has the same structure as for the straight channel. Following similar procedure -see equations (3.105) to (3.109)- implies

$$\frac{\partial \phi_2}{\partial \mathsf{n}} = -\frac{\frac{\partial h}{\partial s}}{\sqrt{\left(\frac{\partial h}{\partial \sigma}\right)^2 + 1}}\langle u \rangle + O\left(\Upsilon \mu^2\right), \qquad \text{on} \quad z = -h(s, \sigma). \tag{7.103}$$

Lateral boundary conditions are only necessary for vertical sidewalls at the still water level. In this case expressions (7.67) are reduced to $S_l = B_0(s)$ and $S_r = 0$, thus (7.43) and (7.44) become

$$v = 0, \qquad \text{on} \quad \sigma = 0, \tag{7.104}$$

$$v = \frac{\mu^2}{J_{(B_0)}}\frac{B_0}{\partial s} u, \qquad \text{on} \quad \sigma = B_0(s). \tag{7.105}$$

Invoking (7.56), (7.58) and (7.37) yields

$$\frac{\partial \phi_2}{\partial \sigma} = 0, \qquad \text{on} \quad \sigma = B_0(s), \tag{7.106}$$

$$\frac{\partial \phi_2}{\partial \sigma} = \frac{\partial B_0}{\partial s}\langle u \rangle + O(\Upsilon \mu), \qquad \text{on} \quad \sigma = B_0(s), \tag{7.107}$$

The boundary value problem for ϕ_2 given by (7.97), (7.101), (7.103), (7.106) and (7.107) is equivalent to that in a straight channel. Following similar procedure as

the one shown in Chapter 3, the following expression for the dispersive function can be found

$$\mathcal{D} = \alpha \frac{\partial \langle u \rangle}{\partial t} + \beta \frac{\partial^2 \langle u \rangle}{\partial t \partial s} + \gamma \frac{\partial^3 \langle u \rangle}{\partial t \partial s^2}, \tag{7.108}$$

where

$$\alpha(s) = \frac{\partial}{\partial s}\left[\widetilde{\chi_1|_{z=0}}\right] - \overline{\frac{\partial \chi_1}{\partial s}}, \tag{7.109}$$

$$\beta(s) = \widetilde{\chi_1|_{z=0}} - \overline{\chi_1} + \frac{\partial}{\partial s}\left[\widetilde{\chi_2|_{z=0}}\right] - \overline{\frac{\partial \chi_2}{\partial s}}, \tag{7.110}$$

$$\gamma(s) = \widetilde{\chi_2|_{z=0}} - \overline{\chi_2}, \tag{7.111}$$

depend on the cross-sectional geometry under the quiescent state and χ_1 and χ_2 are defined by the boundary value problems

$$\frac{\partial^2 \chi_1}{\partial y^2} + \frac{\partial^2 \chi_1}{\partial z^2} = 0 \qquad \text{on} \quad -h(s,\sigma) < z < 0, \tag{7.112}$$

$$\frac{\partial \chi_1}{\partial z} = -\frac{1}{B_0}\frac{dA_0}{ds} \qquad \text{on} \quad z = 0, \tag{7.113}$$

$$\frac{\partial \chi_1}{\partial n} = -\frac{\frac{\partial h}{\partial s}}{\sqrt{\left(\frac{\partial h}{\partial y}\right)^2 + 1}} \qquad \text{on} \quad z = -h(s,\sigma), \tag{7.114}$$

and

$$\frac{\partial^2 \chi_2}{\partial y^2} + \frac{\partial^2 \chi_2}{\partial z^2} = -1 \qquad \text{on} \quad -h(s,\sigma) < z < 0, \tag{7.115}$$

$$\frac{\partial \chi_2}{\partial z} = -\frac{A_0}{B_0} \qquad \text{on} \quad z = 0, \tag{7.116}$$

$$\frac{\partial \chi_2}{\partial n} = 0 \qquad \text{on} \quad z = -h(s,\sigma). \tag{7.117}$$

If the channel banks are vertical, additional boundary conditions are needed

$$\frac{\partial \chi_1}{\partial \sigma} = \left(-\frac{dB_0}{ds}, 0\right) \quad \text{and} \quad \frac{\partial \chi_2}{\partial \sigma} = 0, \qquad \text{on} \quad \sigma = B_0(s), 0. \tag{7.118}$$

Thus, the momentum equation (7.95) becomes

$$\begin{aligned}\left(1 + \mu^2\alpha - \Upsilon\mu\kappa\sigma_c\right)\frac{\partial \langle u \rangle}{\partial t} + \frac{\partial \widetilde{\eta}}{\partial s} + \epsilon \langle u \rangle \frac{\partial \langle u \rangle}{\partial s} \\ + \mu^2\beta\frac{\partial^2 \langle u \rangle}{\partial t \partial s} + \mu^2\gamma\frac{\partial^3 \langle u \rangle}{\partial t \partial s^2} = O\left(\Upsilon\epsilon\mu\right).\end{aligned} \tag{7.119}$$

Flow properties on a cross-sectional plane

The velocities components on a cross-sectional plane are, to $O(\Upsilon\epsilon\mu)$,

$$u(s,\sigma,z,t) = \langle u\rangle + \mu^2(\chi_1 - \overline{\chi_1})\frac{\partial\langle u\rangle}{\partial s} + \mu^2(\chi_2 - \overline{\chi_2})\frac{\partial^2\langle u\rangle}{\partial s^2}, \tag{7.120}$$

$$v(s,\sigma,z,t) = \mu^2\left(\frac{\partial\chi_1}{\partial y}\langle u\rangle + \frac{\partial\chi_2}{\partial y}\frac{\partial\langle u\rangle}{\partial s}\right), \tag{7.121}$$

$$w(s,\sigma,z,t) = \mu^2\left(\frac{\partial\chi_1}{\partial z}\langle u\rangle + \frac{\partial\chi_2}{\partial z}\frac{\partial\langle u\rangle}{\partial s}\right). \tag{7.122}$$

The surface elevation is given by

$$\eta(s,\sigma,t) = \widetilde{\eta} + \mu^2\left(\widetilde{\chi_1|_{z=0}} - \chi_1|_{z=0}\right)\frac{\partial\langle u\rangle}{\partial t} + \mu^2\left(\widetilde{\chi_2|_{z=0}} - \chi_2|_{z=0}\right)\frac{\partial^2\langle u\rangle}{\partial t\partial s}, \tag{7.123}$$

and the pressure by

$$p(s,\sigma,z,t) = \widetilde{\eta} + \mu^2\left(\widetilde{\chi_1|_{z=0}} - \chi_1\right)\frac{\partial\langle u\rangle}{\partial t} + \mu^2\left(\widetilde{\chi_2|_{z=0}} - \chi_2\right)\frac{\partial^2\langle u\rangle}{\partial t\partial s} - \frac{z}{\epsilon}. \tag{7.124}$$

7.3 Analysis of the equations for curved channels

The channel-mean equations for curved channels with a coordinate system located at the right sidewall under the quiescent state are analyzed herein. Alternative forms of equations considering coordinate systems in other positions are studied in Section 7.3.2. The equations of conservation of mass and momentum are

$$\begin{aligned}\left(1 - \Upsilon\mu\kappa\frac{B_0}{2}\right)\frac{\partial\widetilde{\eta}}{\partial t} + \epsilon\frac{B_0'}{B_0^2}\widetilde{\eta}\frac{\partial}{\partial s}(A_0\langle u\rangle)\\ + \frac{1}{B_0}\frac{\partial}{\partial s}([A_0 + \epsilon B_0\widetilde{\eta}]\langle u\rangle) - \Upsilon\mu\frac{\kappa}{B_0}\left(\Gamma\frac{\partial\langle u\rangle}{\partial s} + \vartheta\langle u\rangle\right) &= O(\Upsilon\epsilon\mu),\end{aligned} \tag{7.125}$$

$$\begin{aligned}\left(1 + \mu^2\alpha - \Upsilon\mu\kappa\sigma_c\right)\frac{\partial\langle u\rangle}{\partial t} + \frac{\partial\widetilde{\eta}}{\partial s} + \epsilon\langle u\rangle\frac{\partial\widetilde{\eta}\langle u\rangle}{\partial s}\\ + \mu^2\beta\frac{\partial^2\langle u\rangle}{\partial t\partial s} + \mu^2\gamma\frac{\partial^3\langle u\rangle}{\partial t\partial s^2} &= O(\Upsilon\epsilon\mu).\end{aligned} \tag{7.126}$$

It is first observed that the curvature terms are order $O(\Upsilon\mu)$, implying that for $\Upsilon = \mu$, they are the same order of magnitude than the nonlinear and dispersive terms. For $\Upsilon = \epsilon$, curvature effects become smaller in order of magnitude, and comparable to the effects of the viscous boundary layer proposed in Chapter 6. Note that for $\Upsilon = \epsilon$, the radius of curvature is larger (and the curvature smaller) than the former case. For both cases, however, the radius of curvature is significantly larger than the typical wavelength. As expected, equations (7.125) and (7.126) reduce to the corresponding equations for straight channels (3.95) and (3.124) when curvature is zero.

It should be noted that the leading order error of the terms which are independent of the curvature is $O\left(\epsilon^2, \epsilon\mu^2, \mu^4\right)$, as for the equations equations for straight channels (3.95) and (3.124). The order of magnitude of the leading error associated with the new terms for curved channels is $O(\Upsilon\epsilon\mu)$, implying the error is smaller for $\Upsilon = \epsilon$ than for $\Upsilon = \mu$.

The coefficients in the conservation of momentum have the same structure as for straight channels, i.e.

$$\alpha = \frac{\partial}{\partial s}\left[\widetilde{\chi_1|_{z=0}}\right] - \overline{\frac{\partial \chi_1}{\partial s}}, \tag{7.127}$$

$$\beta = \widetilde{\chi_1|_{z=0}} + \frac{\partial}{\partial s}\left[\widetilde{\chi_2|_{z=0}}\right] - \overline{\chi_1} - \overline{\frac{\partial \chi_2}{\partial s}}, \tag{7.128}$$

$$\gamma = \widetilde{\chi_2|_{z=0}} - \langle \chi_2 \rangle, \tag{7.129}$$

implying that to the order of approximation used, the perturbation solution does not capture the free surface tilting due to curvature. However, the fact that the curvilinear orthogonal coordinate system traces the channel is indeed an implicit inclusion of the curvature in the above equations. This is analogous to the free surface kinematic boundary condition in linear wave theory (e.g. Dean & Dalrymple, 1991; 3.11c), in which even if the nonlinear terms are assumed small

and the surface is not fully tracked, the surface motion is taken into account at the leading order. Note that the time dependent term in (7.125) is a function of the centroid of the surface width, $B_0/2$, whereas the local acceleration in (7.126) is a function of the centroid of the cross-sectional area at quiescent state

$$\sigma_c = \frac{\int_0^{B_0} \sigma h d\sigma}{\int_0^{B_0} h d\sigma} + O(\epsilon). \tag{7.130}$$

These centroids are generally different with the exception of symmetric channels, where $\sigma_c = B_0/2$. The new coefficients associated with curvature

$$\vartheta = \underbrace{\int_0^{B_0} \sigma \frac{\partial}{\partial \sigma}\left(h \frac{\partial \breve{\chi}_1}{\partial \sigma}\right) d\sigma}_{I_{11}} + \underbrace{\int_0^{B_0} h \frac{\partial \breve{\chi}_1}{\partial \sigma} d\sigma}_{I_{12}} - \underbrace{h_{(B_0)} B_0 \frac{\partial B_0}{\partial s}}_{I_{13}}, \tag{7.131}$$

$$\Gamma = \underbrace{\int_0^{B_0} \sigma \frac{\partial}{\partial \sigma}\left(h \frac{\partial \breve{\chi}_2}{\partial \sigma}\right) d\sigma}_{I_{14}} + \underbrace{\int_0^{B_0} h \frac{\partial \breve{\chi}_2}{\partial \sigma} d\sigma}_{I_{15}}, \tag{7.132}$$

depend on the cross-sectional geometry as the quiescent state. From the operational point of view this is an advantage since they are independent on the flow properties, thus can be precomputed. Furthermore, for special geometries, such a rectangular or triangular symmetric cross-sections, the terms involving χ_1 and χ_2 can be solved analytically.

It is worth noting that for uniform channels, $\alpha, \beta, \vartheta = 0$, since $\partial/\partial s = 0$ and $\chi_1 = 0$. The latter is based on the fact that the boundary value problem for χ_1 is forced only by changes on the cross-sectional geometry along the longitudinal axis. For symmetric channels, on the other hand, $I_{12}, I_{15} = 0$ since χ_1 and χ_2 are symmetric with respect to the center of the cross-section. Terms I_{11} and I_{14}, are nonzero since the integrand is not symmetric with respect to the horizontal axis. Finally, for the specific case of a rectangular channel, $\Gamma = 0$, since χ_2 is independent of the spanwise coordinate.

Phase speed

An analytic expression for the phase speed in a nonuniform channel of arbitrary cross-section with varying curvature is not pursued herein. The influence of curvature on the phase speed is assessed by means of the simplest case of a linear nondispersive wave propagating on a uniform channel with rectangular cross-section of depth h and constant curvature. For this specific geometry, equations (7.125) and (7.126) can be reduced, by cross-differentiating and subtracting, to

$$\frac{\partial^2 \widetilde{\eta}}{\partial t^2} - c^2 \frac{\partial^2 \widetilde{\eta}}{\partial s^2} = 0, \tag{7.133}$$

where the phase speed is

$$c^2 = \frac{h}{\left(1 - \Upsilon \mu \kappa \frac{B_0}{2}\right)^2} = h\left(1 + \Upsilon \mu \kappa B_0\right) + O\left(\Upsilon^2 \mu^2\right). \tag{7.134}$$

It is evident that curvature affects the phase speed as a second order effect. Indeed, for concave curves ($\kappa > 0$), the phase speed is larger due to the curvature than that of a straight channel, and viceversa. In a more general statement, wave features depend on the sign of the curvature κ, implying concave and convex channels behave differently. The explanation is found on geometrical grounds. Recall that the coordinate transform in the horizontal plane

$$x(s, \sigma) = \xi - \mu \sigma \sin\theta, \qquad \text{and} \qquad y(s, \sigma) = \zeta + \mu \sigma \cos\theta, \tag{7.135}$$

so that a differential displacement in x is given by

$$dx = \cos\left(1 - \Upsilon \mu \sigma \kappa\right) ds. \tag{7.136}$$

As shown in Figure 7.6, P_1 and P_2 are different points at the same σ coordinate in both a concave and convex channels. For a given increment ds, the displacement dx for a concave channel with $\kappa > 0$ is smaller that that of a convex channel

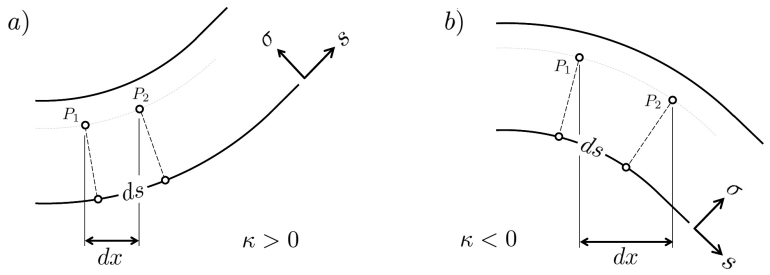

Figure 7.6: Geometrical interpretation of curvature effects in *a*) a concave channel and *b*) a convex channel.

with $\kappa < 0$. Therefore, the position of P_2 is different for both cases. This implies that the solutions for $\widetilde{\eta}$ and $\langle u \rangle$ for a same $s-$coordinate correspond to different cross-sections . Indeed, the area in the $s-\sigma$ plane covered by cross-sections passing through P_1 and P_2 are different. Note that for a straight channel, $dx = ds$, and the governing equations are reduced to those on a straight channel. A physical explanation on why the phase speed is larger (smaller) in concave (convex) channels when compared to a straight channel, remains however unrevealed.

The way in which curvature is incorporated in the present one-dimensional theory differs substantially from two- or three-dimensional theories. In a two-dimensional long wave problem in Cartesian coordinates (x, y), curvature is implicitly included in the governing equation through the boundary conditions and κ does not appear in the governing equations. For two-dimensional problems in general curvilinear coordinates (φ, ψ), curvature is also included through the boundary conditions whereas κ is embedded in the Jacobian. Note that in the latter, curvature is function of two dimensions, i.e. $\kappa(\varphi, \psi)$, whereas in the present theory, it only depends on s. In terms of the physics, two-dimensional theories are able to reproduce complex wave features at a higher computational costs, whereas the present theory only is able to account for flow features on cross-sections which are perpendicular to the main $s-$axis, at low costs.

7.3.1 Application of the new equations to a curved channel

The influence of curvature in the wave flow is explored by means of a simple case in this section. For convenience, hats are omitted for dimensional variables hereafter. Three transitions with different curvature in the horizontal plane are tested; namely an initially concave channel succeeded by a convex section (Figure 7.7.*a*), a straight channel (Figure 7.7.*b*) and a initially convex channel followed by a concave portion (Figure 7.7.*c*). Channels characterized by a rectangular uniform cross-section with a constant width of $B_0 = 1$ m and a depth of $h = h_0 = 1$ m are considered. The governing equations (7.125) and (7.126), in dimensional form, are reduced to

$$\left(1 - \kappa\frac{B_0}{2}\right)\frac{\partial\widetilde{\eta}}{\partial t} + h\frac{\partial\langle u\rangle}{\partial s} + \frac{\partial}{\partial s}\left(\widetilde{\eta}\langle u\rangle\right) = 0, \tag{7.137}$$

$$\left(1 - \kappa\frac{B_0}{2}\right)\frac{\partial\langle u\rangle}{\partial t} + g\frac{\partial\widetilde{\eta}}{\partial s} + \langle u\rangle\frac{\partial\widetilde{\eta}\langle u\rangle}{\partial s} + \gamma\frac{\partial^3\langle u\rangle}{\partial t\partial s^2} = 0, \tag{7.138}$$

where $h = A_0/B_0$ is the depth of the channel. An initial wave amplitude of $a_0 = 0.15$ m and a typical wavelength of $\lambda_0 = O(5\,\text{m})$ are considered. Nonlinear and frequency dispersion are characterized by $\epsilon = a_0/h_0 = O(0.1)$ and $\mu = h_0/\lambda_0 = O(0.2)$, so that the Boussinesq approximation is fulfilled. The geometry is defined in local $x - y$ coordinates with an origin at the beginning of the

Figure 7.7: Different geometries used to test the theory for curved channels. *a*) A straight channel with a concave-convex transition, *b*) a straight channel and *c*) a straight channel with a convex-concave transition.

transition. These curvature $\kappa(x, y)$ is then and then transformed into s coordinate, i.e. $\kappa(s)$. The transition has a sinusoidal shape of the form

$$y(x) = \begin{cases} 0 & x \leq 0 \\ A + A\sin(K_t x - \pi/2) & 0 < x \leq \pi/K_t \\ 2A & \pi/K_t < x \end{cases} \tag{7.139}$$

where A and K_t are chosen to satisfy the relation $B_0 \ll \lambda_0 \ll R$ implicit in the theory. For convenience, $A = 0, 25, 50, 75, 100$ m to assess the sensitivity of the solution, though results for $A = 100$ m are shown hereafter. The transition length is assumed to be 100 m; thus $K_t = 2\pi/200 = 0.0314$ m^{-1}. The curvature and the radius of curvature are given by

$$\kappa(x, y) = \frac{y_{xx}}{\left[1 + (y_x)^2\right]^{3/2}}, \qquad \text{and} \qquad R(x, y) = \frac{1}{\kappa}, \tag{7.140}$$

respectively. To compute the value of the curvature $\kappa(s)$, the arc length is defined by

$$s(x, y) = \int_0^s ds = \int_0^x \sqrt{1 + (y_x)^2}\, dx = \int_0^x \sqrt{1 + \left[AK_t \cos\left(K_t x - \frac{\pi}{2}\right)\right]^2}\, dx, \tag{7.141}$$

which is an elliptic integral of the second kind with no analytic solution, and is solved through numerical integration. The arclength, curvature and radius of curvature as functions of the x coordinate are depicted in Figure 7.8. Note that for big values of A, the radius of curvature R becomes comparable to the wavelength at the two extremes of the transition (e.g. $x = 0, 100$ m), violating the assumption $\lambda \ll R$, and consequently degrading the solution. Note that local effects are expected in the numerical computations since curvature is not continuous at these extremes.

Numerical results for wave evolution along the channels shown in Figure 7.7 are depicted in Figure 7.9. Surface profiles at different instant $\widetilde{\eta}(s)$ are depicted at

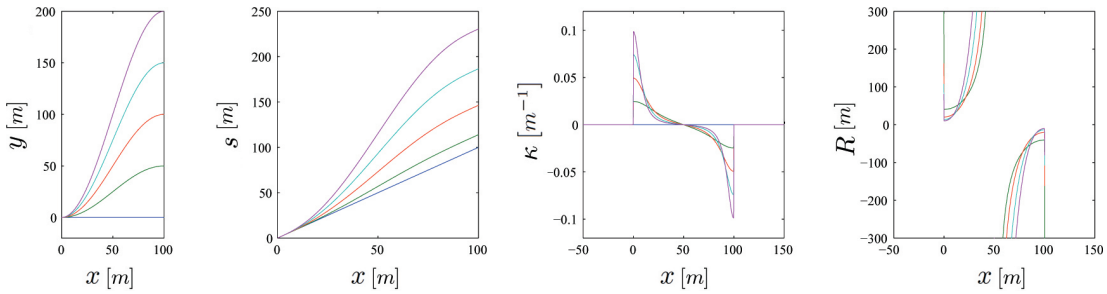

Figure 7.8: The arclength, curvature and radius of curvature as functions of the x coordinate for different values of A. Here $A = 0$ m (blue), $A = 25$ m (green), $A = 50$ m (red), $A = 75$ m (cyan) and $A = 100$ m (purple) are considered.

three different instants; namely at the point between the start and the midpoint of the transition where the curvature effect is more pronounced (panel *a*), near the center of the transition (panel *b*) and at the end of the transition (panel *c*). The maximum amplitude at each point during the simulation $\widetilde{\eta}_{max}(s)$ is depicted in panel *d*. The curvature obtained from equation (7.139) is shown in panel *e*. Note that the transition begins at $s = 50$ m, whereas the in local coordinates, it starts at $x = 0$ m.

Panel *a* shows that the point where the curvature effect on surface elevation is more pronounced ($x = 60$ m) occurs further downstream than the point where curvature is maximum ($x = 50$ m, panel *e*). This implies that the effect of curvature is not instantaneous and there is delay cause by the second order terms. At this point, waves in the concave-convex channel have propagated only through the concave section of the channel, resulting in a slight increase in the wave amplitude and phase speed with respect to the straight channel. For the convex-concave channel, waves have traveled through the convex section and the effects are opposite as a consequence of the change of sign in the curvature. In the latter, phase speed and amplitude are slightly lower than those for a straight

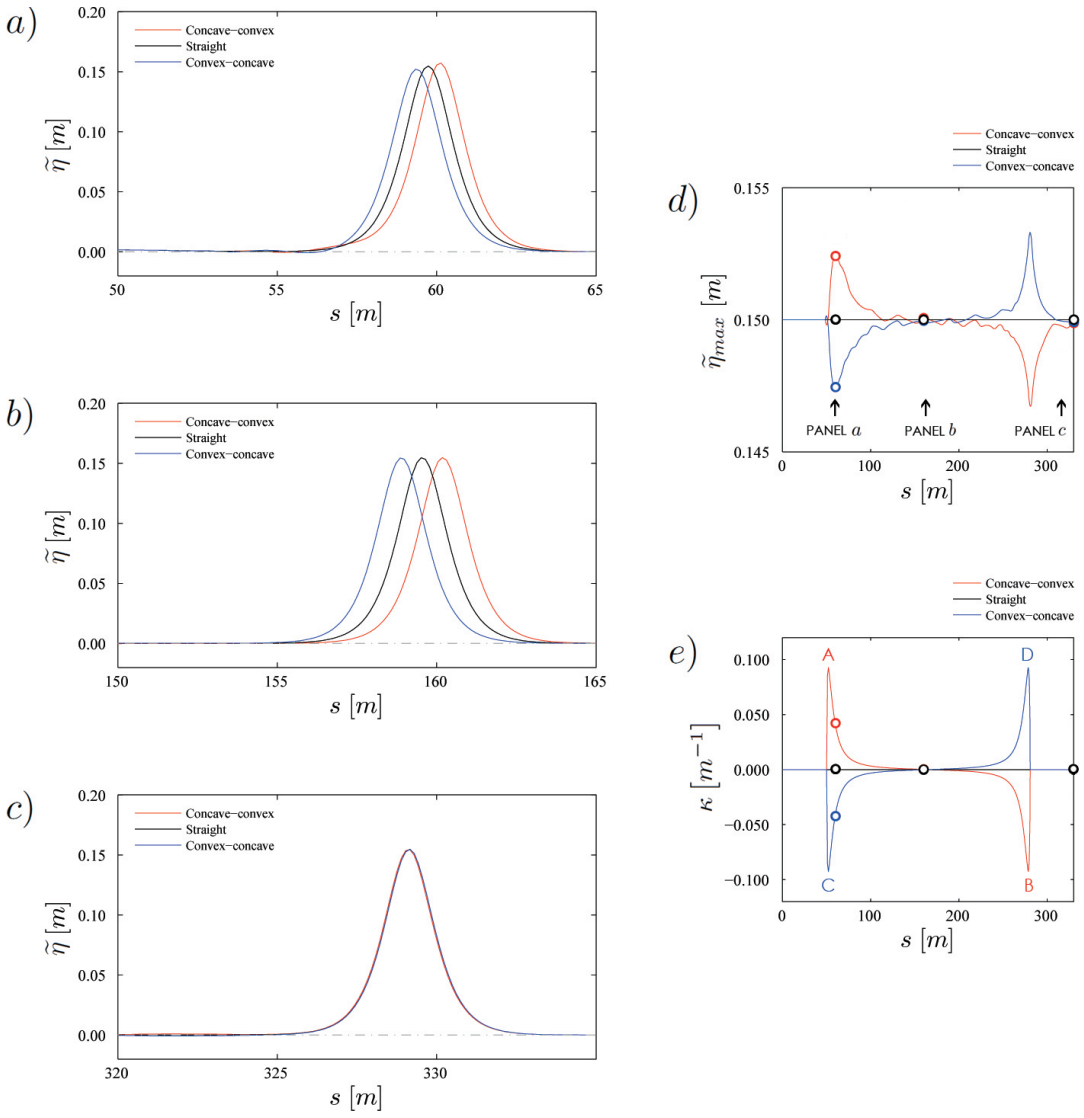

Figure 7.9: Numerical results for a straight channel with a concave-convex transition (red), a straight channel (black) and a straight channel with a convex-concave transition (blue). Surface profiles are shown a) where the curvature effect is more pronounced, *b*) at the center of the transition and *c*) at the end of the transition. Panel *d*) shows the maximum amplitude at each point during the simulation. Panel *e*) depict the curvature along the channels. The initiation (A,C) and end of the transitions (B,D) defined in Figure 7.7 are also included.

channel, and the reduction has the same magnitude as the increment for the concave-convex channel. It should be noted that these small differences are partly due to the fact that waves have traveled only about two wavelengths from the initiation of the transition.

Panel *b* shows that near the middle of the transition, the amplitude is almost equal in all channels but the position of the peak is slightly further for the concave-convex channel (x = 160.2 m) than for the convex channel (x = 158.9 m). This is a consequence of the difference in phase speeds triggered by the sign of the curvature in both cases. Finally, panel *c* shows that the waves have almost recovered the original form at the end of the transition for all cases, implying that the curvature effects are reversible. The trailing wave, however, is slightly different for both cases, but the difference is minor.

It is concluded that *a*) the solution for the wave field in a uniform rectangular channel with curvature in the horizontal plane is locally affected by the magnitude and sign of the curvature, *b*) curvature effects are reversible in channels that recover the alignment after a sinusoidal transition and that *c*) cumulative effects of curvature, such as the generation of trailing waves, appear to be minor. The generalization of all or some of these features to non-symmetric transitions or channels of non-symmetric cross-sections cannot be done at this stage.

7.3.2 Alternative forms of the channel-mean equations

The interesting question on how the location of the coordinate system affects the wave features is addressed in this section. Alternative forms of the governing

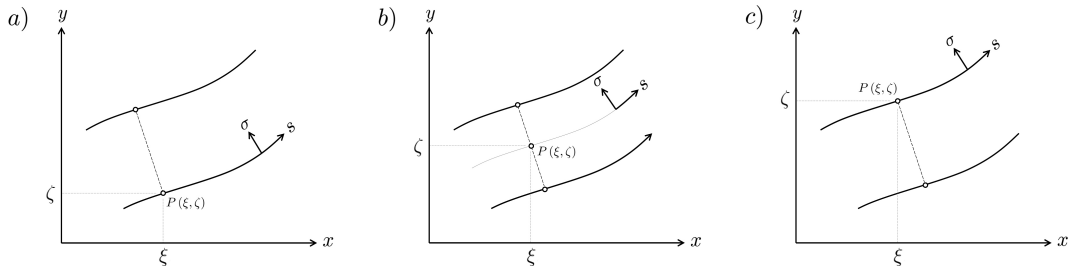

Figure 7.10: Coordinate systems located *a*) at the right sidewall at SWL, *b*) at the center-line at SWL *c*) at the left sidewall under at SWL.

equations considering coordinate systems located at the center-line of the cross-section and at the left sidewall under the quiescent state (SWL) are considered. The derivation of these alternative forms is analogous to the former and thus is omitted herein. Figure 7.10 shows these new coordinate systems and the one used in the previous section. Note that for the same $x = \xi$ position, the cross-section is not the same for all three coordinate systems, thus the results are not strictly equivalent.

Coordinate system located at the center of the channel

For the coordinate system located at the center of the channel at SWL (7.3.2.*b*), the equations of conservation of mass and momentum are

$$\begin{aligned} &\frac{\partial \widetilde{\eta}}{\partial t} + \epsilon \frac{B_0'}{B_0^2} \widetilde{\eta} \frac{\partial}{\partial s} \left(A_0 \langle u \rangle\right) \\ &+ \frac{1}{B_0} \frac{\partial}{\partial s} \left(\left[A_0 + \epsilon B_0 \widetilde{\eta}\right] \langle u \rangle\right) - \Upsilon \mu \frac{\kappa}{B_0} \left(\Gamma \frac{\partial \langle u \rangle}{\partial s} + \vartheta \langle u \rangle\right) \quad = O\left(\Upsilon \epsilon \mu\right), \end{aligned} \tag{7.142}$$

$$\begin{aligned} &\left(1 + \mu^2 \alpha - \Upsilon \mu \kappa \sigma_c\right) \frac{\partial \langle u \rangle}{\partial t} + \frac{\partial \widetilde{\eta}}{\partial s} + \epsilon \langle u \rangle \frac{\partial \widetilde{\eta} \langle u \rangle}{\partial s} \\ &+ \mu^2 \beta \frac{\partial^2 \langle u \rangle}{\partial t \partial s} + \mu^2 \gamma \frac{\partial^3 \langle u \rangle}{\partial t \partial s^2} \quad = O\left(\Upsilon \epsilon \mu\right). \end{aligned} \tag{7.143}$$

The coefficients in the equation of conservation of mass are

$$\vartheta = \underbrace{\int_{-B_0/2}^{B_0/2} \sigma \frac{\partial}{\partial \sigma}\left(h \frac{\partial \check{\chi}_1}{\partial \sigma}\right) d\sigma}_{I_{21}} + \underbrace{\int_{-B_0/2}^{B_0/2} h \frac{\partial \check{\chi}_1}{\partial \sigma} d\sigma}_{I_{22}} - \underbrace{\left[h_{\left(\frac{B_0}{2}\right)} - h_{\left(-\frac{B_0}{2}\right)}\right] \frac{B_0}{4} \frac{\partial B_0}{\partial s}}_{I_{23}}, \quad (7.144)$$

$$\Gamma = \underbrace{\int_{-B_0/2}^{B_0/2} \sigma \frac{\partial}{\partial \sigma}\left(h \frac{\partial \check{\chi}_2}{\partial \sigma}\right) d\sigma}_{I_{24}} + \underbrace{\int_{-B_0/2}^{B_0/2} h \frac{\partial \check{\chi}_2}{\partial \sigma} d\sigma}_{I_{25}}, \quad (7.145)$$

and the centroid of the cross-section reads

$$\sigma_c = \frac{\int_{-B_0/2}^{B_0/2} \sigma h d\sigma}{\int_{-B_0/2}^{B_0/2} h d\sigma}. \quad (7.146)$$

Expressions for α, β and γ retain the structure of equations (7.127) to (7.129). Some similarities and differences are observed with respect to equations (7.125) and (7.132), stemming from a coordinate system positioned at the right sidewall. Among the similarities, it is observed that *i*) asymmetry in the cross-sectional geometry is responsible for the appearance of the curvature terms involving ϑ and Γ, and *ii*) for the specific case of uniform channels, $\vartheta = 0$.

As for differences, it is first noted that there is no curvature term in the time varying derivative of the conservation of mass (7.142). This implies that, for the specific example of a rectangular uniform channel with curvature shown in the previous section, mass is conserved regardless of the curvature. A second feature arises in channels with symmetric cross-sections. For example, for a symmetric triangular channel where the coordinate system is located at the center of the cross-section, functions and χ_1 and χ_2 (See Appendix C)

$$\chi_1(\sigma, z) = -\frac{1}{2}\left(\frac{H}{B_0}\frac{\partial B_0}{\partial s} + \frac{\partial H}{\partial s}\right) z + \left(\frac{1}{4H}\frac{\partial H}{\partial s} - \frac{1}{4B_0}\frac{\partial B_0}{\partial s}\right)\left(z^2 - \sigma^2\right), \quad (7.147)$$

$$\chi_2(\sigma, z) = -\frac{1}{4}\left(2Hz + z^2 + \sigma^2\right). \quad (7.148)$$

are even, thus their derivatives $\partial\chi_i/\partial\sigma$ $(i = 1, 2)$ are odd. Given that h is even, the integrands in I_{22} and I_{25} vanish. The same argument applies to the integrands in I_{21} and I_{24}, thus $\Gamma = 0$. Due to symmetry I_{23} also vanishes therefore $\vartheta = 0$. It is concluded that for symmetric channels with a coordinate system at the center of the cross-section, there is no explicit contribution of curvature in the governing equations. An explanation of why these terms disappear is not given other than with mathematical arguments. Finally, the expression for the phase speed for a linear nondispersive wave propagating on a uniform channel with rectangular cross-section of depth

$$c^2 = h + O\left(\Upsilon^2\mu^2\right), \tag{7.149}$$

is also independent of the curvature. For a coordinate system located at the center or the channel at quiescent state, it is concluded that curvature is only explicit when the cross-section is asymmetric. Indeed, if the cross-section is symmetric, the governing equations (7.142) and (7.143) are simplified to those in a rectangular channel (3.95) and (3.124). Curvature, however, is implicitly used in the adoption of a coordinate system following the geometry of the channel.

Coordinate system located at at the left sidewall

For the sake of completeness, the system of equations for a coordinate system at the left sidewall at SWL is presented below. The conservation of mass and momentum are

$$\begin{aligned}
&\left(1 + \Upsilon\mu\kappa\frac{B_0}{2}\right)\frac{\partial\widetilde{\eta}}{\partial t} + \epsilon\frac{B_0'}{B_0^2}\widetilde{\eta}\frac{\partial}{\partial s}\left(A_0\langle u\rangle\right) \\
&+\frac{1}{B_0}\frac{\partial}{\partial s}\left(\left[A_0 + \epsilon B_0\widetilde{\eta}\right]\langle u\rangle\right) - \Upsilon\mu\kappa\left(\Gamma\frac{\partial\langle u\rangle}{\partial s} + \vartheta\langle u\rangle\right) = O\left(\Upsilon\epsilon\mu\right),
\end{aligned} \tag{7.150}$$

$$\left(1 + \mu^2\alpha - \Upsilon\mu\kappa\sigma_c\right)\frac{\partial\langle u\rangle}{\partial t} + \frac{\partial\widetilde{\eta}}{\partial s} + \epsilon\langle u\rangle\frac{\partial\widetilde{\eta}\langle u\rangle}{\partial s}$$

$$+\mu^2\beta\frac{\partial^2\langle u\rangle}{\partial t\partial s}+\mu^2\gamma\frac{\partial^3\langle u\rangle}{\partial t\partial s^2} \quad = O\left(\Upsilon\epsilon\mu\right). \tag{7.151}$$

The coefficients in the equation of conservation of mass are

$$\vartheta = \int_{-B_0}^{0}\sigma\frac{\partial}{\partial\sigma}\left(h\frac{\partial\check{\chi}_1}{\partial\sigma}\right)d\sigma+\int_{-B_0}^{0}h\frac{\partial\check{\chi}_1}{\partial\sigma}d\sigma+h_{(-B_0)}B_0\frac{\partial B_0}{\partial s}, \tag{7.152}$$

$$\Gamma = \int_{-B_0}^{0}\sigma\frac{\partial}{\partial\sigma}\left(h\frac{\partial\check{\chi}_2}{\partial\sigma}\right)d\sigma+\int_{-B_0}^{0}h\frac{\partial\check{\chi}_2}{\partial\sigma}d\sigma \tag{7.153}$$

and the centroid of the cross-section reads

$$\sigma_c = \frac{\int_{-B_0}^{0}\sigma h d\sigma}{\int_{-B_0}^{0}h d\sigma}+O\left(\epsilon\right). \tag{7.154}$$

Finally, the phase speed becomes

$$c^2=\overline{h}\left(1-\Upsilon\mu\kappa B_0\right)+O\left(\Upsilon^2\mu^2\right) \tag{7.155}$$

Compared to the system of equations for a coordinate system positioned in the right sidewall, it is observed that the limits of all integrals change, and that the curvature term multiplying the time varying derivative changes sign. A practical consequence is, for example, that in this case the phase speed will be comparative smaller for the same value of the curvature. It is also concluded that the solutions for the cross-sectional averaged quantities depend on the choice of the coordinate system used.

CHAPTER 8

CONCLUDING REMARKS

A theory for long waves propagating in channels with arbitrary cross-sections is developed and checked with laboratory experimental data. Significant changes of the channel geometry within a wavelength in the direction of wave propagation are allowed in the new theory, which is constructed by properly integrating the three-dimensional equations for irrotational flows over a channel cross-section and applying the free surface and bottom boundary conditions. The resulting one-dimensional governing equations are expressed in terms of the cross-sectionally averaged velocity component in the direction of wave propagation and the spanwise averaged free surface elevation. The Boussinesq approximation is adopted and the channel's sidewall slopes are assumed to be either of order one, or vertical. The governing equations include coefficients depending only on the channel geometry, which can be solved from boundary value problems defined on the cross-section. In other words, wave features such as amplitude modulation and dispersion are affected by the channel configuration. The velocity, free surface variation and pressure on a cross-section can be recovered once Boussinesq-type equations are solved for the unknown channel averaged quantities.

Following Liu & Orfila's (2004) approach, viscous effects in the bottom boundary layer are heuristically included. The boundary layer, driven by the cross-sectionally averaged pressure gradient in the direction of wave propagation, induces a normal mass flux into the core region, where the velocity is irrotational. The continuity equation is modified accordingly. The role of viscous dissipation partly explains the differences between theory and experimental data obtained

in earlier studies (Chang *et al.*, 1979; Kirby & Vengayil, 1988).

The present theory is used to investigate solitary wave propagation in straight channels with rectangular, triangular and trapezoidal cross-sections. Solitary wave characteristics, such as the wave profile, phase speed and the cross-sectional flow properties, are modified according to the geometry. Numerical computations in uniform channels show spanwise changes in the surface elevation for trapezoidal and triangular cross-sections, which were also observed in earlier experiments (Sandover & Taylor, 1962; Peregrine, 1969; Treske, 1994 and Teng & Wu, 1997). However, other flow features such as *i*) the tendency for waves to break at the sidewall slopes, *ii*) the generation of bores for relatively high wave amplitudes, *iii*) the curvature of the wave crest across the channel, *iv*) the fish-tail pattern observed in the trailing waves and *v*) the generation of unsteady trailing waves, cannot be captured. This is because the longitudinal- and cross-flows are decoupled in the present theory, thus two-dimensional phenomena such as refraction or reflection on the sidewalls are not considered.

The present theory is validated with experimental data for solitary wave evolution in converging and diverging rectangular channels (Chang *et al.*, 1979) and for solitary waves in a uniform channel with a beach slope (Liu *et al.*, 2006). It is shown that the theory with the consideration of viscous boundary layer flows give a good agreement with the experiments. However, in the diverging channels, the agreement is less satisfactory.

By means of studying a hypothetical case, the role of the new terms containing α and β is shown to be significant when waves undergo significant changes in the geometry of the channel within a wavelength, i.e. $dA_0/dx = O(1)$. The relative difference in wave amplitude estimated by the present and Teng & Wu's (1997)

theory can be of the order of 10% after a contraction of a length comparable to the wavelength, and is strongly dependent on the nonlinearity and the cross-sectional geometry.

The one-dimensional cross-sectional averaged long wave model for straight channels is extended to account for the effects of curvature in channels, where the radius of curvature is significantly larger than the typical wavelength. The derivation is based on a specific set of orthogonal curvilinear coordinates, defined from one of the channel's sidewalls. The resulting equations explicitly contain the curvature and new coefficients only depending on the channels geometry. To the order of approximation used, the perturbation solution does not capture the free surface tilting due to curvature. However, the fact that the curvilinear orthogonal coordinate system traces the channel is indeed an implicit inclusion of the curvature in the above equations. From simple examples, it is concluded that the wave field is locally affected by the magnitude and sign of the curvature and cumulative effects of curvature appear to be minor in meandering channels. Finally, the solution for the cross-sectional averaged quantities depends on the position of the coordinate system used.

The present theory could make an important contribution for studying natural streams with arbitrary geometries, when significant changes appear in the along stream direction.

APPENDIX A

ANALYSIS OF 1D THEORIES

The governing equations for the existing one-dimensional theories for channels of arbitrary cross-section (Peregrine, 1968 and 1969; Shen, 1969; Fenton, 1973; Shuto, 1974; Chou, 1981; Kirby & Vengayil, 1988; Teng, 1990 and 2000 and Teng & Wu, 1992, 1994 and 1997) are summarized in this Appendix. For convenience, the original nomenclature and scaling have deliberately been retained and do not necessarily correspond to the present derivation. The reader is referred to the original papers for further analysis. Peters (1966) is not analyzed as it was derived specifically for solitary waves. The work by Teng and Teng & Wu is grouped into Teng & Wu's 1997 theory. Figure A.1 shows typical bathymetric features assumed in each theory.

A.1 Peregrine's 1968 theory

Peregrine (1968) derived Boussinesq and KdV-type equations for long waves in a uniform channel of arbitrary cross-section, based on the assumption that the wave motion along the channel dominates the flow structure. This theory follows a slightly different normalization as the one proposed by Peregrine (1967) in his seminal paper on long waves on a beach.

Peregrine introduces two approaches to obtain the surface elevation $\zeta(x, y, t)$ and the longitudinal velocity $u(x, y, z, t)$. The first approach is achieved by means of the standard perturbation technique. In the first order approximation the pressure is hydrostatic, the surface elevation and the longitudinal velocity are uniform on the cross-section. The second order approximation incorporates the

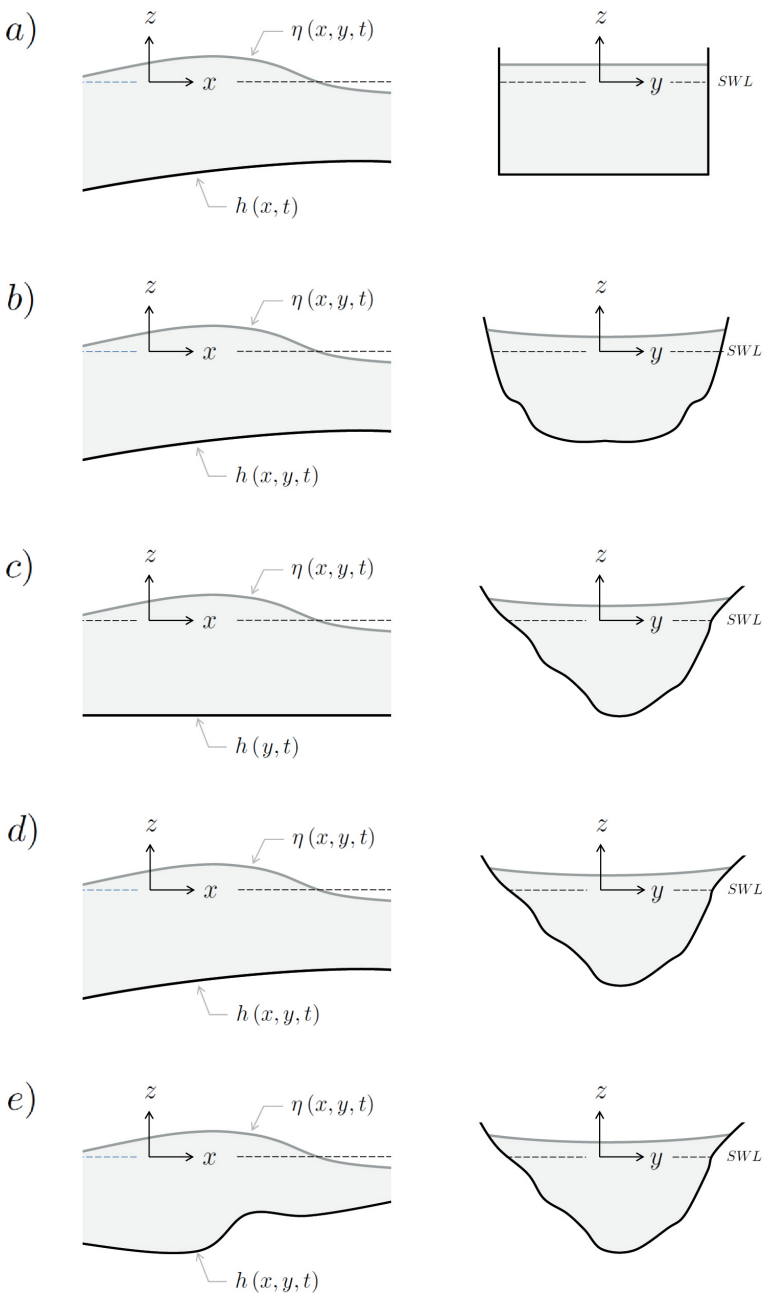

Figure A.1: Cross-sectional features in the existing theories. *a*) Rectangular and slowly varying cross-section analyzed by Shuto (1974) and Kirby & Vengayil (1988). *b*) Symmetric and slowly-varying cross-section studied by Teng & Wu (1997). *c*) Arbitrary and uniform cross-section studied by Peregrine (1968), Shen (1969) and Fenton (1973). *d*) Arbitrary and slowly-varying cross-section studied by Chou (1981) *e*) Arbitrary cross-section with significant changes within a wavelength used in the present theory.

effects of vertical and transverse accelerations of water particles on the pressure, resulting in a variation of the surface elevation and longitudinal velocity across the channel. Peregrine argues that this approach is straightforward for finding approximations to the equations of motion, but inconvenient for finding their solutions, which are valid only for $t_1 = O(1)$. The second approach is based upon the auxiliary variables $\eta(x,t)$ and $u'(x,t)$, which are then related to the physical variables $\zeta(x,y,t)$ and $u(x,y,z,t)$, once the function $\psi(y,z)$ is computed for each cross-section. This solution appears not to depend on the restriction, $t_1 = O(1)$. The non-dimensional mass and momentum equations (P68, eqs. 21,19) are

$$\frac{\partial}{\partial t}\left(\eta + \frac{1}{2}b\eta^2\right) + \frac{\partial}{\partial x}\left(c_0^2 u' + \eta u'\right) + (\psi_B - \psi_A)\frac{\partial^3 u'}{\partial x \partial t^2} = 0, \tag{A.1}$$

$$\frac{\partial u'}{\partial t} + u'\frac{\partial u'}{\partial x} + \frac{\partial \eta}{\partial x} = 0, \tag{A.2}$$

where x is space and t time, $b = B'(0)/B(0)$ is the ratio of the sidewall slope and the width of the channel evaluated at the still level, A_0 the cross-sectional area under the quiescent state and the phase velocity is defined by $c_0^2 = A_0/B_0$, with $B_0 = B(0)$. The nonlinear term $\frac{\partial}{\partial t}\left(\frac{1}{2}b\eta^2\right)$ represents the sidewall effects at the still water level and $(\psi_B - \psi_A)\frac{\partial^3 u'}{\partial x \partial t^2}$ accounts for dispersive effects caused by vertical acceleration, the departure from the hydrostatic pressure distribution and the cross-sectional channel configuration. The functions ψ_A and ψ_B are defined as (P68 eqs.15,13)

$$\psi_A = \frac{1}{A_0}\int\int_{A_0} \psi(y,z)\,dydz, \qquad \psi_B = \frac{1}{B_0}\int_0^{B_0} \psi(y,0)\,dy, \tag{A.3}$$

where $\psi(y,z)$ satisfies the boundary value problem given by (P68, eq.8)

$$\frac{\partial^2 \psi}{\partial y^2} + \frac{\partial^2 \psi}{\partial z^2} = 1, \qquad -h < z < 0, \tag{A.4}$$

$$\frac{\partial \psi}{\partial z} = c_0^2, \qquad z = 0, \tag{A.5}$$

$$\frac{\partial \psi}{\partial n} = 0, \qquad z = -h. \tag{A.6}$$

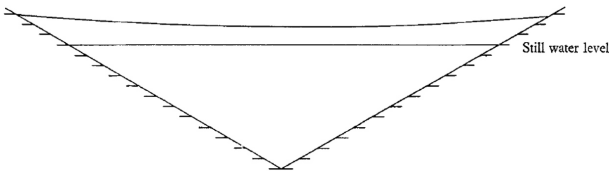

Figure A.2: Solitary wave elevation on a channel of triangular cross-section. P68 computation was carried out for sides of the channel at 60°to the vertical and the amplitude of the wave at the center equal to one third of the mean depth.

The corresponding non-dimensional KdV equation is (P68, eq.22)

$$\frac{\partial u'}{\partial t} + c_0 \frac{\partial u'}{\partial x} + \left(\frac{3 - bc_0^2}{2}\right) u' \frac{\partial u'}{\partial x} - \left(\frac{\psi_B - \psi_A}{2}\right) \frac{\partial^3 u'}{\partial x^2 \partial t} = 0. \tag{A.7}$$

The auxiliary variables $\eta(x,t)$ and $u'(x,t)$ are related to the physical variables $\zeta(x,y,t)$ and $u(x,y,z,t)$ through the expressions (not explicitly derived in the original paper)

$$\zeta = \eta - \frac{B_0}{A_0} \frac{\partial^2 \eta}{\partial t^2} \psi(y,0) + O\left(\delta^3\right), \qquad u = u' + \frac{B_0}{A_0} \frac{\partial^2 \eta}{\partial t \partial x} \psi(y,z) + O\left(\delta^3\right). \tag{A.8}$$

Figure A.2 depicts the cross-sectional changes in the surface elevation for a channel with uniform triangular cross-section computed by P68.

The cross-sectional potential $\phi_1(x_1, y, z, t_1)$ is related to the function $\psi(y,z)$ via $\phi_1 = -\partial u_1/\partial x_1 \psi$, from which the leading order approximation of the transverse velocities can be computed using $v_1 = \partial \phi_1/\partial y$ and $w_1 = \partial \phi_1/\partial z$. The transverse velocities are computed from the expansion $v = \varepsilon^{3/2} v_1$ and $w = \varepsilon^{3/2} w_1$, where ε is the nonlinearity. To the second order, the pressure can be recovered once ψ and u are known.

Peregrine (1969) carried out experimental measurements of the variation of surface elevation across the crests of waves on a fixed position of a trapezoidal channel. Evolution along the channel was not studied and indeed he assumed that the undulations photographed were solitary waves. A rather rudimentary

system of a manually-operated moving vertical paddle was used to generate the waves. The channel had one vertical side and the other side sloped at either 30°, 45° and 60°. The experiments were conducted in a horizontal channel 28 ft long with a rectangular cross-section 30 in wide and 15 in deep. The surface elevation across the crests was compared to P68 theory, showing reasonable agreement for slopes of 30° and 45°. Reliable results were not obtained with a slope of 60°, where waves became somewhat unsteady and three-dimensional effects, such as the fish tail waves mentioned by Sandover and Taylor (1962), became important. Peregrine argues that this behavior is expected as the theory assumes sidewall effects are small. Interestingly, the theory matched the measurements when the waves were close to breaking, even though the surface gradients were so steep that the assumptions on which the theory is based do not hold.

P68 provide a closed system for the problem of weakly-nonlinear, weakly-dispersive long waves propagating in a channel of arbitrary uniform cross-section. The theory appears to be of simple application by is unfortunately restricted to few cases where uniform sections can be assumed. Besides, Peregrine did not pursue computations on long wave evolution.

A.2 Shen's 1969 theory

An asymptotic theory of unsteady finite-amplitude waves in a channel of arbitrary cross-section was derived by means of a multiple-parameter singular perturbation scheme based upon a stretching technique. The theory provides solutions for different long waves regimes ($\delta_1 > \alpha^2$, $\delta_1 = \alpha^2$ and $\delta_1 < \alpha^2$, where δ_1 and

α are related to the wave amplitude and longitudinal length scales respectively) but focuses attention in Boussinesq waves ($\delta_1 = \alpha^2$). No further simplification to KdV equations is pursued. For the Boussinesq regime, Shen uses a standard perturbation technique to find the zeroth and first order approximations. The first order non-dimensional approximation (S69, eqs.25,27,67) resembles the classical two-dimensional shallow water theory for constant depth

$$\frac{\partial u_0}{\partial t} + u_0 \frac{\partial u_0}{\partial x} + \frac{\partial \eta_0}{\partial x} = 0 \tag{A.9}$$

$$\frac{\partial \eta_0}{\partial t} + u_0 \frac{\partial \eta_0}{\partial x} + \frac{A}{z_2 - z_1} \frac{\partial u_0}{\partial x} = 0, \tag{A.10}$$

where x is space and t time, η_0 and u_0 are the leading order solutions for the surface elevation and longitudinal velocity, A is the cross-sectional area, and z_1 and z_2 the intersections of the instantaneous surface with the channel boundaries. Differences in Peregrine's leading order approximation (P68, eqs.6,7) and Shen's equations (A.9) and (A.10) arise in the nonlinear nature of the latter. At this order, the solution for the transverse velocities (S69 eq.28)

$$v_0 = \frac{\partial \psi}{\partial y}, \qquad w_0 = \frac{\partial \psi}{\partial z} \tag{A.11}$$

requires the solution of a BVP on the variable ϕ, with $\psi(x, y, z, t) = -\frac{\partial u_0}{\partial x} \phi(x, y, z, t)$ (S69, eq.32), which has a similar structure as other theories. Shen's boundary value problem, however, is defined in a variable domain where $z = \eta_0$ appears as a parameter, making the calculation coupled with the longitudinal flow (in other theories the surface boundary is evaluated at the still level). Lateral variations in flow properties are found to be caused by changes in the axial velocity through the $\frac{\partial u_0}{\partial x}$ term. The second order approximation provides a system of partial differential equations (S69, eqs.47,48) for variables $F(x, t)$ and $G(x, t)$ in a similar fashion as P68's second order approximation (P68 functions H and U). Due to the extension, the reader is referred to the original paper. Once

these variables are solved, the second order pressure p_1, surface elevation η_1 and velocity u_1 can be obtained (S69, eqs.40-42). The transverse velocities are not explicitly reported but the procedure to compute them is outlined. Transverse effects on the surface elevation due to the non-rectangular cross-section are accounted for (S69, η_1 in p.269) but no solution is elaborated.

In the author's opinion, the approach of successively finding solutions for the first- and second-order approximation may be cumbersome, S69 theory is no further analyzed.

A.3 Fenton's 1973 theory

A steady nonlinear dispersive theory developed in terms of three invariants of channel flow (i.e. the volume flow rate Q, the energy per unit mass at any point R and momentum flux divided by density S) was derived following Benjamin & Lighthill's (1954) approach for rectangular channels. Fenton delivers a KdV equation for unidirectional flows limited to channels which are not broad (F73, eq.3.24). The steady condition reflects that the solution is given on a frame of reference moving with the wave. A boundary value problem on the undisturbed cross-section of the channel (F73, eqs. 3.7-3.11), needs to be solved for $V(y_1, z_1)$, from which the quantity $P_1(y, z)$ (F73, eq. 3.4) is computed. This quantity is later used in one of the constant coefficients, θ_4, of the governing equation. Due to the multiple equations and quantities defined, the reader is referred to the original paper. The KdV model is solved to give the expressions for cnoidal waves and the theory is used to study the bore problem, showing that earlier studies using the linear wave theory are invalid. The governing equation is

not converted back to a fixed coordinate system and therefore the theory is not fully operational. Due to the KdV approximation, the theory cannot account for bidirectional waves or reflection; consequently, mass conservation is not fulfilled. These, plus it's limitation to regular cross-section makes its application to channels of non-uniform cross section, the main concern of this dissertation, inappropriate.

A.4 Shuto's 1974 theory

Shuto developed a KdV-type equation for waves in a non-uniform rectangular channel where non-linearity, dispersion and changes in width and depth were assumed small. An advantage of Shuto's theory is that, due to the simple geometry, the effects of varying depth and width are explicit in the governing equation. This allows the study of shoaling due to changes on the depth or width along the channel. The dimensional KdV equation moving approximately with the wave (S74, eq.45) is

$$\alpha\frac{\partial\eta_0}{\partial X}+\frac{3}{2\sqrt{d^3}}\eta_0\frac{\partial\eta_0}{\partial\xi}+\frac{\kappa}{6}\sqrt{d}\frac{\partial^3\eta_0}{\partial\xi^3}+\frac{\gamma}{2}\frac{b'}{b}\eta_0+\frac{\sigma}{4}\frac{d'}{d}\eta_0=0, \tag{A.12}$$

where x is the space and t represents time, $\eta_0(x,t)$ is the first order surface elevation, $b(x)$ the width, $d(x)$ the still water depth and α, γ and σ are scaling coefficients. A moving and stretched coordinate system ξ and X is used following Johnson's (1973) approach (S74, eq.18)

$$\xi=\int^x\frac{dx}{\sqrt{d}}-t, \qquad\qquad X=\alpha\varepsilon x, \tag{A.13}$$

The ξ-coordinate coincides with the wave frame which moves in the positive x-direction with a local linearized dimensionless wave speed $\sqrt{d}$. When observed

from the X-coordinate, spatial changes with respect to x are small. The Ursell parameter κ^{-1} represents the ratio of the non-linearity ε and relative depth δ. The parameter α is used to scale the $x-$axis, σ to scale the longitudinal variation of the depth (S74, eq.25) and γ the longitudinal variation of the width (S74, eq.26). These parameters are used to compare the relative values of each term in succeeding approximations of the equation. The primes h' and b' represent differentiation with respect to $\sigma\varepsilon x$ and $\gamma\varepsilon x$, respectively,

$$d' = \frac{1}{\sigma\varepsilon}\frac{\partial d}{\partial x}, \qquad b' = \frac{1}{\gamma\varepsilon}\frac{\partial b}{\partial x} \tag{A.14}$$

and account for the along-stream variation of the width and depth. The term with third derivative in equation (A.12) represents frequency dispersion. Shuto's theory is then approximated for special wave regimes. Assuming a cnoidal wave profile and that the surface elevation is independent of the transverse axis y, a law of shoaling is derived and comparisons with experiments carried out, which is later analyzed by Miles (1979a).

Shuto did not converted equation (A.12) back to a fixed coordinate system. Kirby & Vengayil (1988) provide a dimensional version of Shuto's theory in stationary coordinates (KV88, eq.22) which reads

$$b\frac{\partial \eta}{\partial t} + bc\frac{\partial \eta}{\partial x} + \frac{1}{2}\frac{\partial (bc)}{\partial x}\eta + \frac{3bc}{2h}\eta\frac{\partial \eta}{\partial x} + \frac{bch^2}{6}\frac{\partial^3 \eta}{\partial x^3} = 0. \tag{A.15}$$

Miles (1979b, 1980) pointed out that Shuto's model does not conserve mass as reflected waves are disregarded in the KdV approximation, but is adiabatically invariant in energy. These, plus the strong restriction of rectangular cross-section makes this theory specific, thus inadequate for channels of arbitrary cross-section with significant changes within a wavelength treated in this dissertation.

Chang *et al.* (1979) used Shuto's theory to compare with experimental result of solitary waves traveling in a rectangular channel with a linearly varying width and uniform depth. The shoaling law (S74, eq.61) was properly reproduced in linearly diverging channel but not in converging channels, due to nonlinear effects associated with the choice of the spatial variable as the slow variable in the generalized KdV equation.

A.5 Chou's 1981 theory

The theory derived in this paper is restricted to *i*) solitary waves, *ii*) slowly varying cross-sections and *iii*) KdV form of governing equation (C81, eq. 2.18). Chou analyzes rectangular channels with slowly-varying depth and width (C81, eq. 2.19), rectangular channels with slowly-varying depth and constant width (C81, eq. 2.20) and a triangular channel (C81, eq. 2.21). A solitary wave solution for the KdV (C81, eq. 3.10) is proposed, from which he derives the phase speed (C81, eq. 4.2) and a shoaling law (C81, eq. 4.5). The limitations earlier mentioned discourage the use of the theory for channels of arbitrary cross-section with significant changes within a wavelength.

A.6 Kirby & Vengayil's 1988 theory

Kirby & Vengayil (1988) extended Shuto's theory to account for reflections from changes in channel width and length. They start from equation (A.15) assuming *i*) cross-sectional variations in the surface displacement η are weak enough to ignore and *ii*) bottom slope and width changes are small. The surface dis-

placement is written as the sum of the contributions of the forward-scattered wave in the $+x$ direction, η^+, and the back-scattered wave traveling in the $-x$ direction, η^-. By means of an heuristic approach, they add dispersive and non-linear effects to obtain

$$b\frac{\partial \eta^{\pm}}{\partial t} \pm bc\frac{\partial \eta^{\pm}}{\partial x} + \frac{1}{2}\frac{\partial (bc)}{\partial x}(\eta^+ - \eta^-) \pm \frac{3bc}{2h}\eta^{\pm}\frac{\partial \eta^{\pm}}{\partial x} \pm \frac{bch^2}{6}\frac{\partial^3 \eta^{\pm}}{\partial x^3} = 0. \tag{A.16}$$

This coupled system of equations has the advantage of relaxing the one-direction assumption embedded in Shuto's theory. They lead to exact conservation of mass at the level of approximation used. Kirby & Vengayil apply these equations to several problems involving aperiodic and periodic wave motion, among which experiments for solitary waves propagating in diverging and converging channels (Chang et al., 1979) are also analyzed herein. As for Shuto's theory, the strong restriction of rectangular cross-section makes this theory inapplicable channels of arbitrary cross-section.

A.7 Teng & Wu's 1997 theory

In his PhD. dissertation, Teng proposed a theory for weakly-nonlinear weakly-dispersive waves propagating in a channel of arbitrary, symmetric and slowly varying cross-section. The research group at Caltech published a set of papers with the generalized channel Boussinesq (gcB) model for bidirectional waves and the channel Korteweg - deVries model (cKdV) for unidirectional flow. The original theory (Teng, 1990; Teng & Wu 1992) was applied to study the solitary wave evolution, transmission and reflection in channels of convergent and divergent rectangular and parabolic cross-sections (Teng & Wu, 1994), later extended to include the effects of sidewall slope at the waterline (Teng & Wu, 1997)

and used to find an analytical solution for solitary waves in uniform channels with sloping sidewalls (Teng, 2000). The theory allows weak forcing through surface pressure distribution or via a submerged obstacle moving near critical speed. Different versions of the gcB equations and scalings are available in the referred papers[1]. The results from Teng & Wu (1997) are presented herein, unless otherwise noted. The governing equations are

$$\frac{\partial}{\partial t}\left(2b_0\widetilde{\zeta}+S\widetilde{\zeta}^2\right)+\frac{\partial}{\partial x}\left[2b_0\left(\widetilde{h}_0+\widetilde{\zeta}\right)\overline{u}\right] = -\frac{\partial A_d}{\partial t}, \tag{A.17}$$

$$\frac{\partial \overline{u}}{\partial t}+\overline{u}\frac{\partial \overline{u}}{\partial x}+\frac{\partial \widetilde{\zeta}}{\partial x}-\frac{1}{3}\kappa^2\widetilde{h}_0^2\frac{\partial^3\overline{u}}{\partial x^2\partial t} = -\frac{\partial \widetilde{p}_a}{\partial x}, \tag{A.18}$$

where x is space and t time, $h_0(x,y)$ the still water depth, $2b_0(x)$ is the unperturbed channel surface, $S = dy/dz$ represents the sidewall slope at the still level, $A_d(x,t)$ is the area reduction due to a submerged object moving below the unperturbed water surface (i.e. for a fixed bottom is $A_d = 0$), p_a is the atmospheric pressure, $\zeta(x,y,t)$ is the surface elevation and $u(x,y,z,t)$ the longitudinal velocity. Figure A.3 *a* depicts some of the relevant quantities. The width-mean quantities are defined as

$$\widetilde{h}_0(x)=\frac{1}{2b_0}\int_{-b_0}^{b_0}h_0(x,y)\,dy, \qquad \widetilde{\zeta}(x,t)=\frac{1}{2b_0}\int_{-b_0}^{b_0}\zeta(x,y,t)\,dy \tag{A.19}$$

and the section-mean velocity is defined as (TW92, eq.9)

$$\overline{u}(x,t)=\frac{1}{A}\iint_A u(x,y,z,t)\,dydz, \tag{A.20}$$

being $A(x,t)$ the instantaneous cross-sectional area, which is the sum of the unperturbed wetted area $A_0(x)$, the area due to wave motion $A_{\widetilde{\zeta}}(x,t)$ and the area due to a moving bottom or a submerged body as a forcing function $A_d(x,t)$

$$A = A_0(x) - A_d(x,t) + 2b\widetilde{\zeta}+S\widetilde{\zeta}^2, \tag{A.21}$$

[1]Different expressions are eqs. 2.45-2.46 in Teng (1990); eqs. 43-44 in Teng & Wu (1992); eqs. 1-3 in Teng & Wu (1994); eqs. in page 3, Teng & Wu (1997) and eqs. 1a-1b in Teng (2000). Differences arise from different scalings: x is scaled by the wavelength λ in Teng (1990), Teng & Wu (1992,1997), and by the unperturbed water depth h_c in Teng & Wu (1994) and Teng (2000).

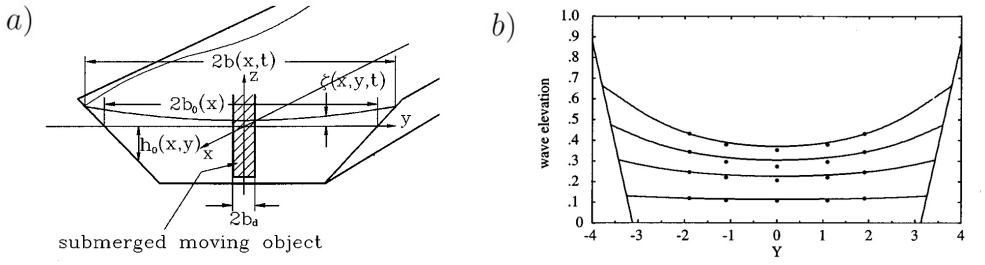

Figure A.3: *a*) A sketch of a non-rectangular channel with a coordinate set-up used by Teng & Wu (1997). *b*) Variation of solitary wave amplitude across the trapezoidal channel. Curved solid lines: theoretical wave profiles of mean amplitude α =0.12, 0.25, 0.34 and 0.43; solid dots: experimental data; two straight solid lines: the inclined channel sidewalls.

The dispersive term is expressed differently among versions: as $\varepsilon^2 \frac{\partial f}{\partial t}(x,t)$ in Teng (1990); as $\varepsilon^2 \psi(x,t)$ in Teng & wu (1992) and as $-\frac{1}{3}\kappa^2 \widetilde{h}^2 \frac{\partial^3 \overline{u}}{\partial x^2 \partial t}$ in Teng & Wu (1994, 1997). The latter introduces the dispersive strength of the cross-section via the shape factor κ (eq. 11, T94). The channel shape factor is defined as

$$\kappa^2(x,t) = \frac{3}{\widetilde{h}_0^2}\left(\widetilde{\Psi} - \overline{\Psi}\right), \tag{A.22}$$

where

$$\widetilde{\Psi}(x) = \frac{1}{2b_0}\int_{-b_0}^{b_0} \Psi(x,y,0)\,dy, \qquad \overline{\Psi}(x) = \frac{1}{A_0}\iint_{A_0} \Psi(x,y,z)\,dydz. \tag{A.23}$$

The function Ψ satisfies the boundary value problem

$$\frac{\partial^2 \Psi}{\partial y^2} + \frac{\partial^2 \Psi}{\partial z^2} = 1, \qquad -h < z < 0, \tag{A.24}$$

$$\frac{\partial \Psi}{\partial z} = \widetilde{h}_0, \qquad z = 0, \tag{A.25}$$

$$\frac{\partial \Psi}{\partial n} = 0, \qquad z = -h. \tag{A.26}$$

The shape factor κ depends explicitly on the cross-sectional shape, being $\kappa = 1$ for the rectangular section. If the channel shape is such that the width increases (or decreases) from the channel bottom to the surface, κ will be greater (or

smaller) than one. Teng & Wu found analytical expressions for semicircular, parabolic and triangular cross sections (TW94, Table 1). Other shapes need to be computed numerically. A conclusion is that the greater the departure of the shape from rectangular, the greater the dispersive effect in the longitudinal evolution of the wave. A moving coordinate system (TW92, eq.46) similar to the one used by Shuto (1974), is used to find the expression in stretched coordinates (TW92, eq.49). The resulting cKdV equation derived with the additional assumption of one direction waves is,

$$\pm\frac{1}{\sqrt{\widetilde{h}_0}}\frac{\partial\widetilde{\zeta}}{\partial t}+\frac{\partial\widetilde{\zeta}}{\partial x}+\left(\frac{3}{2\widetilde{h}_0}-\frac{S}{2b_0}\right)\widetilde{\zeta}\frac{\partial\widetilde{\zeta}}{\partial x}+\frac{\kappa^2\widetilde{h}_0^2}{6}\frac{\partial^3\widetilde{\zeta}}{\partial x^3}+\frac{1}{4}\left(\frac{1}{\widetilde{h}_0}\frac{\partial\widetilde{h}_0}{\partial x}+\frac{2}{b_0}\frac{\partial b_0}{\partial x}\right)\widetilde{\zeta}$$
$$=-\frac{1}{2}\frac{\partial}{\partial x}\left(\frac{1}{2b_0}A_d+\widetilde{p}_a\right), \quad \text{(A.27)}$$

where the effects of varying depth and width are explicit in two terms and can be grouped together into $\frac{1}{4}\frac{\partial}{\partial x}\left(\ln h_0 b_0^2\right)\zeta$. The velocity is (T92, eq.52)

$$\overline{u}=\frac{1}{\sqrt{\widetilde{h}_0}}\left[\widetilde{\zeta}-\frac{1}{4\widetilde{h}_0}\widetilde{\zeta}^2+\frac{\varepsilon^2}{2}\int\psi dx-\frac{A_d}{4b_0}+\frac{\widetilde{p}_a}{2}-\frac{1}{4}\left(\frac{1}{\widetilde{h}_0}\frac{\partial\widetilde{h}_0}{\partial x}+\frac{2}{b_0}\frac{\partial b_0}{\partial x}\right)\int_{x_0}^{x}\widetilde{\zeta}dx\right], \quad \text{(A.28)}$$

where the + (or −) sign holds for right-going (or left-going) waves and x_0 is some station at which $\widetilde{\zeta}$, $\overline{u}$ and all disturbances vanish. The function $\psi=-\frac{1}{3}\kappa^2h^2\frac{\partial^3\overline{u}}{\partial x^2\partial t}$ incorporates dispersive effects.

The quantities $\widetilde{\zeta}$ and $\overline{u}$ are solved through (A.17) and (A.18) or (A.27) once the specific geometry of the cross-section is given and shape factor κ computed from the boundary value problem. Wave features in a cross-sectional plane are determined to second order by using the perturbation expansion. The spanwise variation of wave elevation is found from the Bernoulli equation at the free surface (T90, eq.2.107) once the potential function is found (T90, eqs.2.32, 2.33)

$$\zeta_2(x,y,t)=-\left.\frac{\partial\phi_2}{\partial t}\right|_{z=0}-\left.\frac{1}{2}\left(\frac{\partial\phi_2}{\partial x}\right)^2\right|_{z=0}. \quad \text{(A.29)}$$

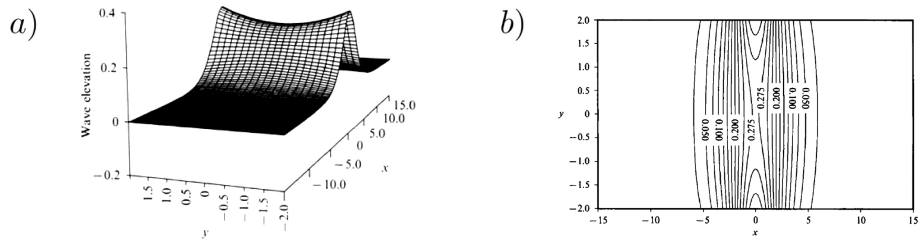

Figure A.4: Solitary wave elevation on a channel of triangular cross-section. *a*) and *b*) depict Teng & Wu (1992) results using the cKdV model for a section-mean amplitude of $\alpha = 0.3$ in a uniform triangular channel of half-vertex angle of 45°.

where $\phi_2(x, y, z, t)$ is related (T92 eq.5) $\phi_2 = -\frac{1}{\alpha\varepsilon}\Psi\frac{\partial\overline{u}}{\partial x}$, being α the non-linearity and ε the relative depth. Figure A.4 depicts the cross-sectional changes in the surface elevation for a channel with uniform triangular cross-section computed by Teng & Wu (1992). In their words, "the wave crest varies across the channel in the form of a sideways saddle with its lowest elevation and widest spread occurring at the centre-plane".

The lateral and vertical velocities are found from the perturbation expansions (T90 eqs. 2.32, 2.35, 2.36) after some manipulation

$$v(x, y, z, t) = -\alpha\varepsilon\frac{\partial\phi_2}{\partial y} + O\left(\varepsilon^3\right), \qquad w(x, y, z, t) = -\alpha\varepsilon\frac{\partial\phi_2}{\partial z} + O\left(\varepsilon^3\right). \tag{A.30}$$

Teng & Wu's theory provide a closed system for the problem of weakly-nonlinear, weakly-dispersive and weakly-forced long waves propagating in a channel of arbitrary, symmetric and slowly varying cross-section. The constrains of symmetry and to slowly longitudinal variations of the geometry, i.e.

$$\frac{\partial A_0}{\partial x} = \frac{\partial}{\partial x}\left(2b_0\widetilde{h}_0\right) = O(\alpha) \tag{A.31}$$

limit the application to natural streams. Supplementary restrictions to the quantities $\partial b/\partial t$ and $\partial\widetilde{h}/\partial t$ may be of concern when dealing with moving bottoms. Teng & Wu indicate that the assumption of symmetric cross-sections can be

relaxed to account for asymmetric channels by following the same derivation steps, provided the channels remain straight. This train of though is not further pursued in the set of papers Teng & Wu published. In the author's opinion, this theory may be extended for more general cases if restrictions such as the symmetry in the cross-section and the slowly longitudinal variations of the geometry are relaxed.

APPENDIX B

SOLVABILITY OF THE BOUNDARY VALUE PROBLEM

The solvability condition of the boundary value problem for ϕ_2 in a fixed bottom is analyzed in this Appendix. The equations derived in Chapter 3 are:

$$\frac{\partial^2\phi_2}{\partial y^2}+\frac{\partial^2\phi_2}{\partial z^2}=-\frac{\partial\langle u\rangle}{\partial x}, \qquad -h(x,y)<z<0, \tag{B.1}$$

$$\frac{\partial\phi_2}{\partial z}=-\frac{1}{B_0}\frac{\partial}{\partial x}\left(\langle u\rangle A_0\right), \qquad z=0, \tag{B.2}$$

$$\frac{\partial\phi_2}{\partial n}=\frac{\langle u\rangle\frac{\partial h}{\partial x}}{\sqrt{\left(\frac{\partial h}{\partial y}\right)^2+1}}, \qquad z=-h(x,y), \tag{B.3}$$

$$\frac{\partial\phi_2}{\partial y}=\langle u\rangle\frac{\partial b_l}{\partial x}, \qquad z=b_l(x), \tag{B.4}$$

$$\frac{\partial\phi_2}{\partial y}=-\langle u\rangle\frac{\partial b_r}{\partial x}, \qquad z=-b_r(x), \tag{B.5}$$

where n lies in the cross-sectional plane. The Gauss theorem reads

$$\iint\nabla\cdot\mathbf{F}da=\oint\mathbf{F}\cdot\hat{n}ds, \tag{B.6}$$

where da and ds are the differential elements of area and contour of the domain defined in the $y-z$ plane, respectively. For $\mathbf{F}=\nabla\phi_2$ the theorem becomes

$$\iint\nabla^2\phi_2 da=\oint\nabla\phi_2\cdot\hat{n}ds. \tag{B.7}$$

Using the Poisson equation and separating the right hand side yields

$$\begin{aligned}\iint\left(-\frac{\partial\langle u\rangle}{\partial x}\right)da &= \int\nabla\phi_2\cdot\hat{n}|_{z=-h(x,y)}\,ds+\int_{-b_r(x)}^{b_l(x)}\nabla\phi_2\cdot\hat{n}|_{z=0}\,dy\\ &\quad+\int_{-h(x,y)}^{0}\nabla\phi_2\cdot\hat{n}|_{y=-b_r(x)}\,dz+\int_{-h(x,y)}^{0}\nabla\phi_2\cdot\hat{n}|_{y=b_l(x)}\,dz,\end{aligned} \tag{B.8}$$

where $\hat{n}|_{z=0}=(0,1)$, $\hat{n}|_{y=-b_r}=(-1,0)$ and $\hat{n}|_{y=b_l}=(1,0)$, so

$$\begin{aligned}-\frac{\partial\langle u\rangle}{\partial x}A_0 &= \int\frac{\partial\phi_2}{\partial z}\cdot\hat{n}\Big|_{z=-h(x,y)}ds+\int_{-b_r(x)}^{b_l(x)}\frac{\partial\phi_2}{\partial z}\Big|_{z=0}dy\\ &\quad-\int_{-h(x,y)}^{0}\frac{\partial\phi_2}{\partial y}\Big|_{y=-b_r(x)}dz+\int_{-h(x,y)}^{0}\frac{\partial\phi_2}{\partial y}\Big|_{y=b_l(x)}dz.\end{aligned} \tag{B.9}$$

Invoking the boundary conditions

$$-\frac{\partial \langle u \rangle}{\partial x} A_0 = \int \frac{\langle u \rangle \frac{\partial h}{\partial x}}{\sqrt{\left(\frac{\partial h}{\partial y}\right)^2 + 1}} ds - \int_{-b_r(x)}^{b_l(x)} \frac{1}{B_0} \frac{\partial}{\partial x} \left(\langle u \rangle A_0 \right) dy + \int_{-h(x,y)}^{0} \langle u \rangle \frac{\partial b_r}{\partial x} dz + \int_{-h(x,y)}^{0} \langle u \rangle \frac{\partial b_l}{\partial x} dz, \tag{B.10}$$

where the differential element ds is expressed as

$$ds = \sqrt{dy^2 + dh^2} = dy \sqrt{\left(\frac{dh}{dy}\right)^2 + 1}. \tag{B.11}$$

Therefore (B.10) reads

$$-\frac{\partial \langle u \rangle}{\partial x} A_0 = \langle u \rangle \int_{-b_r(x)}^{b_l(x)} \frac{\partial h}{\partial x} dy - \frac{1}{B_0} \frac{\partial}{\partial x} \left(\langle u \rangle A_0 \right) \int_{-b_r(x)}^{b_l(x)} dy + \langle u \rangle \frac{\partial b_r}{\partial x} \int_{-h(x,y)}^{0} dz + \langle u \rangle \frac{\partial b_l}{\partial x} \int_{-h(x,y)}^{0} dz, \tag{B.12}$$

or

$$-\frac{\partial \langle u \rangle}{\partial x} A_0 = \langle u \rangle \int_{-b_r(x)}^{b_l(x)} \frac{\partial h}{\partial x} dy - \frac{1}{B_0} \frac{\partial}{\partial x} \left(\langle u \rangle A_0 \right) B_0 + \langle u \rangle \frac{\partial b_r}{\partial x} h_{(x,-b_r)} + \langle u \rangle \frac{\partial b_l}{\partial x} h_{(x,b_l)}. \tag{B.13}$$

Applying the Leibniz rule yields

$$-\frac{\partial \langle u \rangle}{\partial x} A_0 = \langle u \rangle \left\{ \frac{\partial}{\partial x} \int_{-b_r(x)}^{b_l(x)} h dy - \frac{\partial b_l}{\partial x} h_{(x,b_l)} - \frac{\partial b_r}{\partial x} h_{(x,-b_r)} \right\} - \langle u \rangle \frac{\partial A_0}{\partial x} - \frac{\partial \langle u \rangle}{\partial x} A_0 + \langle u \rangle \frac{\partial b_r}{\partial x} h_{(x,-b_r)} + \langle u \rangle \frac{\partial b_l}{\partial x} h_{(x,b_l)}, \tag{B.14}$$

or

$$0 = \overline{u} \frac{\partial}{\partial x} \int_{-b_r(x)}^{b_l(x)} h dy - \langle u \rangle \frac{\partial A_0}{\partial x}. \tag{B.15}$$

By definition, $A_0(x) = \int_{-b_r(x)}^{b_l(x)} h(x,y)\, dy$ so the right hand side equals zero and the solvability condition is fulfilled.

APPENDIX C

BOUNDARY VALUE PROBLEMS FOR χ_1 AND χ_2

Expressions for the coefficients α, β and γ for a rectangular and triangular cross-sections are derived in this Appendix. The corresponding expressions are

$$\alpha = \frac{\partial}{\partial x}\left[\widetilde{\chi_1|_{z=0}}\right] - \overline{\frac{\partial \chi_1}{\partial x}} \tag{C.1}$$

$$\beta = \widetilde{\chi_1|_{z=0}} + \frac{\partial}{\partial x}\left[\widetilde{\chi_2|_{z=0}}\right] - \overline{\chi_1} - \overline{\frac{\partial \chi_2}{\partial x}} \tag{C.2}$$

$$\gamma = \widetilde{\chi_2|_{z=0}} - \overline{\chi_2} \tag{C.3}$$

C.1 Rectangular channel

For a fixed rectangular cross-section, the bottom is not a function of the span-wise dimension and time. Thus $z = -h(x)$ and the bottom boundary conditions (3.114) and (3.117) are reduced to

$$\frac{\partial \chi_1}{\partial n} = -\frac{\partial h}{\partial x}, \qquad \frac{\partial \chi_2}{\partial n} = 0 \tag{C.4}$$

The left and right boundary conditions must be computed for supplementary equations.

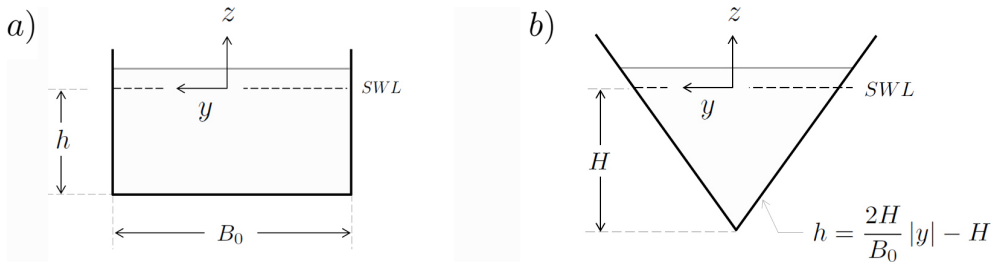

Figure C.1: Definitions for *a*) rectangular and *b*) triangular cross-sections.

Solution for χ_1

χ_1 satisfies the following boundary value problem

$$\frac{\partial^2 \chi_1}{\partial y^2} + \frac{\partial^2 \chi_1}{\partial z^2} = 0, \qquad -h \le z \le 0, \quad -b_r \le y \le b_l, \tag{C.5}$$

$$\frac{\partial \chi_1}{\partial z} = -\frac{1}{B_0}\frac{\partial A_0}{\partial x}, \qquad z = 0, \tag{C.6}$$

$$\frac{\partial \chi_1}{\partial z} = -\frac{\partial h}{\partial x}, \qquad z = -h, \tag{C.7}$$

$$\frac{\partial \chi_1}{\partial y} = \frac{\partial b_l}{\partial x}, \qquad y = b_l, \tag{C.8}$$

$$\frac{\partial \chi_1}{\partial y} = -\frac{\partial b_r}{\partial x}, \qquad y = -b_r. \tag{C.9}$$

A solution in the form

$$\chi_1(y,z) = A + Bz + Cy + Dz^2 + Ey^2 + Fyz, \tag{C.10}$$

is assumed, where A is a constant of integration which does not affect the value of α, β or γ and is thus set to $A = 0$. Plugging into the Poisson equation yields $E = -D$. For the free surface boundary condition at $z = 0$

$$B = -\frac{1}{B_0}\frac{\partial A_0}{\partial x} = -\frac{1}{B_0}\left(h\frac{\partial B_0}{\partial x} + B_0\frac{\partial h}{\partial x}\right) = -\frac{h}{B_0}\frac{\partial B_0}{\partial x} - \frac{\partial h}{\partial x}, \qquad F = 0. \tag{C.11}$$

For the bottom boundary condition at $z = -h$

$$D = \frac{B}{2h} + \frac{1}{2h}\frac{\partial h}{\partial x} = -\frac{1}{2B_0}\frac{\partial B_0}{\partial x}, \qquad E = \frac{1}{2B_0}\frac{\partial B_0}{\partial x}. \tag{C.12}$$

The sidewall boundary conditions at $y = b_l$ and $y = -b_r$

$$C + 2Eb_l = \frac{\partial b_l}{\partial x}, \qquad C - 2Eb_r = -\frac{\partial b_r}{\partial x}. \tag{C.13}$$

are added up to yield, using the expression for E,

$$C = \frac{1}{2}\frac{\partial}{\partial x}(b_l - b_r) - E(b_l - b_r) = \frac{1}{2}\frac{\partial}{\partial x}(b_l - b_r) - \frac{1}{2B_0}\frac{\partial B_0}{\partial x}(b_l - b_r). \tag{C.14}$$

The function χ_1 becomes

$$\chi_1(y,z) = \frac{1}{2B_0}\frac{\partial B_0}{\partial x}\left(-2hz - (b_l - b_r)\,y - z^2 + y^2\right) - \frac{\partial h}{\partial x}z + \frac{1}{2}\frac{\partial}{\partial x}(b_l - b_r)\,y, \qquad \text{(C.15)}$$

It can be easily shown that this solution satisfies the BVP. Function χ_1 for a rectangular channel is shown in Figure C.2, panels *a* to *d*.

Solution for χ_2

χ_2 satisfies the following boundary value problem

$$\frac{\partial^2\chi_2}{\partial y^2} + \frac{\partial^2\chi_2}{\partial z^2} = -1, \qquad -h \le z \le 0, \quad -b_r \le y \le b_l, \qquad \text{(C.16)}$$

$$\frac{\partial\chi_2}{\partial z} = -\frac{A_0}{B_0}, \qquad z = 0, \qquad \text{(C.17)}$$

$$\frac{\partial\chi_2}{\partial z} = 0, \qquad z = -h, \qquad \text{(C.18)}$$

$$\frac{\partial\chi_2}{\partial y} = 0, \qquad y = b_l, -b_r, \qquad \text{(C.19)}$$

where $A_0/B_0 = h$ is the depth. A solution in the form (C.10) is assumed, being A a constant of integration which does not affect the value of the coefficients in the momentum equation and is thus set to $A = 0$. Plugging into the Poisson equation yields $E = -1/2 - D$. The free surface boundary condition is evaluated at $z = 0$ to yield $B + Fy = -h$, where $B = -h$ and $F = 0$. The bottom boundary condition is evaluated at $z = -h$ to yield

$$D = -\frac{B}{2h} = \frac{1}{2}, \qquad \Rightarrow \qquad E = -\frac{1}{2} - D = 0. \qquad \text{(C.20)}$$

The sidewall boundary conditions at $y = b_l$ and $y = -b_r$

$$C = -2Eb_r = 0, \qquad C = 2Eb_l = 0. \qquad \text{(C.21)}$$

The function χ_2 becomes

$$\chi_2(y,z) = -hz - \frac{z^2}{2}, \qquad \text{(C.22)}$$

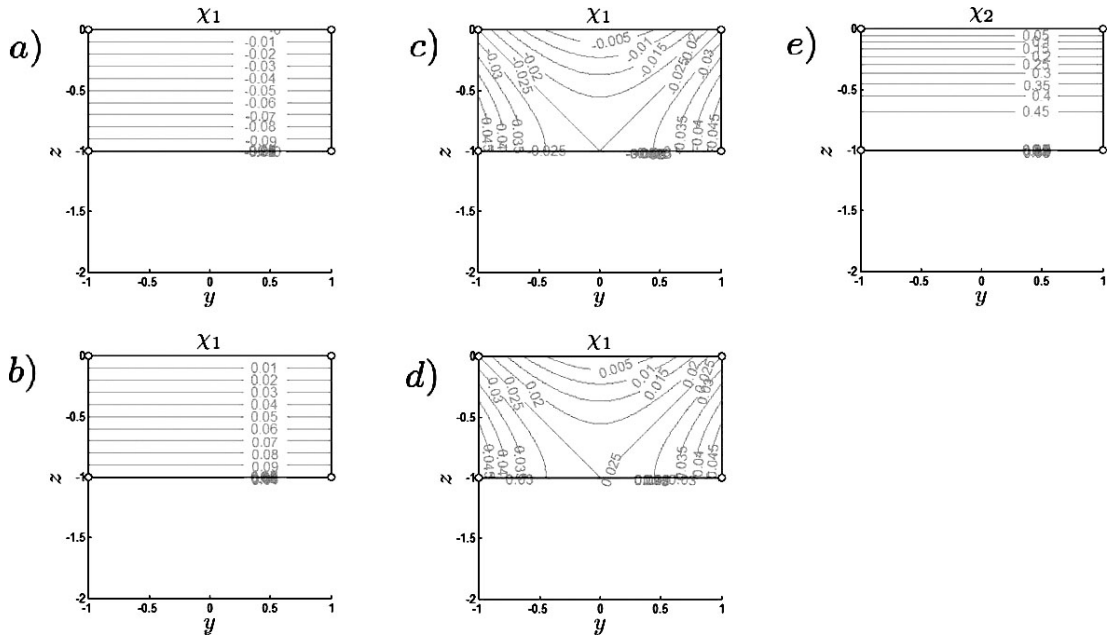

Figure C.2: Functions χ_1 and χ_2 for a rectangular channel. *a*) to *d*) depict function χ_1 for the following conditions: *a*) shallowing channel of constant width ($h_x = -0.1, B_{0x} = 0$); *b*) deepening channel of constant width ($h_x = 0.1, B_{0x} = 0$); *c*) converging channel of constant depth ($h_x = 0, B_{0x} = -0.1$) and *d*) diverging channel of constant depth ($h_x = 0, B_{0x} = 0.1$). *e*) depicts the function $\chi_2$which is locally determined and independent of the longitudinal x-variations of the cross-section.

and is shown in Figure C.2 *d*. Due to the no-flux boundary conditions, the isocontours are perpendicular to the lateral boundaries and parallel to the bottom.

Computation of α, β and γ

For the computation of α, β and γ the additional assumption that both sidewalls change with the same rate so that $b_l = b_r = B_0/2$ is taken. Thus

$$\chi_1(y,z) = \frac{1}{2B_0}\frac{dB_0}{dx}\left(-2hz - z^2 + y^2\right) - \frac{dh}{dx}z. \tag{C.23}$$

where partial derivatives are changed to total derivatives. The relevant quantities derived from χ_1 become

$$\widetilde{\chi_1|_{z=0}} = \frac{B_0}{24}\frac{dB_0}{dx}, \tag{C.24}$$

$$\frac{\partial}{\partial x}\left[\widetilde{\chi_1|_{z=0}}\right] = \frac{B_0}{24}\frac{d^2B_0}{dx^2} + \frac{1}{24}\left(\frac{dB_0}{dx}\right)^2, \tag{C.25}$$

$$\overline{\chi_1} = \frac{h}{2}\frac{dh}{dx} + \frac{B_0}{24}\frac{dB_0}{dx} + \frac{h^2}{3B_0}\frac{dB_0}{dx}, \tag{C.26}$$

$$\overline{\frac{\partial \chi_1}{\partial x}} = \left(\frac{B_0}{24} + \frac{h^2}{3B_0}\right)\frac{d^2B_0}{dx^2} - \left(\frac{1}{24} + \frac{h^2}{3B_0^2}\right)\left(\frac{dB_0}{dx}\right)^2 + \frac{h}{2B_0}\frac{dh}{dx}\frac{dB_0}{dx} + \frac{h}{2}\frac{d^2h}{dx^2}. \tag{C.27}$$

The quantities derived from χ_2 are

$$\widetilde{\chi_2|_{z=0}} = 0, \qquad \frac{\partial}{\partial x}\left[\widetilde{\chi_2|_{z=0}}\right] = 0, \qquad \overline{\chi_2} = \frac{h^2}{3}, \qquad \overline{\frac{\partial \chi_2}{\partial x}} = \frac{h}{2}\frac{dh}{dx}. \tag{C.28}$$

The coefficients become

$$\alpha = -\frac{h^2}{3B_0}\frac{d^2B_0}{dx^2} + \left(\frac{1}{12} + \frac{h^2}{3B_0^2}\right)\left(\frac{dB_0}{dx}\right)^2 - \frac{h}{2B_0}\frac{dh}{dx}\frac{dB_0}{dx} - \frac{h}{2}\frac{d^2h}{dx^2}, \tag{C.29}$$

$$\beta = -\frac{h^2}{3B_0}\frac{dB_0}{dx} - h\frac{dh}{dx}, \tag{C.30}$$

$$\gamma = -\frac{h^2}{3}. \tag{C.31}$$

For the case of a channel of constant width (equivalent to a shoaling beach with no refraction), the above are reduced to

$$\alpha(y,z) = -\frac{h}{2}\frac{d^2h}{dx^2}, \qquad \beta = -h\frac{dh}{dx}, \qquad \gamma = -\frac{h^2}{3}. \tag{C.32}$$

For the case of a linear converging/diverging channel of constant depth as the one used by Chang *et al.* (1979)

$$\alpha = \left(\frac{1}{12} + \frac{h^2}{3B_0^2}\right)\left(\frac{\partial B_0}{\partial x}\right)^2, \qquad \beta = -\frac{h^2}{3B_0}\frac{\partial B_0}{\partial x}, \qquad \gamma = -\frac{h^2}{3}. \tag{C.33}$$

Finally, for channels where $dh/dx, dB_0/dx = O(\epsilon)$, from which the uniform case is a particular example,

$$\alpha, \beta = 0, \qquad \gamma = -\frac{h^2}{3}. \tag{C.34}$$

The value of the γ is equivalent to the coefficient $\overline{\Psi} - \widetilde{\Psi}$ in Teng & Wu (1994).

C.2 Triangular channel

In the triangular cross-section, a specific bottom boundary condition needs to be specified. The Poisson equation and surface boundary condition, on the other hand, remain exactly as in the rectangular channel. There is no need to account for the sidewall boundary conditions as wall are inclined, thus the bottom is entirely defined by the bottom boundary condition. The boundary for a triangular symmetric channel is defined, in dimensional form, by

$$\hat{z} = \hat{h}\left(\hat{x}, \hat{y}\right) = \frac{2\hat{H}}{\hat{B}_0}\left|\hat{y}\right| - \hat{H}, \tag{C.35}$$

where $\hat{H}\left(\hat{x}\right)$ is the maximum depth at the center and $\hat{B}_0\left(\hat{x}\right)$ width at the still water level. The bottom boundary condition for $F = \hat{z} - \frac{2\hat{H}}{\hat{B}_0}\left|\hat{y}\right| + \hat{H}$ is given by

$$\frac{dF}{dt} = \frac{\partial F}{\partial t} + \overrightarrow{V} \cdot \nabla F = u\frac{\partial F}{\partial x} + v\frac{\partial F}{\partial y} + w\frac{\partial F}{\partial z} = 0, \tag{C.36}$$

which for this section reads

$$\frac{2\hat{H}}{\hat{B}_0}\frac{\left|\hat{y}\right|}{\hat{y}}\hat{v} - \hat{w} = \left[\frac{\partial \hat{H}}{\partial \hat{x}} - \frac{\partial}{\partial \hat{x}}\left(\frac{2\hat{H}}{\hat{B}_0}\right)\left|\hat{y}\right|\right]\hat{u}, \qquad \hat{z} = \frac{2\hat{H}}{\hat{B}_0}\left|\hat{y}\right| - \hat{H}. \tag{C.37}$$

Non-dimensionalizing and using the expression for the velocity potential yields

$$\frac{2H}{B_0}\frac{|y|}{y}\frac{\partial \phi}{\partial y} - \frac{\partial \phi}{\partial z} = \mu^2\left[\frac{\partial H}{\partial x} - \frac{\partial}{\partial x}\left(\frac{2H}{B_0}\right)|y|\right]u, \qquad z = \frac{2H}{B_0}|y| - H. \tag{C.38}$$

Invoking the perturbation expansion

$$\frac{2H}{B_0}\frac{|y|}{y}\frac{\partial \phi_2}{\partial y} - \frac{\partial \phi_2}{\partial z} = \left[\frac{\partial H}{\partial x} - \frac{\partial}{\partial x}\left(\frac{2H}{B_0}\right)|y|\right]\langle u\rangle, \qquad z = \frac{2H}{B_0}|y| - H, \tag{C.39}$$

since $\phi = \phi_1\left(x,t\right) + \mu^2\phi_2\left(x,y,z,t\right)$ and $u = \langle u\rangle + O\left(\mu^2\right)$. Since

$$\phi_2\left(x,y,z,t\right) = \chi_1\left(y,z\right)\langle u\rangle + \chi_2\left(y,z\right)\frac{\partial\langle u\rangle}{\partial x} \tag{C.40}$$

yields for χ_1

$$\frac{2H}{B_0}\frac{|y|}{y}\frac{\partial \chi_1}{\partial y} - \frac{\partial \chi_1}{\partial z} = \frac{\partial H}{\partial x} - \frac{\partial}{\partial x}\left(\frac{2H}{B_0}\right)|y|, \qquad z = \frac{2H}{B_0}|y| - H, \tag{C.41}$$

and for χ_2

$$\frac{2H}{B_0}\frac{|y|}{y}\frac{\partial \chi_2}{\partial y} - \frac{\partial \chi_2}{\partial z} = 0 \qquad z = \frac{2H}{B_0}|y| - H. \tag{C.42}$$

Solution for χ_1

χ_1 satisfies the following boundary value problem

$$\begin{aligned}
\frac{\partial^2 \chi_1}{\partial y^2} + \frac{\partial^2 \chi_1}{\partial z^2} &= 0, && -h(x,y) < z < 0, && \text{(C.43)}\\
\frac{\partial \chi_1}{\partial z} &= -\frac{1}{B_0}\frac{\partial A_0}{\partial x}, && z = 0, && \text{(C.44)}\\
\pm\frac{2H}{B_0}\frac{\partial \chi_1}{\partial y} - \frac{\partial \chi_1}{\partial z} &= \frac{\partial H}{\partial x} \mp \frac{\partial}{\partial x}\left(\frac{2H}{B_0}\right)y, && z = \pm\frac{2H}{B_0}y - H. && \text{(C.45)}
\end{aligned}$$

A solution in the form (C.10) is assumed, being A a constant of integration which does not affect the value of the coefficients in the momentum equation and is thus set to $A = 0$. From the governing equation, $E = -D$. From the free surface kinematic boundary condition, $B = -\frac{1}{B_0}\frac{\partial A_0}{\partial x}$ and $F = 0$. The solution becomes

$$\chi_1(y,z) = -\frac{1}{B_0}\frac{\partial A_0}{\partial x}z + Cy + Dz^2 - Dy^2. \tag{C.46}$$

The derivatives become

$$\frac{\partial \chi_1}{\partial z} = -\frac{1}{B_0}\frac{\partial A_0}{\partial x} + 2Dz, \qquad \frac{\partial \chi_1}{\partial y} = C - 2Dy. \tag{C.47}$$

The bottom boundary conditions become

$$\pm\frac{2H}{B_0}(C - 2Dy) + \frac{1}{B_0}\frac{\partial A_0}{\partial x} - 2Dz = \mp\frac{\partial}{\partial x}\left(\frac{2H}{B_0}\right)y + \frac{\partial H}{\partial x}, \qquad z = \pm\frac{2H}{B_0}y - H. \tag{C.48}$$

Separating branches and evaluating in z yields

$$\frac{2H}{B_0}(C - 2Dy) + \frac{1}{B_0}\frac{\partial A_0}{\partial x} - 2D\left(\frac{2H}{B_0}y - H\right) = -\frac{\partial}{\partial x}\left(\frac{2H}{B_0}\right)y + \frac{\partial H}{\partial x}. \tag{C.49}$$

and

$$-\frac{2H}{B_0}(C - 2Dy) + \frac{1}{B_0}\frac{\partial A_0}{\partial x} - 2D\left(-\frac{2H}{B_0}y - H\right) = \frac{\partial}{\partial x}\left(\frac{2H}{B_0}\right)y + \frac{\partial H}{\partial x}. \tag{C.50}$$

Adding yields

$$D = \frac{1}{2H}\left(\frac{\partial H}{\partial x} - \frac{1}{B_0}\frac{\partial A_0}{\partial x}\right). \tag{C.51}$$

Subtracting yields

$$C = -\frac{B_0}{2H}\frac{\partial}{\partial x}\left(\frac{2H}{B_0}\right)y + 4Dy. \tag{C.52}$$

Combining with D and doing some algebra $C = 0$, so χ_1 becomes

$$\chi_1(y,z) = -\frac{1}{B_0}\frac{\partial A_0}{\partial x}z + \frac{1}{2H}\left(\frac{\partial H}{\partial x} - \frac{1}{B_0}\frac{\partial A_0}{\partial x}\right)\left(z^2 - y^2\right). \tag{C.53}$$

Since $A_0 = HB_0/2$, the above becomes

$$\chi_1(y,z) = -\frac{1}{2}\left(\frac{H}{B_0}\frac{\partial B_0}{\partial x} + \frac{\partial H}{\partial x}\right)z + \left(\frac{1}{4H}\frac{\partial H}{\partial x} - \frac{1}{4B_0}\frac{\partial B_0}{\partial x}\right)\left(z^2 - y^2\right). \tag{C.54}$$

Function χ_1 for a triangular channel is shown in Figure C.3, panels *a* to *d*.

Solution for χ_2

χ_2 satisfies the following boundary value problem

$$\frac{\partial^2\chi_2}{\partial y^2} + \frac{\partial^2\chi_2}{\partial z^2} = -1, \qquad -h(x,y) < z < 0 \tag{C.55}$$

$$\frac{\partial\chi_2}{\partial z} = -\frac{A_0}{B_0}, \qquad z = 0 \tag{C.56}$$

$$\pm\frac{2H}{B_0}\frac{\partial\chi_2}{\partial y} - \frac{\partial\chi_2}{\partial z} = 0, \qquad z = \pm\frac{2H}{B_0}y - H, \tag{C.57}$$

A solution in the form (C.10) is assumed, being A a constant of integration which does not affect the value of the coefficient in the momentum equation and is thus set to $A = 0$. Also $E = -1/2 - D$, $F = 0$ and $B = -A_0/B_0$ from the Poisson equation and free surface kinematic boundary condition. This yields

$$\chi_2(y,z) = -\frac{A_0}{B_0}z + Cy + Dz^2 - \left(\frac{1}{2} + D\right)y^2. \tag{C.58}$$

The derivatives becomes

$$\frac{\partial \chi_2}{\partial z} = -\frac{A_0}{B_0} + 2Dz, \qquad \frac{\partial \chi_2}{\partial y} = C - 2y\left(\frac{1}{2} + D\right). \tag{C.59}$$

The left and right sidewall become

$$\pm\frac{2H}{B_0}\left\{C - 2y\left(\frac{1}{2} + D\right)\right\} + \frac{A_0}{B_0} - 2Dz = 0, \qquad z = \pm\frac{2H}{B_0}y - H. \tag{C.60}$$

Evaluating in $(y, z) = (0, -H)$ yields a system of equations for C and D

$$\pm\frac{2H}{B_0}C + \frac{A_0}{B_0} + 2DH = 0. \tag{C.61}$$

Adding and subtracting yield

$$D = -\frac{A_0}{2HB_0}, \qquad C = 0. \tag{C.62}$$

The expression for χ_2 therefore becomes

$$\chi_2(y, z) = -\frac{A_0}{B_0}z - \frac{A_0}{2HB_0}z^2 - \left(\frac{1}{2} - \frac{A_0}{2HB_0}\right)y^2, \tag{C.63}$$

which, since $A_0/B_0 = H/2$, can be written as

$$\chi_2(y, z) = -\frac{1}{4}\left(2Hz + z^2 + y^2\right). \tag{C.64}$$

Function χ_2 for a triangular channel is shown in Figure C.3 *e*. Due to the no-flux boundary conditions, the iso-contours are perpendicular to the lateral boundaries and show a convex behavior which is symmetric with respect to the center line.

Computation of α, β and γ

The relevant quantities derived from χ_1 become

$$\widetilde{\chi_1|_{z=0}} = \frac{B_0}{48}\frac{\partial B_0}{\partial x} - \frac{B_0^2}{48H}\frac{\partial H}{\partial x}, \tag{C.65}$$

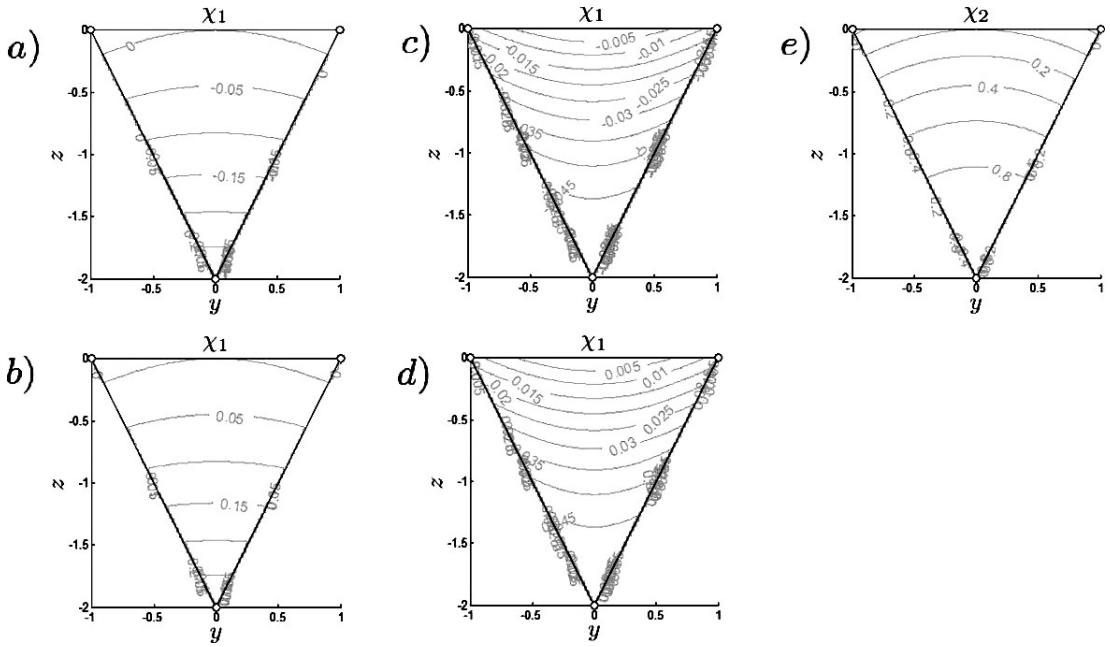

Figure C.3: Functions χ_1 and χ_2 for a triangular symmetric channel. *a*) to *d*) depict function χ_1 for the following conditions: *a*) shallowing channel of constant width ($H_x = -0.1, B_{0x} = 0$); *b*) deepening channel of constant width ($H_x = 0.1, B_{0x} = 0$); *c*) converging channel of constant depth ($H_x = 0, B_{0x} = -0.1$) and *d*) diverging channel of constant depth ($H_x = 0, B_{0x} = 0.1$). *e*) depicts the function $\chi_2$which is locally determined and independent of the longitudinal x-variations of the cross-section.

$$\frac{\partial}{\partial x}\left[\widetilde{\chi_1|_{z=0}}\right] = \frac{B_0}{48}\frac{\partial^2 B_0}{\partial x^2} + \frac{1}{48}\left(\frac{\partial B_0}{\partial x}\right)^2 - \frac{B_0}{24H}\frac{\partial B_0}{\partial x}\frac{\partial H}{\partial x} + \frac{B_0^2}{48}\frac{1}{H^2}\left(\frac{\partial H}{\partial x}\right)^2 - \frac{B_0^2}{48H}\frac{\partial^2 H}{\partial x^2}, \quad \text{(C.66)}$$

$$\overline{\chi_1} = \frac{2}{HB_0}\int_{-B_0/2}^{B_0/2}\int_{\frac{2H}{B_0}y-H}^{0} \chi_1(y,z)\,dzdy = \left(\frac{B_0}{24} + \frac{H^2}{3B_0}\right)\frac{\partial B_0}{\partial x} + \left(H - \frac{B_0^2}{24H}\right)\frac{\partial H}{\partial x}, \quad \text{(C.67)}$$

$$\begin{aligned}\overline{\frac{\partial \chi_1}{\partial x}} &= \left(\frac{B_0}{24} + \frac{H^2}{3B_0}\right)\frac{\partial^2 B_0}{\partial x^2} - \left(\frac{H^2}{3B_0^2} + \frac{1}{24}\right)\left(\frac{\partial B_0}{\partial x}\right)^2 \\ &\quad + \frac{2H}{3B_0}\frac{\partial H}{\partial x}\frac{\partial B_0}{\partial x} + \left(\frac{B_0^2}{24H^2} - \frac{1}{3}\right)\left(\frac{\partial H}{\partial x}\right)^2 + \left(H - \frac{B_0^2}{24H}\right)\frac{\partial^2 H}{\partial x^2}. \quad \text{(C.68)}\end{aligned}$$

The quantities derived from χ_2 are

$$\widetilde{\chi_2|_{z=0}} = -\frac{B_0^2}{48}, \quad \text{(C.69)}$$

$$\frac{\partial}{\partial x}\left[\widetilde{\chi_2|_{z=0}}\right] = -\frac{B_0}{24}\frac{\partial B_0}{\partial x}, \tag{C.70}$$

$$\overline{\chi_2} = \frac{H^2}{3} - \frac{B_0^2}{24}, \tag{C.71}$$

$$\overline{\frac{\partial \chi_2}{\partial x}} = \frac{2H}{3}\frac{\partial H}{\partial x}. \tag{C.72}$$

The coefficients become, after replacing to total derivatives

$$\begin{aligned}\alpha = & -\left(\frac{H^2}{3B_0} + \frac{B_0}{48}\right)\frac{d^2B_0}{dx^2} + \left(\frac{1}{16} + \frac{H^2}{3B_0^2}\right)\left(\frac{dB_0}{dx}\right)^2 - \left(\frac{B_0}{24H} + \frac{2H}{3B_0}\right)\frac{dB_0}{dx}\frac{dH}{dx} \\ & + \left(\frac{1}{3} - \frac{B_0^2}{48H^2}\right)\left(\frac{\partial H}{\partial x}\right)^2 + \left(\frac{B_0^2}{48H} - H\right)\frac{\partial^2 H}{\partial x^2},\end{aligned} \tag{C.73}$$

$$\beta = \left(\frac{B_0}{16} - \frac{H^2}{3B_0}\right)\frac{\partial B_0}{\partial x} + \left(\frac{B_0^2}{48H} - \frac{5H}{3}\right)\frac{\partial H}{\partial x}, \tag{C.74}$$

$$\gamma = \frac{B_0^2}{48} - \frac{H^2}{3}. \tag{C.75}$$

APPENDIX D

PROPERTIES OF CHANNEL-MEAN BOUSSINESQ-TYPE EQUATIONS

The dispersive properties of the cross-sectional averaged Boussinesq equations are studied in this Appendix. Section D.1 provides general comments on how to assess the dispersive and nonlinear properties of Boussinesq-type equations. Section D.2 shows a simple linear analysis of Peregrine's (1968) and Teng & Wu's (1998) theories, found to be the most complete existing theories when this research begun. Section D.3 analyses the dispersive properties, i.e. phase and group speeds, of the cross-sectional averaged Boussinesq equations (3.95) and (3.124).

D.1 General comments

From the theoretical stand point, the Boussinesq equations are valid for weakly-dispersive weakly-nonlinear waves. In practical applications however, its use may cover a wide range of kh values, so it becomes important to evaluate how accurate they are when the limitation $\epsilon = O\left(\mu^2\right) \ll O\left(1\right)$, is violated. The accuracy of Boussinesq theories can be assessed in terms of the linear and nonlinear properties for a wide range of water depths. The linear properties conventionally used are the wave celerity, the group speed, the shoaling gradient and wave kinematics (Madsen & Sorensen, 1992; Lynett & Liu, 2004 and Simarro *et al.*, 2013 among others). Nonlinear performance is assessed analyzing the energy transfer between components (Nwogu, 1993 and 1994). Dingemans (1997) proposes a sequence of steps in which Boussinesq-like models can be analyzed and improved:

- linear frequency behavior
- linear shoaling behavior
- higher-order frequency behavior
- higher-order shoaling behavior

It is well known that the accuracy of the linear dispersion relation -of crucial importance for the performance of Boussinesq models in transitional waters- depends on the reference depth. According to Dingemans (1997) good frequency dispersion properties alone is more important than also having good shoaling behavior. It should be noted that a good dispersion behavior does not mean that deep-water waves can be adequately modeled with Boussinesq-like equations, since the vertical structure remains a quadratic function of the depth, thus departing from the linear theory. The bottom velocities are not necessarily well predicted for large kh in deep waters where the linear theory predicts zero velocity. Significant improvements can be obtained for both linear properties such as linear frequency dispersion, linear shoaling, velocity profile, or nonlinear properties such as amplitude dispersion (Brochini, 2013). For example, Nwogu (1993) considered $z_\alpha = \alpha h$ for the definition of the horizontal velocity, with α being a free coefficient, to improve linear dispersive properties. Kennedy *et al.* (2001) used the constant α_ε in the definition of the reference depth $z_\alpha = \alpha h + \alpha_\varepsilon \eta$, to improve the non-linear performance of the equations.

The analysis shown in this Appendix is restricted to the linear dispersive properties on a wide range of relative water depths using standard procedures (e.g. Nwogu's, 1993). No intention to optimize these properties is achieved as no free coefficients are included in the governing equations (3.95) and (3.124).

D.2 Analysis of existing Boussinesq theories

The dispersive properties of Peregrine's (1968) and Teng & Wu's (1997) Boussinesq-type equations are analyzed herein. For simplicity, a uniform rectangular channel is analyzed, since it fulfills the limitations of both theories. It should be noted that the analysis cannot be extended for channels of arbitrary cross-sections. Peregrine's (1968) equations (A.1) and (A.2) can be simplified to[1]

$$\frac{\partial \eta}{\partial t} + h\frac{\partial u'}{\partial x} + \frac{\partial}{\partial x}(\eta u') + \frac{h^3}{3}\frac{\partial^3 u'}{\partial x^3} = 0, \tag{D.1}$$

$$\frac{\partial u'}{\partial t} + \frac{\partial \eta}{\partial x} + u'\frac{\partial u'}{\partial x} = 0. \tag{D.2}$$

Teng & Wu's (1997) equations (A.17) and (A.18), on the other hand, are simplified neglecting surface and bottom forcing to

$$\frac{\partial \widetilde{\eta}}{\partial t} + h\frac{\partial \overline{u}}{\partial x} + \frac{\partial}{\partial x}(\widetilde{\eta}\overline{u}) = 0, \tag{D.3}$$

$$\frac{\partial \overline{u}}{\partial t} + \frac{\partial \widetilde{\eta}}{\partial x} + \overline{u}\frac{\partial \overline{u}}{\partial x} - \frac{h^2}{3}\frac{\partial^3 \overline{u}}{\partial x^2 \partial t} = 0. \tag{D.4}$$

The difference among them is that Peregrine's includes the dispersive term in the continuity equation whereas Teng & Wu's (and the present theory) considers this term in the momentum equation. In order to evaluate the dispersive properties, these expressions are compared to Ngowu's (1993) Boussinesq equations (N93, eq.25), which explicitly include the reference depth z_α at which the velocity is defined. The one-dimensional version of Nwogu's equations on constant depth (e.g. Wei & Kirby, 1995; eqs.3,4) reads

$$\frac{\partial \eta}{\partial t} + h\frac{\partial u}{\partial x} + \delta\frac{\partial}{\partial x}(\eta u) + \mu^2\left(\alpha + \frac{1}{3}\right)h^3\frac{\partial^3 u}{\partial x^3} = 0, \tag{D.5}$$

$$\frac{\partial u}{\partial t} + \delta u\frac{\partial u}{\partial x} + \frac{\partial \eta}{\partial x} + \mu^2\alpha h^2\frac{\partial^3 u}{\partial x^2 \partial t} = 0, \tag{D.6}$$

[1]Peregrine's (1968) independent variables are not strictly the same quantities defined by Teng $ Wu's (1997), but are equal in the leading order, making a comparison reasonable.

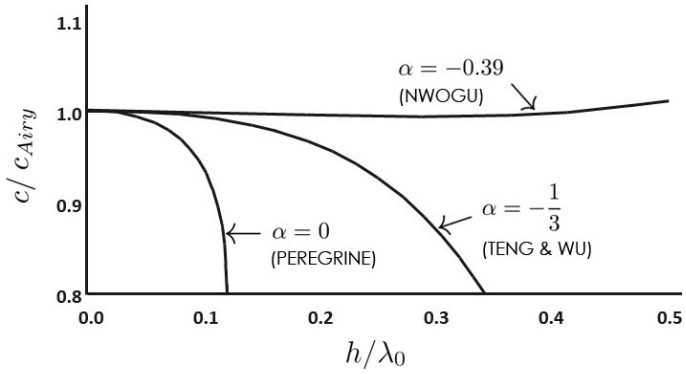

Figure D.1: Ratio of the phase speed c compared to the linear wave theory c_{Airy} for a channel of uniform rectangular cross section. Peregrine's ($\alpha = 0$), Teng & Wu's ($\alpha = -1/3$) and the optimal value of ($\alpha = -0.39$) obtained by Nwogu (1993) are depicted.

where $\alpha = z_\alpha^2/2 + z_\alpha$. By inspection, $\alpha = 0$ and $z_\alpha = 0$ for Peregrine's theory, so the velocity u' is essentially defined at the surface. For Teng & Wu's (and the present theory), $\alpha = -1/3$, corresponding to the standard Boussinesq equations derived in terms of depth-averaged velocities by Peregrine (1967) in his seminal paper for long waves on a beach.

Figure D.1 depicts the ratio of the phase speed computed with different theories and the linear theory (Airy, 1845), which is fully dispersive, therefore exact, in all range of relative depths. The plot covers from zero depth to the deep-water limit. When compared to the linear theory, the computation of the phase speed with Peregrine's theory is poor at increasing relative depths. Teng & Wu's and the present theories have improved dispersive properties, but are still worse than the optimal values of of $\alpha = -0.39$ and $z_\alpha = 0.531h$ proposed by Nwogu (1993). Consequently, Teng & Wu's theory show better dispersion properties than Peregrine's at relatively large depths, but still do not properly reproduce the phase speed at large relative depths.

D.3 Dispersive properties of the channel-mean equations

Linear dispersive properties are analyzed by comparing the phase and group speeds derived from the linearized Boussinesq equations with the expressions obtained from the linear theory, where the assumption of small relative depth is not assumed. The dispersion relation is determined from the linearized version of Boussinesq equations in a rectangular uniform channel

$$\frac{\partial \widetilde{\eta}}{\partial t} + h\frac{\partial \langle u \rangle}{\partial x} = O\left(\epsilon^2, \epsilon\mu^2, \mu^4\right), \tag{D.7}$$

$$\frac{\partial \langle u \rangle}{\partial t} + \frac{\partial \widetilde{\eta}}{\partial x} + \mu^2\gamma\frac{\partial^3 \langle u \rangle}{\partial t \partial x^2} = O\left(\epsilon^2, \epsilon\mu^2, \mu^4\right). \tag{D.8}$$

Cross-differentiating and subtracting yields

$$\frac{\partial^2 \langle u \rangle}{\partial t^2} - h\frac{\partial^2 \langle u \rangle}{\partial x^2} + \mu^2\gamma\frac{\partial^4 \langle u \rangle}{\partial t^2 \partial x^2} = O\left(\epsilon^2, \epsilon\mu^2, \mu^4\right). \tag{D.9}$$

Assume a solution of the form

$$\langle u \rangle = U \exp\left\{i\left(\kappa x - \omega t\right)\right\}, \tag{D.10}$$

where the amplitude U is independent on x and t, $k \in \mathbb{R}$ is the wavenumber and ω the angular frequency. This yields the dispersion relation

$$-\omega^2 + h\kappa^2 + \mu^2\gamma\kappa^2\omega^2 = 0, \tag{D.11}$$

from which the wave number and the phase speed are

$$\kappa = \sqrt{\frac{\omega^2}{h + \mu^2\gamma\omega^2}}, \qquad \text{and} \qquad c^2 = h + \mu^2\gamma\omega^2. \tag{D.12}$$

These wave properties are therefore affected by the dispersive coefficient γ in the second order solution. The leading order solution for the celerity is a well known result for non-dispersive waves whereas the second order solution correspond to weakly-dispersive waves expressed in terms of the mean velocity. The

analysis of linear dispersive properties consist of comparing the phase speed obtained from the Boussinesq equation with the exact linear dispersion relation derived by Airy (1845), which in dimensional form reads

$$\hat{c}_l^2 = g\hat{h}\frac{\tanh\left(\hat{k}\hat{h}\right)}{\hat{k}\hat{h}}. \tag{D.13}$$

To illustrate the influence of the cross-section geometry, simple cross-sections characterized by the expression

$$\gamma = -\frac{1}{3}\kappa^2\overline{h}^2, \tag{D.14}$$

are studied (Teng & Wu, 1994). Here $\overline{h}$ is the section-mean depth and κ^2 is a factor that depends on the channel cross-sectional shape. For a rectangular channel, $\gamma = -h^2/3$ thus $\kappa_{rec} = 1$. Note that $\kappa^2 > 1$ for concave cross-sections and increases as the section departs from rectangular. For semicircular, parabolic and triangular cross-sections, the analytical expressions are

$$\kappa_{cir} = 1.062, \qquad \kappa_{par} = \sqrt{\frac{9}{7} + \frac{1}{15}\left(\frac{b}{\overline{h}}\right)^2}, \qquad \kappa_{tri} = \sqrt{\frac{3}{2} + \frac{1}{8}\left(\frac{b}{\overline{h}}\right)^2}, \tag{D.15}$$

where b is the half-width at the surface. For parabolic and triangular cross-sections with $b = \overline{h}$, these factors become $\kappa_{par} = 1.163$ and $\kappa_{tri} = 1.274$. For a wider triangular channel of $b = 2\overline{h}$, the factor increases to $\kappa_{tri} = 1.414$. Combining D.12 and D.14 yields the dimensional expression for the phase speed

$$\hat{c}^2 = g\hat{h} - \frac{1}{3}\kappa^2 g\hat{h}^3\hat{k}^2. \tag{D.16}$$

Upon division by D.13

$$\left(\frac{\hat{c}}{\hat{c}_l}\right)^2 = \hat{k}\hat{h}\left(\frac{1 - \frac{1}{3}\left(\kappa\hat{h}\hat{k}\right)^2}{\tanh\left(\hat{k}\hat{h}\right)}\right) \tag{D.17}$$

Figure D.2 *a* shows the ratio of Boussinesq to linear wave speed $\hat{c}/\hat{c}_l$ for different cross-section over relative depths h/λ covering up to the deep water limit.

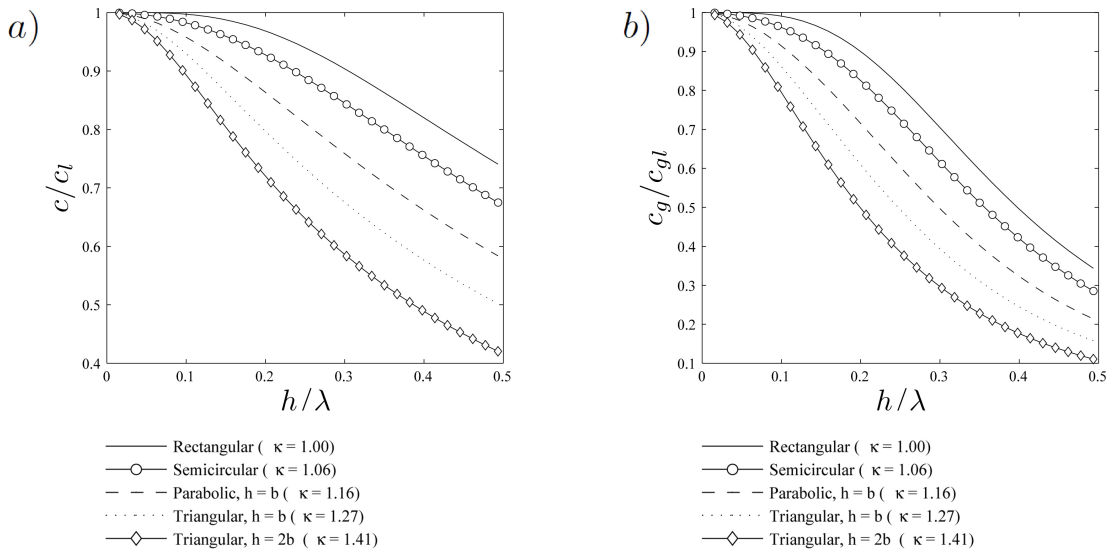

Figure D.2: Ratios of Boussinesq to linear phase speed c/c_l (a) and group speed c_g/c_{gl} (b) for different geometries over relative depths covering up to the deep water limit. The wavelength corresponds to the offshore value given by $\lambda = gT^2/2\pi$.

It is observed that the wave speed is lower than the exact value given by the linear theory for all the cross-sections. The divergence increases with larger relative depths since the assumption of weakly dispersiveness, i.e. $(h/\lambda)^2 \ll O(1)$, is violated. Note that the further the channel departs from the rectangular shape, the dispersive strength is larger and the linear dispersive properties of the Boussinesq-type equations becomes poorer. Therefore, linear dispersive properties of the present theory are section dependent.

The group speed is associated with the propagation of energy, i.e. the wave envelope. For a random waves, alternate groups of large and small waves traveling at this speed occur. The group velocity in dimensional form is obtained from the expression

$$\hat{c}_g = \frac{d\hat{\omega}}{d\hat{k}} = \hat{c} + \hat{k}\frac{d\hat{c}}{d\hat{k}}, \tag{D.18}$$

where by virtue of equation (D.16) and series expansion can be written as

$$\hat{c} = \sqrt{\frac{g\hat{h}}{1 + \frac{1}{3}\left(\kappa\hat{h}\hat{k}\right)^2}} \tag{D.19}$$

Doing some algebra yields to equivalent expressions

$$\hat{c}_g \;\; = \hat{c}\left(1 - \frac{\frac{1}{3}\left(\kappa\hat{h}\hat{k}\right)^2}{1+\frac{1}{3}\left(\kappa\hat{h}\hat{k}\right)^2}\right) \tag{D.20}$$

The latter is equivalent to Nwogu's (1993; eq.30) for $\alpha = -1/3$ corresponding to standard Boussinesq equations. The exact linear dispersion relation derived by Airy (1845) is given by

$$\hat{c}_{gl} = n\hat{c}_l, \qquad \text{where} \qquad n = \frac{1}{2}\left[1 + \frac{2\hat{k}\hat{h}}{\sinh\left(2\hat{k}\hat{h}\right)}\right], \tag{D.21}$$

is a measure of the effect of the relative depth in the group speed. The group speed, normalized with respect to the linear exact solution can be simplified to

$$\frac{\hat{c}_g}{\hat{c}_{gl}} = \frac{\hat{c}}{\hat{c}_l}\left(\frac{1}{n\left[1 + \frac{1}{3}\left(\kappa\hat{k}\hat{h}\right)^2\right]}\right), \tag{D.22}$$

where $\hat{c}/\hat{c}_l$ is obtained from equation D.17. Figure D.2 *b* shows the ratio of Boussinesq to linear group speed $\hat{c}_g/\hat{c}_{gl}$ for different cross-section over relative depths h/λ covering up to the deep water limit. The Boussinesq based group speed is lower than the exact value given by the linear model and tends to deviate more rapidly than the corresponding value of the phase speed c/c_l. As expected, the effect of geometry also affects the group speed, used to quantify the linear dispersion properties of of the governing equations.

The affect of the coefficients α and β in the governing equations (3.95) and (3.124) is not straightforward as these terms depend on x for non-uniform channels. It's analysis along with shoaling properties is not pursued in this dissertation.

APPENDIX E

VISCOUS EFFECTS IN CHANNELS OF ARBITRARY CROSS-SECTIONS

Following Liu & Orfila (2004), an expression for the normal velocity generated in the bottom boundary layer (u^r_ς) is derived in this Appendix. The fluid motion is assumed to be irrotational in the core region including the surface boundary, and rotational in the bottom boundary layer. Integrated along the wetted perimeter, this normal velocity represents a mass flux into the core region (U_ς) which may be introduced in the cross-sectional averaged continuity equation by means of a convolution integral.

Exact govening equations in local curvilinear coordinates

Lets begin from the three-dimensional equations of conservation of mass (3.19) and the linearized x-momentum equation (3.20) including viscous forces

$$\frac{\partial u}{\partial x} + \frac{1}{\mu^2}\left(\frac{\partial v}{\partial y} + \frac{\partial w}{\partial z}\right) = 0, \tag{E.1}$$

$$\frac{\partial u}{\partial t} = -\frac{\partial p}{\partial x} + \alpha^2\left(\frac{\partial^2 u}{\partial x^2} + \frac{1}{\mu^2}\frac{\partial^2 u}{\partial y^2} + \frac{1}{\mu^2}\frac{\partial^2 u}{\partial z^2}\right), \tag{E.2}$$

where the non-dimensional parameters

$$\mu = \frac{\hat{h}_0}{\hat{\lambda}}, \qquad \epsilon = \frac{\hat{a}_0}{\hat{h}_0}, \qquad \alpha^2 = \frac{\hat{\nu}}{\hat{\lambda}\sqrt{\hat{g}\hat{h}_0}}, \tag{E.3}$$

represent measures of frequency dispersion, non-linearity and viscosity. Here $\hat{h}_0$, $\hat{a}_0$, a $\hat{\lambda}$ are the typical channel depth, wave amplitude and wavelength, respectively. $\hat{\nu}$ is the eddy viscosity, assumed constant on the boundary layer, and $\hat{g}$ gravity. The boundary layer is assumed to be a thin layer parallel to the bottom. A curvilinear coordinate system where ξ is tangential and ς perpendicular to the bottom is adopted (Figure E.1). The coordinate transform is defined

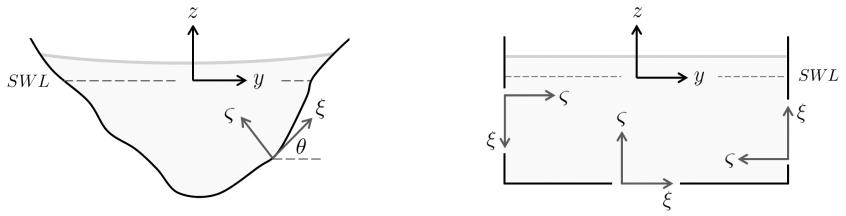

Figure E.1: Definition of local coordinates for *a*) an arbitrary cross-sections and *b*) rectangular cross-sections, as in Chang *et al*. (1979).

locally by

$$\left\{ \begin{array}{c} \xi \\ \varsigma \end{array} \right\} = \left[\begin{array}{cc} \cos\theta & \sin\theta \\ -\sin\theta & \cos\theta \end{array} \right] \left\{ \begin{array}{c} y \\ z \end{array} \right\}, \tag{E.4}$$

where (y, z) represent the coordinates of any point along the boundary. The velocities in the Cartesian and local coordinate systems are related by

$$\left\{ \begin{array}{c} u_\xi \\ u_\varsigma \end{array} \right\} = \left[\begin{array}{cc} \cos\theta & \sin\theta \\ -\sin\theta & \cos\theta \end{array} \right] \left\{ \begin{array}{c} v \\ w \end{array} \right\}. \tag{E.5}$$

For any function $f(y, z)$, with $y(\xi, \varsigma)$ and $z(\xi, \varsigma)$, the derivatives are related by

$$\frac{\partial f}{\partial x_i} = \frac{\partial f}{\partial \xi}\frac{\partial \xi}{\partial x_i} + \frac{\partial f}{\partial \varsigma}\frac{\partial \varsigma}{\partial x_i}, \tag{E.6}$$

$$\frac{\partial^2 f}{\partial x_i^2} = \frac{\partial^2 f}{\partial \xi^2}\left(\frac{\partial \xi}{\partial x_i}\right)^2 + 2\frac{\partial^2 f}{\partial \varsigma \partial \xi}\frac{\partial \xi}{\partial x_i}\frac{\partial \varsigma}{\partial x_i} + \frac{\partial^2 f}{\partial \varsigma^2}\left(\frac{\partial \varsigma}{\partial x_i}\right)^2 \tag{E.7}$$

where, for $x_i = y, z$. Under the transformation (E.4), the equation of conservation of mass (E.1) becomes

$$\begin{aligned} \mu^2\frac{\partial u}{\partial x} + \frac{\partial \xi}{\partial y}\frac{\partial}{\partial \xi}\left\{u_\xi \cos\theta\right\} + \frac{\partial \varsigma}{\partial y}\frac{\partial}{\partial \varsigma}\left\{u_\xi \cos\theta\right\} \\ -\frac{\partial \xi}{\partial y}\frac{\partial}{\partial \xi}\left\{u_\varsigma \sin\theta\right\} - \frac{\partial \varsigma}{\partial y}\frac{\partial}{\partial \varsigma}\left\{u_\varsigma \sin\theta\right\}\frac{\partial \xi}{\partial z}\frac{\partial}{\partial \xi}\left\{u_\xi \sin\theta\right\} \\ +\frac{\partial \varsigma}{\partial z}\frac{\partial}{\partial \varsigma}\left\{u_\xi \sin\theta\right\} + \frac{\partial \xi}{\partial z}\frac{\partial}{\partial \xi}\left\{u_\varsigma \cos\theta\right\} + \frac{\partial \varsigma}{\partial z}\frac{\partial}{\partial \varsigma}\left\{u_\varsigma \cos\theta\right\} = 0. \end{aligned} \tag{E.8}$$

The conservation of momentum (E.2) reads

$$\begin{aligned} \frac{\partial u}{\partial t} = -\frac{\partial p}{\partial x} + \alpha^2\frac{\partial^2 u}{\partial x^2} + \frac{\alpha^2}{\mu^2}\frac{\partial^2 u}{\partial \xi^2}\left(\frac{\partial \xi}{\partial y}\right)^2 + 2\frac{\alpha^2}{\mu^2}\frac{\partial^2 u}{\partial \varsigma \partial \xi}\frac{\partial \xi}{\partial y}\frac{\partial \varsigma}{\partial y} + \frac{\alpha^2}{\mu^2}\frac{\partial^2 u}{\partial \varsigma^2}\left(\frac{\partial \varsigma}{\partial y}\right)^2 \\ +\frac{\alpha^2}{\mu^2}\frac{\partial^2 u}{\partial \xi^2}\left(\frac{\partial \xi}{\partial z}\right)^2 + 2\frac{\alpha^2}{\mu^2}\frac{\partial^2 u}{\partial \varsigma \partial \xi}\frac{\partial \xi}{\partial z}\frac{\partial \varsigma}{\partial z} + \frac{\alpha^2}{\mu^2}\frac{\partial^2 u}{\partial \varsigma^2}\left(\frac{\partial \varsigma}{\partial z}\right)^2. \end{aligned} \tag{E.9}$$

These expressions are exact and valid for the domain bounded by the free surface and the bottom of the channel.

Approximate governing equations in the bottom boundary layer

By means of the following perturbation expansions, the irrotational flow in the core region is separated from the rotational flow in the bottom boundary layer,

$$u = \frac{\partial \phi}{\partial x} + u_0^r + \alpha u_1^r + \ldots \qquad u_\xi = \frac{\partial \phi}{\partial \xi} + \alpha\mu u_{\xi 1}^r + \ldots \qquad u_\varsigma = \frac{\partial \phi}{\partial \varsigma} + \alpha\mu u_{\varsigma 1}^r + \ldots \quad \text{(E.10)}$$

Also $\epsilon = O\left(\mu^2\right) \ll O(1)$ is assumed, implying the Boussinesq approximation. In addition, $\alpha = O\left(\epsilon^2, \mu^4\right)$, meaning that the viscous effects are slightly weaker than the dispersive and non-linear effects. Using the perturbation expansion (E.10) in the conservation of mass (E.8) yields, for the rotational velocity in the boundary layer

$$\begin{aligned}
&\mu^2 \frac{\partial u_0^r}{\partial x} + \alpha\mu^2 \frac{\partial u_1^r}{\partial x} + \alpha\mu \frac{\partial \xi}{\partial y}\frac{\partial}{\partial \xi}\left\{u_{\xi 1}^r \cos\theta\right\} + \alpha\mu \frac{\partial \varsigma}{\partial y}\frac{\partial}{\partial \varsigma}\left\{u_{\xi 1}^r \cos\theta\right\} \\
&-\alpha\mu \frac{\partial \xi}{\partial y}\frac{\partial}{\partial \xi}\left\{u_{\varsigma 1}^r \sin\theta\right\} - \alpha\mu \frac{\partial \varsigma}{\partial y}\frac{\partial}{\partial \varsigma}\left\{u_{\varsigma 1}^r \sin\theta\right\} + \alpha\mu \frac{\partial \xi}{\partial z}\frac{\partial}{\partial \xi}\left\{u_{\xi 1}^r \sin\theta\right\} \\
&+\alpha\mu \frac{\partial \varsigma}{\partial z}\frac{\partial}{\partial \varsigma}\left\{u_{\xi 1}^r \sin\theta\right\} + \alpha\mu \frac{\partial \xi}{\partial z}\frac{\partial}{\partial \xi}\left\{u_{\varsigma 1}^r \cos\theta\right\} + \alpha\mu \frac{\partial \varsigma}{\partial z}\frac{\partial}{\partial \varsigma}\left\{u_{\varsigma 1}^r \cos\theta\right\} \;=\; 0. \quad \text{(E.11)}
\end{aligned}$$

The conservation of momentum (E.9) becomes

$$\begin{aligned}
\frac{\partial}{\partial t}\left(u_0^r + \alpha u_1^r\right) &= -\frac{\partial p}{\partial x} + \alpha^2 \frac{\partial^2}{\partial x^2}\left(u_0^r + \alpha u_1^r\right) \\
&+\frac{\alpha^2}{\mu^2}\left(\frac{\partial \xi}{\partial y}\right)^2 \frac{\partial^2}{\partial \xi^2}\left(u_0^r + \alpha u_1^r\right) + 2\frac{\alpha^2}{\mu^2}\frac{\partial \xi}{\partial y}\frac{\partial \varsigma}{\partial y}\frac{\partial^2}{\partial \varsigma \partial \xi}\left(u_0^r + \alpha u_1^r\right) \\
&+\frac{\alpha^2}{\mu^2}\left(\frac{\partial \varsigma}{\partial y}\right)^2 \frac{\partial^2}{\partial \varsigma^2}\left(u_0^r + \alpha u_1^r\right) + \frac{\alpha^2}{\mu^2}\left(\frac{\partial \xi}{\partial z}\right)^2 \frac{\partial^2}{\partial \xi^2}\left(u_0^r + \alpha u_1^r\right) \\
&+2\frac{\alpha^2}{\mu^2}\frac{\partial \xi}{\partial z}\frac{\partial \varsigma}{\partial z}\frac{\partial^2}{\partial \varsigma \partial \xi}\left(u_0^r + \alpha u_1^r\right) + \frac{\alpha^2}{\mu^2}\left(\frac{\partial \varsigma}{\partial z}\right)^2 \frac{\partial^2}{\partial \varsigma^2}\left(u_0^r + \alpha u_1^r\right). \quad \text{(E.12)}
\end{aligned}$$

Since the boundary layer thickness is of $O(\alpha)$, a stretched coordinate

$$\varsigma = \frac{\alpha}{\mu}\varphi - 1. \quad \text{(E.13)}$$

is introduced. The leading-order continuity equation (E.11) is simplified to

$$\frac{\partial u_0^r}{\partial x} - \frac{\partial}{\partial \varphi}\left(T u_{\varsigma 1}^r\right) = O\left(\frac{\alpha}{\mu}\right), \qquad \text{with} \qquad T = \frac{\partial \varsigma}{\partial y}\sin\theta - \frac{\partial \varsigma}{\partial z}\cos\theta. \tag{E.14}$$

In the above, the free stream velocity is assumed to be independent of ξ. The linearized momentum equation (E.12) becomes

$$\frac{\partial u_0^r}{\partial t} = K\frac{\partial^2 u_0^r}{\partial \varphi^2}, \qquad \text{with} \qquad K = \left(\frac{\partial \varsigma}{\partial y}\right)^2 + \left(\frac{\partial \varsigma}{\partial z}\right)^2. \tag{E.15}$$

Two-point boundary-value problem for u_0^r

To solve for the longitudinal component of the velocity in the boundary layer from (E.15), the mathematical procedures in Mei (1995. Ch.7) is followed. The following boundary and initial conditions are prescribed

$$u_0^r(0,t) = -\langle u \rangle, \qquad \varphi = 0, \tag{E.16}$$

$$u_0^r(\infty,t) = 0, \qquad \varphi \to \infty, \tag{E.17}$$

$$u_0^r(\varphi,0) = h(\varphi) = 0, \qquad t = 0. \tag{E.18}$$

The flux boundary condition at the bottom (E.16) implies the rotational velocity is equal and opposite to the free stream velocity, so the total velocity vanishes at the wall. The second boundary condition (E.17) indicates the rotational velocity vanishes far from the wall. The initial condition (E.18) implies the boundary layer is at rest initially, i.e. $h(\varphi) = 0$. Equation (E.15) is ontegrated using the Fourier sine function

$$\mathcal{F}(\alpha) = \int_0^\infty f(\varphi)\sin(\alpha\varphi)\, d\varphi. \tag{E.19}$$

Performing partial integration repeatedly in the right hand side yields

$$\frac{\partial \mathcal{U}}{\partial t} + K\alpha^2 \mathcal{U} = K\alpha\langle u \rangle. \tag{E.20}$$

Upon integration

$$\mathcal{U} = K\alpha \int_0^t \langle u \rangle e^{K\alpha^2(\tau - t)} d\tau. \tag{E.21}$$

Applying the inverse transform

$$f(\varphi) = \frac{2}{\pi}\int_0^\infty \mathcal{F}(\alpha)\sin(\alpha\varphi)\,d\alpha \tag{E.22}$$

to (E.21) yields

$$u_0^r(\varphi) = \frac{2K}{\pi}\int_0^\infty \left\{\alpha\int_0^t \left.\frac{\partial\phi}{\partial x}\right|_0 e^{K\alpha^2(\tau-t)}d\tau\right\}\sin(\alpha\varphi)\,d\alpha, \tag{E.23}$$

which changing the order of integration becomes

$$u_0^r(\varphi) = \frac{2K}{\pi}\int_0^t \langle u\rangle\left\{\int_0^\infty \alpha e^{-K\alpha^2(t-\tau)}\sin(\alpha\varphi)\,d\alpha\right\}d\tau. \tag{E.24}$$

The integration is carried out by means of a change of variable

$$X^2 = k\alpha^2(t-\tau), \qquad \text{thus} \qquad d\alpha = \frac{dX}{\sqrt{k(t-\tau)}}, \tag{E.25}$$

so

$$u_0^r(x,\varphi,\varsigma,t) = \frac{\varphi}{\sqrt{4K\pi}}\int_0^t \frac{\langle u\rangle(x,\tau)}{\sqrt{(t-\tau)^3}}e^{-\frac{\varphi^2}{4K(t-\tau)}}d\tau + O\left(\frac{\alpha}{\mu}\right). \tag{E.26}$$

Normal velocity to the boundary layer

Combining (E.26) with the continuity equation (E.14) and integrating yields

$$u_{\varsigma 1}^r(x,\varphi,\varsigma,t) = -\frac{1}{T}\int_\varphi^\infty \left\{\frac{\varphi}{2\sqrt{K\pi}}\int_0^t \frac{\langle u\rangle_x}{\sqrt{(t-\tau)^3}}e^{-\frac{\varphi^2}{4K(t-\tau)}}d\tau\right\}d\varphi. \tag{E.27}$$

This implies a normal velocity component is generated inside the bottom boundary layer, which persists outside the boundary layer. Changing the order of integration

$$u_{\varsigma 1}^r(x,\varphi,\varsigma,t) = -\frac{1}{T}\int_0^t \frac{1}{2\sqrt{K\pi}}\frac{\frac{\partial^2\phi}{\partial x^2}(x,\tau)}{\sqrt{(t-\tau)^3}}\left\{\int_\varphi^\infty \varphi e^{-\frac{\varphi^2}{4K(t-\tau)}}d\varphi\right\}d\tau. \tag{E.28}$$

Introducing the variable

$$Y^2 = \frac{\varphi^2}{4K(t-\tau)}, \qquad \text{thus} \qquad d\varphi = 2\sqrt{K(t-\tau)}dY, \tag{E.29}$$

yields, upon integration

$$u^r_{\varsigma 1}(x,\varphi,\varsigma,t) = -\frac{1}{T}\sqrt{\frac{K}{\pi}}\int_0^t \frac{\langle u\rangle_x}{\sqrt{t-\tau}} e^{-\frac{\varphi^2}{4K(t-\tau)}} d\tau. \tag{E.30}$$

Evaluating at the bottom[1] ($\varphi = 0$) yields an expression for the normal rotational velocity

$$u^r_{\varsigma 1}(x,0,\varsigma,t) = -\frac{\mathcal{H}}{\sqrt{\pi}}\int_0^t \frac{\langle u\rangle_x}{\sqrt{t-\tau}} d\tau + O\left(\frac{\alpha}{\mu}\right), \tag{E.31}$$

where

$$\mathcal{H}(\theta) = \frac{K}{T} = \frac{\sqrt{\left(\frac{\partial\varsigma}{\partial y}\right)^2 + \left(\frac{\partial\varsigma}{\partial z}\right)^2}}{\frac{\partial\varsigma}{\partial y}\sin\theta - \frac{\partial\varsigma}{\partial z}\cos\theta} \tag{E.32}$$

is a function defined by the local geometry. This expression is equivalent to Liu & Orfila's equation (2.17). The total mass flux entering (exiting) the core region is computed from the integration along the wetted perimeter s

$$U_\varsigma(x,t) = -\frac{1}{\sqrt{\pi}}\int_0^R \mathcal{H}(\theta)\, ds \times \int_0^t \frac{\langle u\rangle_x}{\sqrt{t-\tau}} d\tau + O\left(\frac{\alpha}{\mu}\right), \tag{E.33}$$

where R is the hydraulic radius. Using an heuristic approach, this flux is included in the cross-sectional conservation of mass (3.58) as

$$\frac{1}{\epsilon}\frac{\partial A}{\partial t} + \frac{\partial}{\partial x}(\langle u\rangle A) = \frac{\alpha}{\mu}U_\varsigma. \tag{E.34}$$

Example on a rectangular channel

For a rectangular channel shown in Figure E.1,

$$\int_0^R \mathcal{H}(\theta)\, ds = -\mathcal{H}\left(-\frac{\pi}{2}\right)\int_0^{-h} dz + \mathcal{H}(0)\int_{-B_0/2}^{B_0/2} dy + \mathcal{H}\left(\frac{\pi}{2}\right)\int_{-h}^0 dz, \tag{E.35}$$

where $\mathcal{H}(-\pi/2) = \mathcal{H}(0) = \mathcal{H}(\pi/2) = -1$. The total flux being transferred from the boundary layer to the core region becomes

$$U_\varsigma(x,t) = \frac{B_0 + 2h}{\sqrt{\pi}}\int_0^t \frac{\langle u\rangle_x}{\sqrt{t-\tau}} d\tau. \tag{E.36}$$

[1]Note this velocity should be evaluated at the limit of the boundary layer to account for the mass flux entering (exiting) the core region from (to) the boundary layer. Since the boundary layer is small, this is a sound approximation.

APPENDIX F

SOLITARY WAVE SOLUTION FOR A UNIFORM CHANNEL WITH $\gamma < 0$

The derivation of a solitary wave solution for the Boussinesq equations follows Mei (1983). The basic idea is to begin from the Boussinesq equations (3.95) and (3.124),

$$\frac{\partial \widetilde{\eta}}{\partial t} + \frac{1}{B_0}\frac{\partial}{\partial x}\left(\langle u\rangle A_0\right) - \epsilon\frac{B_0'}{B_0^2}\widetilde{\eta}\frac{\partial}{\partial x}\left(\langle u\rangle A_0\right) + \frac{\epsilon}{B_0}\frac{\partial}{\partial x}\left(\langle u\rangle B_0\widetilde{\eta}\right) \quad = O\left(\epsilon^2\right), \tag{F.1}$$

$$\frac{\partial \langle u\rangle}{\partial t} + \frac{\partial \widetilde{\eta}}{\partial x} + \epsilon\langle u\rangle\frac{\partial \langle u\rangle}{\partial x} + \mu^2\alpha\frac{\partial \langle u\rangle}{\partial t} + \mu^2\beta\frac{\partial^2 \langle u\rangle}{\partial t\partial x} + \mu^2\gamma\frac{\partial^3 \langle u\rangle}{\partial t\partial x^2} \quad = O\left(\epsilon^2\right), \tag{F.2}$$

derive an approximate ordinary differential equation for the velocity potential $\phi = \int^x \overline{u}dx$, and then find expressions for the surface-mean free surface elevation $\widetilde{\eta}$ and section-mean longitudinal velocity $\langle u\rangle$. Note that due to the Boussinesq approximation the leading order error is $O\left(\epsilon^2, \epsilon\mu^2, \mu^4\right)$. In a uniform channel with arbitrary cross-section

$$\frac{\partial A_0}{\partial x}, \frac{\partial B_0}{\partial x}, \alpha, \beta = O\left(\epsilon\right), \tag{F.3}$$

and the Boussinesq equations are simplified to

$$\frac{\partial \widetilde{\eta}}{\partial t} + \frac{A_0}{B_0}\frac{\partial \overline{u}}{\partial x} - \epsilon\frac{A_0B_0'}{B_0^2}\widetilde{\eta}\frac{\partial \overline{u}}{\partial x} + \epsilon\frac{\partial}{\partial x}\left(\overline{u}\widetilde{\eta}\right) \quad = O\left(\epsilon^2\right), \tag{F.4}$$

$$\frac{\partial \overline{u}}{\partial t} + \frac{\partial \widetilde{\eta}}{\partial x} + \frac{\epsilon}{2}\frac{\partial}{\partial x}\left(\overline{u}^2\right) + \mu^2\gamma\frac{\partial^3 \overline{u}}{\partial t\partial x^2} \quad = O\left(\epsilon^2\right). \tag{F.5}$$

where the advective term is expressed in conservative form and the mean water depth is defined as

$$\overline{h} = \frac{1}{B_0}\int_{-b_r}^{b_l} h\left(y\right)dy = \frac{A_0}{B_0}, \qquad B_0 = b_l + b_r. \tag{F.6}$$

Note that for a rectangular channel, where $B_0' = 0$ and $\gamma = -\overline{h}^2/3$, the standard solitary wave form is a solution of the Boussinesq equations. Introducing the

velocity potential $\phi = \int^x \overline{u} dx$ yields

$$\frac{\partial \widetilde{\eta}}{\partial t} + \overline{h}\frac{\partial^2 \phi}{\partial x^2} - \epsilon \frac{\overline{h} B_0'}{B_0}\widetilde{\eta}\frac{\partial^2 \phi}{\partial x^2} + \epsilon \frac{\partial}{\partial x}\left(\frac{\partial \phi}{\partial x}\widetilde{\eta}\right) = O\left(\epsilon^2\right), \tag{F.7}$$

$$\frac{\partial^2 \phi}{\partial t \partial x} + \frac{\partial \widetilde{\eta}}{\partial x} + \frac{\epsilon}{2}\frac{\partial}{\partial x}\left(\frac{\partial \phi}{\partial x}^2\right) + \mu^2 \gamma \frac{\partial^4 \phi}{\partial t \partial x^3} = O\left(\epsilon^2\right), . \tag{F.8}$$

Equation (F.7) corresponds to Mei's equation (5.1, p.540) with an extra term accounting for the sidewall effect at the still water level. These equations are combined by finding expressions for $\widetilde{\eta}$ and $\partial\widetilde{\eta}/\partial t$ from the conservation of momentum and then replacing in the continuity equation. The momentum equation can be integrated in space from $-\infty$ to x to yield

$$\widetilde{\eta} = -\frac{\partial \phi}{\partial t} - \frac{\epsilon}{2}\left(\frac{\partial \phi}{\partial x}\right)^2 - \mu^2 \gamma \frac{\partial^3 \phi}{\partial t \partial x^2} + O\left(\epsilon^2\right), \tag{F.9}$$

where all the quantities at $x \to -\infty$ vanish for a solitary-type wave. The above corresponds to Mei's equation (5.2, p.540). Taking the derivative in time yields

$$\frac{\partial \widetilde{\eta}}{\partial t} = -\frac{\partial^2 \phi}{\partial t^2} - \epsilon \frac{\partial \phi}{\partial x}\frac{\partial^2 \phi}{\partial t \partial x} - \mu^2 \gamma \frac{\partial^4 \phi}{\partial t^2 \partial x^2} + O\left(\epsilon^2\right). \tag{F.10}$$

Replacing (F.9) and (F.10) in (F.7) and reordering

$$-\frac{\partial^2 \phi}{\partial t^2} + \overline{h}\frac{\partial^2 \phi}{\partial x^2} - \epsilon\left[2\frac{\partial \phi}{\partial x}\frac{\partial^2 \phi}{\partial x \partial t} + \left(1 - \frac{\overline{h} B_0'}{B_0}\right)\frac{\partial^2 \phi}{\partial x^2}\frac{\partial \phi}{\partial t}\right] - \mu^2 \gamma \frac{\partial^4 \phi}{\partial t^2 \partial x^2} = O\left(\epsilon^2\right). \tag{F.11}$$

Derivation of the free surface elevation

Equation (F.11) is a fourth-order nonlinear PDE that can be transformed into an ODE by introducing a moving coordinate system

$$\xi = x - ct, \tag{F.12}$$

where c is the phase speed of the wave, yet to be determined. Thus, the motion is restricted to one direction only. The derivatives become

$$\frac{\partial \phi}{\partial x} = \frac{d\phi}{d\xi}, \qquad \frac{\partial^2 \phi}{\partial x^2} = \frac{d^2 \phi}{d\xi^2}, \qquad \frac{\partial^4 \phi}{\partial t^2 \partial x^2} = c^2 \frac{d^4 \phi}{d\xi^4},$$

$$\frac{\partial\phi}{\partial t} = -c\frac{d\phi}{d\xi}, \qquad \frac{\partial^2\phi}{\partial t^2} = c^2\frac{d^2\phi}{d\xi^2}, \qquad \frac{\partial^2\phi}{\partial t\partial x} = -c\frac{d^2\phi}{d\xi^2}. \tag{F.13}$$

Equation (F.11) is recast to

$$\left(\overline{h} - c^2\right)\frac{d^2\phi}{d\xi^2} + \epsilon c\left(3 - \frac{\overline{h}B_0'}{B_0}\right)\frac{d^2\phi}{d\xi^2}\frac{d\phi}{d\xi} - \mu^2\gamma c^2\frac{d^4\phi}{d\xi^4} = O\left(\epsilon^2\right). \tag{F.14}$$

Rearranging and integrating from $-\infty$ to ξ yields

$$\left(\overline{h} - c^2\right)\frac{d\phi}{d\xi} + \frac{\epsilon}{2}\left(3 - \frac{\overline{h}B_0'}{B_0}\right)c\left(\frac{d\phi}{d\xi}\right)^2 - \mu^2\gamma c^2\frac{d^3\phi}{d\xi^3} = O\left(\epsilon^2\right),$$

where all quantities at $\xi \to -\infty$ vanish for a solitary-type of wave. Multiplying by $2\partial^2\phi/\partial\xi^2$ and integrating from $-\infty$ to ξ yields

$$\left(\overline{h} - c^2\right)\left(\frac{d\phi}{d\xi}\right)^2 + \epsilon\left(1 - \frac{\overline{h}B_0'}{3B_0}\right)c\left(\frac{d\phi}{d\xi}\right)^3 - \mu^2\gamma c^2\left(\frac{d^2\phi}{d\xi^2}\right)^2 = O\left(\epsilon^2\right), \tag{F.15}$$

since again, all quantities vanish at $\xi \to -\infty$. To the leading order F.9 is $\widetilde{\eta} = c\frac{d\phi}{d\xi} + O\left(\epsilon, \mu^2\right)$, thus

$$-\epsilon\left(1 - \frac{\overline{h}B_0'}{3B_0}\right)\widetilde{\eta}^3 + \left(c^2 - \overline{h}\right)\widetilde{\eta}^2 + \mu^2\gamma c^2\left(\frac{d\widetilde{\eta}}{d\xi}\right)^2 = O\left(\epsilon^2\right),$$

which is equivalent to Mei's equation (5.5, p.540) with an extra term due to sidewall slopes. Note that c is retained explicitly in the third term whereas Mei uses the approximations $h = 1$ and $c^2 = 1 + O\left(\epsilon, \mu^2\right)$. Rearranging yields

$$\left(\frac{d\widetilde{\eta}}{d\xi}\right)^2 = \frac{\widetilde{\eta}^2}{\gamma c^2}\left(\left\{1 - \frac{\overline{h}B_0'}{3B_0}\right\}\widetilde{\eta} - \frac{c^2 - \overline{h}}{\epsilon}\right) + O\left(\epsilon^2\right). \tag{F.16}$$

The right hand side must be positive. Since γ could be positive or negative depending on the cross-sectional configuration

$$0 \le \widetilde{\eta} \le \frac{\mathrm{Sgn}\,(\gamma)}{1 - \left(\overline{h}B_0'\right)/\left(3B_0\right)}\left(\frac{\overline{h} - c^2}{\epsilon}\right) \tag{F.17}$$

it is required. At the wave crest, the maximum surface elevation is

$$\widetilde{\eta}_{max} = \frac{\mathrm{Sgn}\,(\gamma)}{1 - \left(\overline{h}B_0'\right)/\left(3B_0\right)}\left(\frac{\overline{h} - c^2}{\epsilon}\right). \tag{F.18}$$

To find the expression for c, the maximum surface elevation $\widetilde{\eta}_{max} = 1$ is evaluated in the above[1]. The dimensionless expressions of c is

$$c^2 = \overline{h} + \epsilon \left\{ 1 - \frac{\overline{h} B_0'}{3 B_0} \right\} \mathrm{Sgn}\left(\gamma\right). \tag{F.19}$$

It is evident that the sidewall slope alters the second order approximation of the phase speed. For $B_0' > 0$ (width at the still water level increasing with elevation) the phase speed is decreased whereas for $B_0' < 0$ it increases. Combining (F.19) with (F.16)

$$\left(\frac{d\widetilde{\eta}}{d\xi}\right)^2 = \widetilde{\eta}^2 \left(1 - \widetilde{\eta}\right) \left\{ \frac{\overline{h} B_0'}{3 B_0} - 1 \right\} \frac{1}{\gamma c^2} + O\left(\epsilon^2\right), \tag{F.20}$$

and taking the square root yields

$$\frac{d\widetilde{\eta}}{d\xi} = \pm A \widetilde{\eta} \sqrt{1 - \widetilde{\eta}} + O\left(\epsilon, \mu^2\right), \qquad \text{where} \qquad A = \frac{1}{c} \sqrt{\frac{1}{\gamma} \left\{ \frac{\overline{h} B_0'}{3 B_0} - 1 \right\}}. \tag{F.21}$$

The positive solution is retained hereafter. Since $\gamma < 0$, the restriction $B_0' \leq 3 B_0 / \overline{h}$ must hold. Integration of (F.21) yields

$$-2 tanh^{-1} \sqrt{1 - \widetilde{\eta}} = A \left(\xi - \xi_0\right) + O\left(\epsilon, \mu^2\right), \tag{F.22}$$

which doing some algebra and considering $sech^2\left(-x\right) = sech^2\left(x\right)$ yields

$$\widetilde{\eta} = sech^2 \left(\frac{A}{2} \xi + \varphi \right) + O\left(\epsilon, \mu^2\right), \tag{F.23}$$

where φ can be set to zero. Using (F.12) and a series expansion for $1/c = 1/\sqrt{\overline{h}} + O\left(\epsilon\right)$ yields and expression for the surface elevation

$$\widetilde{\eta} = sech^2 \left(K \left(x - ct\right)\right) + O\left(\epsilon, \mu^2\right), \tag{F.24}$$

where the effective wavenumber is

$$K = \frac{1}{2} \sqrt{\frac{1}{\overline{h} \gamma} \left\{ \frac{\overline{h} B_0'}{3 B_0} - 1 \right\}}. \tag{F.25}$$

[1]Recall that the dimensional surface elevation is scaled as $\widetilde{\eta} = \hat{a}_0 \widetilde{\eta}$, so that at the maximum elevation, $\widehat{\eta}_{max} = \hat{a}_0$, therefore $\widetilde{\eta}_{max} = 1$.

Derivation of the velocity

Equations (F.7) and (F.8) can be combined to yield, to the leading order

$$\frac{\partial^2\phi}{\partial t^2} + \bar{h}\frac{\partial^2\phi}{\partial x^2} \quad = O\left(\epsilon, \mu^2\right). \tag{F.26}$$

This wave equation solutions of the form $\phi = f(\theta)$, with $\theta = x \mp \sqrt{\bar{h}}t$. Invoking the chain rule

$$\frac{\partial\phi}{\partial x} = \frac{\partial\phi}{\partial\theta}\frac{\partial\theta}{\partial x}, \qquad \text{and} \qquad \frac{\partial\phi}{\partial t} = \frac{\partial\phi}{\partial\theta}\frac{\partial\theta}{\partial t} \tag{F.27}$$

implies

$$\frac{\partial}{\partial t} = \mp\sqrt{\bar{h}}\frac{\partial}{\partial x} + O\left(\epsilon, \mu^2\right), \tag{F.28}$$

where $(\mp)$ corresponds to waves propagating in positive and negatives directions. Expression (F.28) provides a way to swap between space and time derivatives, once a direction of propagation is assumed. The leading order solution of (F.4) is recast using (F.28) to

$$\frac{\partial}{\partial x}\left(\widetilde{\eta} - \sqrt{\bar{h}}\langle u\rangle\right) = O\left(\epsilon, \mu^2\right). \tag{F.29}$$

Integrating from $x = -\infty$ to x and assuming wave vanishes at $x = -\infty$, yields an expression for $\langle u\rangle$ in terms of $\widetilde{\eta}$

$$\langle u\rangle = \frac{\widetilde{\eta}}{\sqrt{\bar{h}}} + O\left(\epsilon, \mu^2\right) = \frac{1}{\sqrt{\bar{h}}} sech^2\left(K\left(x - ct\right)\right) + O\left(\epsilon, \mu^2\right). \tag{F.30}$$

Note that solitary waves may form in any uniform channel of arbitrary cross-section. The dispersive strength γ depends on the cross-sectional geometry, being greater for cross-sections departing from the rectangular (e.g., those with decreasing sidewall slopes) as long as the mean depth is the same. The cross-sectional geometry also affects the effective wavelength of the solitary wave through the dispersive strength, i.e., $\lambda \sim \gamma^{1/2}$, and the sidewall slope $\lambda \sim B_0^{-1/2}$. Thus, the greater the departure of the geometry from rectangular, the longer the solitary wave is.

APPENDIX G

BRANCHING CHANNELS

The literature tackling the problem of waves propagating through junctions is scarce. Shi & Teng (1996) numerically studied waves traveling along a narrow right-angled branching channel and found that a solitary wave splits into two nearly identical solitary waves, with minor reflections and no significant role of the angles corresponding to each branch. Yuhi *et al.* (2002), on the other hand, investigated the collision of two solitary waves in T-shaped and Y-shaped branching channels, finding that the effects of the channel geometry on the transformation of the waves are significant. They studied wide channels where the ratio between the width W' and depth h_0 was of $W'/h_0 = 20-30$, being therefore beyond the range of validity of the present theory.

Shi & Teng (2005) studied long water waves propagating through branching channels of uniform depth and width. The analysis was based on a two-dimensional Boussinesq modeling of different geometries and experiments conducted in a right-angled branching channel. They focused on the effects of channel width, effective wavelength, wave amplitude and angle between channel branches, confirming that wave transmission and reflection are governed primarily by the relative width of the channel. For narrow branching channels (Figure G.1), they found that an incident solitary wave splits into two nearly identical waves of reduced amplitude, regardless of the branching angle. A negative leading reflected wave was observed, and justified arguing that a junction behaves like an expanding channel, where a depression is expected in reflected waves. For wide channels, however, they found a highly two-dimensional wave pattern. For large angles, the transmitted wave amplitude in the downstream

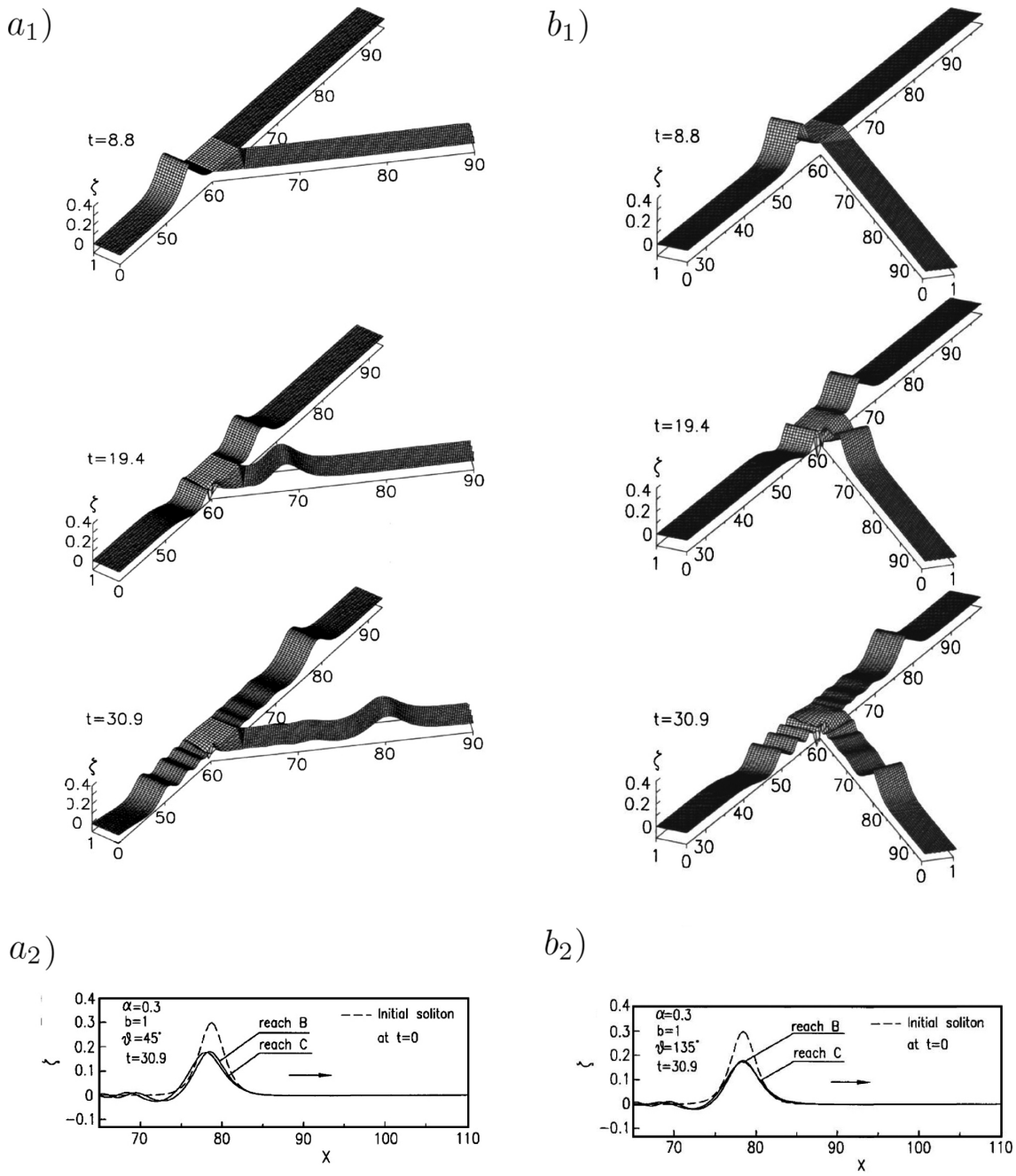

Figure G.1: Numerical results for solitary waves propagating through narrow branching channels *a*) of 45° and *b*) 135°. Panels a_1 and b_1 show the wave elevations at different times from bird's eye view. Panels a_2 and b_2 depict the comparison between the original and transmitted wave profiles along the channel centerline. Adapted from by Shi & Teng (2005).

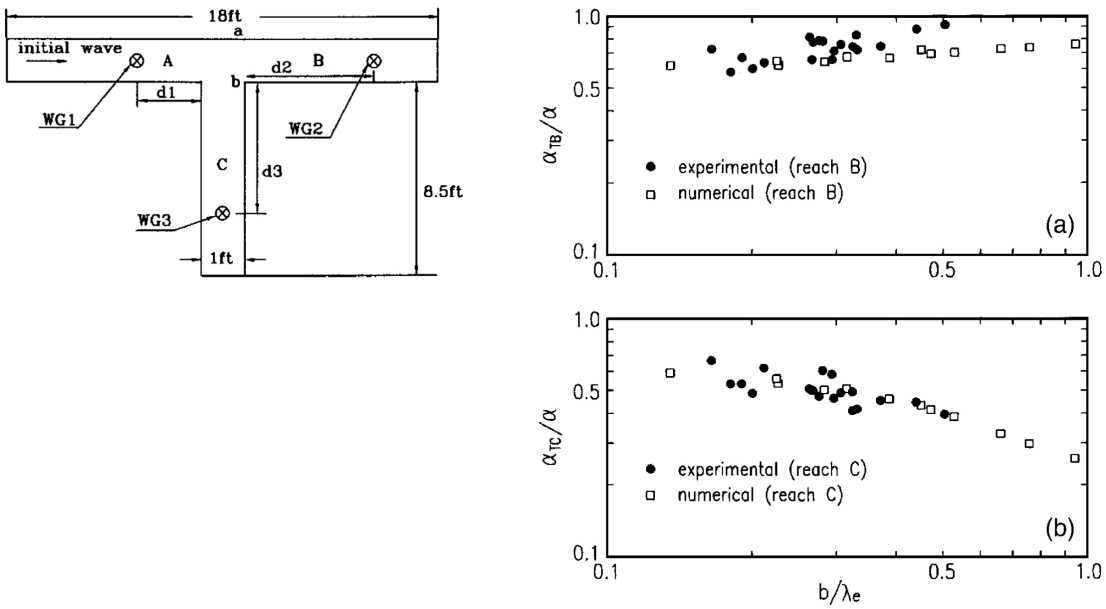

Figure G.2: Comparison between numerical and experimental results for transmitted waves in a T-shaped branching channel. Top right panel: transmitted waves in Reach B. Bottom right panel: transmitted waves in Reach C. Adapted from Shi & Teng (2005).

reach of the main straight channel became greater while the transmitted wave amplitude in the oblique downstream reach became smaller. For 90° turns, they found that both transmitted waves are similar when b/λ_e is small (Figure G.2).

By means of a conformal mapping, Nachbim & da Silva (2012) studied solitary wave propagation through branches. The use on the Schwarz-Christoffel mapping, though promising, was tested in very simple geometries. The extension to more complex geometries is mentioned as part of their future work.

A compatibility condition given by equations (G.18) and (G.31) is derived herein to solve for junctions. The compatibility conditions implies that on the junction, the surface elevation is the same for the concurrent branches and the fluxes sum up to zero. This first order approximation loses detailed information on the

wave features but retains the leading order effects on flow features.

G.1 Theoretical approach

The domain is divided into a near field near in a bend or junction and a far field on each branch, which coordinates are $x^{(i)}$ ($i = 1, 2, ...$) hereafter as shown in Figure G.3. The idea is to define the governing equations for the near field and then solve a coupled system consisting of *i*) two concurrent branches and a bend, or *ii*) three or more concurrent branches and a junction. The far field is represented by the Boussinesq-type of equations (3.95) and (3.124) for the surface-mean elevation $\widetilde{\eta}(x,t)$ and section-mean velocity $\langle u \rangle (x,t)$ for each branch

$$\frac{\partial \widetilde{\eta}}{\partial t} + \frac{1}{B_0}\frac{\partial}{\partial x^{(i)}}\left(\langle u \rangle A_0\right) + \epsilon \frac{B_0'}{2B_0}\frac{\partial \widetilde{\eta}^2}{\partial t} + \frac{\epsilon}{B_0}\frac{\partial}{\partial x^{(i)}}\left(\langle u \rangle B_0 \widetilde{\eta}\right) = 0, \tag{G.1}$$

$$\frac{\partial \langle u \rangle}{\partial t} + \frac{\partial \widetilde{\eta}}{\partial x^{(i)}} + \epsilon \langle u \rangle \frac{\partial \langle u \rangle}{\partial x^{(i)}} + \mu^2 \left[\alpha \frac{\partial \langle u \rangle}{\partial t} + \beta \frac{\partial^2 \langle u \rangle}{\partial t \partial x^{(i)}} + \gamma \frac{\partial^3 \langle u \rangle}{\partial t \partial x^{(i)2}}\right] = 0, \tag{G.2}$$

where $i = 1, 2, 3$ represents each branch. It should be noted that the leading order error of the above equations is $O\left(\epsilon^2, \epsilon\mu^2, \mu^4\right)$. The solution for the near field should ideally be of the same order. In the following section, solutions for the junction are proposed for different levels of approximation.

G.1.1 Equations for the near field

The near field is represented by the standard two-dimensional Boussinesq equations (Peregrine, 1967) expressed in terms of the surface elevation $\eta(x,y,t)$ and the depth-averaged velocity $\breve{\mathbf{u}}(x,y,z) = (\breve{u}, \breve{v})$. In vector form these equations are

$$\frac{\partial \eta}{\partial t} + \nabla \cdot \left[(h + \epsilon\eta)\,\breve{\mathbf{u}}\right] = 0, \tag{G.3}$$

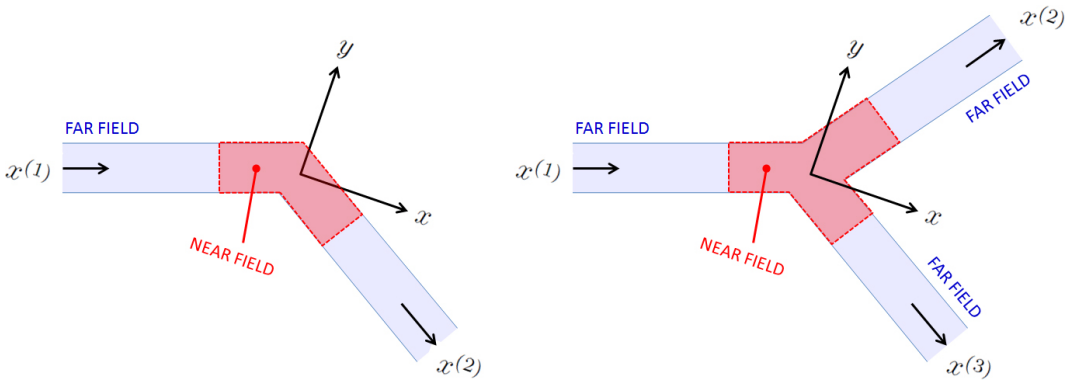

Figure G.3: Definition of regions used to solve the bends (left) and junctions (right).

$$\frac{\partial \breve{\mathbf{u}}}{\partial t} + \nabla\eta + \epsilon\breve{\mathbf{u}}\cdot\nabla\breve{\mathbf{u}} + \mu^2\left[\frac{h^2}{6}\nabla\left(\nabla\cdot\frac{\partial\breve{\mathbf{u}}}{\partial t}\right) - \frac{h}{2}\nabla\left\{\nabla\cdot\left(h\frac{\partial\breve{\mathbf{u}}}{\partial t}\right)\right\}\right] = O\left(\epsilon^2, \epsilon\mu^2, \mu^4\right), \quad \text{(G.4)}$$

where by definition $\nabla = (\partial/\partial x, \partial/\partial y)$. In Cartesian coordinate form, the conservation of mass (G.3) is expressed as

$$\frac{\partial\eta}{\partial t} + \frac{\partial}{\partial x}\left[(h+\epsilon\eta)\,\breve{u}\right] + \frac{\partial}{\partial y}\left[(h+\epsilon\eta)\,\breve{v}\right] = 0. \quad \text{(G.5)}$$

The conservation of momentum in x is

$$\begin{aligned}&\frac{\partial\breve{u}}{\partial t} + \frac{\partial\eta}{\partial x} + \epsilon\left[\breve{u}\frac{\partial\breve{u}}{\partial x} + \breve{v}\frac{\partial\breve{u}}{\partial y}\right]\\ +\mu^2\left[\frac{h^2}{6}\frac{\partial}{\partial x}\left(\frac{\partial^2\breve{u}}{\partial x\partial t} + \frac{\partial^2\breve{v}}{\partial y\partial t}\right) - \frac{h}{2}\frac{\partial^2}{\partial x^2}\left(h\frac{\partial\breve{u}}{\partial t}\right) - \frac{h}{2}\frac{\partial^2}{\partial x\partial y}\left(h\frac{\partial\breve{v}}{\partial t}\right)\right] &= O\left(\epsilon^2, \epsilon\mu^2, \mu^4\right), \quad \text{(G.6)}\end{aligned}$$

being symmetric in the y direction (thus is omitted from the derivation). In the standard two-dimensional Boussinesq equations, the longitudinal coordinate is scaled by the typical wavelength, i.e. $x = \hat{x}/\hat{\lambda}$. In the near field, however, the flow is assumed to be scaled by a typical length associated with the bend or junction. The local depth is used for the scaling, so the coordinates in the near field are defined by $\mathcal{X} = \hat{x}/\hat{h}_0$ and $\mathcal{Y} = \hat{y}/\hat{h}_0$. Since the dimensional coordinates are the same regardless of the non-dimensionalization, this implies

$$x = \mu\mathcal{X}, \qquad \text{and} \qquad y = \mu\mathcal{Y}. \quad \text{(G.7)}$$

By the chain rule, the derivatives are

$$\frac{\partial}{\partial x} = \frac{1}{\mu}\frac{\partial}{\partial \mathcal{X}} \qquad \text{and} \qquad \frac{\partial}{\partial y} = \frac{1}{\mu}\frac{\partial}{\partial \mathcal{Y}}. \tag{G.8}$$

Plugging in (G.5) and (G.6) yields

$$\frac{\partial \eta}{\partial t} + \frac{1}{\mu}\frac{\partial}{\partial \mathcal{X}}\left[h\breve{u}\right] + \frac{\epsilon}{\mu}\frac{\partial}{\partial \mathcal{X}}\left[\eta\breve{u}\right] + \frac{1}{\mu}\frac{\partial}{\partial \mathcal{Y}}\left[h\breve{v}\right] + \frac{\epsilon}{\mu}\frac{\partial}{\partial \mathcal{Y}}\left[\eta\breve{v}\right] = 0, \tag{G.9}$$

and

$$\begin{aligned}\frac{\partial \breve{u}}{\partial t} + \frac{1}{\mu}\frac{\partial \eta}{\partial \mathcal{X}} + \mu\left[\breve{u}\frac{\partial \breve{u}}{\partial \mathcal{X}} + \breve{v}\frac{\partial \breve{u}}{\partial \mathcal{Y}}\right] + \frac{h^2}{6}\frac{\partial}{\partial \mathcal{X}}\left(\frac{\partial^2 \breve{u}}{\partial \mathcal{X}\partial t} + \frac{\partial^2 \breve{v}}{\partial \mathcal{Y}\partial t}\right) \\ -\frac{h}{2}\frac{\partial^2}{\partial \mathcal{X}^2}\left(h\frac{\partial \breve{u}}{\partial t}\right) - \frac{h}{2}\frac{\partial^2}{\partial \mathcal{X}\partial \mathcal{Y}}\left(h\frac{\partial \breve{v}}{\partial t}\right) &= O\left(\epsilon^2, \epsilon\mu^2, \mu^4\right),\end{aligned} \tag{G.10}$$

for the conservation of mass and momentum in x direction respectively. The Boussinesq approximation, e.g. $O(\epsilon) = O\left(\mu^2\right) \ll 1$ has been invoked in the above. It should be emphasized that higher order terms remain small under the coordinate transformation. Arranging in orders of magnitude yields

$$\frac{\partial}{\partial \mathcal{X}}\left[h\breve{u}\right] + \frac{\partial}{\partial \mathcal{Y}}\left[h\breve{v}\right] + \mu\frac{\partial \eta}{\partial t} + \mu^2\left\{\frac{\partial}{\partial \mathcal{X}}\left[\eta\breve{u}\right] + \frac{\partial}{\partial \mathcal{Y}}\left[\eta\breve{v}\right]\right\} = 0, \tag{G.11}$$

and

$$\begin{aligned}\frac{\partial \eta}{\partial \mathcal{X}} + \mu\left\{\frac{\partial \breve{u}}{\partial t} + \frac{h^2}{6}\frac{\partial}{\partial \mathcal{X}}\left(\frac{\partial^2 \breve{u}}{\partial \mathcal{X}\partial t} + \frac{\partial^2 \breve{v}}{\partial \mathcal{Y}\partial t}\right)\right. \\ \left.\underbrace{-\frac{\partial}{\partial t}\left[\frac{h}{2}\frac{\partial^2}{\partial \mathcal{X}^2}\left(h\breve{u}\right) + \frac{h}{2}\frac{\partial^2}{\partial \mathcal{X}\partial \mathcal{Y}}\left(h\breve{v}\right)\right]}_{M}\right\} + \mu^2\left\{\overline{u}\frac{\partial \breve{u}}{\partial \mathcal{X}} + \overline{v}\frac{\partial \breve{u}}{\partial \mathcal{Y}}\right\} &= O\left(\mu\epsilon^2, \epsilon\mu^3, \mu^5\right)\end{aligned} \tag{G.12}$$

for the conservation of mass and momentum in x direction respectively. Let's focus on the term M. Since, in the standard Boussinesq equations, $\partial h/\partial x, \partial h/\partial y = O(1)$, in stretched coordinates this implies

$$\frac{\partial h}{\partial \mathcal{X}}, \frac{\partial h}{\partial \mathcal{Y}} = O(\mu). \tag{G.13}$$

The term M therefore become

$$M = \mu\left\{... - \frac{\partial}{\partial t}\left[\frac{h}{2}\frac{\partial}{\partial \mathcal{X}}\left\{h\frac{\partial \breve{u}}{\partial \mathcal{X}} + \breve{u}\underline{\frac{\partial h}{\partial \mathcal{X}}} + h\frac{\partial \breve{v}}{\partial \mathcal{Y}} + \breve{v}\underline{\frac{\partial h}{\partial \mathcal{Y}}}\right\}\right]\right\}, \tag{G.14}$$

where the underlined terms are $O(\mu)$. Furthermore,

$$\begin{aligned} M = \mu\Bigg\{... - \frac{\partial}{\partial t}\Bigg[\frac{h}{2}\Bigg(h\frac{\partial^2 \breve{u}}{\partial \mathcal{X}^2} + \underline{\frac{\partial h}{\partial \mathcal{X}}}\frac{\partial \breve{u}}{\partial \mathcal{X}} + \underline{\underline{\frac{\partial^2 h}{\partial \mathcal{X}^2}}}\breve{u} + \underline{\frac{\partial h}{\partial \mathcal{X}}}\frac{\partial \breve{u}}{\partial \mathcal{X}} \\ + \underline{\frac{\partial h}{\partial \mathcal{X}}}\frac{\partial \breve{v}}{\partial \mathcal{Y}} + h\frac{\partial^2 \breve{v}}{\partial \mathcal{X}\partial \mathcal{Y}} + \underline{\underline{\frac{\partial^2 h}{\partial \mathcal{X}\partial \mathcal{Y}}}}\breve{v} + \underline{\frac{\partial h}{\partial \mathcal{Y}}}\frac{\partial \breve{v}}{\partial \mathcal{X}}\Bigg)\Bigg]\Bigg\} \end{aligned} \tag{G.15}$$

where the double-underlined terms are $O\left(\mu^2\right)$. Plugging in (G.12) and reordering

$$\begin{aligned} \frac{\partial \eta}{\partial \mathcal{X}} + \mu\left\{\frac{\partial \breve{u}}{\partial t} + \frac{h^2}{6}\frac{\partial}{\partial \mathcal{X}}\left(\frac{\partial^2 \breve{u}}{\partial \mathcal{X}\partial t} + \frac{\partial^2 \breve{v}}{\partial \mathcal{Y}\partial t}\right) - \frac{\partial}{\partial t}\left[\frac{h^2}{2}\frac{\partial^2 \breve{u}}{\partial \mathcal{X}^2} + \frac{h^2}{2}\frac{\partial^2 \breve{v}}{\partial \mathcal{X}\partial \mathcal{Y}}\right]\right\} \\ \underbrace{-\mu\frac{\partial}{\partial t}\left(h\frac{\partial h}{\partial \mathcal{X}}\frac{\partial \breve{u}}{\partial \mathcal{X}} + \frac{h}{2}\frac{\partial h}{\partial \mathcal{X}}\frac{\partial \breve{v}}{\partial \mathcal{Y}} + \frac{h}{2}\frac{\partial h}{\partial \mathcal{Y}}\frac{\partial \breve{v}}{\partial \mathcal{X}}\right)}_{O(\mu^2)} + \mu^2\left\{\breve{u}\frac{\partial \breve{u}}{\partial \mathcal{X}} + \breve{v}\frac{\partial \breve{u}}{\partial \mathcal{Y}}\right\} \\ \underbrace{-\mu\frac{\partial}{\partial t}\left\{\frac{h}{2}\frac{\partial^2 h}{\partial \mathcal{X}^2}\breve{u} + \frac{h}{2}\frac{\partial^2 h}{\partial \mathcal{X}\partial \mathcal{Y}}\breve{v}\right\}}_{O(\mu^3)} = O\left(\mu\epsilon^2, \epsilon\mu^3, \mu^5\right) \end{aligned} \tag{G.16}$$

Expressing the derivatives of h in the original coordinates and manipulating the $O\left(\mu^2\right)$ term yields

$$\begin{aligned} \frac{\partial \eta}{\partial \mathcal{X}} + \mu\left\{\frac{\partial \breve{u}}{\partial t} - \frac{\partial}{\partial t}\left(\frac{h^2}{3}\frac{\partial^2 \breve{u}}{\partial \mathcal{X}^2} + \frac{h^2}{3}\frac{\partial^2 \breve{v}}{\partial \mathcal{X}\partial \mathcal{Y}}\right)\right\} \\ +\mu^2\left\{-\frac{\partial}{\partial t}\left(h\frac{\partial h}{\partial x}\frac{\partial \breve{u}}{\partial \mathcal{X}} + \frac{h}{2}\frac{\partial h}{\partial x}\frac{\partial \breve{v}}{\partial \mathcal{Y}} + \frac{h}{2}\frac{\partial h}{\partial y}\frac{\partial \breve{v}}{\partial \mathcal{X}} + \breve{u}\frac{\partial \breve{u}}{\partial \mathcal{X}} + \breve{v}\frac{\partial \breve{u}}{\partial \mathcal{Y}}\right)\right\} \\ -\mu^3\left\{\frac{h}{2}\frac{\partial}{\partial t}\left(\frac{\partial^2 h}{\partial x^2}\breve{u} + \frac{\partial^2 h}{\partial x \partial y}\breve{v}\right)\right\} = O\left(\mu\epsilon^2, \epsilon\mu^3, \mu^5\right) \end{aligned} \tag{G.17}$$

G.1.2 First order solution

To a leading order error of $O(\mu)$, the conservation of momentum (G.12) becomes

$$\widehat{\nabla}\eta = \frac{\partial \eta}{\partial \mathcal{X}}, \frac{\partial \eta}{\partial \mathcal{Y}} = O(\mu). \tag{G.18}$$

where $\widehat{\nabla} = (\partial/\partial\mathcal{X}, \partial/\partial\mathcal{Y})$ is the gradient in stretched coordinates. This implies $\eta(\mathcal{X}, \mathcal{Y})$ is constant on the domain and therefore $\widetilde{\eta}(\mathcal{X}, \mathcal{Y})$ has the same value for converging branches at the bend/junction.

Conservation of mass, (G.11) is reduced to

$$\frac{\partial}{\partial\mathcal{X}}\left[h\breve{u}\right] + \frac{\partial}{\partial\mathcal{Y}}\left[h\breve{v}\right] = O(\mu), \tag{G.19}$$

Using (G.13) in (G.19) yields

$$\widehat{\nabla}\cdot\breve{\mathbf{u}} = \frac{\partial\breve{u}}{\partial\mathcal{X}} + \frac{\partial\breve{v}}{\partial\mathcal{Y}} = O(\mu). \tag{G.20}$$

By virtue of the Gauss theorem, the above is integrated on a control volume defined in Figure G.4. Since the velocity is already depth-integrated, it suffices to integrate over a surface defined by the instantaneous water level. The left hand side of equation (G.20) becomes

$$I = \iint_{\Omega}\left(\widehat{\nabla}\cdot\breve{\mathbf{u}}\right)dA \quad = \quad \int_{\Gamma}(\breve{\mathbf{u}}\cdot\hat{\mathbf{n}})\,dS = \sum_{i=1}^{N}\int_{\Gamma^{(i)}}(\breve{\mathbf{u}}\cdot\hat{\mathbf{n}})\,dS, \tag{G.21}$$

where $\hat{\mathbf{n}}$ is the unit normal, N is the number of branches ($N = 2$ for bends and $N \geq 3$ for junctions) and S is a differential element in the spanwise direction to each opening. Separating between inlets and outlets

$$I \quad = \quad \sum_{i=1}^{N_{in}}\int_{-s_r^{(i)}}^{s_l^{(i)}}\breve{u}_n dy - \sum_{i=1}^{N_{out}}\int_{-s_r^{(i)}}^{s_l^{(i)}}\breve{u}_n dy, \tag{G.22}$$

where $\breve{u}_n$ is the depth averaged velocity normal to each opening

$$\breve{u}_n(x,y,t) = \frac{1}{h}\int_{-h^{(i)}}^{\epsilon\eta^{(i)}} u_n(x,y,z,t)\,dz, \tag{G.23}$$

and $h(x,y)$ the depth. Rewritting

$$I \quad = \quad \sum_{i=1}^{N_{in}}\int_{-s_r^{(i)}}^{s_l^{(i)}}\left[\frac{1}{h}\int_{-h^{(i)}}^{\epsilon\eta^{(i)}} u_n dz\right]dy - \sum_{i=1}^{N_{out}}\int_{-s_r^{(i)}}^{s_l^{(i)}}\left[\frac{1}{h}\int_{-h^{(i)}}^{\epsilon\eta^{(i)}} u_n dz\right]dy. \tag{G.24}$$

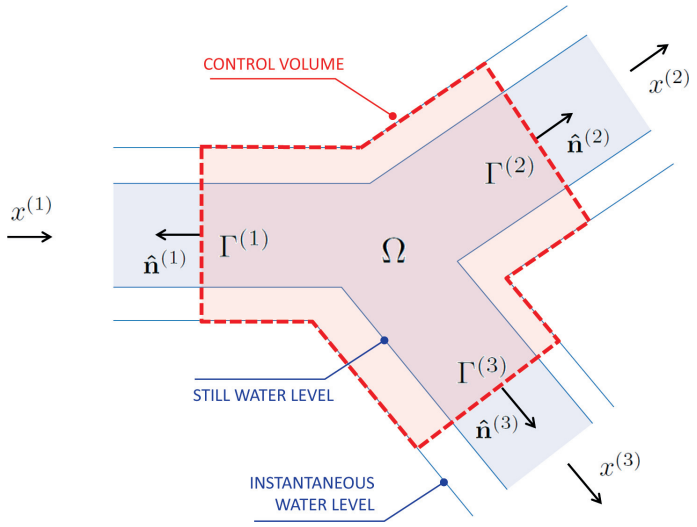

Figure G.4: Definition of control volume at a junction.

Assuming that at each branch the depth is a slowly-varying function constant across each branch, i.e. $h(x,y) = \breve{h}(x) + O(\epsilon)$, yields

$$I = \sum_{i=1}^{N_{in}} \frac{1}{\breve{h}^{(i)}} \int_{-s_r^{(i)}}^{s_l^{(i)}} \int_{-h^{(i)}}^{\epsilon\eta} u_n dz dy - \sum_{i=1}^{N_{out}} \frac{1}{\breve{h}^{(i)}} \int_{-s_r^{(i)}}^{s_l^{(i)}} \int_{-h^{(i)}}^{\epsilon\eta} u_n dz dy + O(\epsilon). \quad \text{(G.25)}$$

Since

$$\langle u_n \rangle (x,t) = \frac{1}{A} \int_{-h^{(i)}}^{\epsilon\eta^{(i)}} u_n (x,y,z,t)\, dz, \quad \text{(G.26)}$$

then

$$I = \sum_{i=1}^{N_{in}} \frac{A^{(i)}}{\breve{h}^{(i)}} \langle u_n \rangle^{(i)} - \sum_{i=1}^{N_{out}} \frac{A^{(i)}}{\breve{h}^{(i)}} \langle u_n \rangle^{(i)} + O(\epsilon). \quad \text{(G.27)}$$

Invoking the expansion of the cross-sectional area, i.e. $A(x,t) = A_0(x) + \epsilon$, yields

$$I = \sum_{i=1}^{N_{in}} \frac{A_0^{(i)}}{\breve{h}^{(i)}} \langle u_n \rangle^{(i)} - \sum_{i=1}^{N_{out}} \frac{A_0^{(i)}}{\breve{h}^{(i)}} \langle u_n \rangle^{(i)} + O(\epsilon). \quad \text{(G.28)}$$

In terms of the surface width, the above becomes

$$I = \sum_{i=1}^{N_{in}} B_0^{(i)} \langle u_n \rangle^{(i)} - \sum_{i=1}^{N_{out}} B_0^{(i)} \langle u_n \rangle^{(i)} + O(\epsilon), \quad \text{(G.29)}$$

which in equation (G.20) yields

$$\sum_{i=1}^{N_{in}} B_0^{(i)} \langle u_n \rangle^{(i)} - \sum_{i=1}^{N_{out}} B_0^{(i)} \langle u_n \rangle^{(i)} = O(\mu), \quad \text{(G.30)}$$

implying that the normal fluxes in all open boundaries are balanced. For a junction of three branches, the above becomes

$$B_0^{(2)} \langle u_n \rangle^{(2)} + B_0^{(3)} \langle u_n \rangle^{(3)} - B_0^{(1)} \langle u_n \rangle^{(1)} = O(\mu), \tag{G.31}$$

The first order solution given by equations (G.18) and (G.31) indicates that the angle of the branches is irrelevant for the flow properties. In mathematical terms, the near field is reduced to compatibility conditions on a single common node where the surface elevation is the same for the concurrent branches and the fluxes sum up to zero. The first order approximation loses some information on the wave features in the branching point, retaining the leading order effects (e.g. such as the tilt in surface elevation shown in Figures 7.1 a_3 and 7.1 b_3) but retains essential flow features.

From the operational perspective, bends and junctions require a different treatment. For bends, curvature plays no role in wave propagation and the far field equations could be applied with no restriction on the plan curvature. A drawback of this approach is that reflection triggered by curvature, though small (e.g. Figures 7.1 a_1 and 7.1 b_1), is neglected. For junctions, on the other hand, a coupled system of equations for concurrent branches has to be solved, provided that the compatibility conditions are fulfilled at the single junction node. The relative angle of the different branches is irrelevant in the solution.

The leading order solution provides an rough characterization of the flow field, which corresponds to empirical observations in narrow channels where the width is much smaller than the typical wavelength. The incompatibility in the orders of magnitudes of the errors of approximation between the near- and far-field solutions implies a degradation of the solution in the vicinity of the bend or junction.

G.1.3 Second order solution

To a leading order error of $O\left(\epsilon,\mu^2\right)$, equations (G.11) and (G.12) are reduced to

$$\frac{\partial \breve{u}}{\partial \mathcal{X}}+\frac{\partial \breve{v}}{\partial \mathcal{Y}}+\frac{\mu}{h}\left(\frac{\partial \eta}{\partial t}+\breve{u}\frac{\partial h}{\partial x}+\breve{v}\frac{\partial h}{\partial y}\right)=O\left(\epsilon,\mu^2\right), \tag{G.32}$$

and

$$\frac{\partial \eta}{\partial \mathcal{X}}+\mu\left\{\frac{\partial \breve{u}}{\partial t}-\frac{\partial}{\partial t}\left(\frac{h^2}{3}\frac{\partial^2 \breve{u}}{\partial \mathcal{X}^2}+\frac{h^2}{3}\frac{\partial^2 \breve{v}}{\partial \mathcal{X}\partial \mathcal{Y}}\right)\right\}=O\left(\mu^2,\epsilon\right) \tag{G.33}$$

where the underlined terms are $O(\mu)$. Equation (G.32) implies

$$\frac{\partial \breve{u}}{\partial \mathcal{X}}+\frac{\partial \breve{v}}{\partial \mathcal{Y}}=O(\mu), \tag{G.34}$$

Equation (G.33) can be expressed as

$$\frac{\partial \eta}{\partial \mathcal{X}}+\mu\frac{\partial \breve{u}}{\partial t}=O\left(\epsilon,\mu^2\right), \qquad \frac{\partial \eta}{\partial \mathcal{Y}}+\mu\frac{\partial \breve{u}}{\partial t}=O\left(\epsilon,\mu^2\right). \tag{G.35}$$

Equations (G.32) and (G.35) constitute a two-dimensional system of equations with a structure which is similar to the linear shallow water equations but where the orders of magnitude is slightly different. In vector form, these equations

$$h\hat{\nabla}\cdot\breve{\mathbf{u}}=-\mu\frac{\partial \eta}{\partial t}-\breve{\mathbf{u}}\cdot\underline{\hat{\nabla}h}+O\left(\epsilon,\mu^2\right), \tag{G.36}$$

$$\hat{\nabla}\eta+\mu\frac{\partial \breve{\mathbf{u}}}{\partial t}=O\left(\epsilon,\mu^2\right), \tag{G.37}$$

can be combined to yield

$$\mu^2\frac{\partial^2 \eta}{\partial t^2}-h\hat{\nabla}^2\eta=-\mu\frac{\partial \breve{\mathbf{u}}}{\partial t}\cdot\underline{\hat{\nabla}h}, \tag{G.38}$$

which is a form of a two dimensional wave equation.

The second order solution given by equations (G.36) and (G.37) require solving a two dimensional slightly modified version of the linear shallow water equations in the near field, with boundary conditions provided from the branches. The

transition between the one-dimensional equations in the far field and the two-dimensional equations for the near field needs an overlapping region where the boundary conditions are provided by its counterpart model. Ideally, both models should be two-way coupled (i.e. solved simultaneously in the near far fields), though simplified approaches can be used (e.g. alternating and/or iterative schemes). Since the unknown variables of each model are essentially different (e.g. cross-sectional averages and depth averaged velocities for the far and near field, respectively), a transformation must be carried out to give adequate physical sense to the exchanging quantities (Sitanggang & Lynett, 2009). It is anticipated that at this order of approximation, the relative angle between branches plays a role in the flow field, and two dimensional flow features, such as reflection in bends, would take reflection into account.

The use of the second order solution is associated with a leading order error of $O\left(\epsilon,\mu^2\right)$, which is larger than in the Boussinesq-type equations in the far field. Its application implies a degradation of the solution in the vicinity of the bend/junction, which can affect the concurrent branches.

Higher order solutions given by equations (G.11) and (G.17) are indeed two-dimensional and incorporate nonlinear terms and third order derivatives. From the conceptual standpoint, these solutions are not that different from the second order solution as they require the use of an hybrid model with different dimensionality for the near and far fields. From the numerical standpoint, the difference with the second order solution relies on the definition of the boundary conditions for the third order derivatives and on the nonlinear terms. From the analytical perspective, its use is consistent with the governing equations for the far field.

BIBLIOGRAPHY

[1] Mohammad Bagus Adityawan, Min Roh, Hitoshi Tanaka, Akira Mano, Akira Mano, and Keiko Udo. Investigation of tsunami propagation characteristics in river and on land induced by the great east japan tsunami. *Journal of earthquake and tsunami*, 06(3):1250033 1–22, 2012.

[2] G. B. Airy. Tides and waves. *Encyclopaedia metropolitana*, 5:241–396, 1845.

[3] F. Benet and J. A. Cunge. Analysis of experiments on secondary undulations caused by surge waves in trapezoidal channels. *Journal of Hydraulic Research*, 9:11–33, 1971.

[4] Natalie Bonneton, Philippe Bonneton, Jean-Paul Parisot, Aldo Sottolichio, and Guillaume Detandt. Tidal bore and mascaret. example of garonne and seine river. *Comptes Rendus Geoscience*, 344:508–515, 2012.

[5] J. Boussinesq. Theorie des ondes et des remous qui se propagent le long d'un canal rectangulaire horizontal, en communiquant au liquide contenu dans ce cnala des vitesses sensiblemente pareilles de la surface au fond. *Journal de mathemtiques pures et appliquees. 2e serie. Tome 17*, pages 55–108, 1872.

[6] Maurizio Brocchini. A reasoned overover on boussinesq-type models: the interplay between physics, mathematicas and numerics. *Proceedings of The Royal Society A*, 469:20130496:1–27, 2013.

[7] P. Chang. The solitary wave in a channel of varying width. Master's thesis, University of California, San Diego, 1978.

[8] Peter Chang, W.K. Melville, and Johns W. Miles. On the evolution of a solitary wave in a gradually varying channel. *Journal of Fluid Mechanics*, 95:401–414, 1979.

[9] Hubert Chanson. *The Hydraulics of Open Channel Flow: An Introduction. Basic principles, sediment motion, hydraulic modelling, design of hydraulic structures*. Elsevier, second edition, 2004.

[10] Hubert Chanson. *Tidal bores, Aegir, Eagre, Mascaret, Pororoca: theory and observations*. World Scientific, 2012.

[11] David A. Clarke. A primer on tensor calculus, June 2011.

[12] Manuel Contreras and Patricio Winckler. Prdidas de vidas, viviendas, infraestructura y embarcaciones por el tsunami del 27 de febrero de 2010 en la costa central de chile. *Obras y Proyectos*, 14:6–19, 2013.

[13] B. de Saint Venant. Theorie du movement non permanent des eaux, avec application aux crues des rivieres et a l'introduction des marees dans leur lit. *Comptes Rendus de l'Academie des Sciences*, 73:147–54 237–40, 1871.

[14] Robert G. Dean and Robert A. Dalrymple. *Water wave mechanics for engineers and scientists*, volume 2 of *Advanced Series on Ocean Engineering*. Advanced Series on Ocean Engineering, 5 Toh Tuck Link, Singapore 596224, first edition, 1991.

[15] Ira Didenkulova and Efim Pelinovsky. Non-dispersive traveling waves in inclined shallow water channels. *Physics Letters A*, pages 3883–3887, 2009.

[16] Ira Didenkulova and Efim Pelinovsky. Nonlinear wave evolution and runup in an inclined channel of a parabolic cross-section. *Physics of Fluids*, 23:086602, 2011.

[17] Marteen W. Dingemans. *Water wave propagation over uneven bottoms. Part 2. Non-linear wave propagation*, volume 13 of *Advanced Series on Ocean Engineering*. World Scientific, 1997.

[18] Robert F. Dressler. New nonlinear shallow-flow equations with curvature. *Journal of Hydraulic Research*, 16(3):205–222, 1978.

[19] U. M. Eidsvig, Z. Medina-Cetina, V. Kveldsvik, S. Glimsdal, C. B. Harbitz, and F. Sandersen. Risk assessment of a tsunamigenic rockslide at aknes. *Natural Hazards*, 56:529–545, 2011.

[20] J. D. Fenton. Cnoidal waves and bores in uniform channels of arbitrary cross-section. *Journal of Fluid Mechanics*, 58:417–434, 1973.

[21] J.D. Fenton and G.V. Nalder. Long wave equations for waterways curved in plan. In *26th Congress of the International Association for Hydraulic Research, London*. International Association for Hydraulic Research, 11-15 September 1995.

[22] H. Fritz, C. Petroff, P. Catalan, R. Cienfuegos, P. Winckler, N. Kalligeris, R. Weiss, S. Barrientos, G. Meneses, Valderas-Bermejo C., C. Ebeling, T. Papadopoulos, M. Contreras, R. Almar, J. Dominguez, and C. Synolakis. Field

survey of the 27 february 2010 chile tsunami. *Pure and Applied Geophysics*, 168:1989–2010, 2011.

[23] A. Galan, G. Simarro, A. Orfila, and Philip L.-F. Liu. Fully nonlinear model for water wave propagation from deep to shallow waters. *Journal of Waterway*, 138:362–371, 2012.

[24] S. Glimsdal, G. K. Pedersen, C. B. Harbitz, and F. Lovholt. Dispersion of tsunamis: does it really matter? *Natural Hazards and Earth System Sciences*, 13:1507–1526, 2013.

[25] M. F. Gobbi, J. T. Kirby, and G. Wei. A fully nonlinear boussinesq model for surface waves. part 2. extension to o(kh)4. *Journal of Fluid Mechanics*, 405:181–210, 2000.

[26] C.B. Harbitz, S. Glimsdal, F. Lovholt, V. Kveldsvik, G. K. Pedersen, and A. Jensen. Rockslide tsunamis in complex fjords: From unstable rock slope at akerneset to tsunami risk in western norway. *Coastal Engineering*, 88:101–122, 2014.

[27] J. T. Kirby, R. A. Dalrymple, and H. Kaku. Parabolic approximations for water waves in conformal coordinate systems. *Coastal Engineering*, 23:185–213, 1994.

[28] James T. Kirby and Padmaraj Vengayil. Nonresonant and resonant reflection of long waves in varying channels. *Journal of Geophysical Research*, 93(C9):10782–10796, 1988.

[29] James T. Kirby, Ge Wei, Qin Chen, Andrew B. Kennedy, and Robert A. Dalrymple. *FUNWAVE 1.0. Fully Nonlinear Boussinesq Wave Model. Documentation and User's Manual. Research Report NO. CACR-98-06*. Center for Applied Coastal Research. Department of Civil Engineering. University of Delaware, Newark, DE 19716, September 1998.

[30] D. J. Korteweg and G. DeVries. On the change of form of long waves advancing in a canal, and on a new type of long stationary waves. *Philosophical Magazine. Series 5*, 39:422–443, 1895.

[31] Sir Horace Lamb. *Hdrodynamics*. Dover Publications, 1932.

[32] Erika Kristina Lindstrom, Geir K. Pedersen, Atle Jensen, and Sylfest Glims-

dal. Experiments on slide generated waves in a 1:500 scale fjord model. *Coastal Engineering*, 92:12–23, 2014.

[33] Dishi Liu. *Uncertainty Quantification with Shallow Water Equations*. Dissertation, Carl-Friedrich-Gauss Faculty, Institute of Technology, University of Braunschweig and the Faculty of Engineering, University of Florence, 2010.

[34] Philip L.-F. Liu and Inigo J. Losada. Wave propagation modeling in coastal engineering. *Journal of Hydraulic Research*, 40(3):229–240, 2002.

[35] P. J. Lynett and P. L.-F. Liu. A two-layer approach to wave modelling. *Proc. R. Soc. A*, 460:2637–2669, 2004.

[36] Per A. Madsen and Ole R. Sorensen. A new form of the boussinesq equations with improved linear dispersion characteristics. part 2. a slowly-varying bathymetry. *Coastal Engineering*, 18:183–204, 1992.

[37] Agnes Maurel, ean Francois Mercier, and Simon Flix. Propagation in waveguides with varying cross section and curvature: a new light on the role of supplementary modes in multi-modal methods. *Proc. R. Soc. A*, 470:1–22, 2014.

[38] C.C. Mei, Michael Stiassnie, and Dick K.-P. Yue. *Theory and applications of ocean surface waves. Part 2: Nonlinear aspects*, volume 23 of *Advanced Series on Ocean Engineering*. World Scientific, 2005.

[39] John Miles. The boussinesq regime for waves in a gradually varying channel. In *Twelfth Symposium. Naval Hydrodynamics*, pages 523–528. National Academy of Sciences, 1979.

[40] John Miles. On the korteweg-de vries equation for a gradually varying channel. *Journal of Fluid Mechanics*, 91:181–190, 1979.

[41] Robert A. Morton, Guy Gelfenbaum, Mark L. Buckley, and Bruce M. Richmond. Geological effects and implications of the 2010 tsunami along the central coast of chile. *Sedimentary geology*, 242:34–51, 2011.

[42] Andre Nachbin and Vanessa DaSilva. Solitary waves in open channels with abrupt turns and branching points. *Journal of Nonlinear Mathematical Physics*, 19:1 – 21, 2012.

[43] O. Nwogu. Chapter 35. nonlinear evolution of directional wave spectra in

shallow water. In *Coastal Engineering Proceedings.*, volume 1, pages 467–481, 1994.

[44] Okey Nwogu. Alternative form of boussinesq equations for nearshore wave propagation. *Journal of Waterway, Port, Coastal and Ocean Engineering. ASCE*, 119(6):618–638, November/December 1993.

[45] D. H. Peregrine. Long waves on a beach. *Journal of Fluid Mechanics*, 27:815–827, 1967.

[46] D. H. Peregrine. Long waves in a uniform channel of arbitrary cross-section. *Journal of Fluid Mechanics*, 32:353–365, 1968.

[47] D. H. Peregrine. Solitary waves in trapezoidal channels. *Journal of Fluid Mechanics*, 35:1–6, 1969.

[48] A. S. Peters. Rotational and irrotational solitary waves in a channel with arbitrary cross. *Communications on Pure and Applied Mathematics*, XIX-4:445–471, 1966.

[49] A. Preissmann and J. A. Cunge. Low-amplitude undulating hydraulic jump in trapezoidal canals. *Journal of Hydraulic Research*, 5:263–279, 1967.

[50] J. Scott Rusell. Report on waves. Technical report, British Association for the Advancement of Science, 1842.

[51] J. A. Sandover and C. Taylor. Cnoidal waves and bores. *La Houille Blanche*, (3):443–465, July-August 1962.

[52] SERNAGEOMIN. Press release (in spanish): Sernageomin entrega mapas preliminares de remociones en masa de la zona del fiordo aisen, de las cercanias de puerto aisen y puerto chacabuco. May 2007.

[53] M. C. Shen. Asymptotic theory of unsteady three-dimensional waves ina a channel of arbitrary cross sectio. *SIAM Journal on Applied Mathematics*, 17:260–271, March 1969.

[54] A. Shi and M. H. Teng. Propagation of solitary wave in channels of complex configurations. In A. T. Chwang, J. H. Lee, and D. Y. Leung, editors, *Proc. 2nd Intl Conf. on Hydrodynamics*, Balkema, Rotterdam, 1996.

[55] Aimim Shi and Michelle H. Teng. Linear and nonlinear modeling of long waves propagating around channel bends. In Billy Edge, editor, *26th International Conference on Coastal Engineering*, pages 433–442, 1998.

[56] Aimim Shi, Michelle H. Teng, and Theodore Y. Wu. Propagation of solitary waves through significantly curved shallow water channels. *Journal of fluid mechanics*, 362:157–176, 1998.

[57] Aimin Shi, Michelle H. Teng, and Mei Sou. Propagation of long water waves through branching channels. *Journal of Engineering Mechanics*, 131(8):859–871, August 2005.

[58] J. B. Shiach and C. G. Mingham. A temporally second-order accurate godunov-type scheme for solving the extended boussinesq equations. *Coastal Engineering*, 56:32–45, 2009.

[59] Nobuo Shuto. Nonlinear long waves in a channel of variable section. *Coastal Engineering in Japan*, 17:1–12, 1974.

[60] Gonzalo Simarro, Alejandro Orfila, and Alvaro Galan. Linear shoaling in boussinesq-type wave propagation. *Coastal Engineering*, 80:100–106, 2013.

[61] K. I. Sitanggang and P. J. Lynett. Multi-scale simulation with a hybrid boussinesq-rans hydrodynamicmodel. *Int. J. Numer. Meth. Fluids*, 62:1013–1046, 2009.

[62] J. J. Stoker. In *Water waves. The mathematical theory with applications*. New York University, 1968.

[63] Ib A. Svendsen. *Introduction to Nearshore Hydrodynamics*, volume 24 of *Advanced Series on Ocean Engineering*. World Scientific, 5 Toh Tuck Link, Singapore 596224, first edition, 2006.

[64] Weiyan Tan. *Shallow water hydrodynamics: mathematical theory and numerical solution for a two-dimensional system of shallow water equations*. Elsevier Oceanography Series, 1992.

[65] M. H. Teng. Boussinesq solution for solitary waves in uniform channels with sloping walls. *Proceedings of the Institution of Mechanical Engineers, Part C: Journal of Mechanical Enginering Science*, 214:781–787, 2000.

[66] Michelle H. Teng. *Forced emissions of nonlinear water waves in channels of arbitrary shape*. PhD thesis, California Institute of Technology, 1990.

[67] Michelle H. Teng and Theodore Y. Wu. Nonlinear water waves in channels of arbitrary shape. *Journal of Fluid Mechanics*, 242:211–233, 1992.

[68] Michelle H. Teng and Theodore Y. Wu. Evolution of long water waves in variable channels. *Journal of Fluid Mechanics*, 266:303–317, 1994.

[69] Michelle H. Teng and Theodore Y. Wu. Effect of cross-sectional geometry on long wave generation and propagation. *Physics of Fluids*, 9(11):1–10, November 1997.

[70] A. Treske. Undular bores (favre-waves) in open channels - experimental studies. *Journal of Hydraulic Research*, 32:355–370, 1994.

[71] R. A. R. Tricker. *Bores, breakers, waves and wakes*. Mills & Boon Limited, 1964.

[72] F. Ursell. The long-wave paradox in the theory of gravity waves. *Mathematical Proceedings of the Cambridge Philosophical Society*, null:685–694, 1953.

[73] Mauricio Villagran, Rodrigo Cienfuegos, Patricio Cataln, and Rafael Almar. Morphological response of central chile sandy beaches to the 8.8 mw 2010 earthquake and tsunami. In *Coastal Dynamics 2013*, 2013.

[74] Ge Wei and James T. Kirby. Time dependent numerical code for extended boussinesq equations. *Journal of Waterway, Port, Coastal and Ocean Engineering. ASCE*, 121(5):251–261, 1995.

[75] Ge Wei, James T. Kirby, Stephan T. Grilli, and Ravishankar Subramanya. A fully nonlinear boussinesq model for surface waves. part 1. highly nonlinear unsteady waves. *Journal of Fluid Mechanics*, 294:71–92, 1995.

[76] Chou Xian-chu. The solitary waves in a gradually varying channel of arbitrary cross-section. *Applied Mathematics and Mechanics*, 2(4):429–440, 1981.

[77] M. Yuhi, H. Ishida, and H. Mase. Numerical study of solitary wave propagation in curved channels. *Proc. 27th Int. Conf. Coastal Eng.*, pages 519–532, 2002.